Ollscoil na hÉireann, Corcaigh

**National University of Ireland, Cork**


# Multiferroic Investigations of Aurivillius Phase Thin Films

Thesis presented by

**Louise Colfer**

**0000-0002-3600-6338**

for the degree of

**Doctor of Philosophy**

**University College Cork**

**School of Chemistry**

Head of School: Professor Anita Maguire

Lead Supervisor: Dr Lynette Keeney

Co-supervisor: Dr Brenda Long

2023

# Table of Contents

## Declaration

This is to certify that the work I am submitting is my own and has not been submitted for another degree, either at University College Cork or elsewhere. All external references and sources are clearly acknowledged and identified within the contents. I have read and understood the regulations of University College Cork concerning plagiarism and intellectual property.

Louise Colfer

29th September 2023

Date

## Acknowledgments

I would like to thank many people for their support and guidance over the course of my PhD. I appreciate the supervision and expertise provided by Dr. Lynette Keeney and Dr. Brenda Long. Thanks to my Mam and Dad, Siobhán and Padraig, along with the rest of my family Seán, John, Joanne, Niamh and Ciara, my extended family and neighbours for their encouragement throughout my life and education. I'm grateful to Michael for his support and always encouraging me to do my best and to the friends I have made in Wexford and Cork for making my time over the last few years very enjoyable.

## Abstract

In recent years, the amount of data being created and processed is growing at a much faster rate than the rate of computational storage technology development. With CMOS technologies reaching their miniaturisation limits, new disruptive materials are needed to increase data storage capabilities. Technological road-maps have identified room temperature, non-volatile magnetoelectric multiferroic materials as promising candidates for memory scaling within future memory storage devices. Although multiferroic memory devices have the potential to revolutionise memory storage technologies, commercial devices successfully utilising multiferroics have not yet come to fruition. The focus of this thesis is to understand and optimise a rare example of a room temperature magnetoelectric multiferroic, $Bi_6Ti_xFe_yMn_zO_{18}$ (B6TFMO; x = 2.80 to 3.04; Y = 1.32 to 1.52; Z = 0.54 to 0.64). Aurivillius phase materials, $(Bi_2O_2)(A_{n-1}B_nO_{3n+1})$, where ferroelectric perovskite units are interleaved between dielectric $[Bi_2O_2]^{2+}$ layers, are flexible scaffolds for technological applications. While earlier studies indicated that B6TFMO is a promising material for future memory devices, my thesis presents significant advances in the characterisation, understanding and optimisation required towards implementing the material in fully realised devices.

In this work, correlation between the octahedral tilting and atomic-level structural distortions with functional electronic and magnetic properties of B6TFMO were determined, revealing that crystal field splitting of the $Ti^{4+}$ octahedra is influenced by its position within the Aurivillius unit cell. Theoretical calculations determined that this is predominantly driven by changes in the extent of tetragonal distortion along the *c*-direction. Atomic scale mapping of polar displacements reveals this has a direct impact on the ferroelectric properties. Polarisation is largest towards the outer perovskite cells, correlating with an increased extent of local tetragonal distortion of octahedral geometries. Experiments demonstrate that tilting of the $BO_6$ octahedra competes with the extent of tetragonal distortion of the $TiO_6$ octahedra, where the degree of octahedral tilting increases towards the central layers of this Aurivillius system, where the magnetic cations preferentially partition. This work presents the first indication that octahedral tilting might be an important enabler of long-range magnetic interactions and subsequent multiferroic behaviour in B6TFMO.

Delving deeper into fundamental understandings of B6TFMO's antipolar and magnetic behaviour, the purposeful inclusion of structural defects within the layered structure of

B6TFMO and how they can impart elastic strain and electrostatic energy changes which in turn influence polar behaviour is explored. The findings show that the vicinal sapphire substrates (mis-cut angle 0.2 º to 10 º) are successful for promoting the propagation of sub-unit-cell defects and disruptions to the periodicity of the Aurivillius phases. This has a marked effect on the film morphology and ferroelectric properties. Macroscopic and local measurements show that defect, crystal grain and ferroelectric domain density increases with increasing substrate mis-cut angle. Atomic resolution polarisation mapping showed that charged domain walls alongside exotic polar vortices are facilitated by OPBs when two OPB defects are spaced 5 nm apart. This work provides insight into methods for successfully controlling defect levels and how polar vortex domain walls and charged domain walls are promoted within layered multiferroics by tailoring the underlying substrate that the film is grown on.

Moving on from vicinal sapphire surfaces, patterned sapphire with *3D* domes were used to encourage the growth of the Aurivillius grains towards an upright geometry. An increased number of non-(00*l*) reflections were present in the B6TFMO films on patterned sapphire along with evidence from STEM imaging showing that B6TFMO grains grow along the incline of the patterned sapphire domes. With the growth of the crystal grains towards an upright geometry it would be expected that access to the major *a*-axis polarisation via out-of-plane measurement would be improved, however with a maximum inclination angle of 60 ° achieved with the *3D* dome architectures, the out-of-plane piezoresponse of the samples remained weaker than the in-plane piezoresponse. Studies of the magnetic properties of the films demonstrated that the B6TFMO samples were ferromagnetic at room temperature. These findings provide further evidence of room temperature multiferroic behaviour in B6TFMO.

Lastly, the role of bismuth excess and substrate strain were investigated to optimise the epitaxial growth of B6TFMO via DLI-CVD. A single-step deposition method on epitaxial substrates was developed to allow the successful synthesis of continuous 45 nm thick B6TFMO films at thicknesses relevant to applications as piezoelectric actuators, sensors and energy harvesters. These films nucleated via a layer-by-layer growth mode and were found to have a strong in-plane ferroelectric response with isotropic domains. Film purity was enhanced with utilisation of epitaxial substrate with appropriate lattice match to B6TFMO

and by optimising the amount of bismuth precursor used. In this work, progress was made towards the optimisation of epitaxially grown B6TFMO films, allowing greater control of film orientation and augmenting strain-induced enhancement of multiferroic properties in future data storage devices.

Overall, this research has increased understanding of the fundamental mechanisms governing the ferroelectric and ferromagnetic properties of B6TFMO. The work has elucidated some of the key requirements fundamental to the manifestation of polar topologies and has created strategies for the tailoring of novel polar topologies. This combination of new material understanding and new growth optimisation of room temperature multiferroics contributes to solving the 'big data' problem. Application of B6TFMO in future technologies based on ultra-high density, energy efficient memory devices, spintronic devices, multilevel resistance control (memristive and synaptic devices) and energy-efficient neuromorphic "brain inspired" devices are envisioned.

# List of Publications

## Publications in Preparation

**Colfer, L.**; Bagués, N.; Noor-A-Alam, M.; Schmidt, M.; Nolan, M.; McComb, D.W.; Keeney, L.; Atomic level origin of the impact of octahedral tilting and tetragonal distortions on the functional properties of the room temperature multiferroic $Bi_6Ti_3Fe_{1.5}Mn_{0.5}O_{18}$.

**Colfer, L.**; Schmidt, M.; Bagués, N.; Conroy, M.; Keeney, L.; Growth of $Bi_6Ti_3Fe_{1.5}Ti_{0.5}O_{18}$ Thin Films on Vicinal Sapphire Substrates to Promote Sub-unit Cell Defects.

**Colfer, L.**; Bansal, M.; Stock, S.; Sheehan, B.; Peters, J.P.; Maity, T.; Keeney, L.; Influence of Patterned Sapphire Substrates on the Multiferroic Properties of Aurivillius Phase Thin Films.

## Journal Publications

Keeney, L.; **Colfer, L**.; Dutta, D.; Schmidt, M.; Wei, G., What lies beneath? Investigations of atomic force microscopy-based nano-machining to reveal sub-surface ferroelectric domain configurations in ultrathin films. *Microstructures* 2023

Moore, K.; O'Connell, E. N.; Griffin, S. M.; Downing, C.; **Colfer, L**.; Schmidt, M.; Nicolosi, V.; Bangert, U.; Keeney, L.; Conroy, M., Charged Domain Wall and Polar Vortex Topologies in a Room-Temperature Magnetoelectric Multiferroic Thin Film. *ACS Applied Materials & Interfaces* 2022

Keeney, L.; **Colfer, L**.; Schmidt, M., Probing Ferroelectric Behavior in Sub-10 nm Bismuth-Rich Aurivillius Films by Piezoresponse Force Microscopy. *Microscopy and Microanalysis* 2022

Keeney, L.; Saghi, Z.; O'Sullivan, M.; Alaria, J.; Schmidt, M.; **Colfer, L**., Persistence of Ferroelectricity Close to Unit-Cell Thickness in Structurally Disordered Aurivillius Phases. *Chemistry of Materials* 2020

## List of Abbreviations

2D: Two-Dimensional

3D: Three-Dimensional

ABF: Annular Bright Field

AFM: Atomic Force Microscopy

ALD: Atomic Layer Deposition AVD (atomic vapour deposition)

C-AFM: Conductive Atomic Force Microscopy

CMOS: Complementary Metal-Oxide Semiconductor

CVD: Chemical Vapour Deposition

CSD: Chemical Solution Deposition

DART-PFM: Dual AC Resonance Tracking Piezo Force Microscopy

DLI-CVD: Direct Liquid Injection Chemical Vapour Deposition

DM: Dzyaloshinskii–Moriya

DRAM: Dynamic Random Access Memory

DFT: Density Functional Theory domain walls (DWs)

EDX: Energy Dispersive X –Ray Spectroscopy

EEPROM: Electrically Erasable Programmable Read-Only Memory

EELS: Electron Energy Loss Spectroscopy

FeRAM: Ferroelectric Random Access Memory

FTJ: Ferroelectric Tunnel Junction

FWHM: Full Width, Half Maximum

HAADF: High Angle Annular Dark Field

H-H: Head-to-Head

hs: high-spin

iDPC: Integrated Differential Phase Contrast Microscopy

*irrep:* Irreducible Representation

LED: Light Emitting Diodes

LGD: Landau-Ginzburg-Devonshire

LPFM: Lateral Piezo Force Microscopy

ls: low-spin

MESO: Magneto-Electric Spin-Orbit

MOCVD: Metalorganic Chemical Vapour Deposition

MFTJ: Multiferroic tunnel junction

MRAM: Magnetic Random Access Memory

NRAM: Nanotube Random Access Memory

NN: Nearest Neighbours

OPB: Out of Phase Boundary

PDOS: Partial Density of States

PFM: Piezo Force Microscopy

ReRAM: Resistive Random Access Memory

RMS: Root Mean Square

RT: Room Temperature

SEM: Scanning Electron Microscopy

STEM: Scanning Transmission Electron Microscopy

T-T: Tail-to-Tail

SQUID: Superconducting Quantum Interference Device

VPFM: Vertical Piezo Force Microscopy

XRD: X-ray Diffraction

TEM: Transmission Electron Microscopy

ZFC-FC: Zero Field Cooled – Field Cooled

## Comments on my Contributions

The majority of the work in this thesis was conducted by me at the Tyndall National Institute, Cork. The Royal Society and Science Foundation Ireland funded the research with L. Keeney as principal investigator. My contributions to the research included the design of experiment, synthesis of samples, characterisation and analysis of materials, interpretation of data and manuscript preparation. L. Keeney (lead supervisor) and B. Long (co-supervisor) guided and managed the planning of the project. The specific contribution of each co-author is outlined below:

**Chapter 3:** M. Schmidt (Tyndall-UCC) prepared cross-section lamella of the samples. N. Bagués (Ohio University) carried out scanning transmission electron microscopy (STEM), integrated differential phase contrast microscopy and electron energy loss spectroscopy and aided in the interpretation of the analysis. D. W. McComb (Ohio University) aided in design of the electron microscopy experiments alongside aiding in the interpretation of the analysis. M. Noor-A-Alam (Tyndall-UCC) carried out the density functional theory calculations and the interpretation of the results. M. Nolan (Tyndall-UCC) contributed to then interpretation of the density functional theory calculations.

**Chapter 4:** M. Schmidt (Tyndall-UCC) prepared cross-section lamella of the samples. L. Keeney (Tyndall-UCC) acquired the atomic force microscopy images using the Bruker Dimension Icon tool. M. Conroy (Imperial College London) and N. Bagués (Ohio University) carried out scanning transmission electron microscopy and aided in the interpretation of the analysis. J. Alaria (University of Liverpool) aided in the acquisition of the X-ray diffraction data using the Rigaku Smartlab instrument at The University of Liverpool, which was operated remotely by myself (L. Colfer). J. Alaria aided in the interpretation of the X-ray diffraction analysis.

**Chapter 5:** B. Sheehan (Tyndall-UCC) prepared cross-section lamella of the samples. L. Keeney (Tyndall-UCC) acquired the atomic force microscopy images using the Bruker Dimension Icon tool. S. Stock and J. Peters (Trinity College Dublin) carried out scanning transmission electron microscopy. M. Bansal and T. Maity (Indian Institute of Science Education and Research, Thiruvananthapuram) acquired and aided in the interpretation of the magnetic measurements.

**Chapter 6:** M. Schmidt and D. Singh (Tyndall-UCC) prepared cross-section lamella of the samples and carried out scanning transmission electron microscopy imaging of the lamella. D. Dutta (Tyndall-UCC) acquired the atomic force microscopy images using the Bruker Dimension Icon tool. B. Sheehan carried out conductive atomic force microscopy using the Bruker Dimension Icon tool.

# 1 Introduction

## 1.1 Memory Storage Research to Overcome the Big Data Problem

Every action performed by a smart device uses and creates data. As technology is becoming further integrated into everyday life through sophisticated smart devices and artificial intelligence systems, more and more data is being created. With over 8 billion people in the world, this data creation begins to stack up. The 'big data' problem has arisen due to the fact that the amount of data being created and processed is growing at a much faster rate than the rate at which computational storage technologies are growing [1]. For example in 2018 the total amount of all data created, captured and replicated had surpassed 33 zettabytes and is predicted to reach over 175 zettabytes in 2025 [2]. The ever-growing demands by society to store and process data is fuelling the need for miniaturised memory storage devices. While CMOS (complementary metal-oxide semiconductor) technologies are reaching their miniaturisation limits (e.g. voltage operation limits) [3], new disruptive materials are needed in order to increase data storage capabilities. The current environmental crisis also demands more energy efficient memory storage solutions.

Traditional hardware for data storage have typically involved the use of on-site storage systems, which are costly to maintain and struggle to keep up with rapid growth of data storage needs and technologies [4]. In recent years, cloud-based storage has become mainstream in providing memory storage infrastructure as a service. Cloud-based storage allows data to be saved in a remote storage facility accessed via a server and has many advantages over traditional hardware memory storage. Cloud-based service providers utilise accessible repositories to store backed-up data. In the event of local data loss, which can happen for example when a hard drive fails, cloud-based storage allows for access to data remotely accessed using an internet connection. Cloud-based storage helps users to avoid investing in costly memory storage systems which can quickly become outdated [4] . Due to the specific and large-scale nature of the storage facilities, cloud-based storage providers can allow users to readily update their data storage plans and offer users services with state-of-the-art memory storage technologies. However, cloud-based storage does have some

disadvantages with concerns over the security of data when stored off site [5] and environmental concerns due to the large amounts of energy required to cool the data centres. In Ireland the total metered electricity consumption from data centres increased from 5 % in 2015 to 18 % in 2022 [6]. With EirGrid [7] projecting that this could increase to up to 30 % of the country's electricity consumption by 2028, this increasing energy consumption negatively impacts the countries climate action targets and could also contribute to rising energy costs.

Some examples of recent emerging hardware storage technologies include resistive random access memory (ReRAM) and nanotube RAM (NRAM). ReRAM is a non-volatile memory, which operates via changes in the state of the resistance in a material. In ReRAM devices, a resistive material, most often a thin metal-oxide, is placed between two electrodes. Applying a pulsed voltage across the metal oxide generates oxygen vacancies in the thin film which charge and drift under the electric field. This changes the resistive state of the material, which is recorded as 1 or 0.The main advantage of this type of memory storage is its low read current e.g. 0.15 mA [8], meaning that it can extend the battery life of devices, thus is currently used often in wearable devices such as hearing aids and smart watches [8] . However, ReRAM doesn't offer the high read/write endurance as seen in devices for example powered by ferroelectric RAM (FeRAM), where FeRAM devices can guarantee over 100 trillion read/write cycles compared to ReRAM devices which can only guarantee up to 1 million read/write cycles [8]. Another new potential memory technology is based on carbon nanotubes, NRAM. These memories are mainly developed at the moment by Nantero and offer a resistive non-volatile memory created using arrays of carbon nanotubes, which due to their small size (diameters as small as 0.9 nm [9]) allow for high storage densities. These devices are built by fitting an array of carbon nanotubes between two electrodes. The layer of carbon nanotubes between the electrodes can be switched between two states: a low resistance state when the carbon nanotubes are brought into contact with one another (1) and a high resistance state when the nanotubes are not in contact (0). Van der Waals forces keep the carbon nanotubes in either state allowing for the technology to be performed under low power [10]. The small movement of atoms in NRAM devices versus the moving of electrons in silicon-based memories allows for NRAM to have a high endurance (over a trillion read/write cycles). Furthermore, they have been shown to operate with very quick switching speeds (picoseconds) [9]. NRAM potentially could replace current volatile dynamic RAM

(DRAM) as they match or improve on DRAM properties and are potentially scalable to 5 nm cell sizes [10], [11]. For NRAM memory chips to become fully commercial, the main obstacles to overcome are ensuring a straightforward production method that allows for the creation of a chip comprised of millions of carbon nanotubes that can bend cleanly and consistently.

FeRAM have two polar ±P memory states stemming from their switchable polarisation. Compared to devices based on older Flash or electrically erasable programmable read-only memory (EEPROM) technologies, commercial FeRAM devices have very fast information writing with write cycle times of 120 ns, they have a high read/write endurance of over $10^{14}$ cycles and are more energy efficient e.g. 92 % lower power consumption than EEPROM memories [12]. However, FeRAM devices do have a destructive read operation and are not ideal for storing large amounts of data. There is also ferromagnetic RAM (MRAM), which work by switching the magnetic sates, ±M of a material. MRAM devices use magnetoresistance to read the memory states. While magnetic memories are non-volatile and have large storage densities, compared to FeRAM they are less energy efficient due to their high power consumption. The magnetic coercivity of a magnetic material is the amount of resistance the material experiences before changing its magnetic state.

Another potential solution to the big data problem is the utilisation of room temperature, non-volatile magnetoelectric multiferroic materials in future memory storage devices. Multiferroic materials that are both ferroelectric and ferromagnetic are ideal for memory storage due to the combined effects of both phenomena. By combining the properties of FeRAM and MRAM, a device could have the speed and energy efficiency associated with FeRAM along with the higher memory density associated with MRAM. Such a device would lead to an increased number of memory states and would aid in device miniaturisation and energy efficiency.

Theoretically, a magnetoelectric multiferroic material would be able to switch between, ±P and ±M. However, due to strong magnetoelectric coupling between the ferroelectric and ferromagnetic states, the four available switching states (+*P*, +*M*), (+*P*, -*M*), (-*P*, +*M*) and (-*P*, -*M*), where *P* represents the polarisation state and *M* represents the magnetisation state, are not absolutely independent of each other and the only combinations that are independently achievable are either (+*P*, +*M*) and (-*P*, -*M*) or (+*P*, -*M*), and (-*P*, +*M*), which of course is not a four-state memory [13]. This issue of strong coupling reducing the

available logic states can be circumvented by forming a multiferroic tunnel junction, where combination of electroresistance and magnetoresistance can result in four state memory effects [14]. Multiferroic tunnel junctions (MFTJs) are made up of an ultra-thin ($< 10$ nm) multiferroic barrier layer which separates two asymmetric oxide and/or metal electrodes [15]. In MFJT devices, electrons are able to tunnel through an ultra-thin multiferroic thin film, providing large electroresistance/magnetoresistance effects with high ON:OFF ratios [16] and a means for non-destructive read-out of non-volatile memory states [14], [17]. When the ultra-thin multiferroic layer acts as a ferroelectric tunnel junction, depending on the direction of the ferroelectric polarisation, it affects how the electron tunnels, leading to either low or high electroresistance states. Simultaneously, the multiferroic layer can act as a magnetic tunnel junction, where the magnetic spin of the electron can be manipulated as it tunnels across, leading to either low or high magnetoresistance states. This behaviour simultaneously allows both high and low electroresistance and magnetoresistance states to be accessed. According to Yang *et al*., devices incorporating MFTJs could offer a pathway to simultaneously accessing eight distinct memory states [18]. This would be a significant advantage over current two-state memory storage devices.

Furthermore, because switching involves domain nucleation and growth, artificial nano-synapses where synaptic strengths evolve depending on the switching pulse amplitude and duration could be created. By varying the pulse amplitude and the duration of switching, different synaptic strengths could be achieved. These multileveled states could then be utilised as memory elements in future neuromorphic memory devices [19], [20].

While the benefits and potential of multiferroic memory devices is clear, no such commercial devices yet exist. In the following sections, the phenomena of ferroelectricity and ferromagnetism and how room temperature multiferroics are exceptionally rare due to the fundamental contra-indication between ferroelectricity (empty $d^0$ electronic structures) and ferromagnetism (occupied $d^n$ electronic structures) are discussed [21], [22]. However, if such devices are realised, they could revolutionise future memory storage technologies.

## 1.2 Ferroelectricity

The discovery of pyroelectricity (the generation of a polarisation in a material due to heating or cooling) in 1824 [23] and of piezoelectricity (the generation of a polarisation in material under the application of a mechanical stress) in 1880 [24] paved the way for investigations that would lead to the discovery of ferroelectricity. The pyroelectricity and piezoelectricity of many materials were investigated and one, Rochelle salt, was noted to have high pyroelectric and piezoelectric excitations, relative to materials such as tourmaline and topaz. Later, investigations of the material have revealed piezotensor constants for the material, such as the $d_{14}$ coefficient was measured to be as high as 2300 $pCN^{-1}$ [25]. 25 years after it was first discovered, piezoelectricity first found applications in sonar technologies during World War I. The discovery of ferroelectricity was possibly slowed due to a misunderstanding of the material properties and dispute on the anomalous dielectric constant reported by Borel in the late 1890's [26], [27]. In Borel's work, the dielectric constants of Rochelle salt were measured using a highly sensitive torsion balance that measured the pondero-motoric forces acting on spherical crystals in an electric field. Here, he measured the Rochelle's dielectric constant's to be $\varepsilon_a = 8.898$, $\varepsilon_b = 6.92$ and $\varepsilon_c = 6.70$ but also noted that the value of $\varepsilon_a$ varied with the strength of the electric field applied along the now known ferroelectric axis. One of the reasons for the low $\varepsilon_a$ value (actual $\varepsilon_a \sim 103 - 104$ @ RT [28]) collected was because there was no metallic electrode within the sphere measured. However, later in 1920, Rochelle salt was the first material where ferroelectricity was accurately measured and characterised [29]. While Rochelle salt was key in the discovery of ferroelectricity, its unstable, complex nature made it unsuitable to fully understand the mechanisms behind ferroelectricity. Materials with simpler structures such as $KH_2PO_4$ [30] and perovskites e.g. $BaTiO_3$ [31], [32] emerged in the 1930s and 1940s. These materials enabled research on the understanding the origins of ferroelectricity [33] and optimising these materials for memory storage applications [34].

### 1.2.1 Origins of Polarisation

In contrast to conductors, insulators do not allow free movement of electrons through a material. When an electric field is applied to an electrically polarisable insulator, it can cause the charge distribution of the electrons around an atom or molecule to shift away from equilibrium, creating a dipole moment. The size of the dipole moment is determined by the separation between the resultant positive and negative charges between atoms or molecules in the material. In ionic materials, the electron density shifts between a positive cation and negative anion. While for polar materials, the formation of a polar bond and thus a dipole moment is determined by the electronegativity difference of the bonded atoms between which the electrons are shared. Dielectric insulators exhibit a polarisation (the dipole moment per unit volume) on application of an electric field (**Figure 1.1 (a)**). In these materials, the electric dipole is induced by the electric field and the strength of the electric dipole is proportional to the electric field applied. In the dielectric case, when the electric field is removed or switched off, the net dipole moment returns to zero. Paraelectric materials are a subgroup of electrically polarisable materials and display a non-linear response to an electric field as shown in **Figure 1.1 (b)**. These materials have randomly orientated dipoles before the application of an electric field with a very weak internal field. On application of the electric field, the dipole moments align and thus give a larger polarisation response compared with dielectrics. When the electric field is removed in paraelectric materials, the dipoles in the material return to their original non-aligned arrangement.

An important subset of the electrically polarisable materials is the ferroelectrics, whose dipole moments can not only be switched by an applied electric field in a non-linear manner, but also their polarisation states remain even when the electric field is removed. These materials have a permanent polarisation and hysteretic electrically switchable polarisation, as **Figure 1.1 (c)** shows. Ferroelectric materials possess an inherent polarisation, however in most cases, an external applied field is required for ferroelectric domains to align in the same direction across a full sample. Initially as an electric field is applied, the dipole moments align in the direction of the electric field. After a particular field is reached, all the dipole moments align along the same direction and the polarisation response saturates. This saturation point is known as the saturation polarisation ($P_s$). When the direction of the applied

electric field is switched towards the opposite direction, there is a lag in the polarisation response, which results in the hysteresis loop in **Figure 1.1 (c)**. Even when the electric field returns to zero, a portion of the polarisation stays at a non-zero value known as the remanent polarisation ($P_r$).

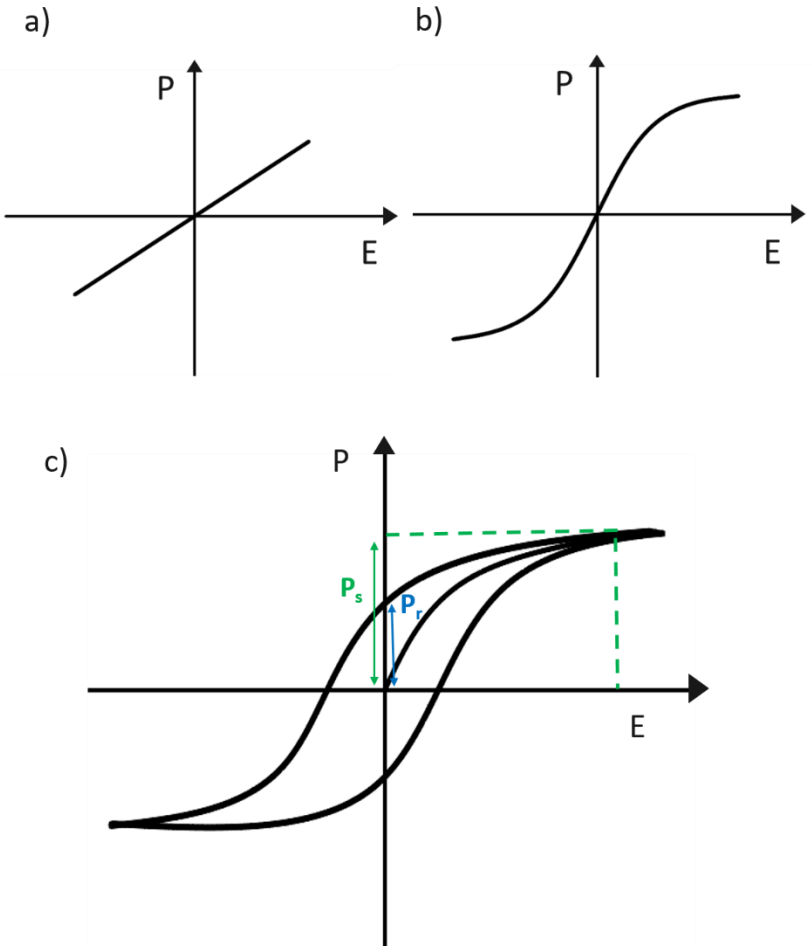


**Figure 1.1** Polarisation (P) versus applied electric field (E) behaviour of for a) dielectric, b) paraelectric and c) ferroelectric materials. The saturation polarisation ($P_s$) (where all the dipole moments align along the same direction) is marked in green. The remnant polarisation ($P_r$) (a non-zero portion of the polarisation which when the electric field returns to zero) is shown in blue.

### 1.2.2 Necessary Conditions for Ferroelectric Behaviour

In addition to the requirement of being polar, ferroelectric crystals must have a non-centrosymmetric structure in order to possess a spontaneous electric dipole moment that can be switched in an applied electric field. Ferroelectric materials display phase transitions where below a particular temperature, the point group symmetry changes to a non-centrosymmetric structure and a reversible spontaneous electric polarisation (polarisation in the absence of an applied electric field) emerges [35]. Out of the 32 crystallographic point groups, 21 are non-centro-symmetric and of these 20 are considered piezoelectric. From the piezoelectric point groups, ferroelectrics can only result from one of 10 polar point groups. Ferroelectrics are a class of materials that are a subset within the piezoelectric family. The piezoelectric effect is the generation of a surface charge in response to the application of an external mechanical stress on a material. There is a linear electromechanical interaction between the mechanical and the electrical state in solid materials, where without an external stress there are no electric dipole moments within the material. All ferroelectrics are piezoelectric (however note that not all piezoelectrics are ferroelectric), therefore their polarisation changes under the influence of an applied stress. Ferroelectrics also have a net spontaneous polarisation resulting from permanent dipole moments existing in the material without the application of any external electric field or stress. As explained previously in **Figure 1.1 (c)**, ferroelectric materials possess inherent polarisation in randomly orientated domains that require an applied field to achieve macroscopic polarisation along a certain orientation. The ferroelectric effect is the change in the surface charge in response to a change in this spontaneous polarisation. Above the ferroelectric Curie temperature ($T_C$) (the point at which a phase transition occurs), a ferroelectric material has a centrosymmetric high-temperature phase where it acts as a paraelectric material. Below $T_C$, a low-temperature phase exits where the symmetry of the material is lowered. This low-temperature phase possesses a net permanent dipole moment, due to the vector sum of the aligned dipole moments in each unit cell. As **Figure 1.1 (c)** illustrates, this polarisation can be induced and switched between at least two stable states with an external electric field [21]. When the electric field goes to zero, a spontaneous polarisation remains. The lag in the change of polarisation with the external electric field is indicative of ferroelectric hysteresis. This

hysteretic behaviour in response to an applied electric field enables ferroelectric materials to have applications in data storage such as FeRAM and FTJ (ferroelectric tunnel junction) devices.

### 1.2.3 Ferroelectric Phase Transitions

With the study of simple ferroelectric structures such as $KH_2PO_4$ and $BaTiO_3$, theoretical understandings of how ferroelectricity and ferroelectric phase transitions occur became more fruitful. In the 1930s, theoretical thermodynamics considering polarisation as a function of the free energy potential had been established by Landau [36]. Landau theory was developed to formulate a general theory to describe phase transitions. The theory uses the concept of an order parameter, the measure of the order before and after a phase transition (in the case of ferroelectrics, polarisation is the order parameter). The order parameter is expanded as a function of the free energy using a power series. From this expansion, the behaviour of a material and its phase transitions can be determined. Both Ginzberg [37], [38] and Devonshire [39] expanded on Landau's theory including additional terms into the free energy expansion which account for fluctuations of the order parameter. This became known as Landau-Ginzburg-Devonshire (LGD) theory and can more accurately describe the evolution of polarisation within ferroelectrics.

When considering phase transitions in ferroelectrics, there are two general categories: first order transitions and second order transitions. First order transitions occur where latent heat is involved and the polarisation is discontinuous e.g. solid-liquid-gas transitions. Second order transitions occurs when the polarisation moves continuously towards zero until $T_C$ and no latent heat is involved e.g. ferromagnetic transitions. **Figure 1.2** illustrates polarisation behaviour for these transitions as a function of temperature [40].

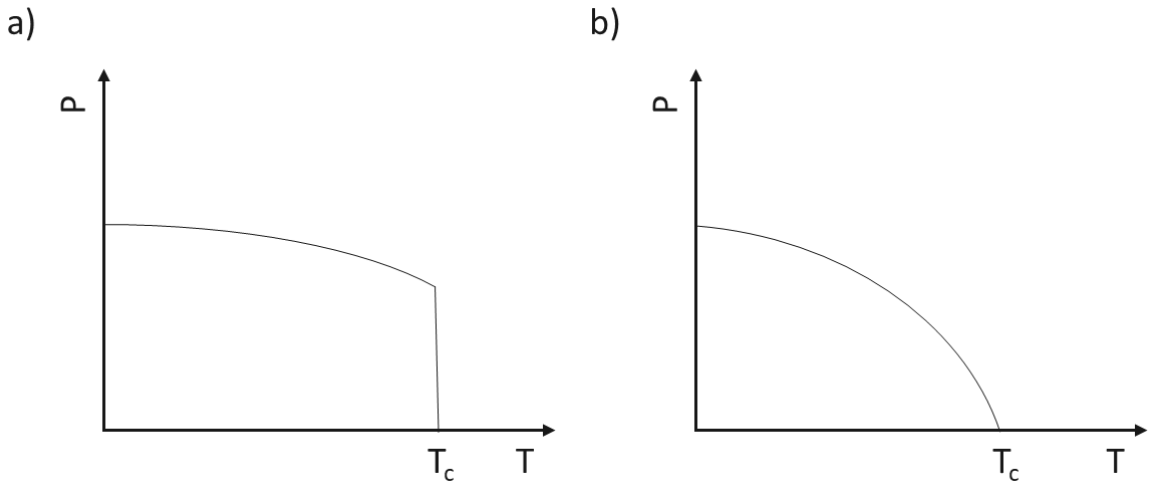


**Figure 1.2** Spontaneous Polarisation (P) *vs* Temperature (T) for a) first order transition and b) second order transition.

Within the scope of these two types of phase transitions, the potential energy as a function of polarisation behaves slightly differently as shown in **Figure 1.3**. Second order transitions are well described using the Landau free energy potential [36]. As shown in **Figure 1.3 (b)**, at and above $T_C$ there is a single polarisation minima equal to zero. This represents the non-polar centrosymmetric phase. However, below $T_C$ a double potential well appears where now there are two non-zero energy minima, which allow for a spontaneous polarisation. These two minima correspond to the two opposite possible polarisation orientations. It should be noted that the majority of ferroelectric systems undergo weakly first order transitions and LGD theory helps describe the behaviour of the polarisation with relation to the free energy in these systems. In first order transitions such as in **Figure 1.3 (a)**, due to the dis-continuity at $T_C$ where there is now a latent heat associated with the phase transition, a mixed phase system occurs, where both paraelectric and ferroelectric phases are present [41].

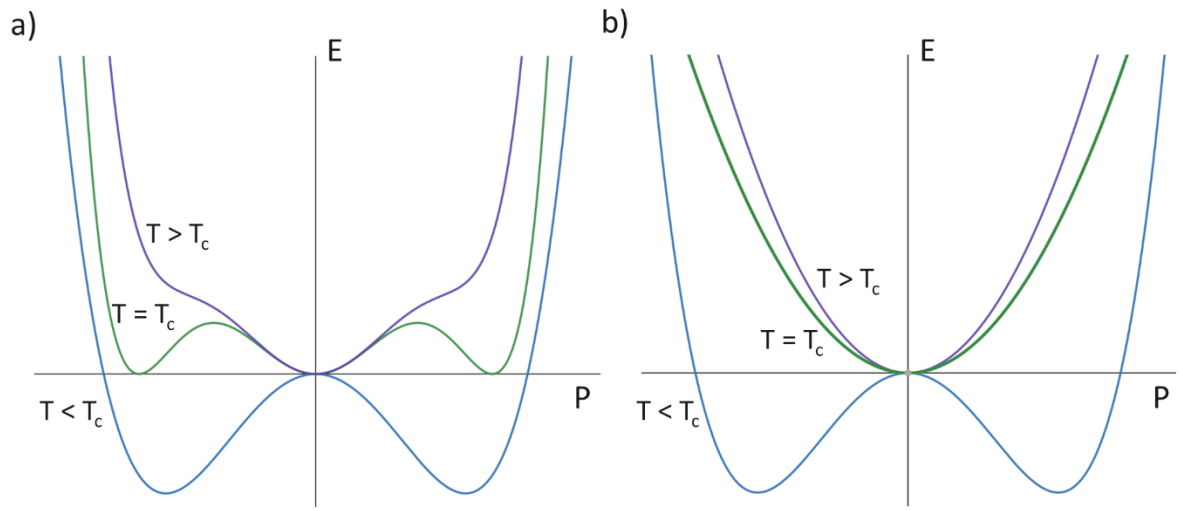


**Figure 1.3** Free Energy Potential (E) *vs* Spontaneous Polarisation (P) for a) first order transition and b) second order transition.

Further advances to the understanding of ferroelectricity came with Kittel's [42] explanation of antiferroelectricity, where adjacent dipoles are oriented oppositely to each other leading to a net zero polarisation. While in the 1960s, soft mode theory was developed by Cochran [43] and Anderson [44] to explain ferroelectricity on a microscopic scale. While soft modes, an excitation which decreases in frequency as it approaches a transition, were first noticed by Raman and Nedungadi in 1940 [45], it was Cochran and Anderson independently who recognised the importance of soft modes in the phase transitions for ferroelectrics.

### 1.2.4 Ferroelectric Materials

The perovskites are a family of materials with the formula $ABX_3$ (where X is often oxygen). Perovskites are very flexible with regards to their chemical and structural parameters and thus have been able to produce a large number of ferroelectric materials such as $BaTiO_3$, $PbTiO_3$ and $PbTiO_3$:$PbZrO_3$ [46], [47]. These materials are made up of corner sharing $BO_6$ octahedra, with the 12-fold coordination *A*-site lying at the meeting point of eight $BO_6$ octahedra as shown in **Figure 1.4 (a)**. Below $T_C$, when in a ferroelectric phase, the electric dipole moment that causes the spontaneous electric polarization in the material is due to the off-centre shift of the *A*-site or *B*-site cations with respect to the $O^{2-}$ anions. The two main mechanisms causing ferroelectricity in perovskites are the *B*-site '$d_0$-ness', and the *A*-site

stereochemical activity of cations with lone electron pairs [48]. For example, in **Figure 1.4 (b)**, the central *B*-site cation is displaced away from its centre, resulting in the crystal structure to possess a lower-symmetry phase and for the structure to yield a net polarisation. This is the mechanism for ferroelectricity in the case of $BaTiO_3$, whereupon a lowering of the temperature below $T_C$ results in the $TiO_6$ octahedra becoming distorted away from the centrosymmetric cubic phase, going from the paraelectric *Pm*-3*m* to the ferroelectric *P*4*mm* space group [49]. This distortion is known as a second-order Jahn-Teller distortion, where below $T_C$, the energy levels of the hybridised orbital between the $Ti^{4+}$ and $O^{2-}$ lose their degeneracy and thus the energy of the distorted structure is lower and more favourable at the lower temperature. In systems such as $PbTiO_3$ or $BiFeO_3$, ferroelectric behaviour is caused by a lone electron pair mechanism. This mechanism is based on the breaking of inversion symmetry by valence electrons. The *A*-site cation, $Pb^{2+}$ or $Bi^{3+}$ is stereochemically active and this contributes to distortion of the lattice relative to the $O^{2-}$ anions, resulting in the polarisation observed below $T_C$. In the $BiFeO_3$ system, two lone pair electrons, which do not take part in the chemical sp-hybridized states, shift away from the $Bi^{3+}$ cation towards the $FeO_6$ octahedra. This shift creates a local dipole and thus the lone pair of electrons induces a spontaneous polarisation in the (111) direction [50], [51].

While perovskites are some of the most prevalent compounds found in the world of ferroelectrics, materials such as tungsten bronze type compounds [52] and layered perovskite structures such as the Aurivillius [53], Ruddlesden-Popper [54] or Dion-Jacobson phases [55], [56] also are of interest to the advancement of the field of ferroelectrics. Recently, CMOS compatible materials such as wurtzite structured AlN based materials e.g. $Sc_xAl_{1-x}N$ [57], [58] and fluorite structured oxides [59], [60], have also been found to show ferroelectric properties. For example $Hf_{0.8}Zr_{0.2}O$ has been grown as ultra-thin (sub-2 nm) films directly on silicon with robust and enhanced ferroelectricity at 1 nm, paving the way for use in sub-5 nm CMOS-compatible ferroelectric devices [61], [62]. Another exciting family of new ferroelectrics are made up of two-dimensional (2D) van der Waal materials [63] which include materials from the Group IV monochalcogenides (SnS, SnSe and SnTe) [64], [65], distorted transition metal dichalcogenides (1T'-$MoTe_2$ and $WTe_2$) [66]–[68], oxy-chalcogenides ($Bi_2O_2Se$) [69] and transition–metal thiophosphates ($CuInP_2S_6$) [70] and layered perovskites ($BA_2PbCl_4$ ($BA_2$ = bis(benzylammonium))) [71]. These materials are free from dangling bonds

thus can be grown on a large variety of substrates without the need for a lattice match and offer unique properties due to their reduced lattice dimensionality.

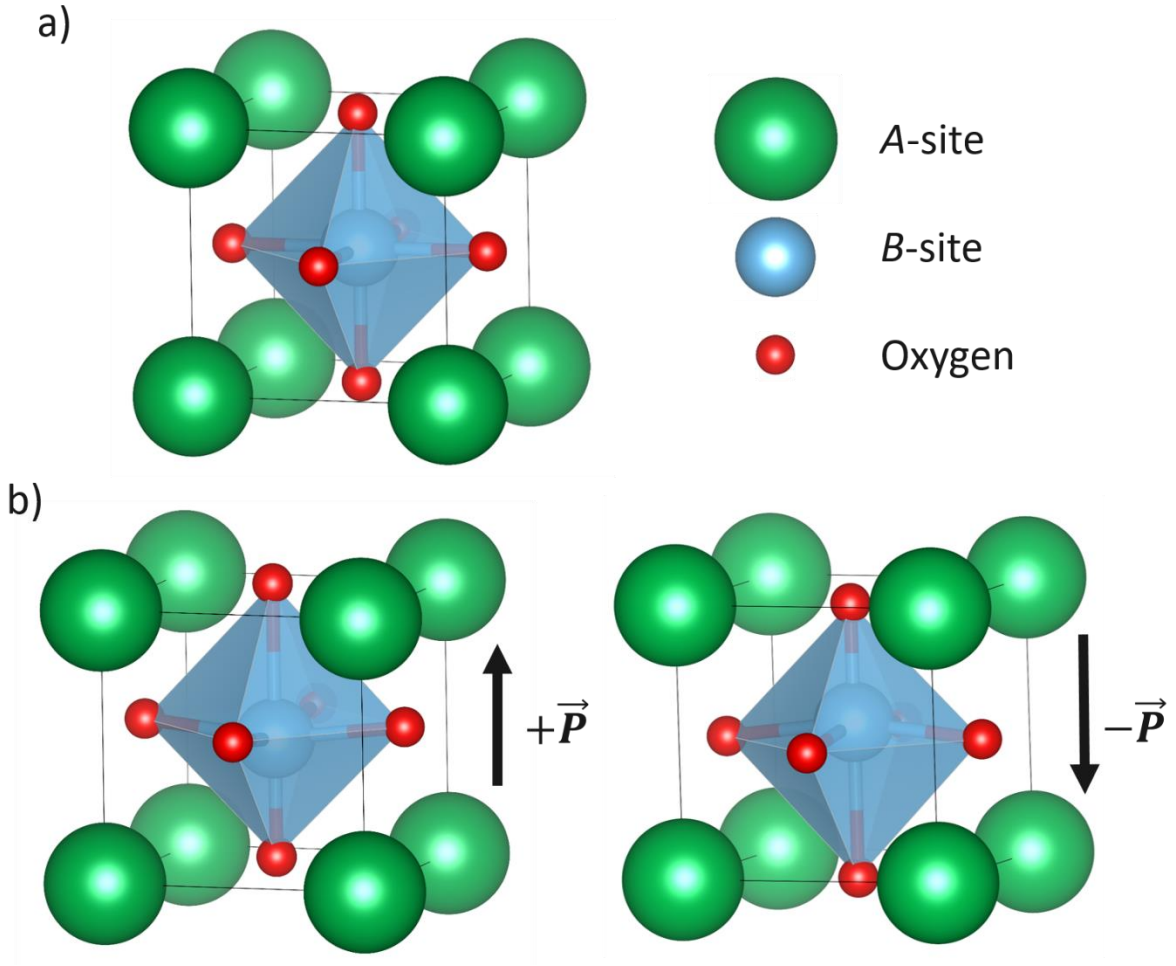


**Figure 1.4** a) centrosymmetric cubic perovskite structure with space group *Pm*-3*m* which occurs above 130 °C. All the bond lengths between the oxygen atoms and *B*-site atoms are equivalent, 2.009 Å. b) a tetragonal perovskite structure where the space group is *P*4*mm*, after the *B*-site cation shifts away from the centre of the $BO_6$ octahedra. Now the structure is not centrosymmetric and a dipole moment is present. Here the direction of the polarisation vector (a result of the reverse displacement of the central *B*-site cation) is indicated. The longer bond in the out of plane direction is now 2.296 Å and the shorter bond is 1.756 Å while the other four bonds are slight elongated compared to the paraelectric phase having a length of 2.009 Å.

## 1.3 Ferromagnetism

In contrast to ferroelectric materials which have only been discovered in the last 100 years, magnetic materials have been observed and noted for thousands of years in ancient Greece, China and South America in materials such as manganite rocks rich in magnetised $Fe_3O_4$ (lodestone). While societies have been aware of magnetism as a physical phenomenon throughout history, it was not until the last 200 years or so that the fundamental understandings of magnetism started to become clear. Nonetheless, some of the first modern scientific writings were about magnetism with 'De Magnete' by William Gilbert in 1600, and over the $17^{th}$ and $18^{th}$ centuries, magnetic compasses became key technologies in sea navigation.

In 1820, Hans Christian Oersted discovered the connection between electricity and magnetism when he showed a current carrying wire produced a field that deflected a compass needle [72]. From this accidental discovery, the modern era of electromagnetism began. 1900 to 1935 can be considered the era of understanding for magnetism, as magnetic behaviour, which challenged classical mechanics, could be explained by quantum mechanics.

### 1.3.1 Origins of Magnetism

Magnetism in solid materials is associated with a magnetic dipole moment, comprised mainly of the spin associated with an electron, which is quantised so that it has only two possible orientations in a magnetic field. The motion of the electron around the nucleus together with the nuclear spin state can also contribute to the magnetic spin. However, given that the magnetic moment of a particle scales such that magnetic moment is proportional to 1/mass, the spin associated with the nucleus of the atom can be neglected.

Most magnets are composed of atoms whose valence electrons are in either partially filled *d* orbitals (transition metals) or partially filled *f* orbitals in (rare earth metals). *d* orbitals in an uncoordinated transition metal have the same energy and are considered degenerate. Once the transition metal is coordinated to ligands in a compound, crystal field splitting occurs. The *d* orbitals lose their degeneracy with the $d_{xy}$,$d_{xz}$, $d_{yx}$ ($t_{2g}$) and the $d_{z^2}$,$d_{x^2-y^2}$ ($e_g$) energy levels splitting into separate energies. In some systems, a further energy splitting can

occur due to the Jahn-Teller effect as shown in **Figure 1.5**. This further splitting is due to the elongation or compression of the transition metal complex. This change in energy splitting can influence the magnetic order of a system as it effects the electronic configuration within the orbitals and thus the potential magnetic exchange mechanisms within different materials. For magnetic systems, both the magnetic contribution from the electron orbital motion and electron spins must be considered (spin-orbit coupling), while the nuclear spin magnetic moment is appreciatively (approx. 2000-fold) weaker and can be (tentatively) ignored. For the compounds of the first series of transition metals, the contribution of orbital angular momentum is effectively quenched and hence is of no significance. Considering the spin-only case, it can be depicted neatly how the change in energy splitting and the number of unpaired electrons within a system can lead to different magnetic moment values, $\mu_{eff}$, where *n* is the number of unpaired electrons.

$$\mu_{eff} = \sqrt{n(n+2)} \qquad 1.1$$

Considering **Equation 1.1** for different material systems, e.g. $d^3$, $d^4$ high spin (hs) and low spin (ls) and $d^9$, the different number of unpaired electrons in these systems, 3, 4, 2 and 1 respectively, will lead to different theoretical magnetic moments. The $\mu_{eff}$ values were calculated to be $d^3$ = 3.87, $d^4$ (hs) = 4.90, $d^4$ (ls) = 2.83 and $d^9$ = 1.73. Hence, experimentally measured magnetic moments can provide some important information about magnetic compounds such as the number of unpaired electrons present and hs *vs* ls states.

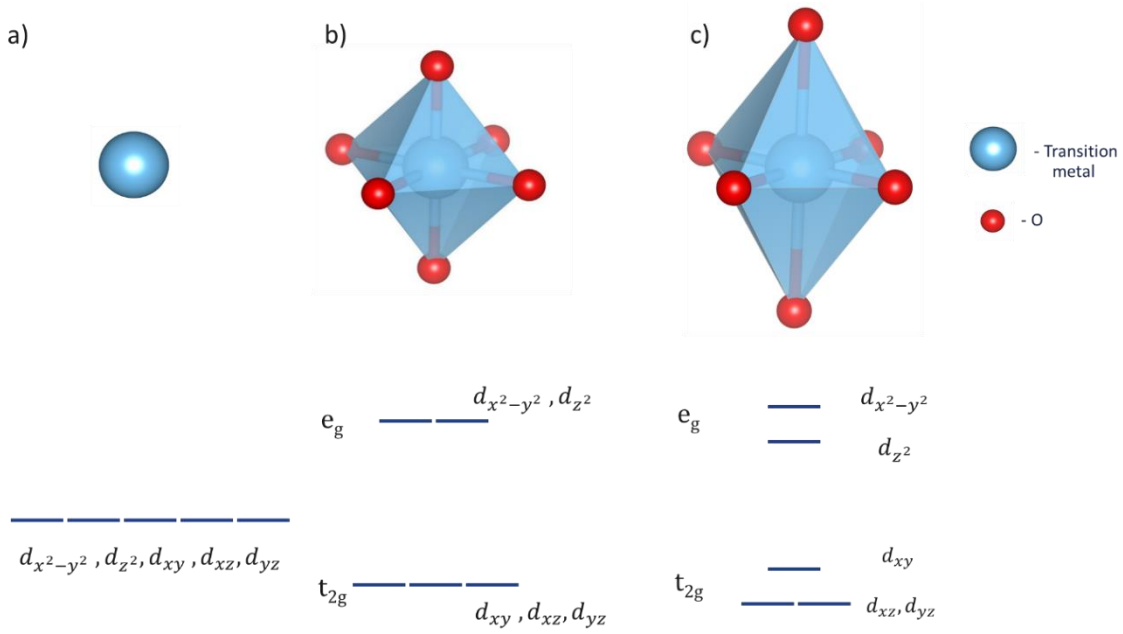


**Figure 1.5** Energy levels of the *d*-orbitals in a transition metal. a) Five degenerate energy levels for an uncomplexed metal ion (no crystal field present). b) Transition metal in an octahedral complex, where the $d_{xy}$, $d_{xz}$, $d_{yz}$ orbitals become lower in energy and comprise of what is called the $t_{2g}$ level, while the $d_{x^2-y^2}$, $d_{z^2}$ orbitals are raised in energy to the $e_g$ level. c) Elongated distorted octahedral (tetragonal): when trans ligands in an $ML_6$ octahedral complex are moved either towards or away from the metal ion. This results in further spitting of the $e_g$ and $t_{2g}$ levels with the orbitals with *z* components become lower in energy on elongation of bonds along the *z*-axis. Such otherwise unfavourable distortions become favourable due to Jahn-Teller effects.

At a microscopic local scale, the spin of the electrons varies through a material, however the electron magnetic spins tend to cancel out where the material has a macroscopic net zero magnetisation value. As described for the electric dipole moment, there are material systems that are exceptions with regards to the magnetic dipole cancelling. In diamagnetic (all electrons are paired) and paramagnetic (possess unpaired electrons) systems, with the application of a magnetic field, a weak response is induced. Diamagnetic materials have a weak, negative susceptibility to magnetic fields and the direction of the magnetic moment in

diamagnetic materials opposes the direction of the applied field. Paramagnetic materials (**Figure 1.6 (a)**) have a weak, positive susceptibility to magnetic fields and are weakly attracted to an applied magnetic field. When the magnetic dipoles of the atoms align in the same direction, (**Figure 1.6 (b)**), a net macroscopic magnetisation is present. However, paramagnetic materials do not retain magnetic properties on removal of the external magnetic field.

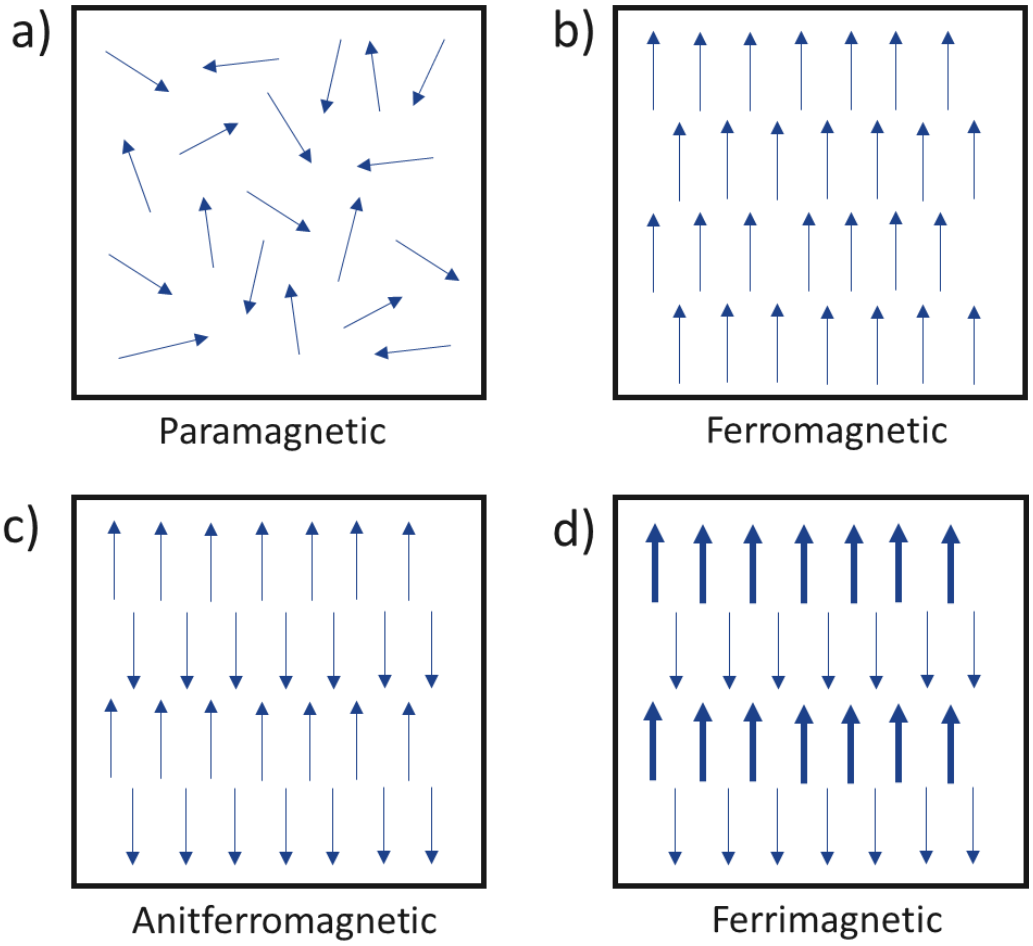


**Figure 1.6** Ordering of the magnetic dipoles in magnetic materials after removal of an external magnetic field.

### 1.3.2 Ferromagnetic Behaviour

Ferromagnetism occurs when a material can exhibit a spontaneous magnetisation formed by spin distributions in the ferromagnetic substance. When the ferromagnetic material is subject to an external magnetic field, this spontaneous magnetisation aligns in a particular direction until it reaches its saturated magnetisation state. When the external magnetic field is removed, the ferromagnetic substance demonstrates residual magnetisation. A ferromagnetic material usually undergoes a phase transition at its ferromagnetic Curie temperature $T_C$. Above $T_c$ ferromagnets have a high temperature phase, where in the absence of an external magnetic field there is no overall magnetic moment, while the low temperature phase (below $T_c$) demonstrates a macroscopic magnetic moment. The magnetic moments align parallel to one another (**Figure 1.6 (b)**) because of orbital interactions due to the quantum mechanical exchange energy. The exchange energy causes the electrons with parallel spins to have lower energy than those that have antiparallel spins [73], [74]. However, at temperatures above $T_C$, the order of the magnetic dipoles is lost. Before the application of an external magnetic field, no magnetisation is observed for some ferromagnetic samples due to domains of magnetic moment cancelling each other out if they are orientated in different directions. In these cases, a magnetic field can be applied and the magnetisation and flux density of the material can be measured. The hysteresis loop of a ferromagnetic material demonstrates the irreversible, non-linear response the magnetism of the material has in response to the application of magnetic field. The hysteresis loop characteristics indicates what type of switching occurs in the ferromagnet and what applications it would be suited to [21]. For example, a square shaped hysteresis loop would indicate a permanent magnet that has two definite switching states and would be useful in applications such as magnetic data storage. Whereas a thin loop would indicate the material is a temporary magnet and could easily loose its magnetisation with the removal of relatively low magnitude applied fields.

### 1.3.3 Magnetic Exchange

The exchange field can be considered to be the internal interaction within the material that promotes the electronic spins in a material to align to a particular magnetic order. This field can give an approximate representation of the quantum theory exchange interaction. The exchange energy is the difference in energy between the relative orientations of the magnetic moments. Direct magnetic exchange, where the exchange between the local electron spin occurs via overlapping atomic orbitals, is an uncommon route to ferromagnetism for transition metal oxides. More often, long-range mechanisms such as superexchange, double-exchange or antisymmetric exchange provide the magnetic order within such systems. The Goodnenough-Kanamori rule [75]–[77], helps predict the expected type of magnetism resulting from the different exchange mechanisms. The rule is based mainly on the Pauli exclusion principal and predicts that for superexchange, antiferromagnetic interactions occur when virtual electron transfer is between half-filled overlapping orbitals. Interactions are ferromagnetic when the virtual electron transfer is from a half-filled to an empty orbital (as is the case between high-spin $Fe^{3+}$ ($d^5$) and $Mn^{4+}$ ($d^3$)) or a filled to a half-filled orbital. The rule starts to fail when mechanisms such as antisymmetric exchange or competing mechanisms appear.

Superexchange [78], [79] occurs between two next-to-nearest cations through an intermediary non-magnetic anion. In ionic solids, the 3*d* orbital of a transition metal cation and the 2*p* orbital in oxygen or fluorine anion interact and depending on the system a magnetic ordering can occur. For example, if there is an unpaired electron in a transition metal cation *d*-orbital, hybridisation can occur via the donation of an electron from the 2*p* orbital of the anion. This exchange interaction often promotes antiferromagnetism (see **Figure 1.7 (a)**) in systems such as MnO and $LaMnO_3$, as a result of the Pauli Exclusion Principle, which prevents electrons of the same spin occupying the same orbital. However, if the next-to-nearest-neighbour cations are orthogonal to one another (having no overlap of their orbitals; see **Figure 1.7 (b)**), it is possible for ferromagnetic ordering to occur, as unpaired electrons in orthogonal orbits tend to align themselves with parallel spins. For example, if the metal ion to the left side of **Figure 1.7 (b)** has its unpaired electron in an $e_g$ orbital and the metal on the right has its unpaired electron in a $t_{2g}$ orbital, and if the transition metal cation

is connected at 90 ° rather than 180 ° to the intermediary anion with zero overlap integral, the electron in the *d* orbital in the left is of the same spin as the electron in the *d* orbital on the right. Therefore, the two metal ions are ferromagnetically linked.

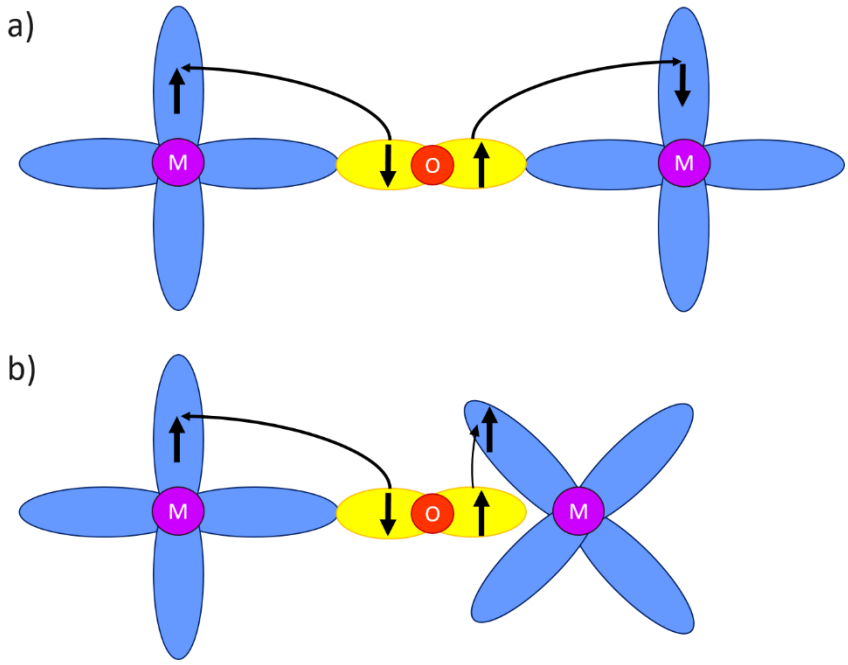


**Figure 1.7** Superexchange interaction in a transition metal oxide a) promoting an antiferromagnetic coupling and b) promoting ferromagnetic coupling.

Double-exchange [80] (**Figure 1.8**) occurs between two transition metal cations that have different oxidation states and generally leads to a ferromagnetic alignment of electron spin. For example, $LaMnO_3$ typically has an antiferromagnetic order via superexchange between the $Mn^{3+}$ cations and $O^{2-}$ anions. However, when there is doping of the La site with atoms such as Sr or Ca, now two Mn valence states, 3+ and 4+, are present. The energy levels in the *d* orbitals fill in accordance with Hund's rule, where the energy levels are first singly occupied. In these systems, it is found that the extra electron associated with the $Mn^{3+}$ cation jumps between the two Mn sites through electrical conduction and thus the electron becomes delocalised. The flipping of spin is not allowed in electron hopping processes; therefore, it is more energetically favourable for both of the Mn cations to have their spin pointing in the same direction leading to a ferromagnetic spin ordering.

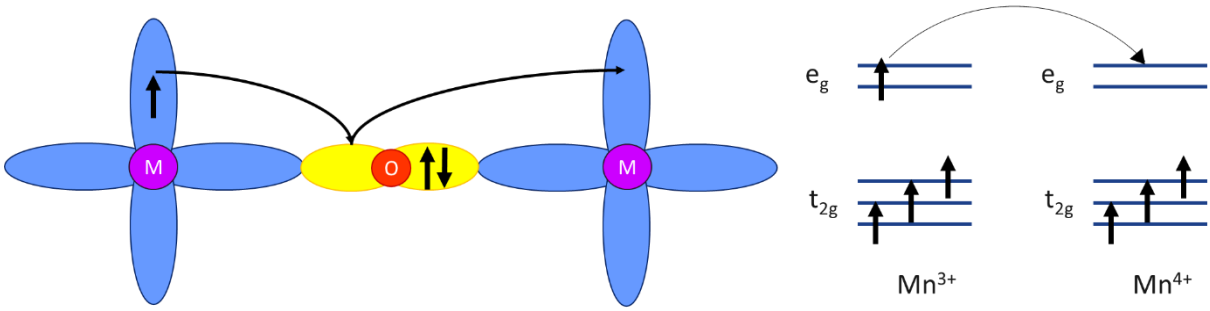


**Figure 1.8** Double-exchange mechanism in a transition metal oxide.

Antisymmetric exchange (Dzyaloshinskii–Moriya interaction) [81], [82], is a form of magnetic ordering that arises through canted spin arrangements (where the electron spins are tilted by a small angle). This is a common route to a small resultant ferromagnetic magnetisation in typically antiferromagnetic materials such as α-$Fe_2O_3$ and $BiFeO_3$. This exchange interaction is of interest to multiferroic systems, as an electric polarisation can be induced by magnetism. In what is known as the 'inverse Dzyaloshinskii–Moriya effect', ionic ligands can be shifted via a spiral magnetic ordering and when all the ligands shift in the same direction, a net polarisation is present [83].

## 1.4 Ferroic Domains and Domain Walls

Classically in both ferroelectric and ferromagnetic structures, domains are regions made up of a uniform direction of electric dipole moment or magnetic moment, usually separated by neutral domain walls (DWs). These domains can form in an analogous fashion for both ferromagnetics and ferroelectrics, in order to minimise the energetics within a material [84]. In a ferroelectric, domains have an inherent electric polarisation, however dipoles in neighbouring domains across the sample are usually orientated in different directions. If a strong enough electric field is applied, the differing domains can align with one another. A

feature of domains that is of significant technological interest are DWs. DWs are 2*D* topological defects that form when a discrete symmetry is broken at a phase transition. Ferroelectric/ferromagnetic DWs are the interfaces between domains having different choices of energy minima (e.g., boundaries between regions with differing dipole orientation/magnitude). The first theory and experiments on DWs were carried out on ferromagnets. Kittel's work [85], [86] on domain scaling is still used today, however these findings were expanded to include ferroelectrics on Rochelle Salt and $KH_2PO_4$ by Mitsui and Furuichi [87]. The properties of the DWs at these interfaces vary, where the class of the DW is determined by the nature of the phase transition and symmetry of the material. Fundamentally, there are three different ways the polarisation/magnetisation direction and magnitude can change at a DW region. These are known as Ising-, Bloch- and Néel-type DWs, as shown in **Figure 1.9**. The Bloch- and Néel–type DWs (**Figure 1.9 (b) and (c)**) are line defects where the axis of rigid rotation of the polarisation/magnetisation changes through the DW, within the plane and perpendicular to the DW plane respectively. It is common for Bloch-type walls to be found in bulk ferromagnets, while Néel walls are often found in thin ferromagnetic films. In Ising-type DWs, the rotation axis of the polarisation/magnetisation remains the same, but the magnitude of the order parameter changes through the wall.

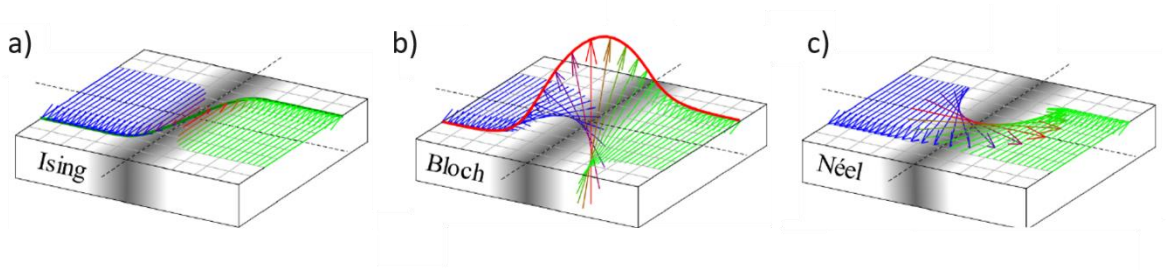


**Figure 1.9** (a)-(c) Display vectors that represent orientation of the polarisation/magnetisation at the DW. (a) Is an Ising-type wall where the polarisation/magnetisation decreases in magnitude at the DW. (b) Is a Bloch-type wall where the polarisation/magnetisation rotates in the plane of the DW but does not change in magnitude and (c) is an Néel-type wall where again the magnitude of the polarisation/magnetisation does not change but they rotate perpendicular to the plane of the DW. Redrawn with permission from Nataf *et al.* [88].

### 1.4.1 Charged Domain Walls in Ferroelectrics

In most ferroelectrics, DWs are neutral to minimise energy costs and do not often carry bound charge. However, charged DWs can also exist, as depicted in **Figure 1.10**. There are now several reports of materials where polar discontinuities are supported at charged DWs, with distinctly enhanced/suppressed electrical conductivity of stark contrast to the bulk material [84]. Polar discontinuity at the charged DW can have a bound negative or positive charge, that will in turn attract mobile charge carriers to the DW. Some key factors in determining ferroelectric DW formation and size are the anisotropy and the dipole-dipole interactions in the material. Typically, these parameters are of the same order of magnitude leading to DWs with thickness of only a couple of nanometres. Due to the relatively small nature of these features (typically < 5 nm), they can be considered true 2*D* topological defects that form when a discrete symmetry is broken at a phase transition. DW sizes of electrically polar materials differs from DW sizes for magnetic domains, where the size of the wall depends on parameters such as the magnetic exchange (which tends towards wider walls) energy and the magneto-crystalline anisotropy (which tends towards narrower walls). In magnetic systems typically the magnetic exchange energy is much larger than the anisotropy thus resulting in wider (10 to 100's of nm) DWs [89].

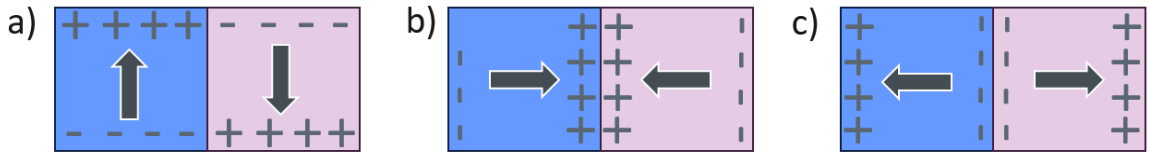


**Figure 1.10** (a)-(c) depict some possible charged states at 180 ° DWs. (a) Depicts a neutral 180 ° DW, (b) is a charged head-to-head (yielding positive bound compensating charges) DW and (c) is a charged 180 ° tail-to-tail wall (yielding negative bound compensating charges) DW.

In **Figure 1.10** a neutral side-by-side DW and two charged DWs are present, known as head-to-head (H-H) and tail-to-tail (T-T) DWs. 180 ° H-H DWs are positively charged while T-T DWs are negatively charged and thus the bound charges that accumulate at these DWs allow for the conductivity of the charged DWs to differ from the surrounding material. In ferroelectric materials there are both intrinsic and extrinsic mechanisms leading to the

formation of charged DWs [88]. As Nataf *et al*. [88] discuss, one example of an extrinsic mechanism is the accumulation of charged point defects at the DW. Some proposed intrinsic mechanisms are: (i) a suppression of the conduction band, where the bandgap is reduced at the DW compared to the bulk material and (ii) a shift of the band structure, where there is band-bending at charged H-H (yielding positive bound compensating charges) and T-T (yielding negative bound compensating charges) DWs [88], [90]. Creation of narrow channels of electrical conductivity within an otherwise insulating ferroelectric matrix and the fact that conducting DWs can be created, annihilated or moved on demand by applying voltage pulses, makes these extremely interesting and useful features to explore for use in future DW devices [91], dynamic nano-circuits [88], memristive devices [92] and spintronic devices [93], [94].

### 1.4.2 Non-trivial Topological Structures

In addition to Ising-type DWs, recent work has showed that more complicated non-trivial DW structures can also exist [95]. Shown in **Figure 1.11** are centre convergent/divergent vertex domains [96], polar vortex DWs [97] and polar skyrmions [98], [99]. In the 1930s and 1940s [85], [100] it was postulated that magnetic spin or polarisation vectors could potentially order as vortex-like structures, where vortices can be identified by the continuous rotation of polarization around a vortex core rather than ordering linearly. The anisotropy for ferromagnetic materials is relatively small and dipole vortices have been observed for many years in zero-dimensional magnets [101], [102], where the magnetostatic energy of the confined ferromagnet is reduced via the formation of flux-closures or a vortex. However the discovery of ferroelectric polar vortex topologies was much slower compared to their magnetic counterparts, with the first DFT predictions in 2003 [103], [104] and first experimental evidence in 2011 [105], [106]. The larger anisotropy/strain energy costs needed for the dipole rotation necessary for the formation of polar topological textures in ferroelectric materials slowed the development of these features when compared to ferromagnetic materials. However, through the development of composite heterostructures such as $(SrTiO_3)_n/(PbTiO_3)_n$ [107], [108], these energy costs could be tackled via interface depolarisation fields and strain/electric-field gradient energies. Polar skyrmions were stabilised within $(SrTiO_3)_{16}/(PbTiO_3)_{16}$ composites on substrates under slight compressive strain, promoting increased *c*-type domains and increased tendency for out-of-plane

polarisation [109]. These features exhibit a continuous rotation of the local polarisation vector forming a closed loop, which then causes the polarisation in adjacent domains surrounding the looped wall to rotate in order to minimise energy within the system. These non-trivial topological features allow for ferroelectric systems to have new exciting properties such as chirality reversal [110], [111] and negative capacitance [112] offer new applications in energy-efficient electronics, ultra-compact data storage and ultrahigh speed data processing [113].

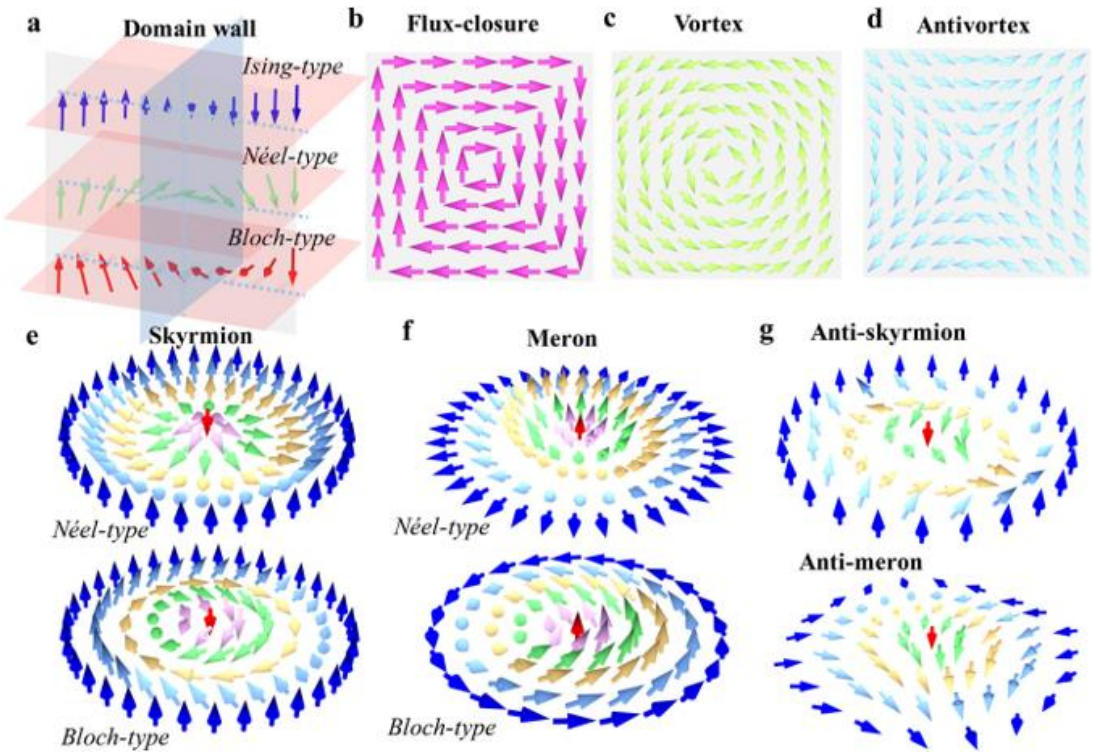


**Figure 1.11** Schematics of various types of topological textures in ferroics. The arrows represent the polarization or magnetization. (a) Different types of domain walls, (b) flux-closure, (c) vortex, (d) antivortex, (e) Néel-type and Bloch-type skyrmion, (f) Néel-type and Bloch-type meron, (g) anti-skyrmion and anti-meron. Redrawn with permission from Das *et al.* [106], under the terms of the Creative Commons Attribution (CC BY) license which permits use, sharing, adaptation, distribution and reproduction in any medium or format, provided the original work is properly cited.

## 1.5 Multiferroic Materials

Multiferroic materials are materials that show at least two ferroic properties within a single phase. The most commonly investigated ferroic properties are ferroelectricity (electric polarisation), ferromagnetism (magnetic moment), ferroelasticity (strain) and more recently ferrotoroidicity (toroidal moment) [114], [115]. It should also be noted that due to the rarity of room temperature multiferroics, materials that exhibit antiferromagnetism and ferrimagnetism, along with ferroelectricity are also considered to be multiferroics, e.g. antiferromagnetism (with a weak canted ferromagnetism) alongside ferroelectricity in multiferroic $BiFeO_3$ [51]. While the term multiferroic, first used by Hans Schmid, [116] is broad and encompasses many properties, in this thesis the focus is on materials with ferroelectric and ferromagnetic properties due to their unique properties which allow them to have applications in multi-level memories.

One of the first magnetoelectric multiferroics reported was nickel iodine boracite, $Ni_3B_7O_{13,}$ discovered by Ascher *et al.* in 1966 [117]. These early materials were very useful as proof of concept for multiferroic materials. However, due to the complex nature of their structures and the large number of inter-atomic bonds, they were very challenging to characterise and therefore difficult to understand the origin of their multiferroic properties. In the 1950s, the search for ferromagnetic and ferroelectric materials began by substituting magnetic $d^n$ *B*-cations (atoms with partially filled d-orbitals), for $d^0$ *B*-cations (atoms with empty d-orbitals), in ferroelectric perovskites, with $(1 - x)Pb(Fe_{2/3}\ W_{1/3})O_3 xPb(Mg_{1/2}W_{1/2})O_3$ being one of the first produced [118] [50]. In this case, the dilution of the magnetic cations in the mixed cation materials meant that the $T_C$ or Néel temperature (the point at which antiferrimagnetic materials become paramagnetic, $T_N$) were often very low and were not useful for room temperature applications. Since the year 2000, research around magnetoelectrics and multiferroics has increased as shown in **Figure 1.12** and different mechanisms from which multiferroicity arises have been discovered, as discussed later in **Section 1.5.3**.

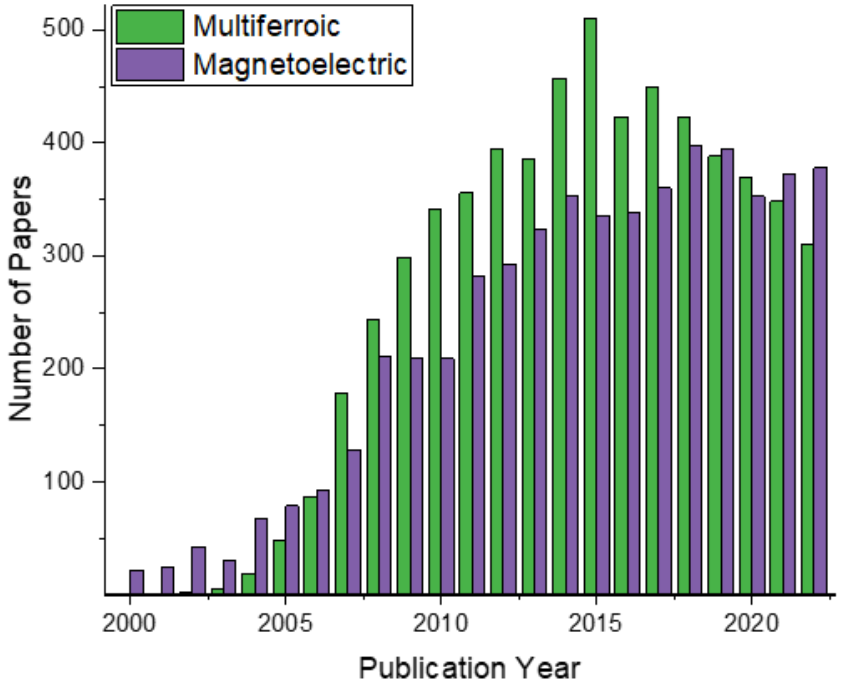


**Figure 1.12** Number of publications with multiferroic or magnetoelectric in their title since 2000. Data is taken from Web of Science database, September 2023.

### 1.5.1 Magnetoelectric Multiferroics

While multiferroics are classed as materials containing at least two ferroic properties within a single phase, going forward through this text, the term multiferroic will refer to multiferroics with both ferroelectricity and ferromagnetism. The diagram in **Figure 1.13** clearly depicts the distinction between a magnetoelectric material and magnetoelectric multiferroics.

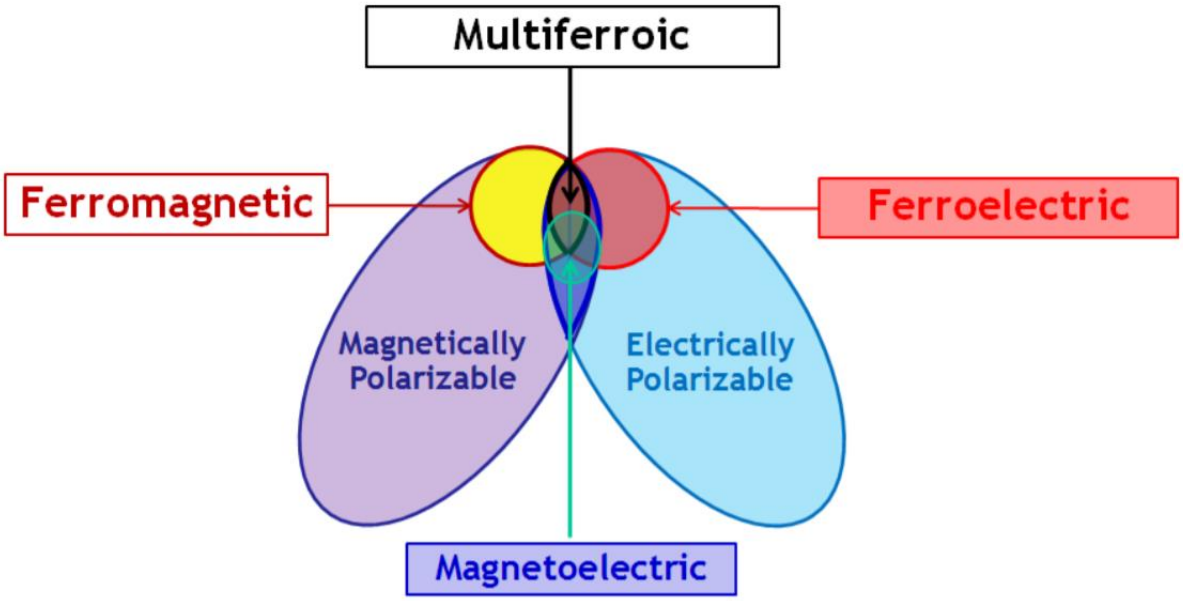


**Figure 1.13** Venn diagram displaying the relationship between multiferroic and magnetoelectric materials. Redrawn with permission from Keeney *et al.* [79].

A magnetoelectric material is one where there is coupling between the material's electric and magnetic components. In a magnetoelectric material, the application of an external electric field can control magnetism and similarly the polarisation can be manipulated using an external magnetic field [119]. However, ferroelectricity or ferromagnetism does not need to be present in the material for it to be magnetoelectric, for example antiferromagnetic $Cr_2O_3$ [120]–[122]. A magnetoelectric multiferroic is a type of material which can be found as a subset within magnetoelectric materials, where both ferromagnetic and ferroelectric (see **Figure 1.13**) are present with a coupling between the electric and magnetic characteristics. Magnetoelectric multiferroics offer a possible pathway to small, fast and energy efficient memory storage devices, for example magneto-electric spin-orbit (MESO) based devices are now being developed by companies such as Intel [123].

These devices will be charge/voltage driven and produce a charge/voltage output. An electric field can be used to induce a change in magnetisation via the magnetoelectric effect. This change can then be read out by the spin-orbit coupling (coupling of an electron's angular momentum with its linear momentum) component, which converts the change in magnetisation into an electric charge. Research by Manipatruni *et al.* [123] with Intel has proposed that devices based on MESO technology will have a 10 to 30 times higher efficiency, will increase device logic density by a factor of 5 and will allow for a 5 times decrease in switching voltage when compared to current state of the art architectures, e.g. CMOS HP (high performance CMOS) and CMOS LP (low power CMOS). However, there are still limitations to this technology, where an increase in the output of Rashba–Edelstein effect voltage from hundreds of μV to hundreds of mV is required. The magnetoelectric component of the devices will also have to operate at voltages of approximately 100 mV in order to be viable. Due to material limitations, this has not been achieved yet with typical switching voltage requirements of 5 V.

### 1.5.2 Why are there so few Multiferroics?

Herein, the fundamental contradictions between the conditions needed for ferroelectricity and ferromagnetism, which signifies that the creation of a material with both behaviours in a single phase is difficult, are discussed. Typically, ferroelectricity stems from the distortion of a crystal system to a non-centrosymmetric structure, often created by electron density transfer from one atom e.g. oxygen to a transition metal with an empty *d* valence shell. However, for ferromagnetism, partially filled *d* valence orbitals are needed, where unpaired electrons can align and produce a magnetic moment. For example, magnetism in transition metals is often caused by the Fermi level of the material lying in the 3*d* and 4*s* energy levels, where both are partially occupied. This means that parallel magnetic spins are lower in energy than anti-parallel magnetic spins and a net magnetic moment is present. If there are no unpaired electrons available there can be no magnetic ordering in the material. By partially filling the *d*-orbital to induce a magnetic moment, the small centre cation which could otherwise be displaced to create a non-centrosymmetric structure loses its tendency to do so. Therefore, adding electrons to the *d*-orbital eliminates the structure's tendency to distort

to a lower symmetry polar phase. Many reasons as to why there are such a low number of multiferroics have been investigated with relation to the *d*-orbital. Recent work [124], [125], has proven that $d^0$-ness is not the hard determining factor to whether a *B*-site cation will undergo a symmetry lowering distortion due to the pseudo-Jahn-Teller effect, but rather that the spin is an important factor. In fact, cations at the *B*-site with certain configurations of unpaired electrons, e.g. the high-spin $d^3$ configurations, as found in $CaMnO_3$ [126] or $SrMnO_3$ [127], have shown that by tuning the material's structural instabilities, both ferroelectricity and ferromagnetism can be present. For example, in the $SrMnO_3$ case [127] when the *A*-site is doped with Ba, such that $Sr_{1-x}Ba_xMnO_3$ x = 0.45, the $Mn^{4+}$ cation provides pathways to both multiferroic properties. Here the normally cubic phase material can maintain a spontaneous distortion to the tetragonal phase, where a ferroelectric distortion is caused due to the elongation of the *c*-axis. Meanwhile under $T_N$ ~185 K, the Mn-O-Mn bond, while slightly distorted, is still close enough to 180 ° such that the antiferromagnetic superexchange mechanism is still present. Even in the light of recent material progress and development, the general competing processes for ferroelectricity and ferromagnetism mean that accomplishing both in one phase to yield room temperature functionality is quite rare.

### 1.5.3 Pathways to Multiferroic Properties

Conventional ferroelectricity is caused by a polar distortion via hybridisation with a $d^0$ transition metal or via stereochemical activity of lone pair electrons. Conventional ferromagnetism is caused by un-paired electron spin in partially filled *d*-orbitals in transition metals or partially filled localised *f*-electron states in rare earth metals. In order to circumnavigate the contradicting requirements of the unfilled or partially filled *d*-orbitals for ferroelectricity and ferromagnetism, respectfully, many different routes have been constructed in order to create materials which combine ferroelectric and ferromagnetic properties, as shown in **Figure 1.14** [48]. Multiferroics can be divided into two groups, Type I and Type II, through the way they achieve their properties. Type I, where ferroelectric and ferromagnetic properties come from two different sources in the material. An example is $BiFeO_3$, where stereochemical active lone pair 6*s* electrons in the $Bi^{3+}$ gives rise to ferroelectric distortions and $Fe^{3+}$ provides unpaired electrons for antiferromagnetism. In Type II multiferroics, ferroelectricity is induced when magnetic ordering breaks the inversion

symmetry of the structure [128]. In Type I multiferroics, ferroelectricity and ferromagnetism occur at different temperatures (the latter often being lower), while for Type II multiferroics, both properties appear at the same temperature point. In **Figure 1.14**, one can see various mechanisms for the origin of multiferroic properties. Type I multiferroics can comprise of composites (e.g. hetero-structure stacks which can be comprised of layers of a non-ferroelectric magnetic material and a non-ferromagnetic ferroelectric material), lone electron pair effects leading to ferroelectricity combined with unpaired *d*-electron magnetism materials, $d^0$ ferroelectricity combined with *f*-electron magnetism materials and novel ferroelectricity with *d*-electron magnetism (e.g. charge ordering and circumventing '$d^0$-ness' along with d-electron magnetism). Some Type II multiferroics can be seen on the right side of the tree in **Figure 1.14**, comprising of multiferroics where for example magnetic ordering or spirals induce ferroelectricity.

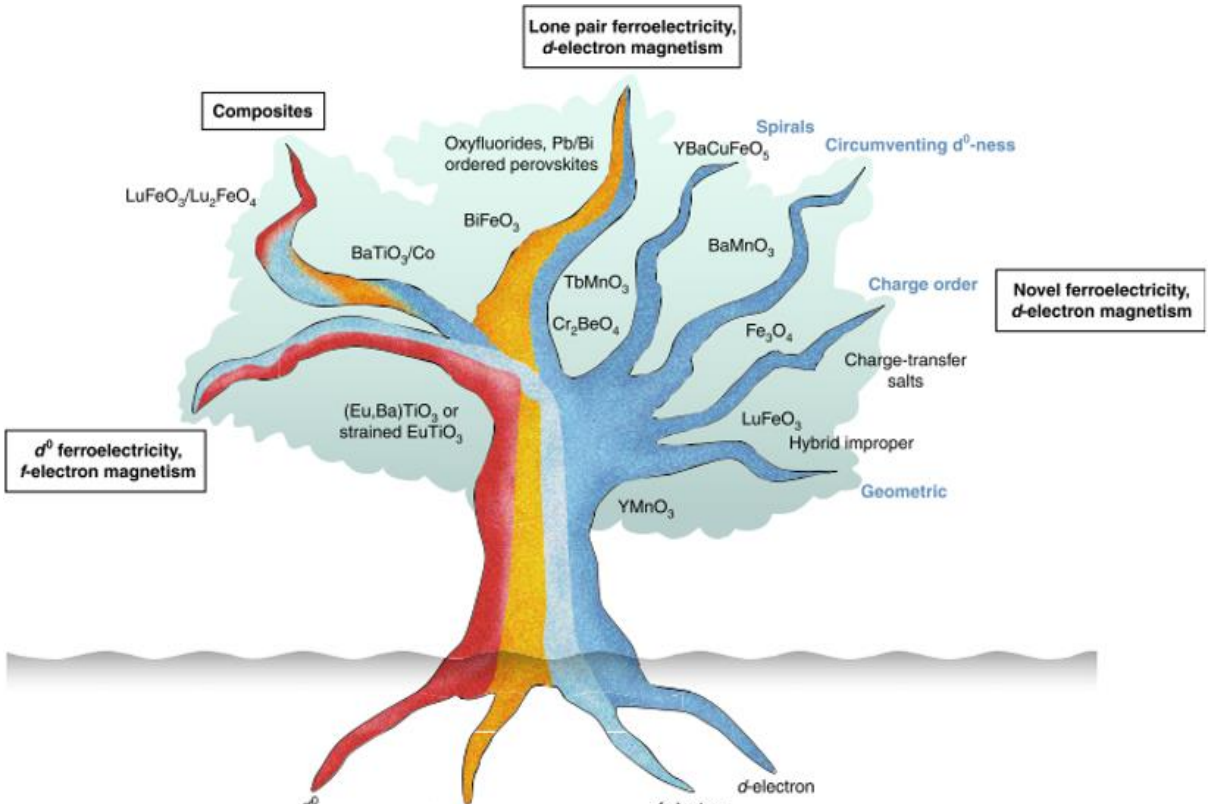


**Figure 1.14** Tree of mechanisms by which both ferroelectricity and ferromagnetism can be observed in a multiferroic material with examples of different materials investigated to date. Reused with permission from Spaldin *et al.* [41].

The hexagonal manganites, $R$MnO$_3$, where *R* is a rare earth metal, are one group of materials with promising properties for development as multiferroics. They are improper

ferroelectrics where their polar distortion is driven by a geometric change in the crystal symmetry. In this case, a distortion of the lattice is induced by ionic size effects. The lattice distortion results in a tilt and rotation of the $MnO_5$ bipyramids around a central $R^{3+}$ ion, thereby breaking the symmetry of the lattice and providing a pathway for a polar distortion to be present [129]. As the polarisation in the materials is improper, an antiferromagnetic order can arise in the Mn sublattice [130]. While the hexagonal manganites such as, $YMnO_3$ and $ErMnO_3$, demonstrate further technological promise due to the coupling between the ferroelectric and ferromagnetic states, their $T_N$ is below 130 K, currently making them unfeasible for room temperature applications.

As discussed in **Section 1.2.4**, perovskite materials are key players in the development of multiferroics. Bismuth Ferrite ($BiFeO_3$), is the most studied multiferroic material. The Ramesh group in 2003 [51] were the first to show an enhancement in polarisation in monoclinic $BiFeO_3$ films compared to the bulk rhombohedral structure. Heteroepitaxial constrained $BiFeO_3$ films displayed room temperature ferroelectricity (~90 μC $cm^{-2}$, $T_c \approx 1100$), and antiferromagnetism ($T_n \approx 640$ K). Ferroelectric distortion in $BiFeO_3$ is a result of the stereochemically active $6s^2$ lone pair of electrons associated with the $Bi^{3+}$ cation at the *A*-site while the *G*-type antiferromagnetism comes from antiparallel $Fe^{3+}$ spins (with magnetic spin arising from the $3d^5$ electrons) at the *B*-site [48], [131]. The spins are not perfectly parallel and canted-spin arrangements mean that a weak ferromagnetic response via the Dzyaloshinskii–Moriya interaction is also present in $BiFeO_3$. While $BiFeO_3$ is one of the few known room temperature multiferroics, its application is still hindered by factors such as its large coercive field, with some of the lowest measured values for films around in 600 nm thickness being between 74-80 kV $cm^{-1}$ [132], [133], while for thinner films larger coercive fields are present as a result of the Kay-Dunn scaling law [134]. One consequence of such large coercive fields is the decomposition of $BiFeO_3$ into magnetite ($Fe_3O_4$) and bismuth oxide ($Bi_2O_3$) compounds. Perovskite structures lend themselves well for compositional adaptation due to their tolerance for accepting a variety of *A*- and *B*-site cations. They can readily facilitate mixed chemical compound structures e.g. $A_xA_{1-x}BO_3$ where the distortion of the symmetry of the structure can be predicted by the Goldschmidt Tolerance factor [135]. Thus, alternating strain [136] and chemically doping $BiFeO_{3,,}$ e.g. $La_{0.15}Bi_{0.85}FeO_3$ [137], has been proved to enhance its properties for applications in technological devices.

As discussed above, significant headway has been made on developing thin film multiferroic materials from the first thin film synthesis of monoclinic $BiFeO_3$ in 2003. Nonetheless, further insight into the mechanisms that allow for multiferroic properties to coexist at room temperature is needed in order to fully optimise materials for working state-of-the-art memory storage devices. While there are multiple routes one could explore in order to try and engineer materials to host at least two multiferroic properties, the focus of this thesis is to develop the multiferroic properties of Aurivillius phase materials.

### 1.5.4 Prospects for Single-phase Multiferroic Topological Structures

While multiferroic topological structures are very rare (as discussed in **Section 1.4.2**), the realisation of these types of features within single-phase multiferroic materials are of high importance to fundamentally understanding the potential of multiferroic materials and their role in emergent memory technologies. Recent studies on $SrRuO_3/PbTiO_3$ (ferromagnetic – ferroelectric) superlattices have demonstrated ferroelectric topologies with an extra periodic perturbation along the vortex core, implying that a type of electrical Dzyaloshinskii–Moriya interaction is present, similar to those which stabilise magnetic spin vortex topologies [138], [139]. As such, these results uncover ferroelectric topological features that experimentally demonstrate a relationship between ferroelectric and ferromagnetic structures. Magnetoelectric skyrmions also have exciting application potential through the advancement of low heat dissipation spintronic devices [140]–[142]. For magnetoelectric skyrmion applications, it has been directed that the use of single-phase multiferroics over composite multiferroic (e.g. $(SrTiO_3)_n/(PbTiO_3)_n$) systems is expected to prevent much of the skyrmion annihilation that can occur through sample edges [143]. While designing room temperature single phase multiferroics with uncommon topological structures and which also operate at room temperature will not be simple, the successful realisation of these types of materials will improve the fundamental understandings of intrinsic inversion asymmetry mechanisms and will further advance the research on magnetoelectric coupling mechanisms.

## 1.6 Aurivillius Phase Materials

Aurivillius phase materials are naturally layered structures consisting of $m$$ABO_3$ perovskite blocks sandwiched between $[Bi_2O_2]^{2+}$ layers, where $m$ has a range of 1-9 [53], [144]–[146]. The Aurivillius phase structure, with general formula $Bi_2O_2(A_{m-1}B_mO_{3m+1})$, can be thought of as a naturally layered nano-composite. Aurivillius phases have a large $c$-axis (in the nanometre range) comprised of the thickness of the $[Bi_2O_2]^{2+}$ layer ($f$ = 4 Å) and the average thickness of the perovskite block, $h$, is influenced by the number of octahedral perovskite units ($m$) in the block, $h = mp$, where $p$ is the average thickness of each perovskite unit cell (also typically ~4 Å). It should be noted that $p$ is only an approximation due to the differently sized cations that can be at the $A$- and $B$-site and considering the unit cell distortion and octahedral tilting that can be found in Aurivillius phase systems. The thickness of the Aurivillius phase's half unit cell can be predicted in terms of the $c$ lattice parameter by $h + f = \frac{c}{2}$ [7]. This equation matches up quite well with experimentally recorded material thickness e.g. approximation for $SrBiTa_2O_9$ equals 24.60 Å, compared to the experimental measurement of 25.02641 Å [147].

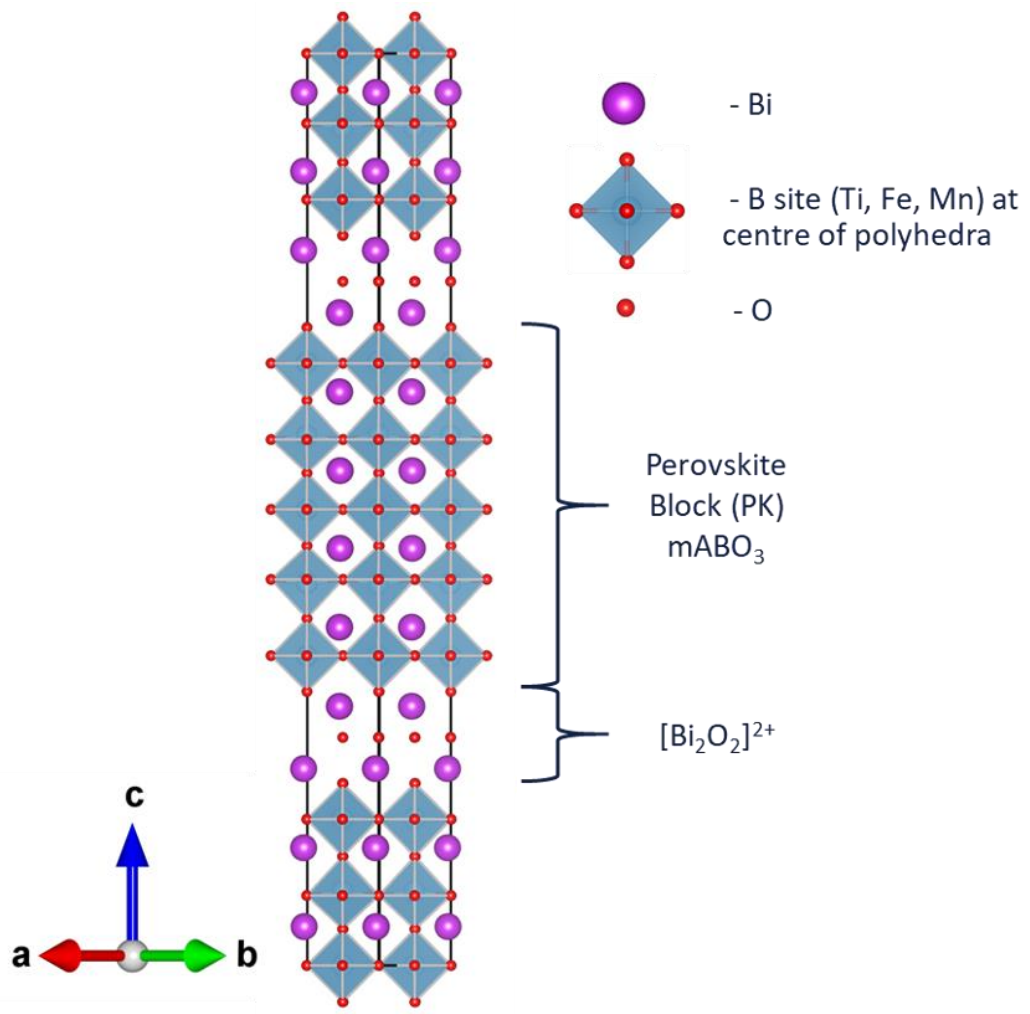


**Figure 1.15** Schematic of five-layered Aurivillius phase $Bi_6Ti_3Fe_2O_{18}$ depicting an *F*2*mm* space group visualised using Vesta software [148] from a .cif structure file generated from data taken from García-Guaderrama *et al.* [149].

### 1.6.1 Composition and Symmetry

Aurivillius phase structures are an ideal scaffold for synthesising multiferroic materials due to the structure's tendency towards ferroelectric distortions and its potential to accept a large number of magnetic cations into its structure without compromising ferroelectricity. Cations that can occupy the large (1.34 to 1.64 Å) 12-coordinate *A*-site include $Na^{1+}$, $K^{1+}$, $Ca^{2+}$, $Sr^{2+}$, $Ba^{2+}$, $Pb^{2+}$ and $Bi^{3+}$, while common cations that occupy the smaller (0.58 to 0.645 Å) *B*-site include $Fe^{3+}$, $Ti^{4+}$, $Nb^{5+}$, $W^{6+}$, $Ta^{5+}$ and $Cr^{3+}$ [148], [149]. Due to the chemical flexibility of Aurivillius compounds, a wide variety exist, where their properties can be tuned for

applications such as memory storage (e.g.$Bi_4Ti_3O_{12}$ [145] and $SrBi_4Ti_4O_{15}$ [150]) and photo-catalysis (e.g. $Bi_2WO_6$ [151]).

The number of perovskite unit cells in the Aurivillius phase (see **Figure 1.16**) impacts the ferroelectric properties of the material. As the value of *m* increases, the coercive electric field needed to induce polarisation decreases [152], [153]. The $[Bi_2O_2]^{2+}$ layer is paraelectric, meaning that the $Bi^{3+}$ ions do not easily move in the direction of an applied electric field. Thus, when *m* values are low, the $[Bi_2O_2]^{2+}$ has a significant impact on the ferroelectric switching of the material. As *m* increases, the contribution of the $[Bi_2O_2]^{2+}$ layer reduces and the overall coercivity of the material decreases. This allows for a lowering of the minimum electric field needed to produce hysteresis loop saturation.

Above the ferroelectric Curie temperature, the Aurivillius phase materials have a high temperature centrosymmetric paraelectric phase, the *I4/mmm* space group. Below the ferroelectric phase transition ($T_c$), there is symmetry lowering within the material to non-centrosymmetric space groups [154]. A strong Bi-O bond is formed between $Bi^{3+}$ in the $(Bi_2O_2)^{2+}$ interface layers and the apex oxygen of the perovskite layer. To complete the outer electron configuration, the axial apex oxygen accepts an electron from the octahedral cation forming a short pair bond with it, which is approximately 0.5 Å shorter than the trans-axial *B*-site oxygen bond. This prompts ferroelectricity via a polar displacement of ions perpendicular to the layer direction and shears the perovskite layer, causing octahedra to rotate. The major polarisation vector is along the lateral (*a*-axis) direction. Whether *m* is an odd or even number greatly affects the ferroelectric behaviour. Aurivillius phases having *even* numbers of *m* perovskite layers crystallise with orthorhombic ($A2_1am$) symmetry and it is favourable to retain the horizontal mirror plane perpendicular to the *c*-axis. In *even* phases, the strain felt on the $BO_6$ octahedra due to the bond formed between a Bi ion and the $[Bi_2O_2]^{2+}$ slab is minimised by keeping its mirror plane perpendicular to the *c*-axis. The mirror plane in *even-m* Aurivillius phases means that the out-of-plane polarisation in the *c*-direction is antipolar with a net zero value. This prohibits out-of-plane polarisation along the *c*-axis in *even*-layered Aurivillius phases and the polarisation is confined to the lateral plane (*a*-axis). Polar Aurivillius phases having *odd m* numbers of perovskite layers crystallise to lower symmetry systems (e.g. *B*2*cb*, *B*2*eb*, *B*1a1). For *odd*-numbered Aurivillius phase configurations, retention of the mirror plane is not energetically favourable. Here, there is a two-fold rotation along the *a*-axis rather

than a mirror plane along the *c*-axis. This enables the *odd* layer phases to possess a minor out-of-plane polarisation along the *c*-direction in conjunction with a major in-plane polarisation.

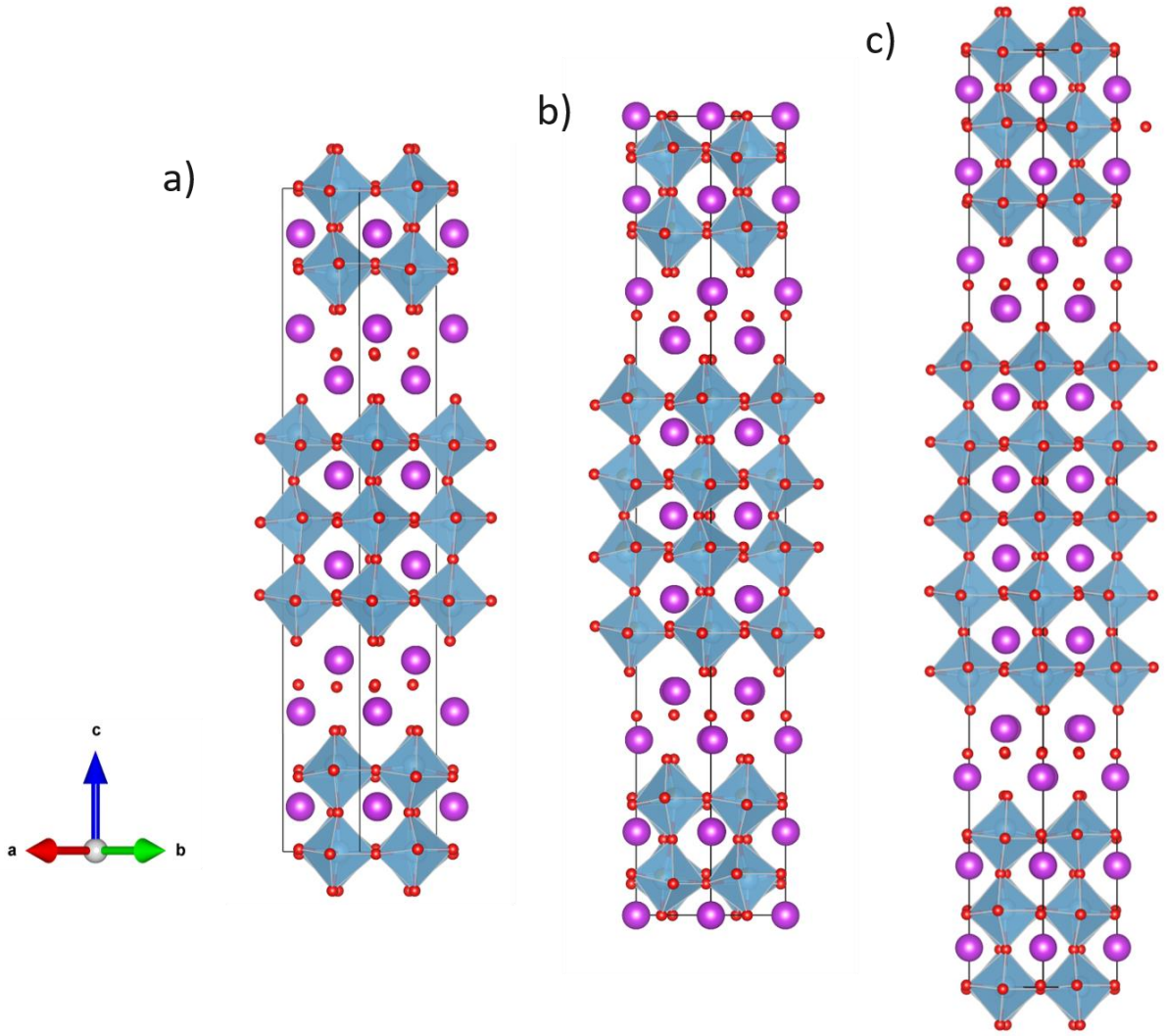


**Figure 1.16** Examples of Aurivillius phases with *odd* and *even* numbers of perovskite layers (*m*): a) three layered (space group *B*1*a*1) $Bi_4Ti_3O_{12}$ [155], b) four layered (space group *A*2$_1$*am*) $Bi_5Ti_3FeO_{15}$ [150] and c) five layered (space group *B*2*cb*) $Sr_2Bi_4Ti_5O_{18}$ [156].

Polar distortion is one mode of symmetry lowering observed in Aurivillius phases. However, in many Aurivillius phase systems, further symmetry lowering occurs through tilting and rotation of the $BO_6$ octahedra. In **Figure 1.17**, the high temperature paraelectric *I*4/*mmm* space group is shown alongside the room temperature *B*1*a*1 space group, where there are three extra tilt modes ($X_1^-, X_3^+, X_2^+$) present alongside the polar distortion [155]. Goldschmidt's tolerance factor, *t* [135],

$$t = \frac{r_o + r_a}{\sqrt{2}(r_o + r_b)} \qquad 1.2$$

where $r_o$, $r_a$ and $r_b$ are the ionic radii of the oxygen, *A*-site and *B*-site ions, respectively, has been used to deduce that a value of $t < 1$ would promote a perovskite system within which the oxygen octahedra tilt [147], [156], [157]. The symmetry lowering modes occur when the relative size of the *A*-site atom becomes too small compared to the *B*-site cation. This in turn causes the oxygen anions to move towards the *A*-site cation. The movement of the oxygen anions causes the empty space around the *A*-site to shrink allowing for the tilting of the $BO_6$ octahedra.

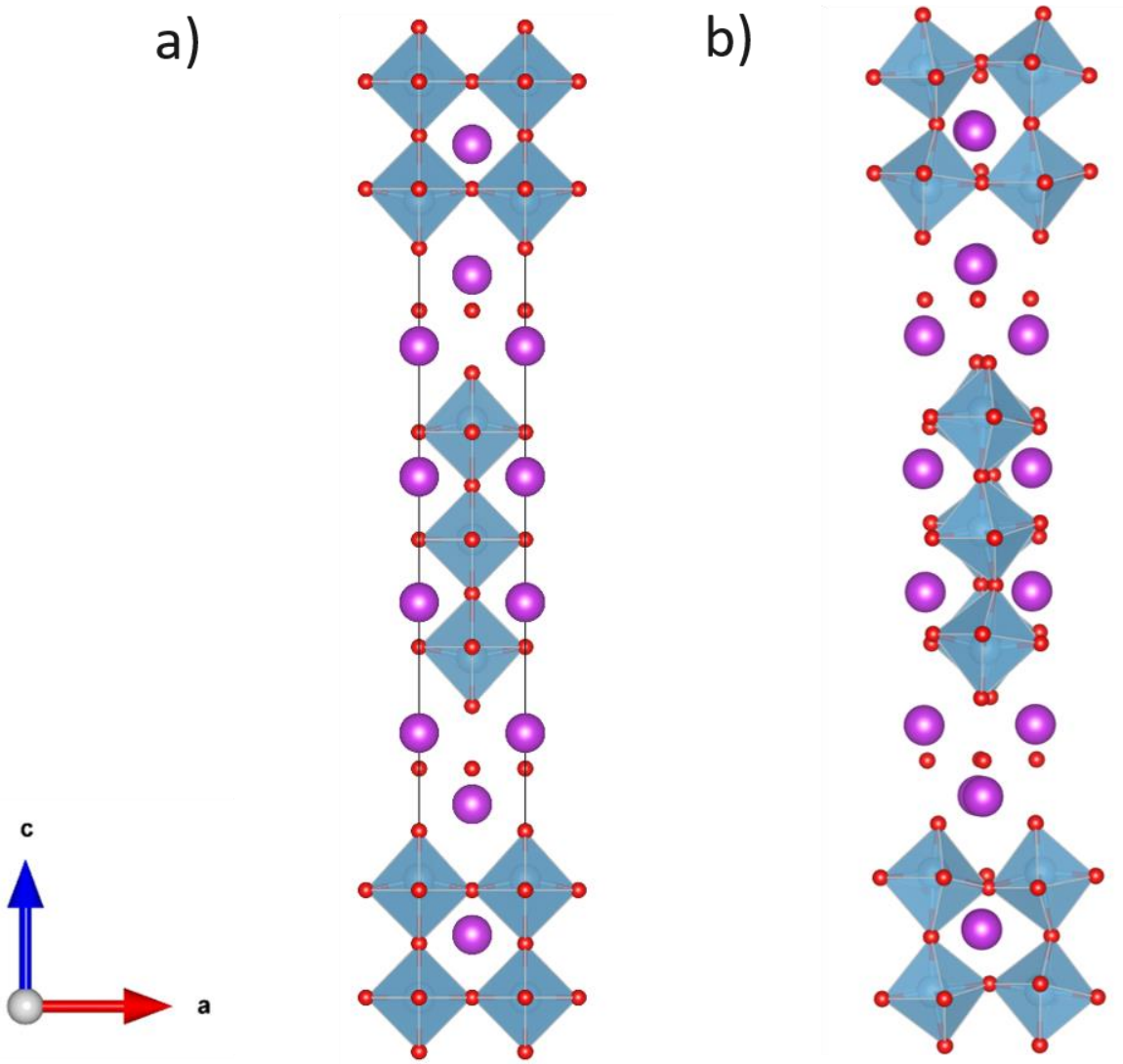


**Figure 1.17** Left: schematic of the centrosymmetric three-layered $Bi_4Ti_3O_{12}$ paraelectric phase (space group *I*4/*mmm)*. Right: schematic of the lower symmetry room temperature ferroelectric phase of $Bi_4Ti_3O_{12}$ with octahedral tilting and rotations (space group *B*1*a*1*)* [155].

Within the perovskite blocks of the Aurivillius systems, it is often found that there are non-equivalent *B*-sites within which the cations can reside, depending on their proximity to the $[Bi_2O_2]^{2+}$ layer. For example, studies of the $Bi_{m+1}Fe_{m-3}Ti_3O_{3m+3}$ system indicate that $Fe^{3+}$ does not occupy these *B*-sites randomly. DFT and electron microscopy studies of the $m = 4$ system, $Bi_5FeTi_3O_{15}$, imply that Fe distribution within the perovskite blocks occurs giving rise to mixed configurations. There is a preference for one Fe cation to occupy a *B*-site next to the $[Bi_2O_2]^{2+}$ layer (outer site) and for the other Fe cation to occupy the *B*-site furthest from the $[Bi_2O_2]^{2+}$ layer (inner site) as can be seen in **Figure 1.18**, [158], [159]. Rietveld analysis of neutron diffraction data from the $Bi_5Ti_3CrO_{15}$ ($m = 4$) system reveals that the Cr cations partition partially into the central two perovskite layers [160]. Given the varying number of perovskite unit cells, cations and symmetries for different Aurivillius phase structure types, the cation site preference will vary for each individual material.

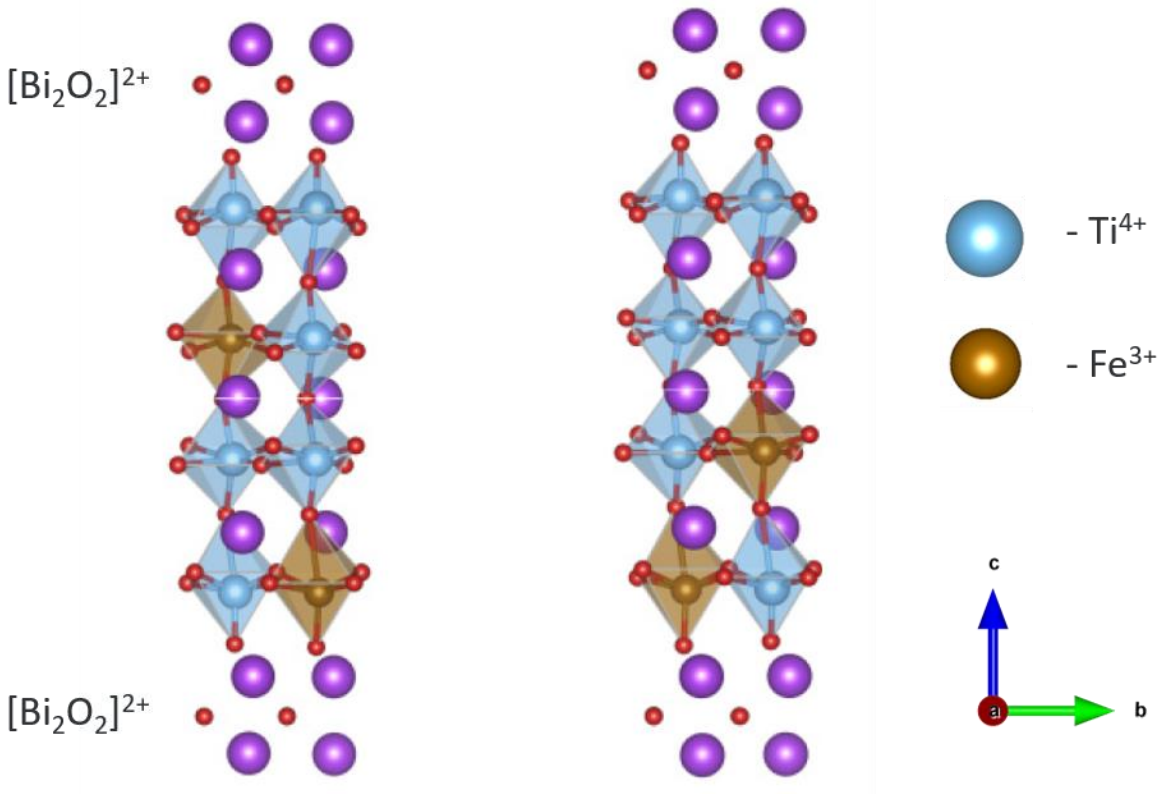


**Figure 1.18** Two examples from DFT (density functional theory) calculations [159] of the preferred *B*-site positions for $Fe^{3+}$ within the $m = 4$ $Bi_5FeTi_3O_{15}$ Aurivillius phase system Adapted with permission from Campanini *et al.* [158]. Copyright 2019 American Chemical Society.

### 1.6.2 Multiferroic Five Layered Aurivillius Phase: $Bi_6Ti_xFe_yMn_zO_{18}$

In the Aurivillius phase $Bi_6Ti_3Fe_{1.5}Mn_{0.5}O_{18}$ (B6TFMO), ferroelectric polar displacements are created through the presence of $Bi^{3+}$ at the *A*-sites and $Ti^{4+}$ at the *B*-sites of the perovskite blocks. At the *A*-site, polar displacement is enabled via the stereo-chemical activity of the $Bi^{3+}$ lone pair of electrons. The distortion of the $TiO_6$ octahedra provides a route to ferroelectricity observed in the B6TFMO system due pseudo Jahn-Teller distortions, created by the hybridisation between the empty 3*d* orbitals of the $Ti^{4+}$ cations and the formally filled 2*p* states of $O^{2-}$ anions [161]. In the case of B6TFMO, incorporation of Fe and Mn magnetic cations provides a means to create long-range magnetic order within a ferroelectric framework and a single-phase room temperature magnetoelectric multiferroic is formed. B6TFMO displays saturation magnetization ($M_S$) values of 215 emu/cm$^3$ and in-plane saturation polarization ($P_s$) values of > 26 μC/cm$^2$. Furthermore, its domains have displayed reversible magnetoelectric switching characteristics (as show in **Figure 1.19**), positioning B6TFMO as an exciting candidate for future magnetoelectric devices [162], [163].

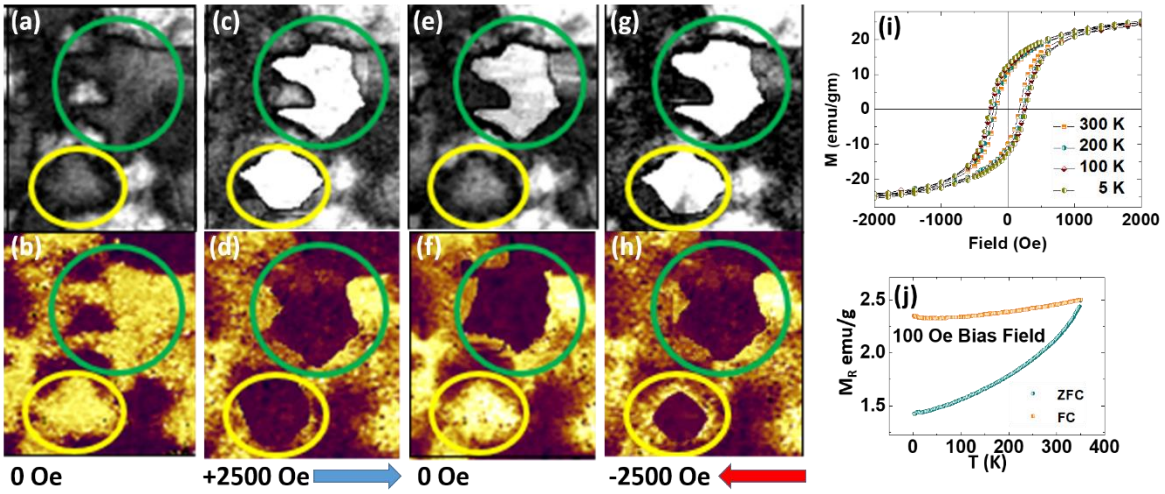


**Figure 1.19** Representative data demonstrating multiferroic behaviour of *m* = 5 Aurivillius phase samples. (a) - (h) Irreversible (encircled green) and reversible (encircled yellow) magnetoelectric switching of ferroelectric domains in B6TFMO under a varied magnetic field. (i) Magnetization (M) vs magnetic field (Oe). (j) Zero field cooled (ZFC) and field cooled (FC) measurements ($M_R$ vs T). The saturated hysteresis loops and clear split between ZFC-FC curves demonstrate the ferromagnetic nature of B6TFMO at RT. Adapted with permission from Faraz *et al.* [163].

Chemical composition studies by Keeney *et al.* [164] have shown that cation partitioning of Mn towards the central layers of the perovskite block (furthest from the $[Bi_2O_2]^{2+}$ interface) occurs, and is key to the room temperature ferromagnetic properties observed in B6TFMO. Possible contributing factors towards the cation partitioning in B6TFMO could be the elastic strain and electrostatic energy within the material. Electrostatically it has been hypothesised [160] from Mandelung calculations that $Ti^{4+}$ moves towards the outer perovskite cells in order to maximise the interactions with the oxygen anions found in the $[Bi_2O_2]^{2+}$ layer. Using Kikuchi's model [144] for Aurivillius phases the compressive forces felt by the perovskite layers (3.89 Å) next to the $[Bi_2O_2]^{2+}$ layers (3.80 Å) should be considered. These forces cause the larger Mn and Fe atoms to be driven towards the central perovskite cells, where the effects of the interlayer strain are much weaker. It has also been noted from Shannon site distortion parameters that $Ti^{4+}$ has a preference to occupy more distorted octahedra over Mn or Fe, hence preferring the perovskite unit cells next to the $[Bi_2O_2]^{2+}$ interlayers, which undergo the most compressive strain. Cation partitioning of Mn allows for an increase in the probability of nearest-neighbour magnetic interactions in the central layer by up to 90 % compared to when the magnetic cations are randomly distributed over the five available *B*-sites. In B6TFMO there are a few possible routes to ferromagnetic behaviour, e.g. superexchange interactions [75] between $Fe^{3+}$ (hs)-O-$Mn^{3+}$ (ls) or $Fe^{3+}$ (hs)-O-$Mn^{4+}$. Double-exchange mechanisms, which arise from the delocalisation of electrons, could also be a potential route to ferromagnetism in B6TFMO through $Mn^{3+}$ (hs)-O-$Mn^{4+}$ nearest neighbour interactions. Therefore, this increase in the nearest-neighbour magnetic interactions in the central perovskite cells creates more pathways for magnetic exchange mechanisms and thus helps explain the pathways to B6TFMO's magnetic properties at room temperature.

### 1.6.3 Structural Defects in Aurivillius Phase Systems

The manner by which domains form in multiferroic thin films and their properties are highly dependent on the energetics of the system. They are also influenced by the local defects structures that from within the films during growth. Layered oxide thin films are extremely prone to structural defects such as stacking faults, twin boundaries and out of phase boundary (OPB) defects [165], [166]. A number of defect types are very commonly

found within layered materials such as the Aurivillius phases. In this section, defect types, including stacking faults, 'anatase'-type, OPBs and intergrowths of different *m* phases are discussed.

Stacking faults are two-dimensional planar defects. They occur in crystal systems when there is a deviation in the regular stacking sequence of the crystal planes [167]. In a perfect crystal, the stacking sequence within a material remains constant through the entire crystal, however when the sequence is disrupted, a stacking fault can form. Stacking faults can occur in a material during crystal growth, as part of other defects within the structure (e.g. partial dislocations) or they can evolve from other defects (such as from the result of an OPB defect). A common type of stacking fault observed in Aurivillius phase materials is the addition or subtraction of a perovskite unit cell between the $[Bi_2O_2]^{2+}$ layers at an OPB defect, thus leading to regions where *m* changes by ±1, or potentially more than 1, where stacking faults are considered as intergrowths of differing *m* numbers.

Intergrowths within crystal systems refer to the presence of additional layers or crystal phases within the structure. The nature of intergrowths found within different structures can be determined by the compatibility of the new intergrowth phase with the parent phase, where factors such as the tolerance factor (as discussed in **Section 1.6.1**) are important. Intergrowths of different *m* phases, as shown in **Figure 1.20 (a)**, are often utilised in Aurivillius structures to enhance material properties [168], [169]. For example Noguchi *et al.* [170], created a $Bi_4Ti_3O_{12}$-$SrBi_4Ti_4O_{15}$ intergrowth structure which demonstrated an enhanced remnant polarisation when compared to simple $Bi_4Ti_3O_{12}$ or $SrBi_4Ti_4O_{15}$ materials on their own. Another type of intergrowth phase which has been observed in the B6TFMO system [171], is known as an 'anatase'-type planar defect, as seen in ***Figure 1.20*** **(b)**. This is a bismuth poor intergrowth in B6TFMO that appears where the $[Bi_2O_2]^{2+}$ layer usually resides. The 'anatase'- type planar defect is made up of chains of edge-sharing $BO_6$ octahedra and form "S"-shaped tunnels, which contain *A*-cation columns. Where these defects occur in perovskite and Aurivillius systems, the "S"-shape tunnels are stabilised by double columns of sterochemically active *A*-site cations with lone electron pairs e.g. $Bi^{3+}$. These type of defects have previously been seen in the Ti doped $Bi_{0.9}Nd_{0.15}FeO_3$ system from MacLaren *et al.* [172], [173] and at hetrointerfaces in $PbTiO_3$/$BiFeO_3$ bilayers from Liu *et al.* [174]. They are also evident in complexes created by Batuk *et al.* [175], [176] who have systematically engineered

a new perovskite-based layered structure, $Bi_{3n+1}Ti_7Fe_{3n-3}O_{9n+11}$ ($AB_4O_{11}$ + $3nABO_3$ where A = Bi, B = Fe, Ti). In this material the 'anatase'-type, "S"-shaped tunnels are interleaved between the perovskite layers. In Aurivillius phase systems, it has been noted that stacking faults and intergrowths of different *m* phases often accompany other defects. In this case they can appear at the stepped defect that occurs at the 'anatase'-type interface, likely compensating for shifts in the lattice structure or chemistry between the Aurivillius phase and the 'anatase'-type defect. Further examples of intergrowth families that can be engineered using the Aurivillius phase include the Sillén-Aurivillius phase [177], [178] where the material is made up using regular intergrowths of Aurivillius-like and Sillén-like blocks, $[M_2O_2]/[MNb_2O_7]/[M_2O_2]/[X]$, where M = Bi, Pb, Sr etc. and X is a halide. The Sillén-like blocks are oxyhalides and these intergrowth phases also have potential applications in ferroelectrics [179]–[181] along with water splitting processes [182], [183].

OPB defects are defined as defects created when a fraction of the unit cell in a material is displaced in the *c*-axis direction between two neighbouring regions, as shown in **Figure 1.20 (c)**. Anti-phase boundary defects are a special case of OPB defects when this displacement is 0.5 unit cells in the *c*-axis direction. These defects, which form during thin film synthesis, appear as 'steps' when viewed edge-on and can significantly influence the properties of the materials [184]–[189]. They often nucleate at the substrate-film interface and can then propagate up through the entire thin film, accompanied by perturbations to the crystal lattice, inducing local strain fields and non-uniform electrostatics.

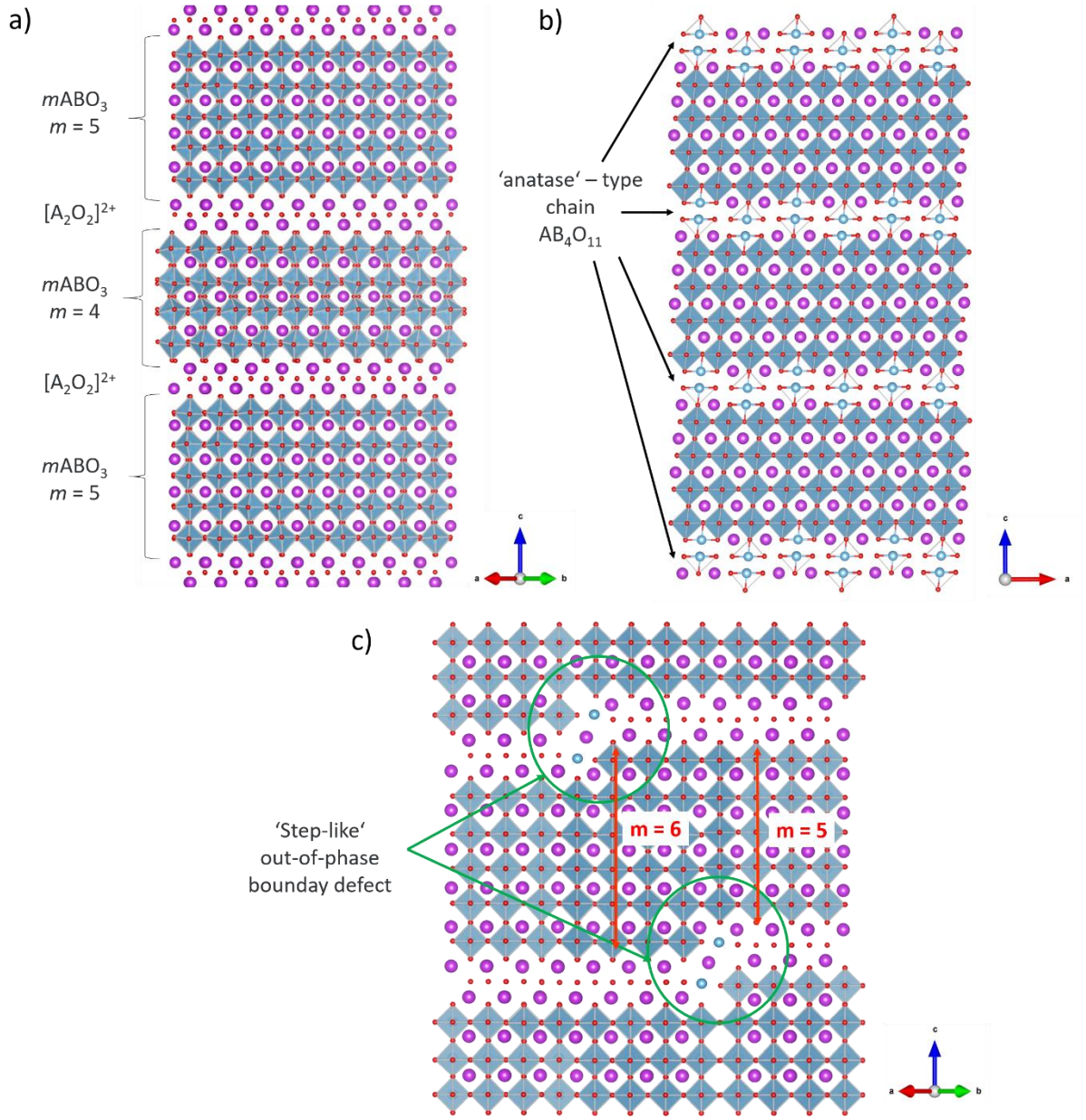


**Figure 1.20** Schematic of some common defects found in Aurivillius phase materials. In a) an $m$ = 4 intergrowth can be observed in an otherwise $m$ = 5 Aurivillius phase structure. b) Depicts the 'anatase'-type intergrowth in a four-layered system which is made up of edge-sharing $BO_6$ octahedra and double columns of the $A$-cation. This is found where the $[Bi_2O_2]^{2+}$ interface layer is usually resides. c) Demonstrates an example of OPB defects within Aurivillius phases at the $[Bi_2O_2]^{2+}$ layer. The unit cell is displaced in the $c$-axis direction by approximately one perovskite unit cell. Between the two OPB defects (circled in green) in the structure, a short-range $m$ = 6 stacking fault is present.

OPB defects and their effects on the multiferroic Aurivillius phase properties are not well understood, however due to the unusual polar topologies observed near these defects as discussed later in **Section 1.6.4**, further insight into how they form within Aurivillius phases would be advantageous in order to utilise the structural defects in a controlled manner to enhance particular properties. Recent work on the even-layered ferroelectric $Bi_5FeTi_3O_{15}$, has shown that ferroelectric domain engineering can be achieved using particular underlying substrates to order structural defects. It has been proposed that $Bi^{3+}$ vacancies are present at these defect regions [190]. In the thin film growth of Aurivillius phases, factors such as substrate, bismuth migration and changes to local stoichiometry play an important role [191]. While epitaxial substrates are necessary for conformal growth of thin films, the rigid epitaxy set by the physical constraints of the underlying substrate and a low degree of structural rearrangement during bismuth migration and film growth can result in microstructural defects forming within the film. Often this is seen as a disadvantage, however for domain engineering, it means that the OPB defects that form at the interface could be controlled to propagate throughout the whole film due to the lack of restructuring during the film growth. There are currently considered to be four primary nucleation mechanisms for OPB defects as shown in **Figure 1.21**, known as **(a)** nucleation layer, **(b)** steric, **(c)** *a*-*b* misfit and **(d)** inclined *c*-misfit along with one secondary mechanism known as **(e)** crystallographic shear [166].

OPB defects caused by the **(a)** nucleation layer mechanism often arise due to different terminations on the epitaxial substrate surface where a particular plane in the crystal structure of an Aurivillius phase is energetically preferred (e.g. on $TiO_2$ terminated or SrO terminated $SrTiO_3$). However, it is also possible that the nucleating layer could have more than one part of the lattice which is energetically favourable to grow on. At the point where two growth regions meet, the difference of the fraction of a unit cell difference between the regions forms an OPB defect. OPB defects created through **(b)** steric mechanisms are formed due to the atomic scale topography of the substrate. When steps edges occur across the surface of a substrate, the height difference between each step can create OPB defects. At these step edges, the crystal structure may nucleate at the same layer but because of the displacement caused by the step edge, an OPB defect will form where the two nuclei meet. Factors that would have an impact on this type of OPB nucleation are vicinal surface, step height, substrate structure and nuclei density. It is likely that for this type of nucleation

mechanism, vicinal surfaces may increase the chances of an OPB occurring during thin film growth. There are two types of misfit mechanisms which lead to OPB formation. The **(c)** *a*-*b* misfit mechanism occurs where a misfit dislocation forms in the nucleation layer of the thin film as it is growing. The subsequent material continues to grow with the changed layer ordering. The inclined **(d)** *c*-misfit mechanism occurs when in the layered oxide the *c*-axis grows at an incline to the epitaxial substrate, and the mis-match of the layered-oxide to the epitaxial substrates leads to OPB formation [166].

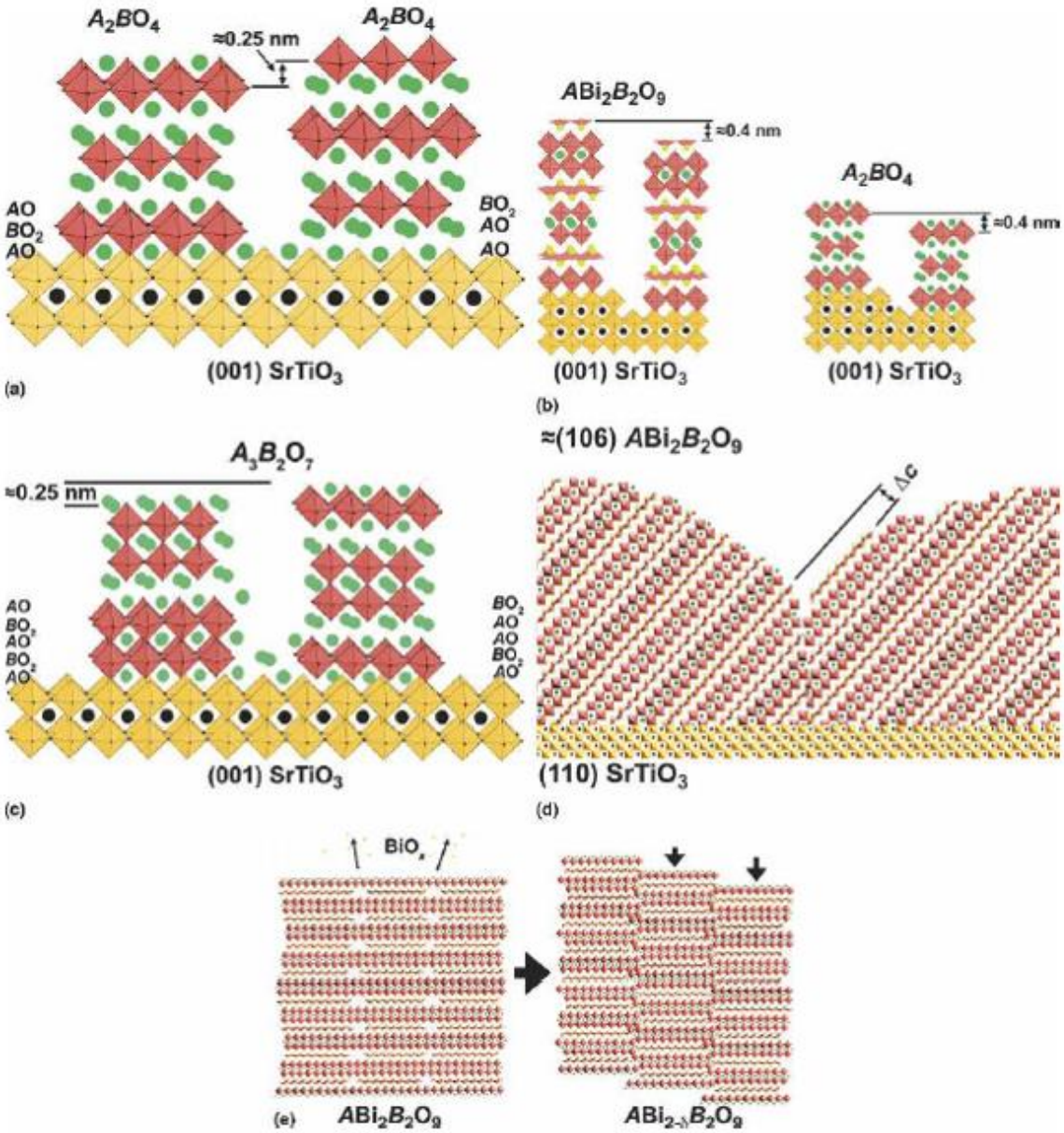


**Figure 1.21** Schematic of four primary mechanisms: (a) nucleation layer, (b) steric, (c) *a*-*b* misfit and (d) inclined *c*-misfit along and one secondary mechanism: (e) crystallographic shear by which structural defects can form at a substrate/film interface. Redrawn with permission from Zurbuchen *et al.* [166].

### 1.6.4 Discovery of Charged Domain Walls and Polar Vortex Topologies near Defect Regions within Multiferroic B6TFMO

In Aurivillius phase materials, where the perovskite layers are interleaved between $[Bi_2O_2]^{2+}$ dielectric layers, the strain and electrostatic energy conditions experienced by the perovskite unit cells at particular sites within the structure differs. For example, a perovskite unit cell directly next to the $[Bi_2O_2]^{2+}$ interface will experience a stronger compressive strain in the in-plane, *a*-axis direction, than a perovskite unit cell that is further away from the $[Bi_2O_2]^{2+}$ layer. The differences in strain and electrostatics at different sites can be augmented by the presence of structural defects within the material. For example the inclusion of OPB defects and thus the disruption to the $[Bi_2O_2]^{2+}$ interface, has been shown by Moore *et al.* [192] to lead to unexpected polar topologies. This research on B6TFMO reveals that OPB defects encourage the formation of 180 ° nominally charged H-H and T-T charged DWs, in ~100 nm thick B6TFMO films. This differs from findings on the even layered $Bi_5Ti_3FeO_{15}$ where it was found that nominally charged DWs are lost from the material once it becomes thicker than ~2 nm [193].

Initial findings determined that under certain conditions (where OPB defects are spaced 3 to 4 nm apart [192]), there is a continuous rotation of the local polarisation vector where both the magnitude of polarisation and rotation angle of the polarisation changes within the B6TFMO structure, such that resulting topological features cannot be considered as prototypical Ising, Néel or Bloch-type DWs. **Figure 1.22** shows an example of the polar vortex topologies that can be observed in B6TFMO, where the size of the arrow indicates the magnitude of the displacement and the colour indicates the direction. The preliminary data also indicates that in B6TFMO, there is an augmented partitioning of the $Mn^{3+}$ magnetic cations towards the vortex core. This indicates possible increased electric conductivity at the ferroelectric vortex core, similar to electric field gradient observations of electron concentration at the core of the vortex for $PbTiO_3/SrTiO_3$ [194] multilayers and $BiFeO_3$ [195]. Thus, by gaining further insight into the formation of these vortices and how to control their creation, B6TFMO as a multiferroic could potentially be utilised within low-power electric-field controlled magnetic devices.

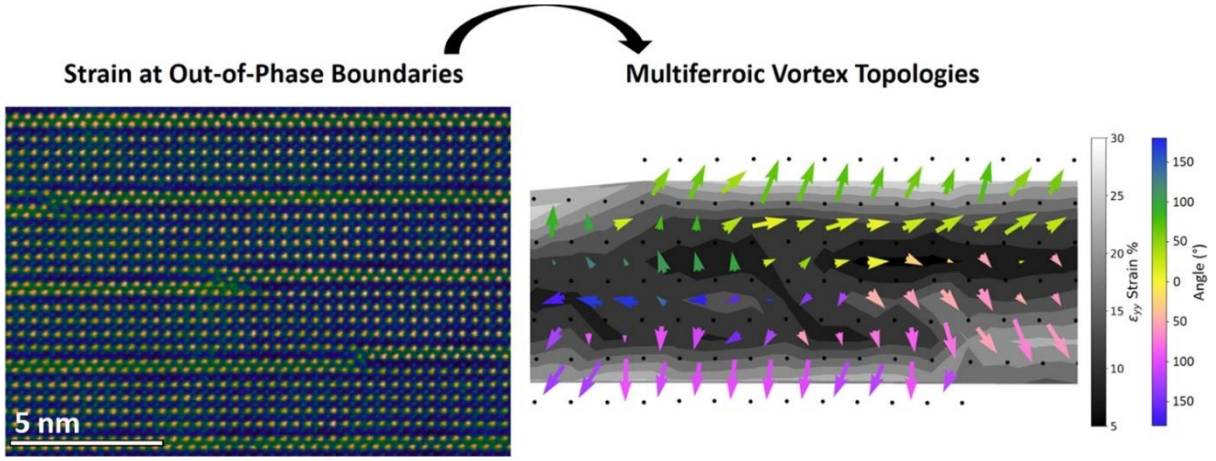


**Figure 1.22** Visualisation of the ferroelectric polar vortex topologies which can be observed in B6TFMO's (110) orientation in regions with OPB defects. Redrawn with permission from Moore *et al.* [187], under the terms of the Creative Commons Attribution (CC BY 4.0) license which permits use, sharing, adaptation, distribution and reproduction in any medium or format, provided the original work is properly cited.

## 1.7 Aims of Thesis

While the multiferroic B6TFMO Aurivillius phase system has the potential to radically improve memory storage technologies, there are still barriers to its optimisation, miniaturisation and integration into device architectures. It is fundamentally necessary to understand the sub-unit-cell characteristics governing multiferroic behaviour before its properties can be optimised and exploited. Therefore, a major focus of this thesis is to ascertain the influence of sub-unit cell interfaces and structural defects on the multiferroic properties of B6TFMO. Given that previous work [192] on B6TFMO has shown it is a potential candidate material for use in DW and vortex topology based nano-electronic devices, a goal of this thesis is to gain deeper understanding of the role of the $[Bi_2O_2]^{2+}$ interface layers within the Aurivillius structure. This, along with realising the impact of disruptions to the interlayers via OPB defects will aid in exploiting B6TFMO's properties for revolutionary memory storage technologies and DW device applications. Optimising the synthesis of B6TFMO films on substrates that can alter polarisation direction and epitaxial substrates is another target of the thesis. Epitaxial growth ensures that well defined multiferroic films with the correct

orientation can be grown and furthermore allows for strain-induced enhancement of multiferroic properties in technologically relevant devices.

Previous descriptions of the atomic structure and determinations of cation location preferences, for example the inclusion of manganese and its preference for the central perovskite layers [164], [192], has advanced comprehension of the fundamental mechanisms governing ferromagnetism in B6TFMO. In **Chapter 3** the impact of the $[Bi_2O_2]^{2+}$ interface on the local cation environments and the multiferroic properties of B6TFMO thin films grown by DLI-CVD is investigated. High resolution scanning transmission electron microscopy (STEM) is used in conjunction with electron energy loss spectroscopy (EELS) to spatially probe atomic-resolution electronic structure at the differing crystallographic *B*-site sites within the B6TFMO structure. STEM- integrated differential phase contrast (iDPC) imaging was used to view the light oxygen atoms within the structure. First principle theoretical calculations of atom resolved partial density of states (PDOS) help deconvolute the driving factors to the changes observed in the local cation environments of the *B*-site cations in B6TFMO and their influence on multiferroic behaviour.

OPB defects and stacking fault defects, commonly found in layered Aurivillius phase materials, have been recently shown to influence the formation of charged DWs and facilitate the formation of exotic polar vortexes in B6TFMO. This occurs naturally, without the need for an artificial interface or strain engineering [192]. However, the issue with uncontrolled defect propagation in B6TFMO is that the presence of the structural defects can vary considerably between samples, leading to inconsistent material properties. In order to synthesise reliable thin films for real world applications, it is necessary to devise methods to control the density of structural defects and potentially enhance the associated emergent properties. In **Chapter 4**, deposition of B6TFMO films on vicinal sapphire substrates (with a slightly off-axis substrate cut of 0.2 $^{o}$ to 10 $^{o}$) with a controlled density of atomic steps is explored using direct liquid injection chemical vapour deposition (DLI-CVD) in order to deliberately encourage structural defect formation into the growing layers.

In odd-layered Aurivillius phases, only a minor out-of-plane ferroelectric response is measured in *c*-axis orientated grains, which is the material's preferred growth direction. This response is permitted due to the breaking of the mirror plane within the material's perovskite layer blocks that are interleaved between $[Bi_2O_2]^{2+}$ layers [154], [160]. However, the crystal

symmetry of B6TFMO dictates that the major polarization comes from grains that lie along the *a*-plane, which is the in-plane, lateral direction in conventional B6TFMO films [196]. By improving the accessibility of the *a*-plane and major polarization vector in vertical architectures employing B6TFMO could improve its ability to be utilised in circuit designs for device applications. In **Chapter 5**, sapphire substrates patterned with dome-like structures are utilised in order to investigate how an inclined patterned surface will influence the growth of B6TFMO and affect its multiferroic properties.

Impurity free RT multiferroic B6TFMO films have been successfully grown on non-epitaxial sapphire substrates as shown in **Chapters 3, 4, 5** and previous work [162], [163] using a two-step deposition technique. However, this method does not accommodate the synthesis of conformal B6TFMO films that are > 80 nm in thickness. To synthesise thinner conformal films of B6TFMO, required for integration into future commercial memory devices, epitaxial substrates must be employed. However, while the epitaxy imposed by substrates allows for the growth of conformal films sub-10 nm, this epitaxial growth can be confounded by the presence of impurity phases [171]. In **Chapter 6**, two factors are investigated to reduce impurity phases in ~45 nm B6TFMO films synthesised using DLI-CVD. The first set of investigations considers the influence of epitaxial strain. The second study explores the influence of the bismuth precursor.

# 2 Experimental Methods

## 2.1 Thin Film Synthesis

There are several different physical and chemical methods for thin film deposition including those which use solid-phase, liquid-phase and vapour-phase processes. Solid phase deposition is not very popular due to the relatively slow movement of atoms in a solid in comparison to liquids or gases. Liquid phase or wet chemistry techniques have widespread uses due to their overall simplicity and versatility. Solution processed thin film deposition can occur via a variety of deposition mechanisms, where the thin film is deposited from a precursor solution. While the semiconductor industry commonly utilises these deposition methods for the deposition of resists, advanced solution processed techniques are increasingly used in emerging technologies that utilise unusual substrates that are for example, curved, patterned or stretchable (e.g. for plastic electronics and displays) [197].

Chemical solution deposition (CSD) is a solution based thin film growth method where films are deposited via solution onto a substrate, similar to the process displayed in **Figure 2.1**. CSD is a commonly used deposition method due to its simplicity along with its relatively low precursor and apparatus costs. It is often used as a screening technique for the development of new compositions before using more expensive and specialised deposition methods. CSD solutions are usually prepared by mixing the chemical precursors with suitable solvents, such that the desired material composition is achieved with a suitable viscosity. With this technique, the stoichiometry of the resulting solution can easily be adjusted by changing the precursor amounts used.

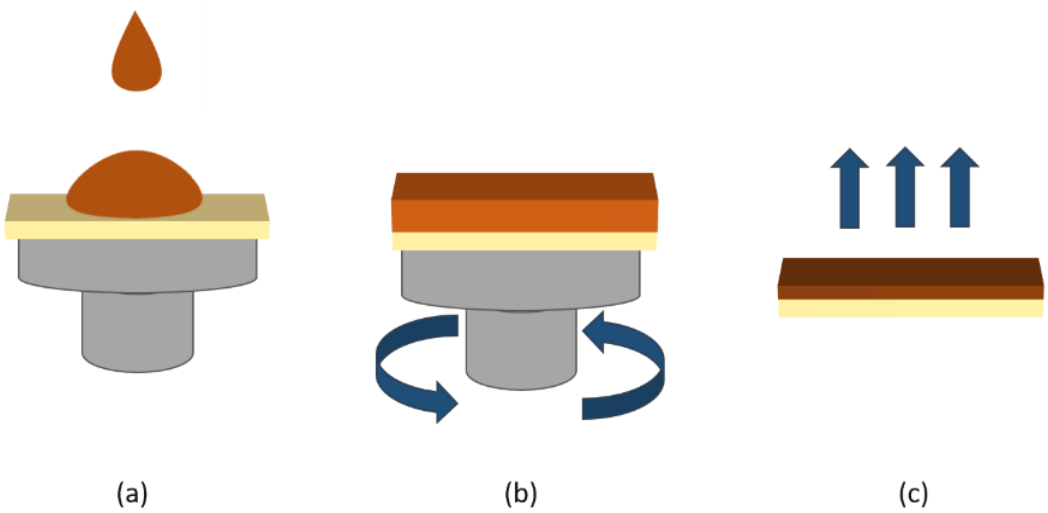


**Figure 2.1** Steps involved in the spin coat process, (a) the precursor solution is dropped onto a substrate, (b) the chuck spins, creating an even coating of the precursor solution over the substrate and (c) evaporation of the solvent occurs during a "baking step" enabling the formation of a thin film.

B6TFMO Aurivillius phase films were first synthesised by Keeney *et al.* [198] using a CSD method, as described via **Figure 2.2**. This recipe is based on a modification of previous work [162]. Lactic acid and acetylacetone solvents were used as they allowed for the chemical precursors to dissolve and produce stable solutions with no precipitation. Furthermore, the chelating ligands of the selected precursors allow for the protection of the reactive sites of the metal ions in solution, preventing them from entering into any undesirable side reactions. The spin-coating step allowed for the deposition of a thin film of the material, while the organic solvents were pyrolzed during the subsequent hot-plate "baking" step. Finally, the high temperature furnace anneal at 850 °C provided the required thermodynamic energy for the deposited film to crystallise into the Aurivillius phase.

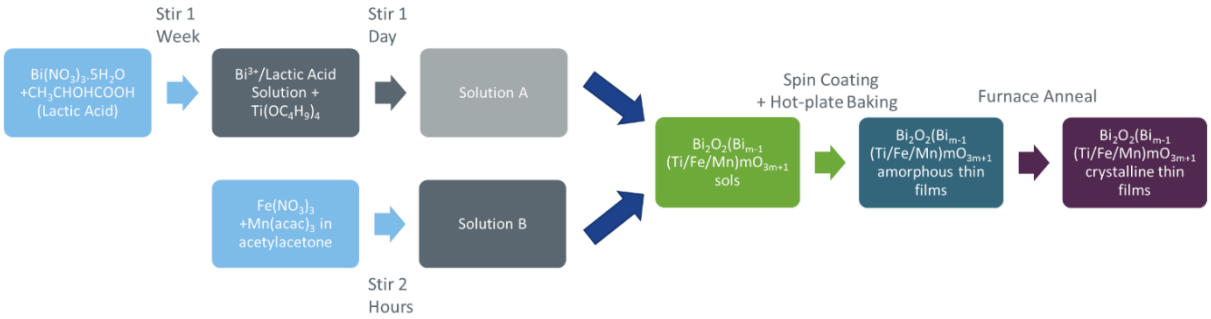


**Figure 2.2** Schematic of chemical solution deposition process to obtain Aurivillius phase crystalline thin films.

Vapour-phase deposition techniques are a commonly used for thin film growth and are divided into two main subsections, physical vapour deposition (PVD) and chemical vapour deposition (CVD). Both of these techniques involve vaporising a liquid or solid source material as a means to deposit a film on a substrate surface. PVD is an atomistic approach to vapour deposition, and includes molecular beam epitaxy (MBE), sputtering, and pulsed laser deposition (PLD) processes where, for example PLD has been used to synthesise Aurivillius phase thin films by other groups [199], [200].

CVD techniques, first developed in the nineteenth century [201], [202], involve processes where gaseous precursors on or near a heated substrate can react such that a new solid material is formed [203]. In CVD, the vapour phase precursors can be created from a number of different means; they may already be present in the vapour phase or are vaporised from a liquid or solid phase. This technique has many advantages over CSD. CVD allows for initial higher deposition temperatures (100 - 1300 °C), which can often directly produce crystalline films thus reducing the need for a post-anneal step [204]. CVD allows for the development of thin films with a more controlled thickness, lower porosity and overall improved uniformity over the substrate. It is also industrially scalable. Depending on the size of the reaction chamber, it can accommodate large number of wafers e.g. 100 mm (4 inch) x 15, 150 mm (6 inch) x 9 or 200 mm (8 inch) x 6 wafers [205], [206]. Another chief advantage of CVD techniques for growing Aurivillius B6TFMO, over for example PVD methods such as MBE, is the high gas pressure (0.6 to 70 mbar) and relatively higher oxygen rich environments ( 100 to 2000 sccm; 5 to 70 % $O_2$) which can prevent the re-evaporation of volatile $Bi_2O_3$ [207], [208].

There are a number of different types of CVD processes, such as atomic layer deposition (ALD), low-pressure CVD (LPCVD), ultrahigh vacuum CVD (UHVCVD), metal-organic CVD (MOCVD), aerosol-assisted CVD (AACVD) and direct liquid injection CVD (DLI-CVD). In this body of work, all the films synthesised and studied were deposited via DLI-CVD.

## 2.2 Chemical Vapour Deposition: Direct Liquid Injection Chemical Vapour Deposition

The instrument used in this research to deposit the Aurivillius phase B6TFMO thin films is the AIXTRON AIX 200/4FE DLI-CVD, as described in **Figure 2.3**. When depositing thin films via DLI-CVD, a number of parameters must be considered in order to achieve the desired film, such as the reaction chamber design, the precursors along with their chemistry, the substrate, temperature and pressure [203], [209].

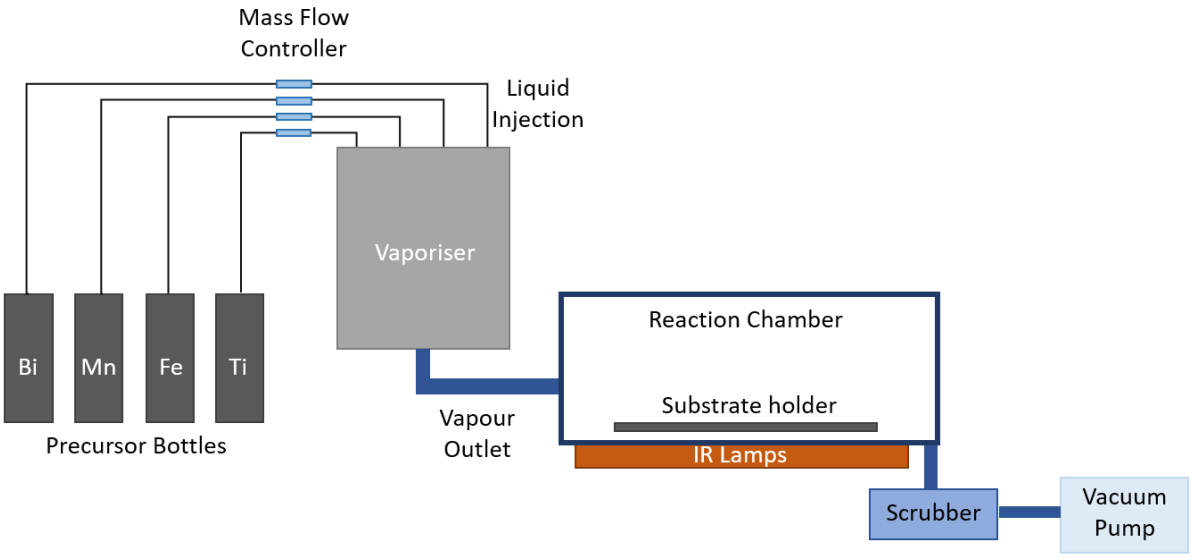


**Figure 2.3** Schematic of the DLI-CVD system.

In DLI-CVD, precursors are utilised in liquid form, where they are injected into a vaporisation chamber before passing into the reaction chamber containing a heated substrate. There are number of different types of reactions by which the solid film on the substrate can form from the vapour phase, such as thermal, decomposition, reduction, exchange and coupled reactions [209]. How the gaseous precursors react on the surface of a substrate can be described by the equation

$$gaseous\ precursors\ (g) \rightarrow\ solid\ material\ (s) + gaseous\ products\ (g) \qquad 2.1$$

In order to get a laminar flow (a type of fluid flow where the gas can travel in a smooth and regular path) of the gaseous precursors over the heated substrate in the reaction chamber, the CVD tool is engineered in a particular manner. The gaseous precursors flow through the CVD reaction chamber and due to fluid mechanics and laminar flow dynamics a boundary layer forms between the heated substrate and the main gas flow. This boundary layer is made up of five main reaction zones as shown in **Figure 2.4**, where the velocity, temperature and concentration of the precursor changes such that they can react together and deposit the desired film [209]. Homogenous gaseous reactions can occur in zone 1, the stagnant boundary layer. Zone 2 marks the interface between the coating layer and the stagnant boundary layer where heterogeneous reactions occur. These reactions are typically the reactions that determine the properties of the material coating on the surface and determine the film deposition rate. Zone 3 signifies the region of the deposited film. Due to the often high temperatures that CVD operates at, here there can be further solid-state reactions in this layer. Zone 4 is a diffusion zone between the substrate and the coating layer, where intermediate phases can form. Here the reactions are critical to the adhesion of the material coating to the substrate. Zone 5 is the heated substrate where in this region the temperature and the composition of the substrate play roles in the formation of the film on the substrate.

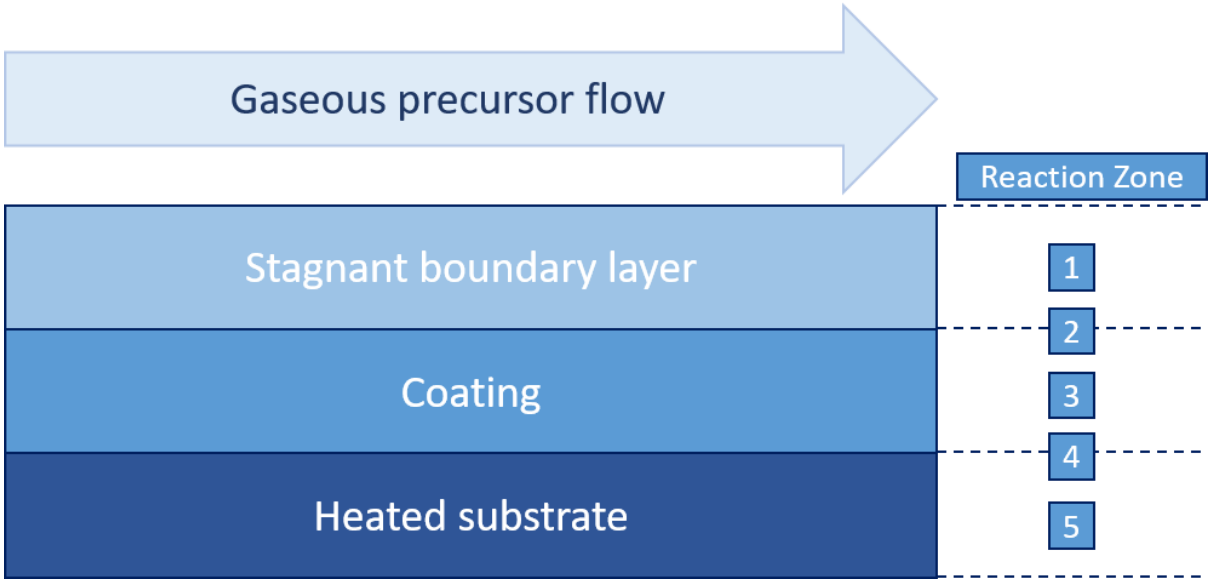


**Figure 2.4** CVD reaction zones between the main gaseous precursor flow and the heated substrate. Zone 1 is the stagnant boundary layer, zone 2 is the interface between the stagnant boundary layer and the coating layer, zone 3 is the deposited film (the coating layer), zone 4 is the interface between film and substrate and zone 5 is the heated substrate.

CVD processes typically occur via the steps described in **Figure 2.5**. Initially the gaseous precursors, in this example AX and $Z_2$, enter the reaction chamber via the main gas flow. Here the precursors can initially react in the gas phase or be directly transported to the heated substrate surface where adsorption can occur. Once on the substrate surface heterogeneous reactions between the atoms and surface diffusion can then occur which results in the nucleation and formation of the coating or thin film on the substrate surface. Then the by-products of the reactions can be desorbed from the surface, where they leave the reaction chamber via the main gas flow.

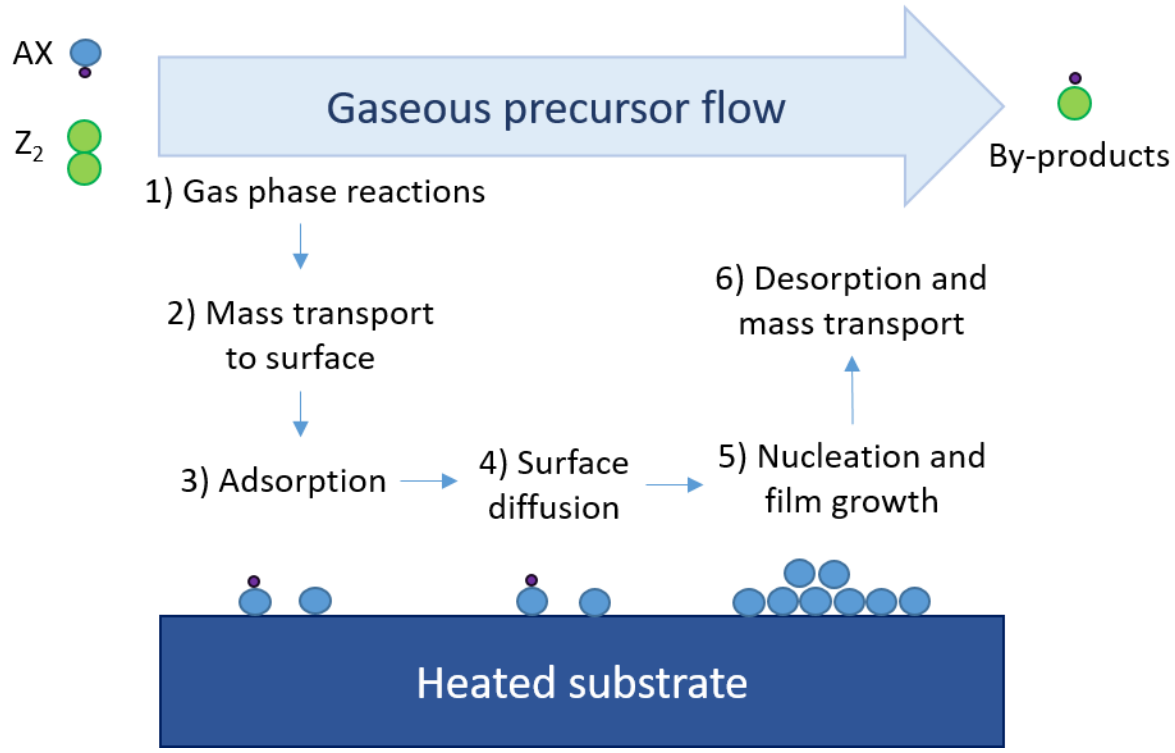


**Figure 2.5** Schematic describing the elementary physiochemical steps of a typical CVD process. Initially gaseous precursors, for example AX and $Z_2$, are transported into the reaction chamber via the gas flow. The precursors can then either directly adsorb to the surface or react in the gas phase before adsorption. Heterogeneous reactions and surface diffusion take place on the substrate surface where nucleation of the film and its growth then takes place. Lastly, the by-products of the reaction are desorbed from the surface and are carried out of the reaction chamber.

The growth rate of a thin film can be heavily influenced by the temperature and pressure of the substrate and reaction chamber. As shown in **Figure 2.6**, three main growth phases occur with relation to temperature. At low temperatures, the growth rate is determined by the kinetics of the chemical reactions taking place in the gas phase or at the substrate surface. This is known as kinetically controlled growth. In this growth region, the material growth rate rises exponentially with temperature. As the temperature increases, the growth rate becomes independent of temperature, but is controlled by the mass transport of the reactants to the substrate surface. This is known as the diffusion-controlled region. Finally, at the highest temperatures, the material growth rate becomes slower due to an increased desorption of the precursors before they can react and produce the desired material on the substrate surface [203].

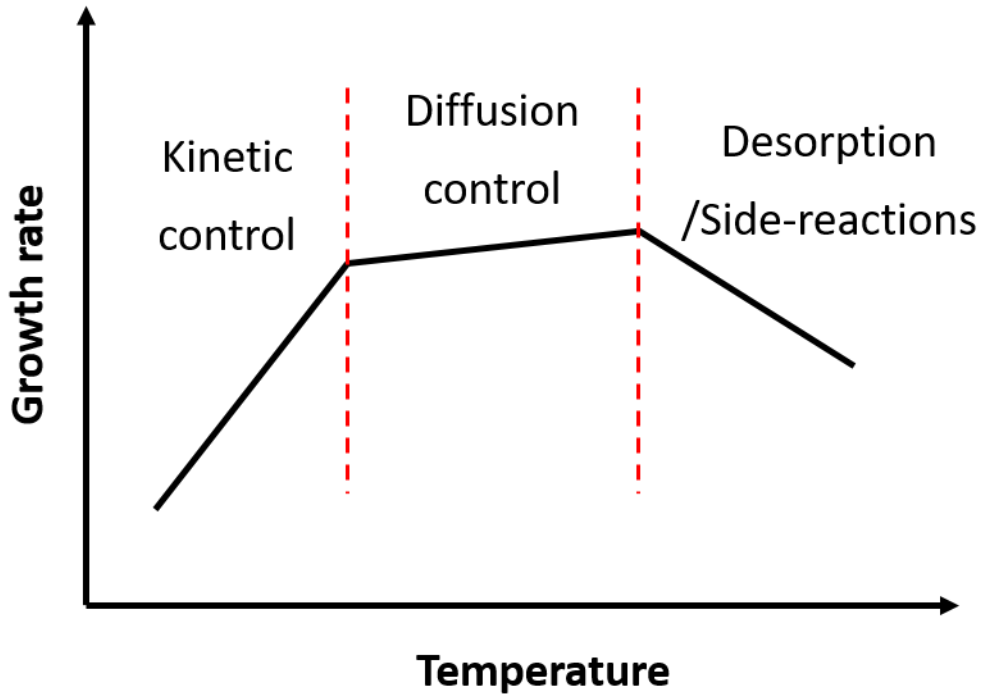


**Figure 2.6** Diagram depicting the influence of temperature on film growth rate during a CVD process, indicating the different growth regions available.

The pressure maintained in the reaction chamber is also crucial to the growth rate and formation of films using CVD. From atmospheric pressure (1000 mbar) to about 10 mbar, a significant boundary layer is present above the substrate. Due to a short mean free path of the gas molecules at these pressures, the gas phase reactions play an important role in the deposition process. At these pressures, the mass transport of the precursors to the surface is also important towards controlling the film deposition rate. Once the pressure of the chamber moves to below ~ 1 mbar, then gas phase reactions become less important. The gas molecules now have a longer mean free path and can readily pass through the thinner boundary layer above the substrate where the material growth is determined by surface reactions [203].

Choosing the correct precursors for a particular CVD process is critical to achieving high quality films. Key properties needed for suitable CVD precursors are that they are stable during storage and delivery to the reaction chamber while also being reactive enough to undergo viable reactions near or at the substrate surface to produce the desired new material. They also must be able to produce volatile by-products that can be carried out of the chamber via the main gas flow [207], [210]. The AIXTRON AIX 200/4FE DLI-CVD tool has four precursor lines. When depositing B6TFMO films, the four precursors used were $Bi(THD)_3$,

$Ti(O\text{-}iPr)2(THD)_2$ , $Fe(THD)_3$ and $Mn(THD)_3$ where THD represents tetramethylheptanedionate and O-iPr represents isopropoxide. These precursors were dissolved in toluene such that the Bi, Ti and Fe precursor solutions had a 0.1 mol $dm^{-3}$ concentration and the Mn precursor solution had a concentration of 0.025 mol $dm^{-3}$. All precursors were purchased from Epivalence Ltd.

The AIXTRON AIX 200/4FE DLI-CVD tool shown in **Figure 2.3**, has four stainless steel containers from which the liquid precursors are injected into the vaporiser (TriJet™ evaporation unit). Flow meters control the volume of liquid precursor injected into the vaporiser, while the precursor lines and vaporiser are kept at 220 °C, to prevent any condensation and blockages. From the vaporiser, the gaseous precursors enter the hot-wall reaction chamber. In this work, a conventional simultaneous DLI-CVD is used, where the injected precursors enter the reaction chamber at the same time and are carried over the heated, rotating susceptor plate that holds the substrates. In order to control the film growth rate, thickness and stoichiometry, the pulse frequency of the injections, the number of pulses and the valve opening times for each precursor is changed, respectively. The chemical precursors in oxygen and nitrogen gas that flow over the substrate are then removed from the reaction chamber through the exhaust where unreacted precursor and by-products are removed by a scrubber system.

The surface termination of the substrate is also an important parameter to consider when growing a thin film. For many thin film multiferroics, having a substrate with an atomically flat singly terminated surface is essential. Substrates can have a variety of different terminations depending on their composition and the crystallographic plane in which they are cut. However, they often have mixed surface terminations and are not atomically flat when purchased from commercial providers. Many different treatments, such as thermal treatments, wet etching (either acids or bases) and deionised water soaks have been developed on their own or combined together in order to achieve atomically flat, singly terminated substrate surfaces. For example (001) $SrTiO_3$, can be SrO or $TiO_2$ terminated. These are neutral terminations and through high resolution synchrotron-radiation photoemission spectroscopy it has been proved that the $TiO_2$ group is more stable and energetically favourable than SrO [211]. In the case of perovskite substrates such as $SrTiO_3$ or $NdGaO_3$, methods such as annealing, deionised water treatments and acid etching have all

been proven to achieve surface terminations and create uniform step terraces on substrate surfaces [190], [212]–[215].

Substrates with vicinal (mis-cut) surfaces offer a potential route to control the formation of OPB defects and domain walls within Aurivillius phase thin films. The mis-cut angle of a substrate surface is the degree at which the surface of the sample is cut away from a particular crystallographic plane. Typically, substrates used for epitaxial growth have a very low mis-cut surface of > 0.5 °. However there have been studies carried out growing both perovskites and Aurivillius phase materials on substrates with higher mis-cut angles [216], [217]. A substrate with a high degree mis-cut angle have been shown to increase the number of stacking faults within the deposited material, which can affect material properties and thin film growth. For example, it has been shown that for the deposition of the perovskite $Pb(Mg_{1/3}Nb_{2/3})O_3$-$PbTiO_3$, the use of epitaxial substrates with a 10 ° mis-cut (when compare to substrates with no mis-cut), can prevent the formation of a lead deficient pyrochlore phase within the material [217]. While for $Bi_5FeTi_3O_{15}$ films, the increase of an $NdGaO_3$ substrate mis-cut from 0.02 ° to 0.05 ° results in modification of the ferroelectric domain patterns [190].

## 2.3 Characterisation Methods

### 2.3.1 X-ray Diffraction

With the discovery of X-rays just before the turn of the century [218], in 1912 Laue *et al.*[219] measured the first diffraction pattern through the cubic zinc blende structure; however, Laue *et al.*[219] were not fully able to deconstruct how this pattern related to the material's crystal structure. Following from this work, W.H. Bragg and W.L. Bragg [220] developed the technique of X-ray diffraction (XRD) as it is known today. X-rays, which have a wavelength on the nanometre scale, similar to that of the distances between atoms in crystals, mostly pass through a material unchanged, however a small amount of the X-rays scatter in different directions. The periodic nature of crystals allow for the incident X-rays to reflect off planes of atoms and the resulting reflected light from a of particular atomic plane will interfere in a manner dependant on the angle of the incident light and the spacing between the atomic planes, as shown in **Figure 2.7**. When this interference is constructive, it is known as

diffraction and the relationship by which this can happen in a periodic crystal structure is summarised by Bragg's law:

$$2dsin\theta = n\lambda \qquad 2.2$$

Where *d*, the path length, is the spacing between atomic planes, θ is the incident angle between the X-ray and the atomic plane, λ is the wavelength of the incident X-ray and *n* is an integer value. Bragg's law states that when an incident X-ray passes through a crystal and interacts with the surface of an atomic plane at an angle θ, there will be a scattering angle reflected back equal to θ. When the path difference is equal to an integer number of wavelengths (nλ), constructive interference will occur and a reflected signal can be detected.

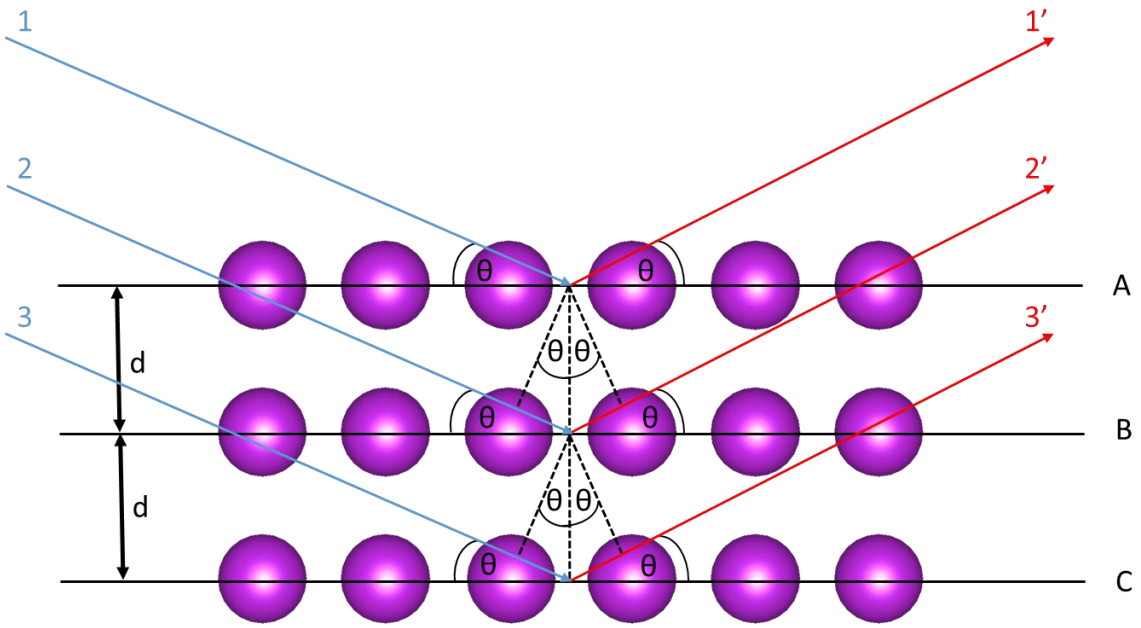


**Figure 2.7** Schematic of the Bragg condition. Incident x-rays 1, 2 and 3 are reflected from the atomic crystal panes A, B and C. The X-rays are reflected from the planes at an angle θ, where the reflected X-rays 1', 2' and 3' interfere with each other. If constructive interference occurs, can be detected by an increase in signal.

Laboratory XRD measurements typically use a monochromatic X-ray source generated via bombardment of a metal source (commonly Cu or Ge) with a beam of electrons. The core electrons excited in the metal source emit X-rays of a desired energy when decaying back to their ground states. The X-ray beam is then passed through a collimator to ensure only a single

wavelength remains. The monochromated X-rays then can travel through a series of slits and filters in order to optimise the beam for sampling. The application of divergence slits sharpens diffraction peaks at the cost of peak intensities. Masks can be used to ensure sampling occurs over a certain sample area. Filters, such as Nickel for a Cu X-ray source, to remove $K_\beta$ radiation in order to give a cleaner data set mainly comprised of just $K_\alpha$ radiation [221]. In modern instruments, the diffracted beam within which crystal information is contained is collected using a radiation detector known as a diffractometer. The resulting pattern is then used to analyse the sample.

XRD has been incredibly important for allowing chemists to determine the atomic arrangement of various materials, from initially simple crystals such as sodium chloride and diamond [222], [223] to now complicated biologic proteins such as ribosome containing 404,714 atoms in its crystal structure [224]. In materials chemistry, XRD is commonly used to characterise the crystal phase, orientation and thickness. Structural properties such as a material's lattice parameter, strain, epitaxial relationship, phase composition and grain size are also determined using XRD and are crucial parameters when assessing thin film growth in materials such as the Aurivillius phases. The Aurivillius phases, which are mixed layer materials (made up of alternating a number of $ABO_3$ perovskite layers between $Bi_2O_2$ fluorite layers), can have a variable number of perovskite layers within their structure. XRD is an extremely useful tool to determine what Aurivillius phase has been synthesised, as peak position and shape differs depending on the number of perovskite layers in the structure. XRD can also be used to determine the level of ion substitution into the structure and to determine if any chemical impurities are within the material by analysing the peak positions. While the peak shape and peak full width half max (FWHM) values can provide information on the presence of possible structural defects within the films.

In this thesis, the majority of the XRD patterns analysed are of Aurivillius phase thin films. These were acquired using a symmetric XRD set up in the Bragg condition as shown in **Figure 2.7.** The data is presented using 2θ values, where 2θ is the angle between the incident X-ray beam and the deflected beam. The Aurivillius phase thin films have a preference to grow along the *c*-axis direction, thus in the 2θ scans, the majority of peaks are made up from (*00l*) reflections, (where *hkl* are Miller indices, used to describe the position of crystal planes). Rocking curve measurements were also carried out on particular peaks. For these

measurements, the detector is set to the position of an expected Bragg reflection and then the sample is tilted. This measurement aids in the understating of the orientation of the crystallites and strain, where for a perfect defect free crystal a very sharp peak would be acquired.

XRD measurements were performed using a Panalytical X'Pert MRD Diffractometer (Cu Kα radiation λ = 0.1541876 nm) (45 kV, 40 mA). Rocking curve analysis was performed remotely using a Rigaku Smartlab with a 9 kW Cu rotating anode, a 2-bounce Ge monochromator, and a Hypix detector.

### 2.3.2 Atomic Force Microscopy

Atomic force microscopy (AFM) is a surface measurement technique first developed in the late 1980's by Binning *et al.* [225] in order to investigate electrically non-conductive materials. AFM was developed as an extension of scanning tunnelling microscopy [226] (STM) which by utilising quantum tunnelling through a conductive sample could allow surface imaging at the atomic scale. AFM is a scanning probe technique where a sharp tip (radius = 1 to 20 nm), attached to a larger stiff cantilever, is raster scanned across the surface of a sample in order to measure its properties. With AFM a larger variety of materials can be investigated in comparison to STM, as instead of measuring current, the interactive forces between a tip attached to a cantilever and sample surface are utilised to visualise surface topography. The cantilever acts as a spring where its bending or deflection is proportional to the forces felt between the tip and surface. If the cantilever has a known spring constant, Hooke's law can be used to determine the force between the tip and the sample surface. AFM measurements are taken and recorded when a laser is directed onto the cantilever, as described in **Figure 2.8**. As the cantilever moves across a surface, the reflection of the laser beam from the cantilever changes with the deflection of the cantilever in response to surface features. This reflected beam meets a position sensitive photodiode where the laser reflection is detected and recorded. The photodiode measurements are then used to produce a topographic image of the features on a sample surface [227].

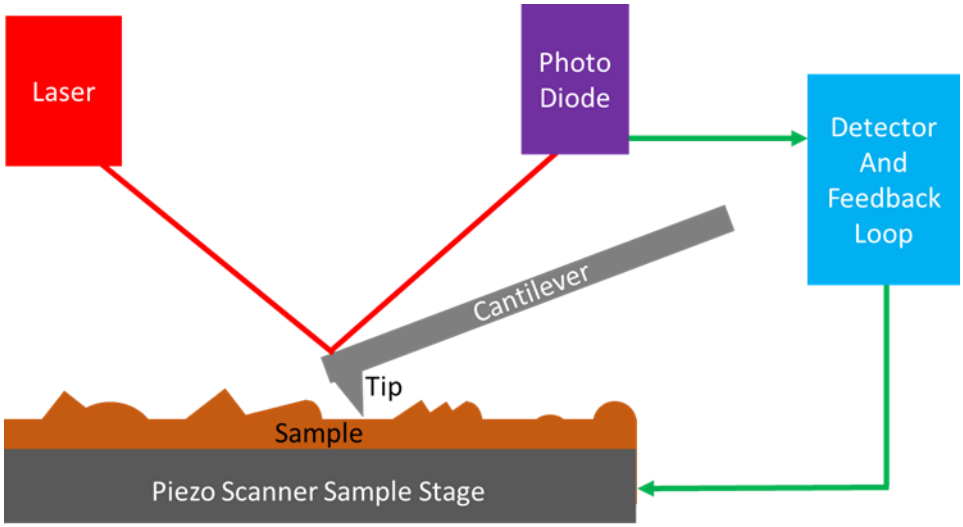


**Figure 2.8** Schematic of a general set up for AFM measurements.

When carrying out AFM measurements, three regimes are to be considered when dealing with the force interactions between the tip and the surface, as shown in **Figure 2.9**. The first regime is when the tip is very far from the surface and the forces between the tip and surface are negligible. The second regime occurs when the tip is closer between (10 to 100 nm) to the surface and there is an attractive tip-surface interaction. The final regime happens when the tip is very close or in contact (0.1 to 10 nm) with the surface and there is a repulsive force / interaction between the tip and the surface. Different methods of AFM measurements operate in the different regimes; contact modes in the repulsive regime and non-contact modes in the attractive regime. The various operational modes are commonly divided into two different categories: static (non-oscillating cantilever) and dynamic (oscillating cantilever).

Constant force contact mode [225], a static form of AFM, measures topography by keeping the tip in constant contact with the sample surface in the repulsive regime. In this operational mode, the laser beam deflection off the cantilever as it scans is processed into a feedback loop such that the force between the tip and sample is kept constant using a piezo-scanner. The surface map is then a product of the changing sample/tip position needed to keep the force between them constant. In this measurement method, strong forces are felt between the sample and the tip, thus, the sample should be hard in order to avoid damage from the AFM tip. It should also be noted the surface features measured should be in the

nanometre range, as due to the tip dimensions, the true heights of the larger lateral features can be difficult to capture.

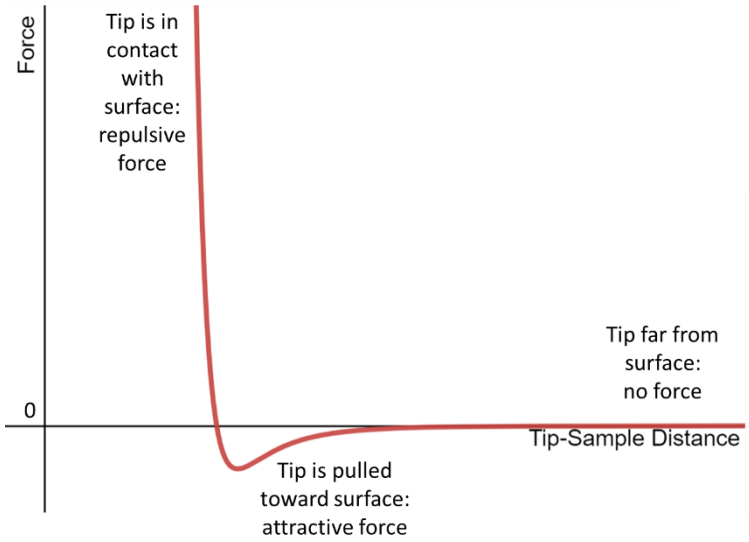


**Figure 2.9** AFM tip and sample surface force interactions as a function of distance (Lennard-Jones potential).

Dynamic mode techniques are considered a less harsh measurement method, useful for use on biological or softer (e.g. polymers) samples that could be damaged by the strong interaction in the contact mode measurements. Dynamic modes such as non-contact and tapping (AC), also use the cantilever as a spring. In non-contact [228], [229] mode, the cantilever is oscillated at a fixed frequency using a drive amplitude. In this mode, the tip is oscillated at a fixed frequency at or near its resonance frequency while raster scanning the sample surface. During scanning, the phase between the drive amplitude of the oscillation and the actual amplitude of the cantilever oscillation changes indirectly with the surface features. The oscillation amplitude depends on the frequency shift of the resonance of the cantilever as the tip approaches the surface. Attractive forces between the tip and the surface leads to the cantilever having a lower frequency, while repulsive forces cause the resonance frequency of the cantilever to increase. In non-contact mode the tip is operated in the attractive regime. Looking at **Figure 2.9**, the relationship between the forces acting on the tip and the tip-sample distance can be seen. Using the feedback loop in the AFM system, the drive amplitude is set to a fixed value, to keep the tip oscillating at the fixed frequency. To maintain this set drive amplitude value the sample/tip distance is adjusted while scanning and this adjustment can be used to provide topography images of the sample surface.

Tapping (AC) mode AFM is a frequently used form of AFM and relies on an oscillating cantilever with intermittent contact of the tip to the sample surface. It has advantages over both contact and non-contact measurement modes due its ability to deal with the contamination layer, usually made up of water that is present on samples measured at ambient conditions. In constant force contact mode, the strong capillary forces of the contamination layer could drag the tip laterally and result in image distortions. In non-contact mode, unintentional contact with the surface can cause the capillary forces to contribute to the force interactions while measuring, while in tapping mode the tip intentionally has to pass through this contamination layer and the stiff cantilever has enough energy at the contact point to overcome any attractive forces caused by the contamination layer. In comparison to non-contact mode, tapping mode still oscillates at a fixed frequency and the amplitude of the cantilever oscillation is measured, however much larger oscillation amplitudes are utilised. The amplitude only depends on the tip-sample distance and a drive frequency close to the resonance frequency of the cantilever in free air (often ~5 % below) is used. As the tip is brought into contact with the sample surface, it enters the repulsive regime, which in turn causes the resonance amplitude of the cantilever to decrease. The feedback loop of the AFM system is used to keep the drive amplitude constant during raster scanning of the surface. The changes in the amplitude and phase of the oscillations are measured and height and force images of the sample surface can be produced.

While it is critical to pick the optimal operational mode for a particular sample when imaging, the lateral resolution and quality of sample imaging is highly dependent on the tip of the probe used in AFM. Tips vary in size usually with a radius below 15 nm attached to a stiff cantilever, that is of the order of a few hundred microns in length attached to a larger cantilever holder which the AFM user picks up with tweezers and slots into the probe holder connected to the electronics of the AFM tool. The tip geometry determines the outcome of the AFM imaging as shown in **Figure 2.10**. Therefore selecting a tip with an appropriate radius for the features one is imaging and ensuring that the tip shape is as expected i.e. not damaged, is crucial for accurate imaging of a surface. Tip wear and shape degradation can occur from repeated contact with sample surfaces or by picking up contaminants from the surface while imaging. The material of the tip is usually made of silicon or silicon nitride with silicon tips being sharper but more prone to wear than the silicon nitride tips. Other tip

materials, such as diamond, can also be acquired. These are very hard tips which are extremely wear-resistance and long lasting, thus are useful for electrical measurements. The ability to apply different coatings to AFM probe tips, alongside modifications to the AFM set-up, open doors to a wide variety of sample properties that can be characterised, such as Kelvin probe microscopy [230], magnetic force microscopy [231] and piezoresponse force microscopy [232].

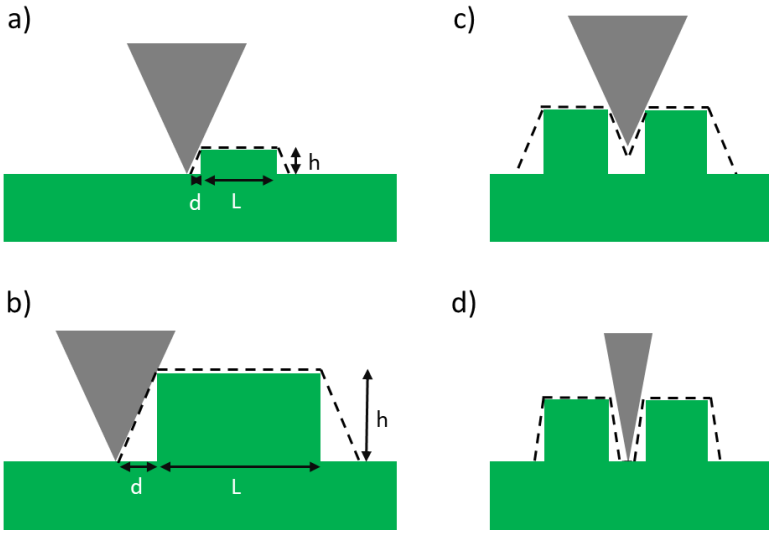


**Figure 2.10** Schematic visualising how tip dimensions can affect imaging of surface features. In a) and b) the image distortion of the feature being measured can be visualised using the black dotted line. c) and d) show how a tip with a narrow radius can image surfaces to a higher resolution.

In this thesis, the majority of AFM imaging was performed using an Asylum research MFP-3D AFM in AC tapping mode. Oxford Instruments AC160TS-R3 and Olympus AC240TS (Al reflex coated, 15 nm tip radius, 300 kHz resonant frequency and Al reflex coated, 7 nm tip radius, 70 kHz resonant frequency respectively) probes were used for imaging.

A commercial Bruker Dimension Icon in PeakForce Tapping mode (with Bruker SCANASYST-AIR probes, Al reflex coated, 2 nm tip radius, 70 kHz resonant frequency), was also used to measure substrate surfaces in this work. The smaller tips of the probes allowed for higher resolution imaging needed in order to obtain topographical profiles of the surface steps on substrates before thin film deposition.

### 2.3.3 Piezoresponse Force Microscopy

With the discovery of scanning probe techniques in the 1980s, a flurry of new adaptions to AFM were realised in order to further characterise material properties. One property of interest was the nano-scale polar behaviour of ferroelectric materials. Different techniques were developed, such as Electrostatic Force Gradient and Effective Surface Potential, which are non-contact microscopy modes that can be used to image nanoscale electrostatic surface potentials [233]. Contact operational modes, such as Scanning Capacitance Microscopy, Scanning Near Field Optical Microscopy and Piezoresponse Force Microscopy emerged, which are able to characterise ferroelectric properties of the sample surface below the scanning tip. Piezoresponse Force Microscopy (PFM) is the technique used in this research to probe ferroelectric response at nano-scale. It was developed by Güthner and Darnsfeld [232] in 1992 and takes advantage of the inverse piezoelectric effect, which was discovered by the Curie brothers in the 1880s [24]. The piezoelectric effect occurs in a crystal when an electric field is produced by putting mechanical stress or strain onto the material. When the piezoelectric effect is reversed, it is known as the inverse piezoelectric effect. Here an electrical field is applied to a crystal, which causes the crystal structure to expand or contract. In PFM, the tip which is coated (usually with a metal or alloy) in order to be conductive, is used to apply a local AC (alternating current) voltage to the sample while raster scanning its surface. Changes due to the electromechanical strain are detected. If the material is piezoelectric, an electromechanical change to the surface as a result of the applied AC voltage is detected, as shown in **Figure 2.11**. If the polarisation component being measured is in the out-of-plane (perpendicular to the surface) direction, the vertical deflection of the cantilever indicates the direction of the electromechanical response. The direction of this response is dependent on the direction of the polarisation component. For example, if a positive voltage is applied to the sample where the out-of-plane polarisation vector is pointing upwards, the material will contract as shown in **Figure 2.11 (b)**. For materials where the polarisation component acts along the in-plane (parallel to the surface) direction, the displacement of the crystal caused by the spontaneous polarisation is measured through the torsional bending of the cantilever.

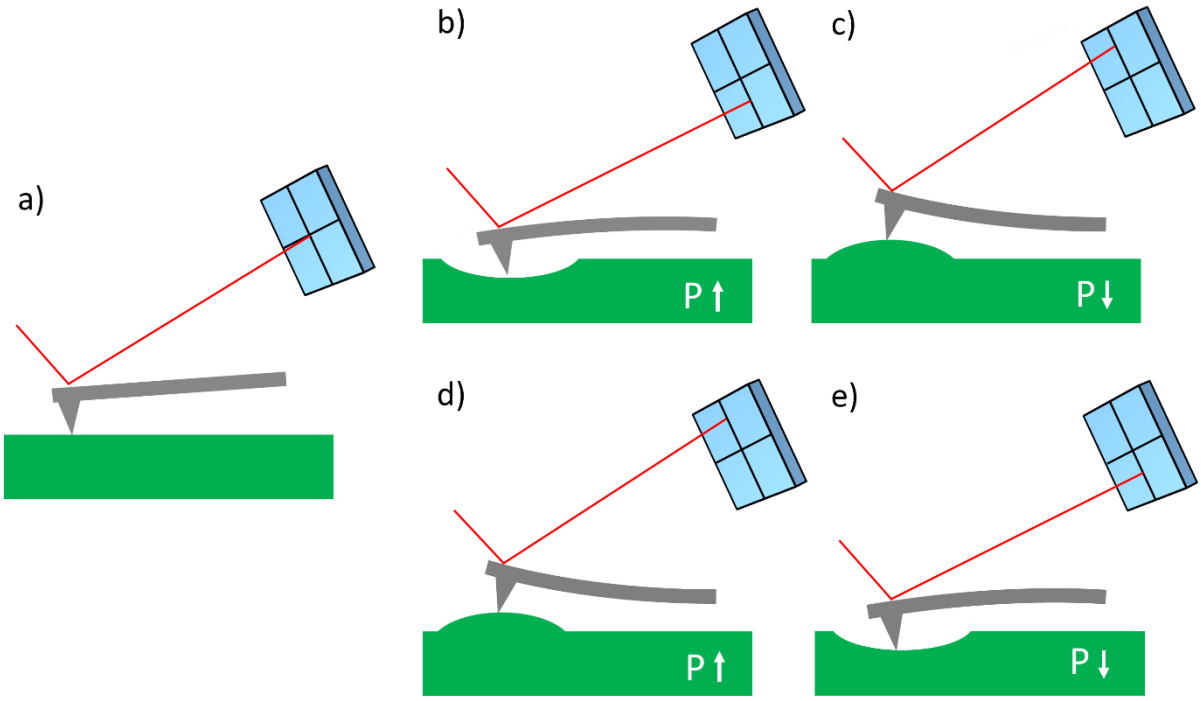


**Figure 2.11** Schematic indicating how the application of an electrical voltage to a piezoelectric material can locally alter the shape of the surface where it is applied. In a) no voltage is applied in b) and c) a positive voltage is applied to the samples while in d) and e) a negative voltage is applied to the samples.

PFM can also be used to switch the spontaneous polarisation in ferroelectric materials and to "write" and "read" ferroelectric domains. By applying a DC voltage to a ferroelectric through a conductive tip where the DC voltage exceeds the coercive field of the material, the spontaneous polarisation can be switched in a particular direction.

In this thesis, PFM was performed using an MFP-3D$^{TM}$ Asylum Research instrument. Two types of probes were used over the course of the research: the Oxford Instruments AC240TM-R3 electrilevers (Ti/Pt coated silicon probes, Al reflex coated, 25 nm tip radius, 70 kHz resonant frequency)) and the Adama AD-2.8-SS super sharp boron-doped diamond probes (< 5 nm tip radius, 75 kHz resonant frequency). PFM was conducted in lateral (LPFM) and vertical (VPFM) Dual AC Resonance Tracking (DART-PFM) modes [234]. The DART-PFM method of measuring boosts the measured signal while reducing instrumental crosstalk. In this measurement method, the contact resonant frequency is tracked while imaging over the

changing sample topography using a feedback loop. As the contact frequency changes through the feedback loop, the drive frequency can then be adjusted to optimise the PFM signal. **Figure 2.12** demonstrates haw the how the drive frequency changes in DART-PFM when imaging over surfaces with different roughness. The initial drive frequencies ($f_1$ and $f_2$) are set such that amplitudes are equal, $A_1 = A_2$. However because the contact resonance frequency shifts while imaging over a sample with non-zero roughness, amplitudes $A_1$'and $A_2$' are recorded. These amplitudes are no longer equal, and here the feedback loop detects this difference as an error signal, which the controller uses to track the resonance frequency changes and to adjust the drive frequencies accordingly. The change in drive frequency in accordance with the new resonate frequency resets the amplitude values to once again be equal, boosting the signal of the PFM measurement.

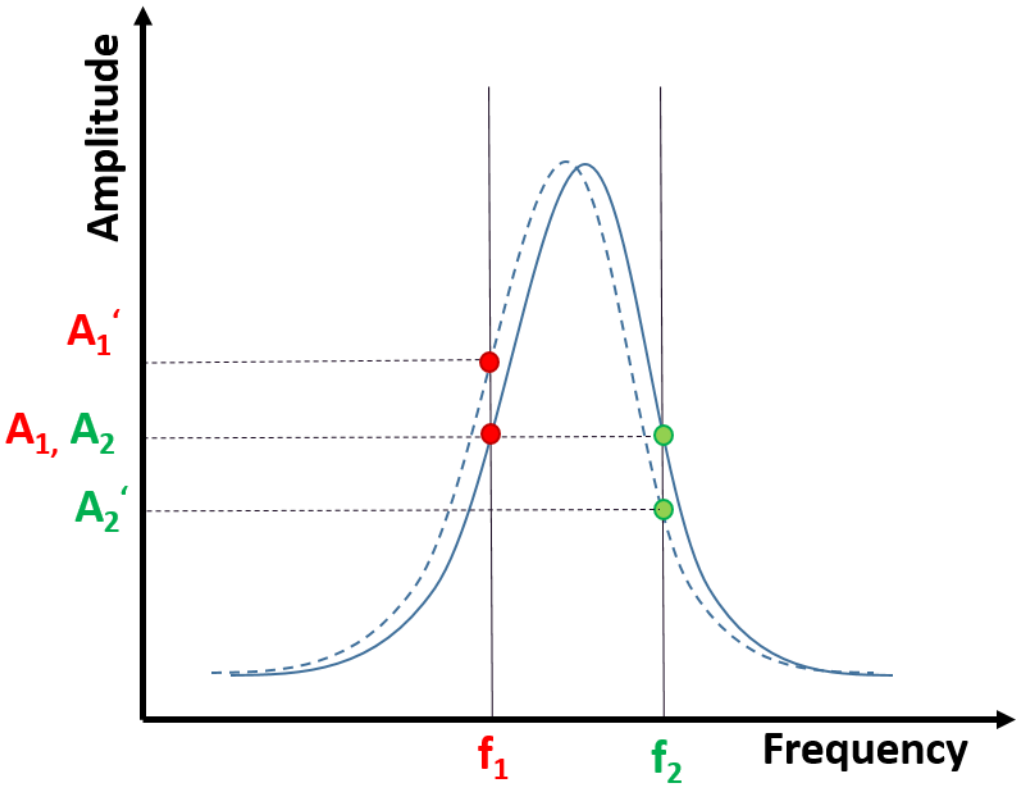


**Figure 2.12** Diagram demonstrating DART-PFM feedback loop is required to adjust to accommodate changes to sample topography during imaging.

### 2.3.4 Transmission Electron Microscopy

The transmission electron microscope (TEM) was first developed by Knoll and Ruska in 1931 [235], where the barrier on microscope resolution that had been imposed by visible light was overcome by using an electron beam. Further development of the electron microscope lead to the development of the scanning electron microscope and the scanning transmission electron microscope in 1935 and 1938 by Knoll [236] and von Ardenne respectively [237], [238]. Initially, the resolution limit of electron microscopes was ~10 nm, two orders of magnitude smaller the 200 nm theoretically smallest resolution from optical microscopes [239]. Now electron microscopes have been developed such that atomic scale images of ~0.1 nm can be captured [240], [241].

A TEM operates by using a high voltage electron beam that passes through a sample specimen to create an image as demonstrated in **Figure 2.13**. A high voltage passes through an electron source where under vacuum an electron beam is created. The electron beam is then focused onto a thin sample specimen using an electromagnetic lens. Once the beam passes through the specimen, it is focused onto a fluorescent screen where an image is formed. The image is formed from different shades (from black to white) according to the density of the specimen it had passed through, thus forming an image of the sample.

Samples for TEM must be very thin, in order for the electrons to pass through the sample specimen and form an image. In material science and especially when investigating thin films types in this thesis, a thin cross section of the material is acquired to investigate properties such as thickness and composition. The samples is this work were acquired using the focused ion beam method [242], where a thin cross-section (ideally 40 to 80 nm), is cut from the original sample piece and attached to a copper grid for TEM analysis. After the cross-section is cut, often further thinning can be carried out by milling the sample [243].

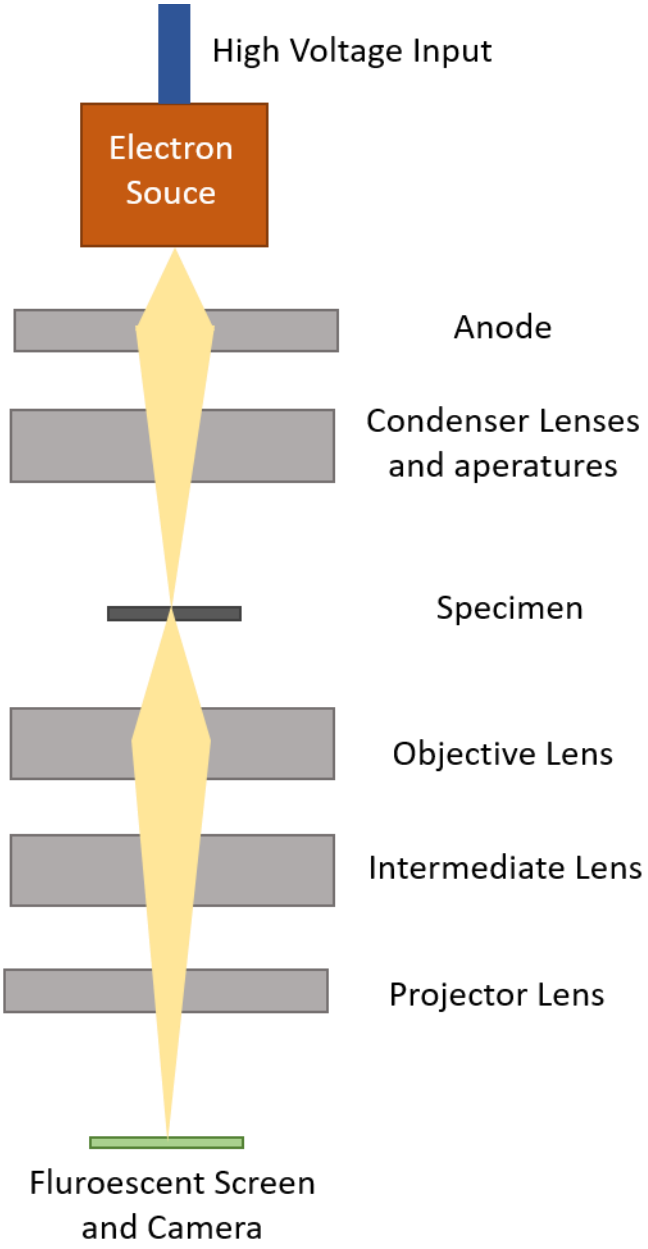


**Figure 2.13** Schematic of a basic TEM setup.

Scanning transmission electron microscopy (STEM) is a type of TEM where extra scanning coils are in placed the system such that the electron beam becomes more focused. The focused beam then scans line by line over the sample specimen to create an image. Aberration-corrected STEM imaging increases the focus of the electron beam and typically offers better resolution than traditional TEM. Abberration-corrected STEM is very useful when visualising at atomic resolution and can be used in conjunction with chemical analysis tools such as energy dispersive X-ray spectroscopy or electron energy loss spectroscopy. High-angle annular dark field (HAADF) STEM imaging was utilised in this thesis for investigating the

structure of the Aurivillius phase and the presence of sub-unit cell defects. In this technique, the HAADF detector measures inelastically scattered electrons hitting the sample at high angles. The image intensity from this technique is proportional to 1.4 of the square of the atomic number. Thus, it results in bright spots most visible for heavy atoms. In the case of B6TFMO, it is useful for visualising the heavy Bi atoms, and also enables the visualisation of the *B*-site cations.

In order to directly visualise the light oxygen atoms in B6TFMO at sub-Å resolution, integrated differential phase contrast (iDPC)-STEM imaging was used in **Chapter 3** [244]. The technique allows for the observation of low Z-elements, such as oxygen, using a bright contrast and dark background with a higher signal to noise ratio when compared to competing techniques, such as annular bright field STEM (ABF-STEM) [245].

STEM and TEM imaging was carried out with many collaborators using tools such as the FEI Titan FEG (S)TEM at 300 kV, a JEOL JEM 2100 in bright field mode at 200 kV, a Thermo Fisher Scientific Themis Z operated at 200 kV and a Thermo-Fisher Scientific FEI double aberration-corrected monochromated Titan Themis Z at 300 kV.

### 2.3.5 Electron Energy Loss Spectroscopy

Electron energy-loss spectroscopy (EELS) is a method of quantifying the atomic structure and chemical composition of a material by measuring the kinetic energy of electrons after they have passed through a sample piece. When electrons travel through a material, there is an interaction between them and the electrostatic field of the atomic nuclei and electrons through which they pass, as shown in **Figure 2.14**. There are two types of interactions which the electrons can undergo when they pass through a material: elastic scattering (columbic interaction with atomic nuclei) and inelastic scattering (columbic interaction with atomic electrons). In the case of EELS, the inelastic primary process of electron excitation (where the traveling electron is scattered and transfers energy to an atomic electron) is utilised. Here, the traveling electrons produced via an electron beam passing through the sample piece are measured by a high-resolution electron spectrometer**.** Then the scattered electrons are separated by energy and a plot of the number of electrons detected as a function of energy is produced [246].

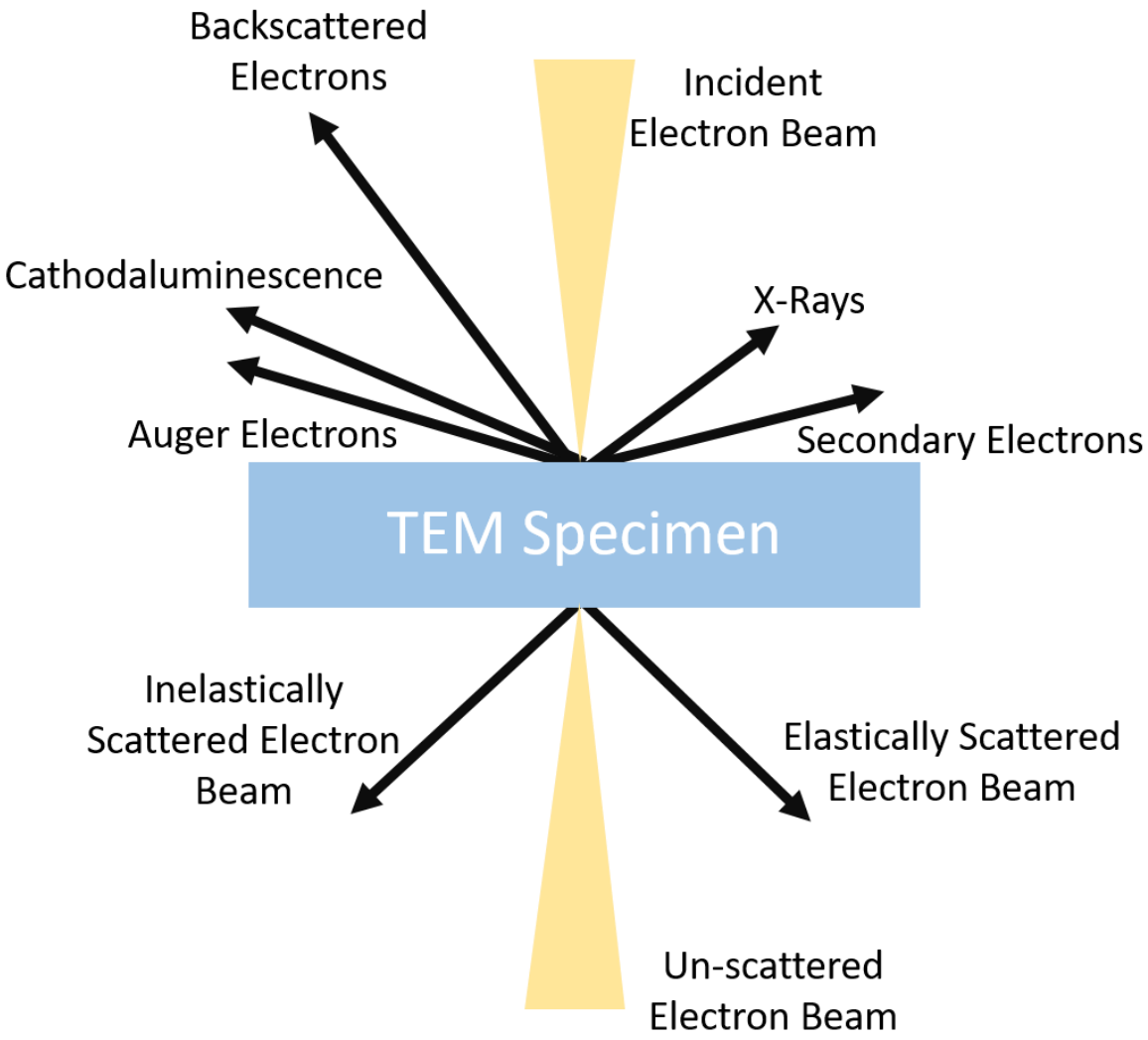


**Figure 2.14** Illustration of the common interactions between a TEM sample specimen and the electron beam.

As the electron beam passes through a sample, the majority of electrons are passed through without any energy loss and this is the first peak measured, the zero-loss peak. This peak can be used to align the measured energy-loss data and to give information about the sample's thickness. Energy-loss caused by outer shell atomic electrons are found at energies of < 50 eV and is known as the low-loss or valence region of the EELS spectrum. Higher energy loss caused by the inner-shell electrons > 50 eV show ionisation features that represent the inner-edges, where the intensity initially rises rapidly. Then as the energy loss increases, the intensity decreases more gradually. The point at which the edge feature begins approximately represents the binding energy of the corresponding shell, which is dependent on the atomic number of the scattering atom, thus the element type within samples can be determined.

There is also a fine structure associated with the core-loss edges that reveals information about the bonding, oxidation state or energy band structure of the atoms within the sample [246], [247].

When carrying out EELS experiments, the tool is often incorporated into a STEM/TEM setup. Here, typical electron beam energy ranges between 60 to 300 keV are used to probe the samples, such that local concertation of elements from an EELS spectrum can be correlated to a sample image such that atomic resolution can be obtained. The main limitations to EELS spectroscopy is the sample thickness. When the sample thickness increases above ~70 nm, the interaction of the primary electrons within the sample results in the electrons undergoing multiple energy loss events (Plasmon, Auger, secondary electron), thus reducing the signal-to-noise ratio of the EELS data.

EELS - spectrum imaging (SI) was performed a Titan3 G2 60–300 with a monochromated Schottky-FEG and a Gatan Quantum with both an UltraScan 1000 CCD and a K2 direct electron detector.

### 2.3.6 Superconducting Quantum Interference Device Measurements

In 1962, Josephson [248] first formulated the theory for tunnelling between superconductors, the premise from which a superconducting quantum interference device (SQUID) is based. His theory indicated that electron tunnelling between two superconductors with a thin insulator layer between them would lead to a supercurrent (a current that flows without dissipation). This current is defined in equation 2.3:

$$i = I_C \sin \varphi \qquad 2.3$$

Here the supercurrent passing through $i$, is defined by the critical current, $I_c$ and the phase, φ. There are two types of Josephson effects: AC and DC. In the DC effect, a current can flow without any applied voltage. This current is proportional to the phase difference between the wavefunctions of the tunnelling electrons [249].

In an AC junction, as shown in **Figure 2.15**, the Josephson junction will oscillate with a characteristic frequency, which is proportional to the voltage across the junction. The difference in the phase between the two superconductors can then be measured through either effect. Because the phase of a quantum state is altered by magnetic flux, the Josephson

junction can be used to measure the magnetic flux [249]. In an AC effect based SQUID device, if a constant current is maintained, the measured voltage from the device only varies with changes due to the phase at the two junctions, which is dependent on the change in the magnetic flux. Thus, by measuring the voltage the magnetic flux change can be determined.

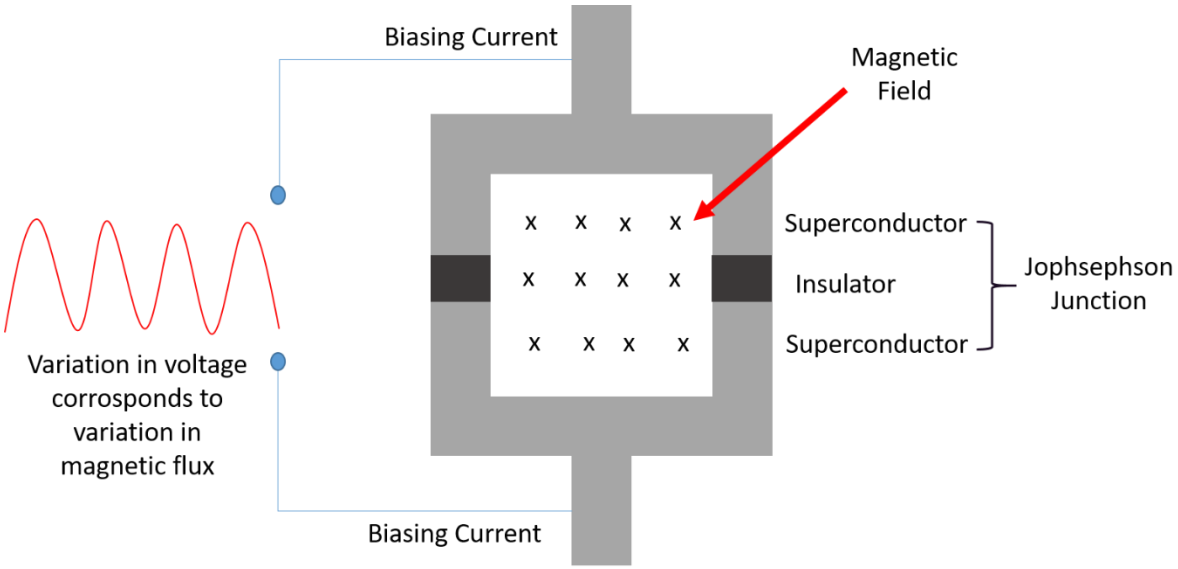


**Figure 2.15** Schematic of how the magnetic flux can be measured using the AC Josephson effect.

Modern SQUID magnetometry tools often operate at cryogenic temperatures e.g. 0 K up to and above room temperature. Detection of the magnetic flux quanta is performed as a sample is moved up and down within the tool. SQUID magnetometry is very useful for the measurement of thin films such as those in this thesis with thickness of 100 nm and below due to its sensitivity. The technique can detect magnetisation as low as $10^{-8}$ emu (using a Quantum Design MPMS3 magnetometer). In this work, SQUID magnetometry was used to measure the magnetic response (M) of the B6TFMO films as a function of temperature (T) and as a function of an applied magnetic field (H). When measuring the magnetic behaviour of the material in response to an applied magnetic field, a non-linear response is measured for materials that are, for example, ferrimagnetic, anti-ferromagnetic or ferromagnetic. For example, a ferromagnetic material produces a hysteresis loop when measuring the magnetisation in the presence of an applied field. It will have a net magnetisation value even when the applied field is removed. These measurements can be performed at a variety of temperatures to investigate the influence of temperature on the magnetic response. SQUID

magnetometry measurements are also used to extract information such as the coercive field or saturation magnetisation of the material.

Furthermore, Zero Field Cooled (ZFC) – Field Cooled (FC) measurements can provide more information on the magnetic nature of a material. For the ZFC measurements the sample is cooled down to ~2 K without the presence of an external magnetic field. As there is no magnetic field in this measurement, the magnetic spin of the electrons in the material are not orientated. Then a magnetic field is applied to the sample at low temperature and the material is brought up to room temperature, while the magnetisation is recorded. The FC measurement is then recorded with the applied magnetic field maintained while the temperature is decreased back down to 2 K, where the spins have the opportunity to orientate. The remanence (the magnetisation after removing the magnetic field) of the material can then be measured by removing the magnetic field and measuring the magnetisation as the temperature is brought back up to room temperature. The ZFC-FC measurements are useful for determining the transition temperature of a material below the point at which the two sets of data diverges and can indicate a ferromagnetic or antiferromagnetic character.

The magnetic measurements were performed in a Quantum Design MPMS3 magnetometer.

## 2.4 Simulation Methods

### 2.4.1 Polarisation Mapping

With the development of high resolution TEM and STEM imaging techniques such that the atomic components of materials can be imaged as discussed in **Section 2.3.4**, software has been developed in order to investigate local polarisation within ferroelectric materials. Through the use of atomic displacement mapping, local properties of ferroelectric materials have been investigated, such as ferroelectric domain walls [250], [251] and polar vortices [107], [109] as discussed in **Section 1.4.2**.

In this thesis, atomic displacement mapping of the *B*-site cations from HAADF-STEM images was carried out using the Atomap Python package [252] and the TEMUL Toolkit Python package [253], [254]. These packages are built on Hyperspy, which is a python library that

enables the interactive analysis of data [255]. The Atomap package allows for the determination of the *A*- and *B*-site atom positions from a HAADF-STEM image. Following this, 2*D* Gaussian refinement can then completed on each atomic column, such that a variety of structural information can be extracted, e.g. the distance between atoms. Image analysis and mapping, as well as polarization vector analysis, could then be carried out using the TopoTEM module of the TEMUL Toolkit Python package. An example workflow is shown in **Figure 2.16**.

In order to get the atom positions for the brighter *A*-site cations and construct an *A*-site sublattice, the Atomap, "*get_atom_positions"* function was used. The fainter *B*-site positions and subsequent sublattice were then located using the help of an appropriate zone axis from the *A*-site sublattice via the "*construct_zone_axes", "find_missing_atoms_from_zone_vector"* and *"find_nearest_neighbors"* functions. If there were any issues with the atomic positions from this automation, the interactive "*add_atoms_with_gui"* function could be used to correct the data before using the "*refine_atom_positions_using_2d_gaussian"* function to compete the 2D Gaussian refinement of the atom positions.

When the *A*- and *B*- cation positions are saved (as seen in **Figure 2.16 (b)**), they can be used in the TopoTEM package to find and plot the polarisation vectors due to the displacement of the *B*-site cations (as seen in **Figure 2.16 (c)**) using the "*get_polarization_from_second_sublattice"* and "*plot_polarisation_vectors"* functions.

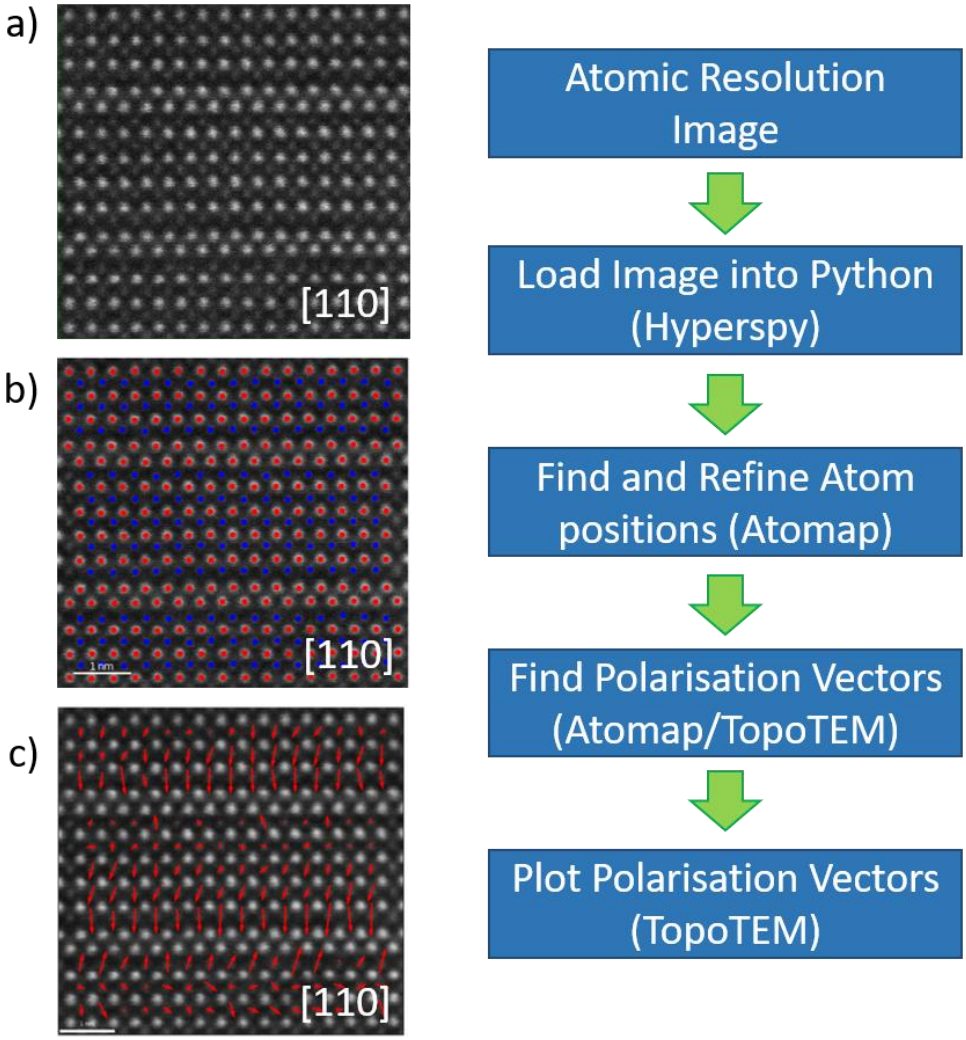


**Figure 2.16** Example workflow for the calculating and plotting polarization vectors from atomic resolution images.

### 2.4.2 Diffracted Intensities From Faulted Xtals

Diffracted Intensities From Faulted Xtals (DIFFaX) is a FORTRAN based code designed by Treacy *et al.* [256] where XRD patterns of materials can be simulated by creating a specific structure file. Within the structure file, the crystal system and measurement parameters can be set. To create an accurate structure file of a crystal, the atoms in the structure are considered as layers, which interact through stacking operations of different probabilities. The programme allows for the inclusion of planar defects into a crystal structure, letting one model the impact of these defects on the diffraction pattern of a given crystal. The FORTRAN

code has five operations from which diffraction information can be acquired. The main two functions used in this work were: 0 - Point and 3 - Powder Pattern. The Point function, can be used to find out details on the intensity, scattering angle position and layer structure factors for a reciprocal lattice point. The function views one point at a time as input by the user. Powder Pattern Function calculates a powder pattern within a specified 2θ range and 2θ stepsize input through the DIFFaX interface.

When constructing the read file of a structure, there are four separate sections to be considered: Instrumental, Structural, Stacking and Transitions where the DIFFaX manual version 1.813 [257] was used to understand these sections. In the Instrumental section of the structure file, the radiation type e.g. X-ray and wavelength is selected along with an option for instrumental broadening. There are three types of instrumental broadening profiles, Gaussian, Lorentzian and Pseudo-Voight and this parameter is only important with regards to the powder pattern outputs. In most cases, a Gaussian or Lorentzian broadening is appropriate to use, where the degree of the FWHM of the reflections can be set. However, if using the Pseudo-Voight broadening, it should be noted that as this broadening varies with scattering angle, four input parameters are required. Three (u, v, w) to control the FWHM and another (σ) to control the contribution of the Gaussian and Lorentzian components to the broadening.

The Structural section of the file is where the details of the crystal structure are input. The unit cell parameters and point symmetry are specified. The cell dimensions are made up of *a*, *b*, *c* and γ, where *c* is perpendicular to the *a*-*b* plane. The value of *c* is an important value as it provides a reference along the stacking direction from which the *z*-competent of the stacking vectors can be defined. This section can also let the creator define the Laue symmetry of the calculated diffraction data. It is recommend to use the UNKNOWN function for this component and let DIFFaX work out the symmetry of the structure. However if the user wishes to control this parameter, there are 12 possible options: 10 diffraction point groups (-1, 2/M(1), 2/M(2), MMM, -3, -3M, 4/M, 4/MMM, 6/M, 6/MMM) , UNKOWN and AXIAL. The twelfth option AXIAL was used in this thesis as it constrains DIFFaX to only integrate along the (*00l*) axis, which replicates the XRD patterns measured for thin films. In this section, the number of layers that will be created needs to be defined and an optional line which defines

the width of the crystal in the horizontal *a* and *b* directions can be defined, in his work it was left as infinite.

Next, the different atomic layers are defined for the structure. They are labelled as Layer 1, Layer 2 etc. In this section, the structure of each layer is created. Initially, the symmetry of the layer structure can be defined as either NONE or CENTROSYMMETRIC. If CENTROSYMMETRIC, only the asymmetric half of the atom coordinates need be entered. In each Layer the atoms contained in the layer are defined. The atom name and oxidation state is selected and each atom within a Layer is given a label of 1, 2, 3 etc. The *x* coordinate relative to the *a*-axis and the *y* coordinate relative to the *b*-axis are defined here as fractional coordinates of a unit cell. The *z* coordinate relative to the *c*-axis is left at zero here, and in the Transitions section, the spacing between the layers in the *c*-axis direction is defined. It should be noted, that in this section, a distinct layer must be created for layers, even if they are structurally identical but have different stacking behaviour in the vertical *c*-axis direction. The final two parameters to fill in this section are the isotropic Debye-Weller factor and occupancy factor.

In the Stacking section, simply the order of the stacking of the layers created in the Structural section are defined. There are two options: EXPLICIT and RECURSIVE. In this thesis, the EXPLICIT option is used where a unique, fixed sequence of layers is defined by the user. The RECURSIVE option allows the calculations to be carried out for a statistical ensemble of crystallites, each with a distinct stacking sequence, but weighted by the probability that such a sequence will occur.

Finally, the Transitions section is used to define the stacking in the *c*-axis direction between each distinct layer as ordered in the Stacking section. Firstly, for each distinct layer, a line is created to describe the transition between it to each other layer that was created in the Structural section. The stacking probability is defined between 0 and 1, typically selected as 1 divided by the number of distinct layers in the structure. For layers that have no transition between them i.e. they are never stacked next to one another, the components of the stacking vector can be left as 0. When there is a transition between two layers, i.e. when they are stacked next to one another; a *z*-component of the stacking vector relative to the *c*-axis is defined. In this work, experimental neutron diffraction data was acquired from the literature

to find the distance between a particular set of layers in the *c*-axis direction and subsequently used for the *z*-component of the stacking vector relative to the *c*-axis.

For this work structure files were created for *m* = 4, 5 and 6 Aurivillius phases based on the data from [150], [258], [259]. Furthermore, additional layers were created to describe *m* = 4 and 6 intergrowths within an *m* = 5 structure file. Through using the EXPLICIT stacking function within the structure file and DIFFaX, the impact of the density and position of the intergrowths within the *m* = 5 Aurivillius phase could be examined.

### 2.4.3 Density Functional Theory

Density Functional Theory (DFT) is a computational modelling method used to investigate the electronic or nuclear structure of systems comprised of many bodies, such as atoms or molecules [260]. It begins with the quantum mechanical many-body Hamiltonian to calculate the electron density that minimises the total energy in a given system. DFT calculations were performed using Vienna Ab initio Simulation Package (VASP5.4) [261], where the atom resolved density of states for the different perovskite layers within the Aurivillius phase system could be determined. In these types of calculations, the impact of factors such as electrostatic boundary conditions, epitaxial strain, and structural changes on the electronic density of sates of the atoms within the system can be explored.

# 3 Atomic Level Origin of the Impact of Octahedral Tilting and Tetragonal Distortions on the Functional Properties of the Room Temperature Multiferroic $Bi_6Ti_3Fe_{1.5}Mn_{0.5}O_{18}$

In this chapter, all research is the work of the author, with the exception of the following contributions from collaborators: M. Schmidt (Tyndall-UCC) prepared cross-section lamella of the samples. N. Bagués (Ohio University) carried out scanning transmission electron microscopy (STEM), integrated differential phase contrast microscopy and electron energy loss spectroscopy and aided in the interpretation of the analysis. D. W. McComb (Ohio University) aided in design of the electron microscopy experiments alongside aiding in the interpretation of the analysis. M. Noor-A-Alam (Tyndall-UCC) carried out the density functional theory calculations and the interpretation of the results. M. Nolan (Tyndall-UCC) contributed to then interpretation of the density functional theory calculations

## 3.1 Introduction

Data storage devices based on multiferroic materials, possessing simultaneous ferroelectric and ferromagnetic memory states, have the potential to revolutionise future information storage [48]. Exploitation of single-phase multiferroic materials in tunnel junction devices offers the opportunity to combine both electroresistance states with magnetoresistance states, thus providing four or more bits in a single memory cell [18]. This offers a clear advantage in data storage capacity compared with existing computer memories, which use either electric or magnetic polarisation to store information separately in single-bit devices [262]. The capability to magnetoelectrically couple ferroelectricity and ferromagnetism enables electric field (and thus voltage rather than current) control of magnetism, paving the way for energy-efficient data storage devices [263]. Furthermore, the ability to tune domain nucleation and growth signifies that multiferroic materials may conceivably serve as unique multi-level memory elements in the quest for low-power neuromorphic memory systems [264], [265].

In practice however, due to the fundamental opposing requirements of ferroelectricity (requiring empty *d* orbitals) and ferromagnetism (requiring partially occupied *d* orbitals), single-phase multiferroic materials that display room temperature (RT) operation

are exceptionally rare [22]. Of the multiferroic materials that do exist, the material properties relevant for multi-state storage are currently limited to weak polarization and coupling values, which has prevented the realisation of such devices commercially [48]. $BiFeO_3$ is the most widely studied single phase multiferroic material [51], but suffers from issues including: the magnetic order is primarily antiferromagnetic and it displays only a weak (~2 emu/cm$^3$) residual moment from a canted spin structure. This prohibits linear magnetoelectric coupling between polarisation and magnetisation in $BiFeO_3$ and only higher-order magnetoelectric effects are possible with the assistance of large threshold magnetic fields (~3 to 18 T) [266]. This is clearly incompatible with low-energy spintronics [48], [267].

Despite the fundamental conflict between ferroelectricity and ferromagnetism, innovative routes have been employed towards the design and discovery of truly single phase multiferroic materials, including a group of materials termed "geometrically driven multiferroics", where ferroelectricity results from long-range dipole-dipole interactions and oxygen rotations within a magnetic framework [268]. For example, improper ferroelectricity ($T_c$ ~1250 K) in $YMnO_3$ is driven by polyhedral tilting of the $MnO_5$ block and is compatible with the coexistence of antiferromagnetism ($T_N$ ~80 K) [129], [269]–[271]. Despite substantial research on other hexagonal $RMnO_3$ systems (where R = Sc, Y, In, Dy–Lu) [269], a rare earth manganite that demonstrates both ferroelectricity and ferromagnetism at room temperature is yet to be discovered [22].

An attractive approach is to modify the chemistry within layered materials to combine multiple functionalities that tend not to coexist in simpler oxides into a single phase complex oxide. Pitcher *et al*. [272], employed compositionally controlled tilt engineering in a layered Ruddleson-Popper system to impose the appropriate combination of octahedral tilts to simultaneously generate spontaneous magnetisation and polarisation at RT. Although ferroelectric switching was not demonstrated, it was shown that the magnetic structure of the $(Ca_ySr_{1-y})_{1.15}Tb_{1.85}Fe_2O_7$ system was directly affected by the chemically induced polar $c^+$ tilt, with weak ferromagnetism produced by canting of the $Fe^{3+}$ moments and the magnitude of the magnetoelectric coupling increasing with the magnitude of the $c^+$ tilt.

In recent years, it has been demonstrated that the fundamental contra-indications between ferroelectricity and ferromagnetism [22] can be circumvented by combining the

chemistries required for multiferroicity through creating a new layered Aurivillius composition [162]–[164], [273]. Bismuth-based Aurivillius phase materials are naturally layered structures with a general formula $(Bi_2O_2)(A_{m-1}B_mO_{3m+1})$, where dielectric bismuth oxide $(Bi_2O_2)^{2+}$ fluorite-type layers are interleaved with *m* numbers of ferroelectric perovskite-type units. Aurivillius phases are considered "proper" ferroelectrics where ferroelectricity arises from polar distortions of the *A*-site (e.g. through stereo-chemical activity of the $Bi^{3+}$ $6s^2$ lone pair electrons) and *B*-site (e.g. through second order Jahn-Teller distortions of $Ti^{4+}$) cations. Tilts or rotations of the $BO_6$ octahedra contribute to non-polar structural distortions [161]. The flexible and layered nature of this class of material permits engineering its composition to modify and enhance key properties e.g. incorporating Co can alter the band gap [274], [9]. When magnetic Fe and Mn cations are integrated into this ferroelectric framework, a unique, stable, single-phase RT ferroelectric/ferromagnetic multiferroic is formed. As shown in **Figure 3.1**, the *m* = 5 phase $Bi_6Ti_xFe_yMn_zO_{18}$ (B6TFMO; x = 2.80 to 3.04; y = 1.32 to 1.52; z = 0.54 to 0.64) has five perovskite layers interleaved between $(Bi_2O_2)^{2+}$ fluorite-type layers, while intermixing differing types of *A*-site (Bi) and *B*-site (Ti, Mn, Fe) cations within the scaffold drives both ferroelectricity and ferromagnetism within the same structural phase [162]–[164], [273]. B6TFMO displays saturation magnetization ($M_S$) values of 215 emu/cm$^3$ (two orders of magnitude larger than $BiFeO_3$) [266] and in-plane saturation polarization ($P_s$) values of > 26 μC/cm$^2$ [275]. Electron microscopy [164] and density functional theory (DFT) [192] studies demonstrate that the inclusion of manganese within the B6TFMO structure is crucial to promoting long-range ferromagnetic order. Detailed micro- and nano-structural analysis, combined with rigorous statistics (confidence level ≥99.5 %), conclude that ferromagnetic secondary phase impurities do not influence the ferromagetic behaviour [273]. Moreover, B6TFMO demonstrates the reversible linear magnetoelectric switching necessary for practical RT magnetoelectric device applications compatible with low-energy nano-electronics and spintronics [162], [163].

The presence of the $[Bi_2O_2]^{2+}$ interface layers interleaved within the structure imparts an elastic strain energy gradient through the Aurivillius layers, due to layer mismatch between the differing lateral dimensions of the $[Bi_2O_2]^{2+}$ layers (*a* = 3.80 Å) compared to the perovskite lattice layers (*a* = 3.89 Å) [149]. In addition, the layer of oxygen anions in the $[Bi_2O_2]^{2+}$ interface layer provides electrostatic energy variations within the Aurivillius structure. Furthermore,

below the ferroelectric transition temperature, a strong bond is formed between the bismuth cation in the $[Bi_2O_2]^{2+}$ interface layer and an apex oxygen of the adjacent perovskite layer. As well as having an "inductive effect" on the *B-O* bond distances in the layer direction (*c*-axis) [156] and prompting ferroelectricity via a polar displacement of ions perpendicular to the layer direction, the shorter *Bi-O* bond (e.g. 2.42 Å compared with 2.65 Å in $Bi_4Ti_3O_{12}$) shears the perovskite layer, resulting in tilting and rotation of the $BO_6$ octahedra [154], [155]. For the case of B6TFMO, substitution of Ti/Fe with magnetic Mn and Fe cations (necessary to achieve the *m* = 5 multiferroic phase), results in an even more complex bonding environment for the transition metal cations at the available perovskite-type *B*-sites of the Aurivillius phase structure (**Figure 3.1**). Atomic resolution energy dispersive X-ray analysis studies have revealed that cation partitioning occurs in B6TFMO due to elastic strain and electrostatic energy contributions, which vary as a function of distance from the $[Bi_2O_2]^{2+}$ fluorite-type layers [144], [149], [160], [164], [276], [277]. This partitioning is revealed as a preference for Mn to locate predominantly in the central perovskite layers within the five-layered perovskite block enabling an increase in the probability of nearest-neighbour magnetic interactions in the central layer by up to 90 % compared to a scenario where the magnetic cations are randomly distributed over the five available *B*-sites in a perovskite block [164].

Consequently, previous descriptions of the atomic structure and the demonstration of the preferred cation locations has advanced understanding of the fundamental mechanisms governing ferromagnetism in this interesting single phase multiferroic. However, given that functional electronic and magnetic properties that drive the application in storage are strongly correlated with octahedral tilting and local structural distortions within perovskite systems and their heterostructures [110], [272], [278]–[283], the tailoring of the B6TFMO composition to promote enhanced multiferroic behaviour requires a detailed atomic level understanding of the influence of local symmetry lowering distortions and octahedral tilting on the fundamental electronic structure, ferroelectric properties and magnetic coupling interactions that arise from differing chemical bonding environments within this complex layered system. This information is currently lacking for B6TFMO multiferroics.

Accordingly, this paper aims to fill that crucial gap in understanding the multiferroic behaviour of B6TFMO. The use of high resolution scanning transmission electron microscopy (STEM) in conjunction with electron energy loss spectroscopy (EELS) to spatially probe atomic-

resolution electronic structure at the possible crystallographic perovskite *B*-site sites within the B6TFMO structure is described. It is revealed for the first time how crystal field splitting of the $Ti^{4+}$ cation is influenced by its position within the Aurivillius unit cell. First principles density functional theory (DFT) calculations of atom resolved partial density of states (PDOS) show that this is predominantly driven by changes in the extent of tetragonal distortion along the *c*-direction, on moving from the $[Bi_2O_2]^{2+}$-perovskite interface through to the central layer of the *m* = 5 perovskite block.

High angle annular dark field (HAADF) STEM imaging, together with integrated differential phase contrast (iDPC) imaging, allows observation of the positions of the light oxygen atoms at both the [110] and [100] orientation in the system. Atomically-resolved evidence for complex octahedral tilting is demonstrated to have variable tilt amplitudes across the perovskite layers, which competes with the magnitude of the tetragonal distortion of the $TiO_6$ octahedra. Atomic scale mapping of polar displacements reveals that polarisation is largest towards the outer perovskite cells, correlating with an increased extent of local tetragonal distortion of octahedral geometries. The degree of octahedral tilting increases and the tetragonal distortion decreases towards the central layers of this Aurivillius system, where the magnetic cations preferentially partition.

## 3.2 Methods

Direct liquid injection chemical vapour deposition (DLI-CVD) methods similar to Faraz *et al.* [163] were used to deposit B6TFMO thin films on *c*-sapphire. Samples from two different growth runs were synthesised by DLI-CVD via a horizontal flow AIXTRON AIX 200/4FE AVD (atomic vapour deposition) system [284], [285]. The films had a nominal stoichiometry of $Bi_6Ti_3Fe_{1.5}Mn_{0.5}O_{18}$. The films were deposited using a 22 % to 23 % bismuth excess [286], [287] in order to mitigate the loss of volatile bismuth [288] during the two-step growth process [286]. The 0.100 mol $dm^{-3}$ bismuth, iron and titanium precursors in toluene solution, $Bi(thd)_3$, $Fe(thd)_3$ and $Ti(O\text{-}iPr)_2(thd)_2$ (where thd = 2,2,6,6- tetramethyl 3,5-heptanedionate and O-iPr = isopropoxide), were purchased from Epivalence Ltd. The 0.025 mol $dm^{-3}$ manganese precursor was prepared by dissolving $Mn(thd)_3$ (99 %, STREM chemicals) in anhydrous toluene (99.8 %, Sigma-Aldrich) under $N_2$ in a glovebox. The substrate was loaded into the reactor chamber set at a pressure of 10 mbar while the temperature of the

rotating susceptor-heated sample holder was set to 630 °C. The conditions were maintained for the entirety of the deposition process. The low vapour pressure precursors were then injected using nitrogen pulses into the Trijet Vaporizer of the DLI-CVD system, where they entered a reactor growth chamber via lines maintained at 220 °C. Precursors were mixed with reactive $O_2$ gas during the growth run. A total gas flow of 3000 sccm (standard cubic centimetres per minute) was maintained in the growth chamber comprised $O_2$ run gas and $N_2$ carrier gas where the $O_2$ flow was 1000 sccm. The precursor volumes were controlled electronically by setting the opening time for each injection to be between 1.6 and 10.9 ms, depending on the precursor and using the continuous injection mode where the injections pulsed at a frequency of 1 Hz. 800 injections of each precursor was used and the net volumetric precursor injection ratios were approximately 7.4:3:1.5:0.5 for $Bi(thd)_3$, Ti(O-iPr)2$(thd)_2$, $Mn(thd)_3$, and $Fe(thd)_3$, respectively over the duration of the growth run. After thin film deposition via DLI-CVD (Step One), the samples were post-annealed in atmosphere for 1 hr at 850 °C (Step Two) in order to produce crystalline Aurivillius phase films. The thicknesses of the subsequent B6TFMO films were approximately 95 nm.

A FEI DualBeam Helios NanoLab 600i Focused Ion Beam instrument was used to prepare the lamella cross sections of the B6TFMO films. Transition electron microscopy (TEM) cross sections were prepared by depositing C and Pt as electron-beam induced layers, followed by an ion-beam induced C layer for protection. The lamellas were thinned at 0.28 nA/30 kV with final polish at 47 pA/5 kV. High angle annular dark field (HAADF)-scanning transmission electron microscopy (STEM) imaging and integrated differential phase contrast (iDPC)-STEM imaging were performed using a probe-corrected Thermo Fisher Scientific Themis Z operated at 200 kV with a convergence semi-angle of 18 µm. iDPC-STEM images were obtained using 4-segment annular detector with hole on the center. Annular dark field (ADF) images were collected simultaneously with an annular field detector for correlation. A live high-pass filter was applied to iDPC-STEM images to reduce the low frequency information.

Electron energy loss spectroscopy (EELS) - spectrum imaging (SI) was performed at 300 kV using an image-corrected Titan3 G2 60–300 with a monochromated Schottky-FEG and a Gatan Quantum with both an UltraScan 1000 CCD and a K2 direct electron detector. EELS was acquired in STEM mode with collection (β) to convergence (α) angle ratios of $\beta/\alpha = 1–2$.

No significant variations were observed with larger β/α ratio tested to improve the S/N. Data was collected with a dispersion of 0.1 eV/channel. Dual-EELS was used for energy shift correction, but was not available with the K2.

A re-bin function using Gatan GMS software was utilised to try and improve the signal:noise of the EELS data. This function consists of summing the intensities of neighbouring pixels into a single pixel. The number of pixels within the data set is reduced. In this analysis the horizontal (x-component) of a data set was summed into one pixel and the number of vertical (y-components) was not changed. For example, in **Figure 3.2** the data set was re-binned from a 100 x 70 pixel to a 1 x 70 pixel data set. The data for the change in peak energy of the Ti $L_3$ from re-binned EELS spectra was calculated using Gatan's Digital Micrograph EELS module. For each data set, non-linear least-square (NLLS) fitting (Gaussian and Lorentzian) in Gatan's Digital Micrograph EELS module was used on the Ti $L_{2,3}$-edge. The energy positions (eV) of Ti $L_{2,3}$ peaks were then plotted as a function of distance through the perovskite layers. The average shift of the Ti $L_3$ $e_g$ peak was calculated by utilising the EELS spectra of the outer and centre perovskite layers using annular dark field images. The Ti $L_{2,3}$ peak values were obtained using multipeak fit in origin. In the graphs shown in **Figure 3.2**, the energy of the $L_3$ $e_g$ peak goes from 458.4 to 458.45 eV at the outer layers to 458.5 to 458.55 eV at the centre layer.

The atomic scale polarisation mapping was carried out on STEM-HAADF images by first using Atomap software [252] that analyses the positions of atomic columns using *2D* elliptical Gaussian distributions. Once the *A*- and *B*- site positions of the atoms are determined, the polarisation vectors are found by reversing the measured *B*-site displacement, using the TEMUL toolkit [254].

Spin-polarized density functional theory (DFT) calculations were performed using Vienna Ab initio Simulation Package (VASP5.4) [261]. The ion-electron interactions were described by the projector augmented wave (PAW) methods [289]. The exchange and correlation effects were described by the Perdew–Burke–Ernzerhof (PBE) functional of the generalized gradient approximation (GGA) [290], [291]. A rotationally invariant Hubbard U correction [292] was added to the 3*d* states of Fe and Mn, where U = 5.5 eV was used for all Fe atoms (the typical range of U values for Fe in multiferroic $BiFeO_3$ is between 5 and 7 eV [293], [294], and 3.0 eV was used for Mn atoms [192]. The number of valence electrons

for Bi, Ti, Fe, Mn, and O is 5 (valence electron configuration: $6s^2\ 6p^3$), 4 (valence electron configuration: $3d^3\ 4s^1$), 8 (valence electron configuration: $3d^7\ 4s^1$), 7 (valence electron configuration: $3d^6\ 4s^1$), and 6 (valence electron configuration: $2s^2p^4$), respectively. The plane-wave expansion was truncated at a cut-off energy of 600 eV. Similar to the previous DFT calculations [192], a unit cell of $Bi_{24}Ti_{11}Fe_6Mn_3O_{72}$ stoichiometry is used. In accordance with previous experimental observation of cation ordering as well as theoretical studies [192], Mn atoms at the 'inner' perovskite block are considered. The convergence threshold of energy for the self-consistent calculations was $10^{-6}$ eV. The structural optimization was carried out by minimizing forces on all the atoms until they were smaller than 0.01 eV $Å^{-1}$. A 4 × 4 × 2 Monkhorst-Pack k-point mesh [295] was used for structural optimization and the (density of states) DOS calculations. The use of symmetry is switched off using ISYM = -1 for both structural optimizations and DOS calculations. Gaussian Fermi smearing method (smearing width of 0.01 eV) with 2001 energy bins were used for DOS calculations. Atomistic structures are visualised using the VESTA *3D* visualisation program [296].

## 3.3 Results and Discussion

### 3.3.1 Electronic Structure Description of Perovskite Layers within B6TFMO

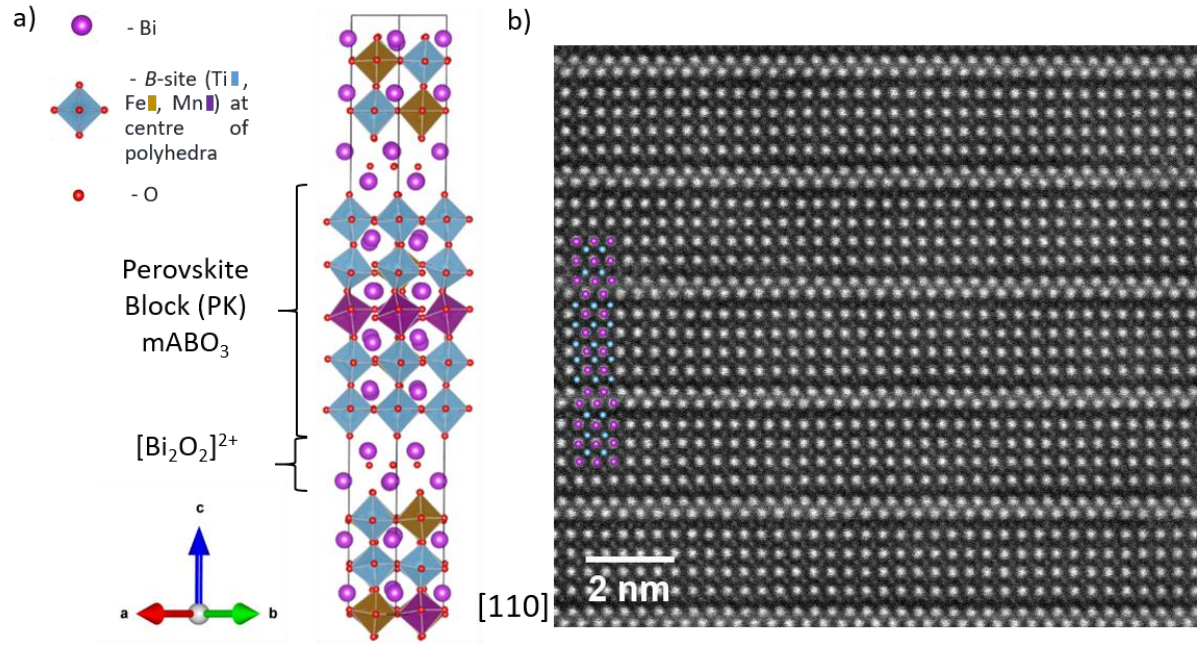


**Figure 3.1** a) Atomistic structure of one unit cell of the five layered, $m = 5$, B6TFMO ferroelectric structure with *B*-site displacement and octahedral tilting (as calculated from DFT and discussed as Configuration: *b* in **Sections 3.3.2 and 3.3.3**). Dielectric $[Bi_2O_2]^{2+}$ layers are sandwiched between perovskite $ABO_3$ units where $Bi^{3+}$ occupies the *A*-sites (purple), and transition metal cations occupy the *B*-sites (blue/purple/gold) of the $BO_6$ octahedra. b) HAADF-STEM image of demonstrating the layering within B6TFMO projected down [110].

**Figure 3.1 (a)** depicts a model of the 5 layer multiferroic phase B6TFMO where one dielectric $[Bi_2O_2]^{2+}$ layer and five $ABO_3$ perovskite layers correspond to half a unit cell. HAADF-STEM imaging of the atomic structure of B6TFMO, shown in **Figure 3.1 (b)**, confirms the $m = 5$ phase Aurivillius structure of B6TFMO. Areas without any structural defects such as stacking faults or out-of-phase boundaries (regions where the structure is misaligned by a fraction of a unit cell) are presented. Here, work on atomic and chemical characterisation of B6TFMO is built on [164], [192] and now, for the first time spatially resolved EELS is used to investigate the local electronic structure of the perovskite sites within its layers.

**Figure 3.2 (a)** shows the STEM-EELS spectra of the Ti $L_{2,3}$, O K, Mn $L_{2,3}$ and Fe $L_{2,3}$-edges for three different layered regions within B6TFMO's unit cell: an "outer", "intermediate" and "centre" perovskite layer **Figure 3.2 (b)**. The outer layers are defined as those closest to the $[Bi_2O_2]^{2+}$ interfaces, the centre layers are defined as those furthest from the $[Bi_2O_2]^{2+}$

interfaces, with intermediate referring to the perovskite layers in between. It can be observed that the STEM-EELS measurements of the preferred locations for Ti, Mn and Fe are in agreement with previous HAADF-STEM energy dispersive X-ray analysis (EDX) chemical characterisation of B6TFMO [164]. Titanium is the most abundant *B*-site cation in B6TFMO, therefore the Ti $L_{2,3}$-edge is the most intense peak in the EELS spectra. This confirms previous EDX observations of a significant increase in the *B*-site proportion of Mn [164] in the central layers, confirming a distinct preference for partitioning of magnetic Mn towards the centre perovskite layers.

The O K-edge within B6TFMO provides electronic information on the bonding between O and its neighbouring cations. Typically, in the O K-edge fine structure for metal oxides, much information can be gained about the local geometry of the complex [297], [298]. While peak splitting can be observed within the O K-edge as shown in **Appendix I Figure I.1 (c, d)**, the splitting between the $t_{2g}$ and $e_g$ peaks is not as well defined compared to the splitting within the Ti $L_{2,3}$-edge demonstrated in **Appendix I Figure I.1 (a-b)**. Given that B6TFMO is a complex multi-cation oxide, it should be noted that the individual contributions of Ti, Mn and Fe to the O K-edge structure would be difficult to deconvolute. Accordingly, the Ti $L_{2,3}$-edge was selected for further investigation of the electronic structure and subtle chemical bonding changes through the B6TFMO structure, that is from the interface of the $[Bi_2O_2]^{2+}$-perovskite interface to the central of the perovskite block.

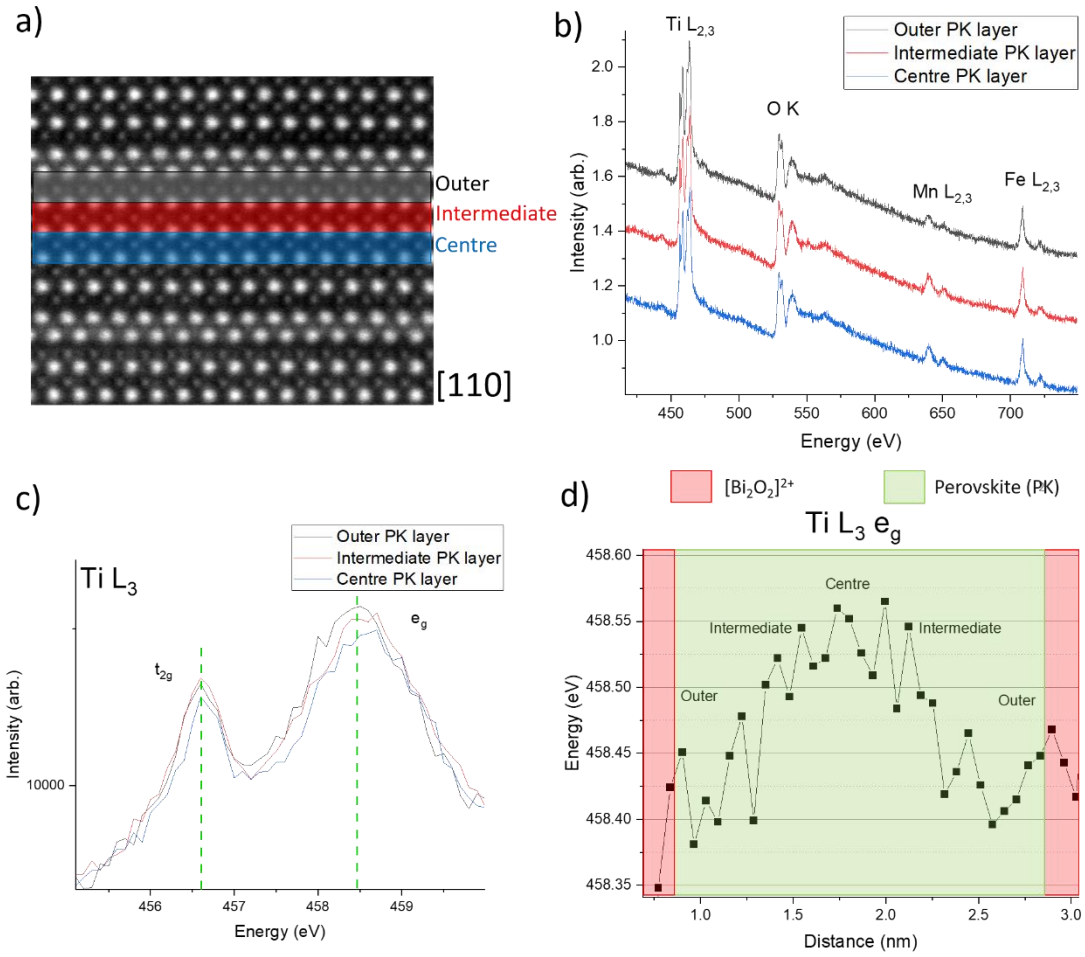


**Figure 3.2** a) HAADF STEM image of B6TFMO representing the regions outer (black), intermediate (red) centre (blue) from which STEM-EELS spectra were acquired. b) Normalised EELS spectra representing the three types of perovskite (PK) layers (outer, intermediate and centre) within a B6TFMO unit cell. Annular dark field images were used to extract the EELS spectra. c) Detail of the Ti $L_3$ peak from EELS spectra taken from three types of perovskite layers, outer (black), intermediate (red) and centre (blue). d) Plot of the change in peak energy of the Ti $L_3$ from re-binned EELS spectra. The data set from this figure was re-binned from a 100 x 70 pixel to 1 x 70 pixel data set.

If the Ti cation is in a well-defined coordination environment, the degeneracy of the 3*d*-orbital final states is lifted due to the crystal field effect arising from hybridisation with the occupied 2*p* orbitals of oxygen. This causes a splitting of the energy levels of the *d* orbitals. For octahedral complexes, the energies of the $t_{2g}$ inter-axial orbitals ($d_{xz}$, $d_{yz}$, $d_{xy}$) decrease (become more stable) and the energy levels of the $e_g$ axial orbitals ($d_{x2-dx2}$, $d_{z2}$) increase, owing

to the increased repulsion between electrons in the axial 3*d* orbitals and oxygen 2*p*. The L-edge of the Ti cation consists of two edges, $L_3$ and $L_2$ which represent the core shell electrons from the $2p_{1/2}$ and $2p_{3/2}$ transitioning above the Fermi level into the unfilled 3*d* energy levels. When determining the presence of the $Ti^{4+}$ and $Ti^{3+}$ oxidation states using EELS, the peak position together with the $L_3$ and $L_2$ intensity ratio are typically used. For the case of reduction from 4+ to 3+, the $L_{2,3}$ peaks shift to lower energies, while both the shape and intensity of the doublets change for the different Ti oxidation states due to the changing number of valence electrons. An octahedral environment results in a $t_{2g}$-$e_g$ splitting and thus four peaks are observed in the $L_{2,3}$-edge. For $Ti^{4+}$ cations, the characteristic doublets are well resolved, with clear separation between the $t_{2g}$ and $e_g$ peaks, while for the $Ti^{3+}$ oxidation state the doublet is typically not as well defined. Spatially resolved EELS data reveals that the $t_{2g}$-$e_g$ crystal field splitting (Δ) is present through the outer, intermediate and centre perovskite layers, indicating an oxidation state of +4 for the Ti cation throughout the B6TFMO structure.

Importantly, layer by layer analysis of the EELS spectra taken from the perovskite layers shown in **Figure 3.2 (c)** demonstrate an increase in the value of Δ through the layers from outer layer to centre layer. The average increase from the outer perovskite layer to the centre perovskite layer is 0.13 ± 0.06 eV. Since this is within a single dataset, this implies that that there is a change in the magnitude of the crystal-field splitting across the five-layer structure. This change in Δ through the layers was observed in two different sample pieces from different DLI-CVD growth runs, and measured on different days with two different types of EELS detectors. Eleven EELS data sets were used to calculate the average Δ value, as seen in **Appendix I Table I.1**. Each data set had two $e_g$ values for the outer perovskite layer and one $e_g$ value for the centre layer, therefore for each data set, two Δ values were obtained (twenty two data sets were obtained in total, **Appendix 1 Table I.1**). From the spatially resolved EELS spectra, it can be seen that the position of the $t_{2g}$ peak position remains constant. It appears this change in Δ is due to a shift in the energy of the $e_g$ peak increasing in energy moving from the outer to centre perovskite layers. The trend of increased Δ values towards the centre layers was observed for all measurements.

**Figure 3.2 (d)** and **Appendix I Figure I.2** display representative plots of $e_g$ peak energy as a function of distance through the perovskite layers of B6TFMO, where an energy shift of ~0.1 eV is observed from outer to centre perovskite layer. The fact that the $t_{2g}$ level does not

appear to be changing while the $e_g$ peak energy position shifts position, indicates that this change in the energy levels is not due to an oxidation state change. It is conceivable that a number of factors which are not mutually exclusive could contribute to the changes observed in the density of states of the $e_g$ energy level. Recent work [110], [278] on $(PbTiO_3)_n/(SrTiO_3)_n$, has shown in these systems with polar vortices that the Ti 3*d* orbital interactions change as a function of their position within the heterostructure. Given that B6TFMO could be considered a natural heterostructure made of interleaving $[Bi_2O_2]^{2+}$ layers and $BiTi[Fe,Mn]O_3$ perovskites, in the following sections, possible contributions to the changes observed in the $L_3$ $e_g$ peak of B6TFMO are considered, such as the tetragonal distortion and tilting of the $BO_6$ octahedra imposed by the $[Bi_2O_2]^{2+}$ interlayer.

### 3.3.2 Correlations of $BO_6$ Octahedral Distortions with Electrical Polarisation at Differing Perovskite Layers within B6TFMO

As determined previously [144], [160], [164], [192], [258], the $[Bi_2O_2]^{2+}$-perovskite interface within the B6TFMO unit cell drives a change in the elastic strain energies and electrostatic energies across B6TFMO's perovskite layers. Within the perovskite layer block, there are three distinct crystallographic *B*-sites [156], [159], [164], [258], which lie within the outer, intermediate and centre perovskite layers. Kikuchi's model [144] of the Aurivillius phases considers the compressive forces felt at the outer perovskite layers (pseudocubic $a$ = 3.89 Å) imposed by the $[Bi_2O_2]^{2+}$ interface ($a$ = 3.80 Å) and shows how the change in elastic strain energy within Aurivillius phases is critical to the stability of a particular phase. The approach developed by Moore *et al.* [192] , found that the strain imposed onto the perovskite layers results in the average c/a ratio changing from ~1.25 for the outer layers to ~1.15 at the centre layers of the perovskite cells. When considering the impact of strain to the environment within which the Ti cations reside, it is clear that the bond lengths between the transition metal and the O ligands will be altered. It follows that the more highly strained $BO_6$ octahedra next to the $[Bi_2O_2]^{2+}$ interface should be more tetragonally distorted compared to those further from the interface.

To examine how elastic strain and tetragonal distortion affect local electronic structures, first the atom resolved partial density of states (PDOS) around the conduction band region of Ti in a model structure of B6TFMO was analysed, denoted Configuration: *a*

(shown in **Figure 3.3**), using Density Functional Theory + Hubbard (DFT+U) calculations. The $d_{x2-y2}$ orbital dominates around the conduction band minimum of the outer Ti atoms, nearest the $[Bi_2O_2]^{2+}$ block. **Figure 3.3** shows that $d_{x2-y2}$ gradually shifts toward the Fermi level moving from the centre (e.g. Ti1) to intermediate (e.g. Ti2) to outer (e.g. Ti4) Ti atoms. However, the $d_{z2}$ orbital shows the opposite trend and moves towards higher energy. In the energy range of 3.0 to 3.5 eV, the $d_{z2}$ contribution increases moving from centre (e.g. Ti1) to intermediate (e.g. Ti2) to outer (e.g. Ti4) Ti atoms. The simulations reveal that this happens because the outer Ti cations (and also the Fe cations) are significantly displaced towards the $[Bi_2O_2]^{2+}$ interlayers, resulting in significant distortions to the $TiO_6$ octahedra and the out-of-plane/axial Ti-O distances. This atomic displacement along the *c*-axis direction of B6TFMO reduces the hybridisation interaction between the axial $d_{x2-y2}$ orbitals of Ti and the 2*p* orbitals of the oxygen atoms on the *a*-*b* plane, but increases the interaction between the axial $d_{z2}$ orbitals of Ti and one of the oxygen atoms along the *c*-axis direction. In addition, a similar pattern of shifting for the $d_{x2-y2}$ and $d_{z2}$ orbitals of the Ti atoms is observed moving from the outer to the intermediate perovskite layers in another model of B6TFMO, denoted Configuration *b*, as illustrated in **Figure 3.1 (a)** and **Appendix I Figure I.5**. These two models explore the role of different distributions of cations within the same composition. It should be noted that there are no Ti atoms present in the central perovskite layer of the Configuration: *b* therefore it cannot be used in the same way as Configuration: *a* for a direct comparison to the crystal-field splitting of Ti as observed by EELS in **Figure 3.2**. Nevertheless, the same anti-polar displacement of the intermediate and outer Ti atoms along the *c*-axis direction is observed, as depicted in **Appendix I Figure I.8**.

In particular, it is found that Ti/Fe/Mn *B*-site cations that are located either above or below the centre *B*-site cations of each perovskite block displace in the opposite direction along the *c*-axis, resulting in one short and one long Ti-O distance of 1.77 Å and 2.56 Å (see **Figure 3.3**) in the *c*-direction. This is because each block is sandwiched between two $[Bi_2O_2]^{2+}$ interlayers along the *c*-axis direction. Hence, for each five-layered perovskite block, there would be a net zero electric dipole moment along the *c*-axis direction if the horizontal mirror plane was allowed to persist. For the odd-layered Aurivillius phases, tilting of the $BO_6$ octahedra leads to loss of the mirror plane below the ferroelectric Curie temperature and a minor polarisation component along the *c*-axis is enabled [154], [160]. The principal net

electric polarisation component is created along the *b*-axis direction, originating from each Ti/Fe/Mn atom shifting from its centre position, resulting in alternative short and long metal oxygen bonds (see **Figure 3.3**) along the *b*-axis. The in-plane ferroelectric displacements are stabilised by the Jahn-Teller distortions. Note that different atomic and magnetic configurations of Fe, Mn, and Ti atoms having differing magnitudes of octahedral tilting as shown in **Appendix I Figure I.5** have been examined. The same anti-polar atomic displacements of the Ti cations irrespective of magnetic configuration and tilting were found, showing that the distortions are driven by the influence of the $[Bi_2O_2]^{2+}$ interlayers. Similar $d_{x2-y2}$ and $d_{z2}$ orbital shifting in each perovskite block for differing arrangements of the Ti, Fe and Mn cations within the structure was noted. Here it is proposed that the intrinsic orbital position shifting of Ti derived electronic states across the perovskite block, which arises from the atomic displacement and tetragonal distortion of Ti, is the primary origin of the shift in crystal field splitting (Δ) from the outer perovskite layer to the centre perovskite layer observed within the spatially resolved EELS data of B6TFMO. It is noteworthy that the relative intensity of the peaks in the L3-edge does not change significantly with the change in Δ, which might be expected based on the DOS associated with $d_{x2-y2}$ and $d_{z2}$ moving apart as indicated in the DFT results. However, the shift to higher energy of the $d_{z2}$ orbital is due to increased hybridization with the O2p. This will increase the DOS in this energy window and will also increase the transition matrix element, while the opposite effect will occur for the $d_{x2-y2}$ orbitals, meaning a marginal net effect on the peak intensities.

The impact of strain and tetragonal distortion imposed by the $[Bi_2O_2]^{2+}$ interlayer on the ferroelectric properties can be observed further through local polarisation mapping of the atomic-scale displacements within B6TFMO via quantification of high-resolution HAADF-STEM signals. As described earlier, the principle component of spontaneous polarisation in Aurivillius phase systems lies within the plane along the *b*-axis. Using the full HAADF-STEM image in **Appendix I Figure I.3 (a),** the average displacements of the *B*-site cations along the *b*-axis are calculated (**Appendix I Figure I.3 (b))** to be 0.199 ± 0.006 Å, 0.268 ± 0.009 Å and 0.243 ± 0.009 Å for the outer, intermediate and centre perovskite unit cells respectively. The DFT+U optimised structures in **Appendix I Figure I.4** demonstrate corresponding displacements along the *b*-direction. The difference on bond lengths between the alternative short and metal oxygen bonds along the in-plane direction reflects the atomic

displacement along the *b*-direction, and demonstrate the same trend. These in-plane displacement values are similar in magnitude to values calculated by Campanini *et al.* [158] on the *m* = 4, $Bi_5Ti_3Fe_2O_{15}$, where *B*-site cation displacement values along the in-plane, *b*-axis were up to ~ 0.25 Å.

Due to the breaking of the horizontal mirror plane within the odd layered Aurivillius systems (with retention of a two-fold rotation axis parallel to *a*), a minor out-of-plane polarisation component is allowed in conjunction with the major ferroelectric polarisation along the *b*-axis direction. This results in domains within *m* = 5 B6TFMO displaying either a net-up or net-down out-of-plane polarisation [162], [191]. The local polarisation component within the perovskite unit cells can be measured via quantification of the displacement of the *B*-site cation in the *c*-axis direction, the strength of which varies as a function of layer. As shown in the DFT calculations above, the *B*-site cations within the centre perovskite layer of the B6TFMO system are close to the centre of the pseudo-cubic perovskite unit cell along the *c*-axis direction, as compared with the *B*-site cations in the outer layers which are displaced away from the $[Bi_2O_2]^{2+}$ interface in an antipolar arrangement. From analysis of **Appendix I Figure I.3 (a)**, it was calculated that the average *B*-site cation displacements away from the centre of the unit cell along the *c*-axis direction are 0.426 ± 0.142 Å, 0.184 ± 0.095 Å and 0.054 ± 0.062 Å for the outer, intermediate and centre perovskite unit cells respectively. Similar displacements along the *c*-direction showing the same overall trend are observed from the DFT+U optimised structures (see **Appendix I Figure I.8**). Values for the out-of-plane displacement for the outer perovskite layer (0.426 Å) in *m* = 5 B6TFMO are comparable to that found for the perovskite layers next to the $[Bi_2O_2]^{2+}$ interfaces in other Aurivillius systems. Newnham *et al.* [154] reported out-of-plane *B*-site cations displacements in the layers next to $[Bi_2O_2]^{2+}$of 0.42 Å and 0.35 Å for the $Bi_3TiNbO_9$ (*m* = 2) and $Bi_4Ti_30_{12}$ (*m* = 3) systems, respectively. Atomic scale mapping of polar displacements reveals that polarisation is largest towards the outer perovskite cells, correlating with the increase in the local tetragonal distortion of the octahedral $TiO_6$ geometries.

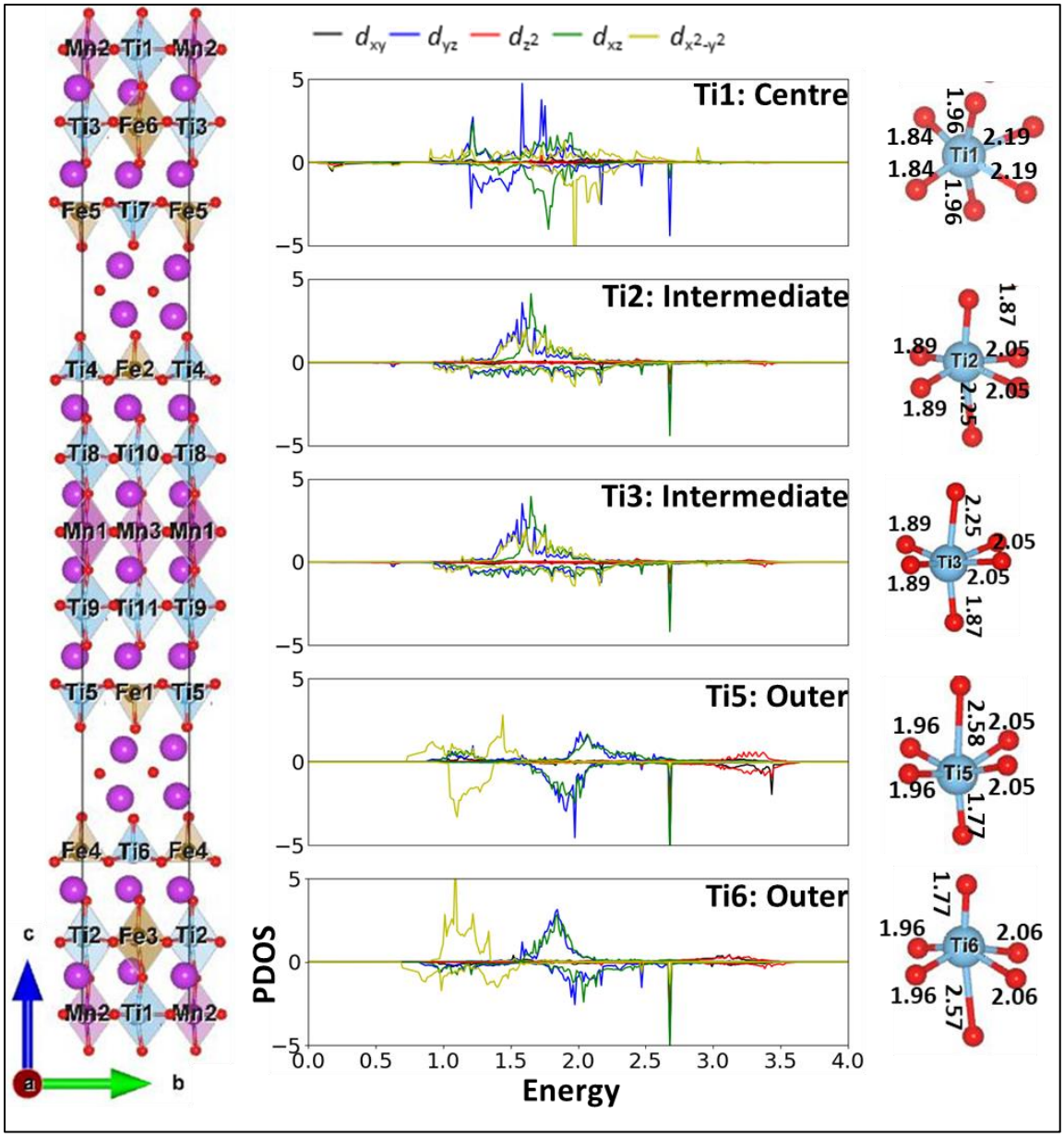


**Figure 3.3** The fully optimized structure (both lattice parameters and atomic positions) of $Bi_{24}Ti_{11}Fe_6Mn_3O_{72}$ (Configuration: *a*). The calculated lattice parameters for *a*, *b*, and *c* are 5.48 Å, 5.61 Å, and 51.03 Å, respectively, which are in good agreement with previous reports [162], [163], [192]. The Ti-O bond lengths are in Å units. (Right) All the Ti atoms are off-centre displaced along the negative *b*-axis, making alternative short and long Ti-O bonds, which facilitates an in-plane ferroelectric polarisation. Interestingly, in addition to the displacement along the *b*-direction, the Ti atoms also undergo displacement along the *c*-direction. However, if the horizontal mirror plane is allowed to persist, this displacement does not result in a net dipole moment, because the Ti atoms located above the central perovskite layer move upward, while those below the layer move downward. (Centre) The atom resolved PDOS are

shown for selected Ti atoms (see **Appendix I Figure I.4** for calculations for all Ti atoms), where positive (negative) PDOS represents an up (down) spin channel. The Fermi energy ($E_F$) is set at 0 eV. The configuration (left) is in a ferrimagnetic state with a net magnetic moment of 15.000 $\mu_B$ per unit cell, where Fe1, Fe2, Fe3, Fe4, Fe5, Fe6, Mn1, Mn2, and Mn3 atoms contribute -4.317 $\mu_B$, -4.317 $\mu_B$, 4.355 $\mu_B$, 4.318 $\mu_B$, 4.318 $\mu_B$, 4.355 $\mu_B$, 3.858 $\mu_B$, -2.919 $\mu_B$, and 3.846 $\mu_B$, respectively. The magnetic contribution from the other atoms is minor; for example the contribution from the Ti1-11 atoms is 0.045 $\mu_B$, 0.103 $\mu_B$, 0.103 $\mu_B$, -0.071 $\mu_B$, -0.071 $\mu_B$, 0.077 $\mu_B$, 0.077 $\mu_B$, 0.023 $\mu_B$, 0.023 $\mu_B$, 0.019 $\mu_B$, and 0.019 $\mu_B$, respectively. PDOS of all the Ti atoms and all the Ti-O bond lengths along *c*-direction are shown in **Appendix I Figure I.4** and **Figure I.8**, respectively.

### 3.3.3 Analysis of *$BO_6$* Octahedral Tilting at Differing Perovskite Layers within B6TFMO

Although it is well-established that functional electronic and magnetic properties are profoundly associated with octahedral tilting within perovskite systems [110], [272], [278]-[283], the nature of the *$BO_6$* octahedral tilt system and the full behaviour of the oxygen anions in the relatively new B6TFMO multiferroic system is hitherto unknown. It has been proposed [161], [299] that symmetry lowering in the Aurivillius phases is caused by tilting of the oxygen octahedra around the *a*-axis (tilt mode designated by the irreducible representation (*irrep*) notation $X_3^+$), rotations of the oxygen octahedra around the *c*-axis (i*rreps* $X_2^+, X_1^-$), (shown in **Appendix I Figure I.6**), and the polar cation motions along the *a*-axis (*irrep* $\Gamma_5^-$), which when coupled together contribute to a material's ferroelectric ground state. Goldschmidt's tolerance factor [135], $t = \frac{r_o + r_a}{\sqrt{2}(r_o + r_b)}$, where $r_o$, $r_a$ and $r_b$ are the ionic radii of the oxygen, *A*-site and *B*-site ions respectively, has been used to deduce that $t < 1$ would promote a perovskite system with an instability towards an octahedral tilting distortion [147], [156], [157]. This tolerance factor can also be applied to the Aurivillius phases, where octahedral tilting is commonly observed [150], [155], [156], [160], [161] due to divergences between the *A*-O and *B*-O interatomic distances.

Research on the *m* = 3 phase, $Bi_4Ti_3O_{12}$ (BTO), has showed the importance of analysing the contributions of the light oxygen atoms to denoting the symmetry and space group of the material. In the 1990s it was proposed that above the Curie temperature ($T_c$) ~675 $^oC$, BTO

adopts the aristotype *I*4/*mmm* structure, while at RT a subgroup of *Fmmm*: *B*1*a*1 is present [300]–[302]. However, theoretical calculations found no triggering mechanism to support a single transition from the *I*4/*mmm* to *B*1*a*1 space group [299], leading researchers to revisit the BTO system in 2019 [155], where an intermediate paraelectric phase above $T_c$ was discovered corresponding to the *irrep* $X_2^+$ mode, *P*4*/mbm* (**Appendix I Figure I.6**). The BTO case highlights the significance of the oxygen octahedral tilting on the resultant symmetry and polar properties of the Aurivillius structure and demonstrates that visualisation of the light atoms is critical for correct structural characterisation of a material. It has also been found for the higher phase *m* = 4 systems [150], $Bi_5Ti_3FeO_{15}$ and $SrBi_4Ti_4O_{15}$ that at RT the *A*2$_1$*am* space group is present, which allows movement of the oxygen atoms and *B*O$_6$ octahedral tilting, rather than the once proposed *Fmm*2 space group [303]. Analysis on the *m* = 3 and *m* = 4 systems shows the advantages neutron diffraction has over X-ray diffraction, as in these systems the additional symmetry lowering arises from displacements of the oxygen atoms via octahedral tilting, which do not give rise to strong reflections within X-ray diffraction patterns.

Of the five-layered Aurivillius phases that have been investigated, one of the most compositionally similar materials to B6TFMO is $Bi_6Ti_3Fe_2O_{18}$, where García-Guaderrama *et al.* [258] deduced the space group to be *F*2*mm* via synchrotron X-ray powder diffraction, which did not detect tilting of the $TiO_6$ octahedra. However, samples of the five layered Aurivillius system $A_2Bi_4Ti_5O_{18}$, substituted by Ca, Sr, Pb or Ba at the *A*-sites, were refined to the orthorhombic *B*2*eb* space group in a neutron diffraction study by Ismunandar *et al.* [156]. The tolerance factors were calculated to be 0.97, 1.0, 1.02 and 1.06 for Ca, Sr, Pb or Ba substituted structures, respectively, with an increase in the degree of octahedral tilting corresponding with a decrease in the tolerance factor, as shown in **Appendix I Table I.2**. The tolerance factor value of B6TFMO is 0.90, where $r_b$ was calcultated using a 3:1.5:0.5 ratio for $Ti^{4+}$:$Fe^{3+}$:$Mn^{3+}$. This tolerance factor of < 1 indicates that octahedral tilting within B6TFMO is favourable.

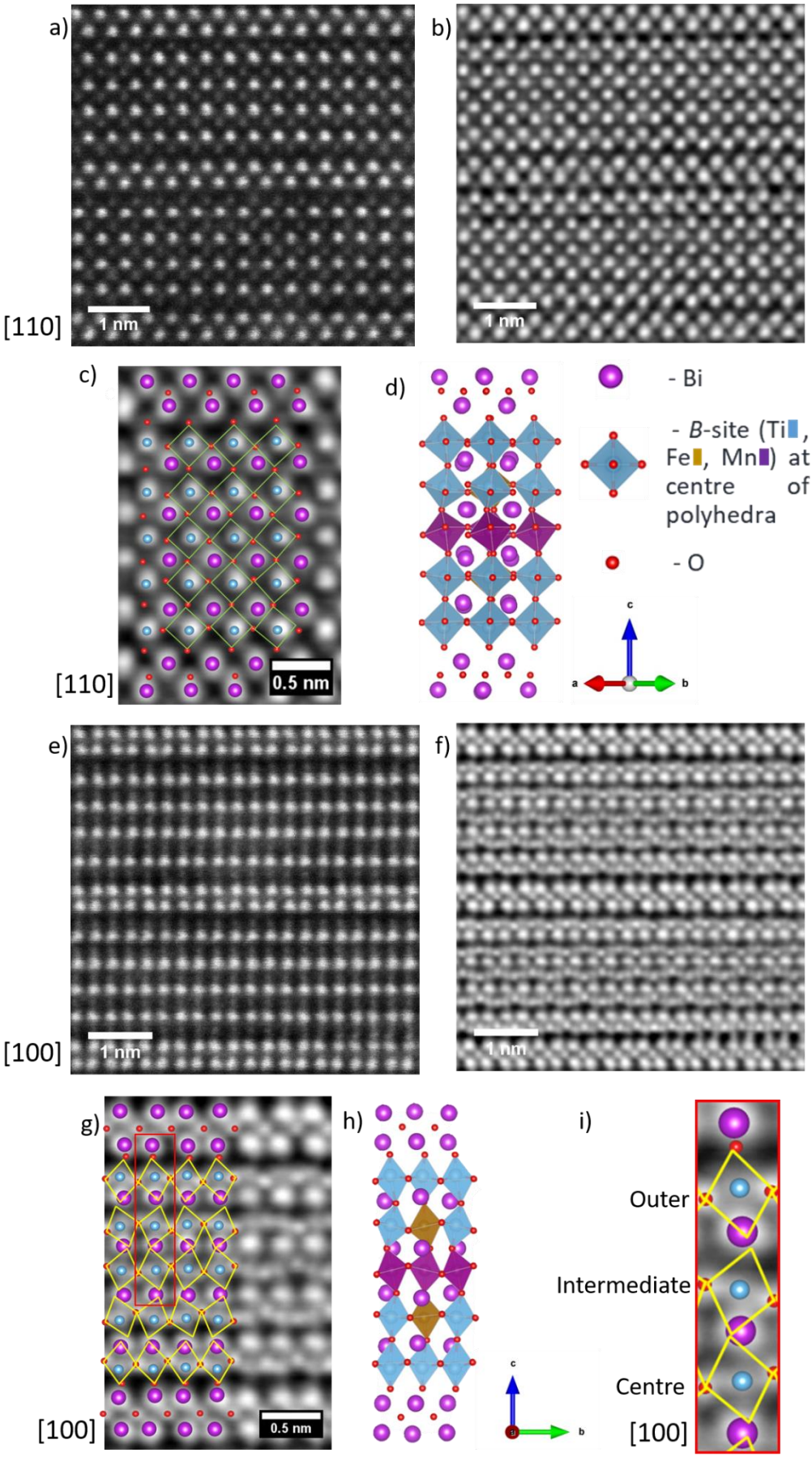
a)
b)
[110]
1 nm
1 nm
c)
d)
- Bi
- B-site (Ti, Fe, Mn) at centre of polyhedra
- O
[110]
0.5 nm
c
a
b
e)
f)
[100]
1 nm
1 nm
g)
h)
i)
Outer
Intermediate
Centre
[100]
0.5 nm
c
b

**Figure 3.4** a) HAADF-STEM and b) iDPC-STEM images of B6TFMO projected down [110]. c) Enlarged region where identifiers for atoms and polyhedra are overlaid, d) comparison of the five layered Aurivillius phase calculated from DFT+U in Configuration: *b* where not all the outer and intermediate perovskite cells have the same arrangement of *B*-site cations. This half-unit cell corresponds to the atomic arrangement of Configuration: *b* (i) shown in **Appendix I Figure I.7 (c)** when projected down [100] (see **Appendix I Figure I.5** for the whole unit cell and **Appendix I Figure I.8 and Figure I.9** for the bond lengths, angles, and atomic displacement along the *c*-axis direction). Significant tilting is observed for the octahedra within this structure, however tilting is mostly hidden in the [110] projection as the positions of alternating oxygen atoms overlap in the [110] view. e) HAADF-STEM and f) iDPC-STEM images of B6TFMO projected down [100]. g) Enlarged region where identifiers for atoms and polyhedra are overlaid onto the image. h) Comparison to the DFT structure corresponding to arrangement (i) in **Appendix I Figure I.7 (c)** and to the centre of Configuration: *b* in **Appendix I Figure I.8 and Figure I.9**, projected down [100]. This image illustrates why octahedral tilting is more clearly observed in the iDPC-STEM images when projected down [100] compared with down [110]. i) An enlarged region from g) showing ''outer'', ''intermediate'' and ''centre'' perovskite octahedra. The enlarged region within the red inset displays the increased tilting of the octahedra moving from the ''outer'' to ''centre'' perovskite layer.

iDPC-STEM, can be used for the direct atomic resolution of light atoms at sub-Å resolution [244]. The technique allows for the observation of low Z-elements, such as oxygen, using a bright contrast and dark background with a higher signal to noise ratio when compared to competing techniques such as annular bright field STEM (ABF-STEM) [245]. Due to the *2D* nature of STEM imaging a definitive space group cannot be determined for B6TFMO using this characterisation technique. However, information can be gained about the $BO_6$ tilting by imaging the system in multiple crystal orientations. In this work iDPC-STEM imaging is used to visualise the light oxygen atoms as a function of layer within the Aurivillius phase and gain a greater understanding of their bonding environments within the perovskite layers.

In **Figure 3.4**, iDPC-STEM measures the oxygen anions in the [110] projection (**Figure 3.4 (a-c))** and down the [100] projection (**Figure 3.4 (e-g)**). Using the oxygen atoms the impact of the $[Bi_2O_2]^{2+}$ interface on displacement of the *B*-site cations can be observed. The oxygen

atoms are displaced away from the apex bond between the perovskite layer and the $[Bi_2O_2]^{2+}$ layer as seen in **Figure 3.4 (i)** [154]. This displacement is lessened moving towards the central perovskite layer, corresponding with the DFT results in **Figure 3.3**, **Appendix I Figure I.4** and **Figure I.8**. Viewing the structure through the [100] projection confirms that there is cooperative $BO_6$ octahedral tilting within the B6TFMO structure. As shown in **Figure 3.4 (d, h)**, for DFT calculated B6TFMO Aurivillius phases demonstrating octahedral tilting, the tilted nature of the oxygen atoms in the equatorial plane is hidden in *2D* imaging down the [110] direction, due to the alternating nature of the octahedral tilting parallel to *b*. This is in contrast to the [100] projection where the tilting of the oxygen can be clearly seen. From analysis of the oxygen positions and comparing to the literature, it appears as though a tilt mode similar to the *irrep* $X_3^+$ (**Appendix I Figure I.6**), which accounts for out-of-plane (parallel to *c*) anti-phase tilting of the octahedra with respect to each other in the *a*-*b* plane, is present. Within the DFT calculations and *m* = 5 systems shown in **Appendix I Figure I.7**, it can be observed that the degree of tilting increases moving towards the central perovskite layer. The average degree of the octahedral tilting is approximated from **Figure 3.4 (g), (i)** and **Appendix I Figure I.7**, with values displayed in **Appendix I Table I.2**. The increasing degree of the tilting through the layers towards the centre in B6TFMO suggests that there is a rotation of the inner octahedral layers around *c*, possibly similar to the *irrep* $X_2^-$ mode, at the centre as well as the *irrep* $X_3^+$ tilt mode (**Appendix I Figure I.6**). The B6TFMO system demonstrates a relatively large tilting of the oxygen atoms, with approximate tilt angles for the octahedra along <010> being $\pm 5$ ° for outer, $\pm 11$ ° for intermediate and $\pm 16$ ° for centre layers. This complex octahedral tilting, with variable tilt amplitudes across the perovskite layers, competes with the extent of tetragonal distortion of the $TiO_6$ octahedra. The more tetragonally distorted outer $TiO_6$ octahedra next to the $[Bi_2O_2]^{2+}$ layers rotate the least. Significantly, tetragonal distortion is lowest and the degree of octahedral tilting is highest at the centre layers of B6TFMO, where the magnetic cations preferentially partition.

The same method for approximating the out-of-plane tilt for the structures simulated via DFT+U calculations was applied to the experimental data in **Figure 3.4 (g)** and (**Appendix I Figure I.7 (a)**). There are two different trends between Configuration: *a* and Configuration: *b* (**Appendix I Table I.2**). Configuration: *a* does not show the same trend of increased tilt angle towards the centre perovskite layers that is observed for the experimental iDPC data and the neutron diffraction data from Ismunander *et al.* [156]. Analysis indicates comparatively minor

out-of-plane tilting along <010>. The octahedra do not tilt along the *b*-axis in an alternating pattern in Configuration: *a* as indicative of the *irrep* $X_3^+$ tilt mode (**Appendix I Figure I.6**), which differs to the other data and structures examined (**Appendix I Table I.2**). Configuration: *b* however shows evidence of tilting similar to the *irrep* $X_3^+$ tilt mode and a more similar trend to the experimental data, where the degree of tilting appears to increase moving from the outer Ti atoms to the centre Ti atoms. For example, take the five perovskite layers shown in column 1 of arrangement (i) in **Appendix I Figure I.7 (c)** (corresponding to the centre of Configuration: *b* in **Appendix I Figure I.8** and **Figure I.9**). Moving down the *c*-axis from the top $[Bi_2O_2]^{2+}$ layer to the layers below, the out-of-plane tilt angle changes from: -6 ° for outer (top), +13 ° for intermediate (top), -14 ° for centre, +6 ° for intermediate (bottom) and +2 ° for outer (bottom). Due to the changing arrangement of the Ti, Fe and Mn cations in Configuration: *b*, the measured tilt values vary depending on the arrangement of the cations. The range of tilt values for the outer, intermediate and centre octahedra is $\pm$2 to 6 °, $\pm$1 to 13 ° and $\pm$6 to 14 ° respectively. It is clear for all arrangements of atoms within Configuration: *b* that the magnitude of tilt angle at the outer $BO_6$ octahedra is always smaller than that at the centre $BO_6$ octahedra and shows the same trend to the tilting seen in the experimental data, **Appendix I Table I.2**. Some of the outer and intermediate tilt angles in Configuration: *b* are similar if not greater than those observed for the $A_2Bi_4Ti_5O_{18}$ *m* = 5 Aurivillius system. Of the compositions within this system previously characterised [156] by neutron diffraction, $Ca_2Bi_4Ti_3O_{18}$ presents the highest orthorhombic distortion ( *t* = 0.97), and displays tilt angles of $\pm$11 ° for centre, $\pm$10 ° for intermediate and $\pm$7 ° for outer perovskite octahedra as shown in **Appendix I Table I.2**. The slightly larger tilting observed in the experimental iDPC data and Configuration: *b* is consistent with the tolerance factor for the B6TFMO composition (*t* = 0.90), which is lower than that of $Ca_2Bi_4Ti_3O_{18}$. Moreover, studies in this work indicate that it is necessary for the B6TFMO structure to adapt to accommodate differing arrangements of *B*-site atoms, which manifests in different magnitudes of octahedral tilting observed for different B6TFMO configurations. In Configuration: *b* there are regions where $FeO_6$ and $MnO_6$ octahedra are next to one another in a perovskite layer (e.g. **Appendix I Figure I.7 (c)**), while in Configuration: *a*, $FeO_6$ and $MnO_6$ octahedra are further apart (e.g. **Appendix I Figure I.7 (b)**). It appears from Configuration: *b,* that when Fe and Mn are next to each other in the structure, a larger octahedral tilting occurs through the perovskite layers. This is possibly as a result of the structure adapting to accommodate the different metal-oxygen distances in Ti-

O, Fe-O and Mn-O. For example, the longest Ti6-O, Fe2-O, and Mn1-O bonds along the *c*-axis direction in the configuration *b* are 2.50 Å, 2.52 Å, and 1.99 Å, respectively (**Appendix I Figure I.8** shows how the bond lengths vary along the *c*-axis direction in the both configurations). Consistent with previous literature [156], [160] on the Aurivillius phases, calculations herein show that octahedral tilting facilitates minimisation of the electrostatic potential and stabilisation of the material.

Along with displaying significantly different magnitudes of octahedral tilt angles, differing deviations in bond angle from 180 ° along the *c*-axis direction are observed for the two configurations from DFT+U calculations. The positions of all oxygen and *B*-site atoms can be accurately measured from the DFT simulated structures, where **Appendix I Figure I.8** displays bond angles at each *B*-site cation between two *B*-O bonds and **Appendix I Figure I.9** displays bond angles at each oxygen (O)-site between two *B*-O bonds. However, given that Configuration: *a* and Configuration: *b* display similar anti-polar atomic displacements of Ti cations and similar $d_{x2-y2}$ and $d_{z2}$ orbital shifting within the atom resolved PDOS data (**Figure 3.3**, **Appendix I Figure I.4 and Figure I.5**), it is proposed that octahedral tilting does not have a significant effect on crystal field splitting. The atomic displacement and tetragonal distortion of Ti is the principal driving factor leading to the changes observed in the $L_3$ $e_g$ EELS peak going from outer to centre perovskite layer.

Since the highest degree of octahedral tilting is towards the central layers where the magnetic cations preferentially partition, it is interesting to consider the implications of octahedral tilting on the magnetic properties of B6TFMO. The calculated net magnetic moment for Configuration: *b* (33.892 $\mu_B$ per unit cell), which demonstrates larger tilt amplitudes at the central layer, is more than two times higher than that calculated for Configuration: *a* (15.000 $\mu_B$ per unit cell). However, it is essential to note that Configuration: *a* and Configuration: *b* exhibit distinct distributions of *B*-site cations, and as established from previous studies [192], magnetization values are highly dependent on cation site order.. From these examples, it is not possible to deconvolute the individual contributions of octahedral tilting and cation site order to the resultant magnetic moment. While octahedral tilting itself may not be a driver of magnetism in B6TFMO, it appears that tilting of the perovskites is necessary to allow the magnetic iron and manganese cations to locate next to each other within the centre perovskite layers. It follows that perovskite octahedral tilting could be a

necessary requirement to enable long-range magnetic interactions and subsequent multiferroic behaviour in B6TFMO.

## 3.4 Conclusions

The naturally layered B6TFMO material displaying room temperature multiferroic properties and exotic topological features [162], [163], [192], shows potential for use in revolutionary nanoelectronic and spintronic applications. To facilitate an enhanced understanding of the mechanisms driving multiferroic behaviour which are required for applications, in this work the influence of local symmetry lowering distortions and octahedral tilting on the functional polar and magnetic properties has been investigated. Atomic resolution electron microscopy in conjunction with first principles calculations to correlate fundamental electronic structure with local chemical bonding environments within B6TFMO has been presented.

Spatially-resolved HAADF-STEM EELS detected discrete changes in the crystal field of the $Ti^{4+}$ cations, with $e_g$-$t_{2g}$ splitting, $\Delta$, increasing from the outer to the centre perovskite layers of the structure. Density functional theory (DFT) calculations with Hubbard U corrections, of the atom resolved projected density of states shows that the distortion of the perovskite unit cells, imparted by their proximity to the $[Bi_2O_2]^{2+}$, is the main factor affecting the $e_g$ energy levels and changes to crystal field splitting. Atomic-resolution HAADF-STEM imaging confirms anti-polar atomic displacements of the Ti cations due to the influence of the $[Bi_2O_2]^{2+}$ interlayers and demonstrates that polarisation is largest towards the outer perovskite cells, which is coupled with the strong increase in tetragonal distortion of the octahedral $TiO_6$ geometries in these outer layers.

HAADF-iDPC imaging and DFT calculations reveal complex cooperative tilting of the $BO_6$ perovskite octahedra which is in competition with the extent of tetragonal distortion across the perovskite layers. Tetragonal distortion is lowest and the degree of octahedral tilting is greatest at the centre layers of B6TFMO, where the concentration of magnetic cations is highest. Theoretical calculations show that changes in the cooperative octahedral tilting through the layers aids in minimisation of the electrostatic potential and stabilisation of the material. The impact on the splitting $\Delta$ is independent of the distribution of tilt angles

and the magnetisation in the supercell used showing that this phenomenon is driven by the introduction of tetragonal distortions at the fluorite-perovskite interface. Observations, from both iDPC experiments and DFT simulations, demonstrating that the perovskite octahedra are required to tilt more at the central layers in order to accommodate magnetic cations close to each other at the centre indicate that octahedral tilting might be an important enabler of long-range magnetic interactions and resultant multiferroic behaviour in B6TFMO. These results for a naturally layered material show that engineering of interfaces in hetrostructures is a promising way to control the ferroelectric behaviour of potential multiferroic materials.

# 4 Growth of $Bi_6Ti_3Fe_{1.5}Ti_{0.5}O_{18}$ Thin Films on Vicinal Sapphire Substrates to Promote Sub-unit Cell Defects

In this chapter, all research is the work of the author, with the exception of the following contributions from collaborators: M. Schmidt (Tyndall-UCC) prepared cross-section lamella of the samples. M. Conroy (Imperial College London) and N. Bagués (Ohio University) carried out scanning transmission electron microscopy and aided in the interpretation of the analysis. L. Keeney (Tyndall-UCC) acquired the atomic force microscopy images using the Bruker Dimension Icon tool. J. Alaria (University of Liverpool) aided in the acquisition of the X-ray diffraction data using the Rigaku Smartlab instrument at The University of Liverpool, which was operated remotely by myself (L. Colfer). J. Alaria aided in the interpretation of the X-ray diffraction analysis.

## 4.1 Introduction

Room temperature multiferroics with coupled ferroelectricity and ferromagnetism have exciting applications in future memory storage technologies such as domain wall [304]–[306] and magnetoelectric spin orbit logic devices [48], [264]. Aurivillius phase $Bi_6Ti_3Fe_{1.5}Mn_{0.5}O_{18}$ (B6TFMO) is a rare example of a room temperature (RT) magnetoelectric multiferroic that has been successfully synthesised through both chemical solution deposition (CSD) [162] and direct liquid injection chemical vapour deposition (DLI-CVD) [286] methods on *c*-*m* plane (0.2 °) sapphire substrates. Aurivillius phase systems are naturally layered structures having a general formula $(Bi_2O_2)(A_{m-1}B_mO_{3m+1})$, where dielectric bismuth oxide $(Bi_2O_2)^{2+}$ fluorite-type layers are interleaved with *m* numbers of ferroelectric perovskite-type units. B6TFMO is an example of one such layered system where $m = 5$. Whereas the large unit cell (*c*-axis lattice parameter = 49.3 Å) and flexible nature of the Aurivillius phase structure is beneficial for allowing B6TFMO to maintain its ferroelectric properties while also accommodating magnetic cations such as Mn/Fe, the resulting films are also prone to structural defects. As with other layered materials having high structural anisotropy such as the Ruddlesden-Popper [54], Dion-Jacobson [55], [56] and layered cuprate [307] phases, out-of-phase boundary (OPB) defects, intergrowths and stacking faults are a common occurrence and can significantly impact material properties in thin films [165], [166]. Local strain and electrostatic changes induced

by structural defects have been observed to affect the physical properties within many material systems. At anti-phase boundary (APB) defects the in $PbZrO_3$, the antiferrroelectric arrangement of dipole moments is broken, with the new arrangement resulting in a local net ferroelectric behaviour at the APB defect [185]. These defects can also create favourable conditions for domain switching as seen in the $BiFeO_3$ system [184] and aid in the formation of ferroelectric domains. For example, when the Ruddlesden-Popper phase $Ca_{3-x}Sr_xTi_2O_7$ is doped with Sr ions, there is an increase in the presence of OPB defects, which in turn increases the number of charged domain boundaries within the material [187]. In magnetic systems such as $Fe_3O_4$, the density of APB defects has been observed to have a negative impact on thin films. The strong antiferromagnetic interactions across the boundaries degrade the electronic and magnetic properties of the thin films [188], [189]. Recent studies on the B6TFMO system [192] have demonstrated that disruptions to the Aurivillius phase lattice by OPB defects and stacking-faults have a marked influence on the internal elastic strain and electrostatic energy gradients within the structure. These defects have the positive impact of increasing the extent of magnetic cation partitioning towards the central layer in B6TFMO, thereby facilitating elevated magnetic ion interactions**.** Furthermore, OPB defects facilitate the formation of extraordinary polarisation profiles such as nominally charged domain walls and unusual polar vortex domain wall topologies. Since charged domain walls can be created, annihilated or moved on demand by applying simple voltage pulses, they are an emerging research focus in nano-electronics and domain wall devices. Owing to the highly anisotropic nature of ferroelectrics, the internal characteristic length scales of polar topological structures are much smaller (~4 to 10 nm) than ferromagnets (~10 to 100 nm), making them ideally suited to ultra-high density, energy efficient memory devices [88], [91], [97]. In addition to energy-efficient data-storage capabilities, these recent discoveries of defect-driven polar topology formation [192] demonstrate the wider technological potential of multiferroic B6TFMO.

Fascinatingly, these topologies are observed naturally in multiferroic B6TFMO without the need for an artificial interface and in the absence of external strain engineering. However, the drawback of uncontrolled defect propagation means that the type and density of these defects can vary considerably from sample to sample and from grain to grain within samples. Defect density can even vary from region-to-region within the same grain. It is therefore

pertinent to devise strategies to regulate and tailor the density of structural defects to control and enhance the associated emergent properties. In this work, B6TFMO thin films have been deposited on mis-cut vicinal sapphire substrates having a slightly off-axis substrate cut (0.2 $^{o}$ to 10 $^{o}$) in order to deliberately encourage structural defect formation within the growing layer during DLI-CVD synthesis.

## 4.2 Methods

Aurivillius phase thin films with a nominal stoichiometry of $Bi_6Ti_{3.0}Fe_{1.5}Mn_{0.5}O_{18}$ were synthesised by DLI-CVD via a horizontal flow AIXTRON AIX 200/4FE AVD (atomic vapour deposition) system [284], [285]. The films were deposited using a 22 % bismuth excess [286], [287] in order to mitigate the loss of volatile bismuth [288] during the two-step deposition and crystallisation process [286]. Sapphire substrates (cleaned with isopropyl alcohol followed by deionised water and dried using $N_2$ gas) with varied vicinal surfaces (mis-cut angles of 0.2 °, 0.5 ° and 10 °) were utilised for this study. For the deposition step (Step One), the substrates were loaded together into the reactor chamber during the same growth run where the B6TFMO thin films were deposited. Therefore, the films discussed were synthesised under the exact same growth conditions and the underlying substrate was the only varying factor. The 0.100 mol $dm^{-3}$ bismuth, iron and titanium precursors in toluene solution, $Bi(thd)_3$, $Fe(thd)_3$ and $Ti(O\text{-}iPr)_2(thd)_2$ (where thd = 2,2,6,6- tetramethyl 3,5-heptanedionate and O-iPr = isopropoxide), were purchased from Epivalence Ltd. The 0.025 mol $dm^{-3}$ manganese precursor was prepared by dissolving $Mn(thd)_3$ (99 %, STREM chemicals) in anhydrous toluene (99.8 %, Sigma-Aldrich) under $N_2$ in a glovebox. The sapphire substrates were loaded into the reactor chamber set at a pressure of 10 mbar while the temperature of the rotating susceptor-heated sample holder was set to 630 °C. These conditions were maintained for the entirety of the deposition process. The low vapour pressure precursors were then injected using nitrogen pulses into the Trijet Vaporizer of the DLI-CVD system, where they entered a reactor growth chamber via lines maintained at 220 °C. Precursors were mixed with reactive $O_2$ gas during the growth run. A total gas flow of 3000 sccm (standard cubic centimetres per minute) was maintained in the growth chamber comprised $O_2$ run gas and $N_2$ carrier gas where the $O_2$ flow was 1000 sccm. The precursor volumes were controlled electronically by setting the opening time for each injection to be between 1.6 and 10.9 ms, depending on the relevant precursor. A continuous injection mode was employed where the

injections pulsed at a frequency of 1 Hz. 800 injections of each precursor were pulsed and the net volumetric precursor injection ratios were approximately 7.4 : 3.0 : 1.5 : 0.5 for $Bi(thd)_3$, $Ti(O\text{-}iPr)2(thd)_2$, $Mn(thd)_3$, and $Fe(thd)_3$, respectively over the duration of the growth run. After thin film deposition via DLI-CVD in Step One, the samples were post-annealed in atmosphere for 1 hr at 850 °C (Step Two) in order to produce crystalline Aurivillius phase films. The thicknesses of the subsequent B6TFMO films (as measured by STEM) were approximately 94 nm, 112 nm and 94 nm on the 0.2 °, 0.5 ° and 10 ° mis-cut sapphire substrates respectively.

Atomic Force Microscopy (AFM) of the bare sapphire substrates was carried out in order to obtain topographical profiles of the surface steps. A commercial Bruker Dimension Icon in PeakForce Tapping mode (with Bruker SCANASYST-AIR probes, Al reflex coated, 2 nm tip radius, 70 kHz resonant frequency), was used. Further AFM and Piezoresponse Force Microscopy (PFM) was performed using an MFP-3D$^{TM}$ Asylum Research instrument. AFM on this instrument was carried out using AC mode with Olympus AC240TS probes (Al reflex coated, 15 nm tip radius, 70 kHz resonant frequency). PFM was conducted in lateral (LPFM) and vertical (VPFM) Dual AC Resonance Tracking (DART-PFM) mode [234]. The DART-PFM mode was used to boost the vertical piezo signal. This method of measuring boosts the measured signal while reducing instrumental crosstalk. Drive amplitudes of 1 to 2 $V_{AC}$ and 2 to 3 $V_{AC}$ were used for measurement of the piezoresponse in LPFM and VPFM modes respectively at centre drive frequencies in the range of 742 to 792 kHz for the LPFM measurements and 258 to 282 kHz for the VPFM measurements. A frequency width of 10 kHz was used for all the measurements. The probes used were Olympus AC240TM-R3 electrilevers (Ti/Pt coated silicon probes, Al reflex coated, 25 nm tip radius, 70 kHz resonant frequency)).

X-ray diffraction (XRD) measurements were performed using an X'pert Diffractometer (Cu Kα radiation λ = 0.1541876 nm) (45 kV, 40 mA). The typical 2θ scan range was from 5 ° to 40 ° and a step size of 0.005 °. In order to assess phase purity and crystalline quality of the samples, rocking curve analysis was performed remotely from Tyndall-UCC through a collaboration with the University of Liverpool, where the sample was tilted by varying ω at a fixed 2θ angle. These curves were captured using a Rigaku Smartlab with a 9 kW Cu rotating anode, a 2-bounce Ge monochromator, and a Hypix detector. In this chapter, the XRD diffraction patterns were indexed using reference data from García-Guaderrama *et al.* [258] for the $m$ = 5 phase.

Simulated XRD patterns of different Aurivillius phase structures were computed using the FORTRAN based code DIFFaX (Diffracted Intensities From Faulted Xtals), designed by Treacy *et al.* [256]. This software allows the user to create a "read file" of a structure where the material is not viewed by its unit cell, but rather viewed as a series of stacked layers interconnected by stacking vectors (transitions) where the "*c*" crystallographic axis is defined along the layered stacking direction. DIFFaX can then produce a simulated diffraction pattern by computing the diffraction intensities layer by layer. DIFFax exploits the recurring patterns found in randomised stacking sequences to compute the average interference wave-function scattered from each layer type occurring in a faulted crystal [256]. Reference data of atomic positions from previous experimental measurements by Hervoches *et al.* [150] (powder neutron diffraction) for the $m = 4$ phase, by García-Guaderrama *et al.* [258] (powder X-ray diffraction) for the $m = 5$ phase and by Krzhizhanovskaya *et al.* [259] (powder X-ray diffraction) for the $m = 6$ Aurivillius phase were used in order to build the DIFFaX files. Monochromatic X-ray radiation was used where the X-ray value used in the structure file was 1.5406 nm.

A FEI DualBeam Helios NanoLab 600i Focused Ion Beam instrument was used to prepare the lamella cross sections of the B6TFMO films. Transition electron microscopy (TEM) cross sections were prepared by depositing C and Pt as electron-beam induced layers, followed by an ion-beam induced C layer for protection. The lamellas were thinned at 0.28 nA/30 kV with final polish at 47 pA/5 kV. High angle annular dark field (HAADF)-scanning transmission electron microscopy (STEM) imaging were performed using a probe-corrected Thermo Fisher Scientific Themis Z operated at 200 kV with a convergence semi-angle of 18 µm at Ohio State University. Further STEM analysis was carried out using a Thermo-Fisher Scientific double tilt STEM holder in the Thermo-Fisher Scientific FEI double aberration-corrected monochromated Titan Themis Z at the University of Limerick, where the microscope was operated at 300 kV.

## 4.3 Results and Discussion

### 4.3.1 Simulations of X-ray Diffraction Patterns from Non-periodic Layered Aurivillius Structures

As previously described in **Section 1.6.3**, when OPB defects are incorporated into the B6TFMO layered structure, often there will be regions where there is a disruption of the usual five perovskite layer stacking sequence, as shown in **Figure 4.1**. This is due to the fact that an OPB defect (represented by areas within the yellow circle in the schematic in **Figure 4.1**) occurs at a point where the unit cell misaligns by a fraction of the *c*-axis lattice parameter. Thus, in regions close to OPB defects, the B6TFMO material can commonly have stacking-fault regions. Here there are four or six perovskite layers between the $[Bi_2O_2]^{2+}$ interlayers, before another OPB defect occurs bringing the area back to the $m = 5$ phase, as seen inside the red circle within the schematic and within the orange inset of the HAADF-STEM image in **Figure 4.1**. From previous work on the $m = 3$ and $m = 4$ Aurivillius phases by Deepak *et al*. [165], [308], it has been observed that such disruptions to periodicity in the Aurivillius phases leads to scattering of X-rays and resultant peak broadening. Increased levels of XRD peak broadening and splitting is associated with films possessing high levels of structural defects [166]. As a key goal of this study is to assess whether growth on vicinal substrates can deliberately promote structural defects within B6TFMO, DIFFaX simulation software was used in order to assist with the interpretation of XRD data of $m = 5$ Aurivillius phase thin films which may have high a density of structural defects and associated stacking faults. DIFFaX is a FORTRAN based code designed by Treacy *et al.* [256] (as discussed in **Section 2.4.2**) that computes diffraction from layered crystals that contain stacking faults. Stacking is treated recursively by DIFFaX meaning that diffraction intensities are calculated by taking into account that the scattered wave function from a crystal centred on a particular layer is equivalent to the scattering contribution from that layer plus the scattered wavefunction from the displaced crystal centred at the next layer. Within this work it is used to simulate Aurivillius phase structures

with structural intergrowths of $m = 4$ and/or $m = 6$ stacking faults within an overall $m = 5$ phase film.

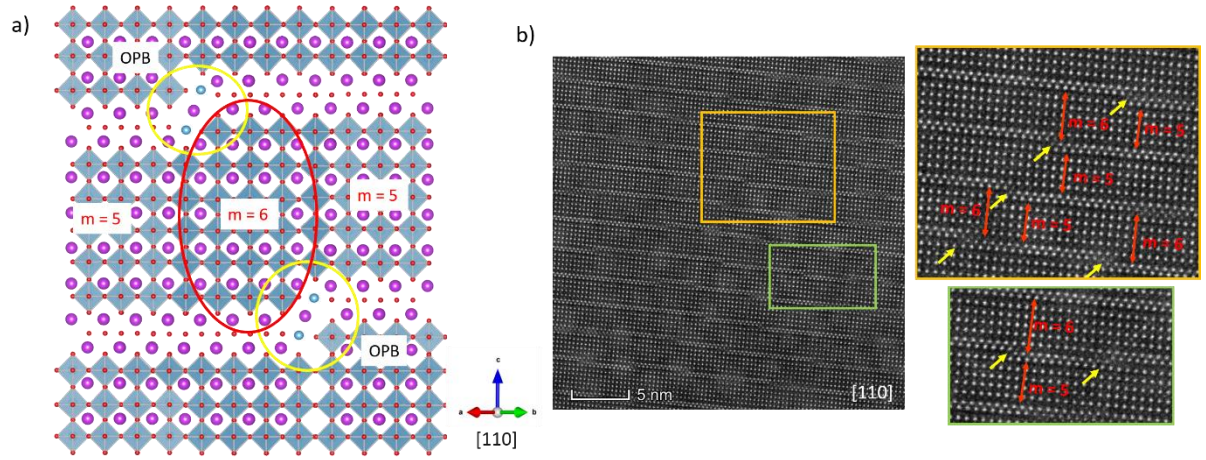


**Figure 4.1** Left: Schematic of OPB defects (yellow circles) and a resulting $m = 6$ intergrowth (red circle). Middle: HAADF-STEM image of regions in a B6TFMO film demonstrating OPBs and associated stacking-faults. Right: Enlarged HAADF-STEM images of the regions marked by orange and green rectangles in the middle image. These images show OPB defects (yellow arrows) propagating through the B6TFMO thin film grown on sapphire substrates with a 0.5 ° mis-cut angle. These images demonstrate how the number of perovskite layers present between the $[Bi_2O_2]^{2+}$ can vary in the proximity of OPB defects. For example here $m = 6$ intergrowths can be observed directly at stacking fault regions associated with the OPB defect (region within the orange rectangle) and at wider stacking fault regions associated with the nearby presence of OPB defects (region within the green rectangle).

To validate the accuracy of the simulated patterns built using DIFFaX, initially structure files for XRD patterns of phase pure Aurivillius materials were simulated and compared to the patterns projected from experimentally obtained neutron diffraction data through VESTA visualisation software [296]. In order to permit for instrumental broadening within the DIFFaX simulated XRD patterns, a 0.18 ° Gaussian function was applied within the DIFFaX structure file. Following this, it was determined that the FWHM (full width at half maximum) value of the DIFFaX simulated (00$\underline{12}$) reflection approximately matched the VESTA projected experimental (00$\underline{12}$) reflection value, where the FWHM value was 0.16876 ± 0.00016 and 0.16871 ± 0.00143 for the DIFFaX simulated and experimental data respectively. Allocating for instrumental broadening removed the large amplitude of the Laue oscillations (a product

of coherently diffracting unit cells and a structure's *c*-axis lattice parameter), which are commonly much larger in simulated XRD patterns in comparison to experimentally acquired data [309]. **Appendix II Figure II.1** shows a DIFFaX simulated XRD pattern of the (00*l*) reflections for the *m* = 4, 5 and 6 layered Aurivillius phases with a thickness of 24 unit cells (~120 nm). **Appendix II Table II.1** demonstrates that the 2θ positions of the reflections for the *m* = 5 Aurivillius phase simulated via the constructed DIFFaX structure files are exactly the same as the positions obtained using VESTA to project the corresponding reflections from experimental neutron or X-ray diffraction data [150], [258], [259], [296]. The intensities of the reflections from both DIFFaX simulation and VESTA projection methods also show the same overall trend, for example using both methods the (00$\underline{12}$) reflection for the *m* = 5 phase is the most intense. This intensity is determined by the predicted structure factor ($F_{hkl}$) for the material, which describes the amplitude and phase of the X-ray diffracted from a crystal lattice plane.

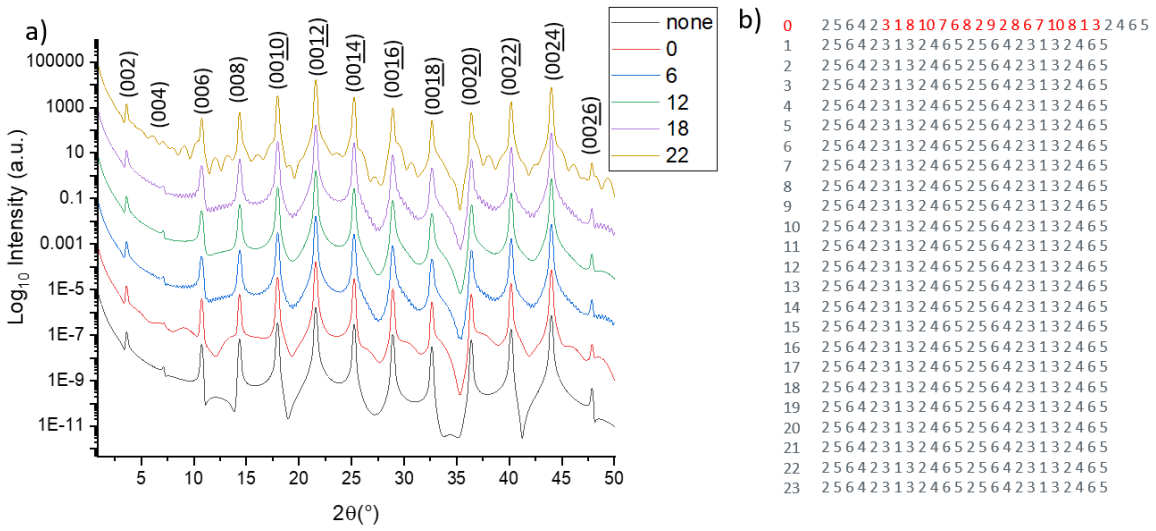


**Figure 4.2** a) Simulated XRD patterns for a 24 unit cell thick *m* = 5 Aurivillius phase film produced using the DIFFaX software package [256]. The figure illustrates the impact of inserting one *m* = 6 fault, equivalent to an intergrowth of one half of an Aurivillius phase, as it moves through a 24 unit cell from layer 0 (shown by the stacking sequence in (b)), towards layer 22. The instrumental broadening is set to Gaussian 0.18 °.

DIFFaX allows the user to add structural stacking faults as 'layers' into the material structure. To investigate how one such fault influences the peak position and peak shapes of

the *m* = 5 Aurivillius phase, structure files were made where one *m* = 6 fault, equivalent to an intergrowth of one half of an Aurivillius phase unit cell, were incorporated into the *m* = 5 structure file. These new structures can aid in visualising how the inclusion of stacking fault defects can impact the resulting XRD pattern measured from the structure. It should be noted that when OPB defects and associated stacking faults are present in a thin film, they typically only change the local phase of the structure over a short distance. The OPB itself has a lateral dimension shorter than 0.5 nm. While the high resolution electron microscopy studies so far demonstrate that the lateral distances of the *m* = 4 or 6 intergrowths and stacking faults created as a result of a proximal OPB defect can range from ~0.4 nm (the size of a perovskite unit cell) up to distances of ~50 nm [164], [192]. Intergrowths with lateral distances of between 1 to 10 nm can be observed in **Figure 4.1**. DIFFaX only limits the dimensions of the simulated thin film in the *c*-axis direction, leaving the size of the film in the *a*-*b* (lateral) direction infinite. Therefore, these simulations do not give an exact replica of an experimental Aurivillius phase thin film having stacking faults associated with OPB defects, but rather indicate which reflections may be most impacted by the inclusion of intergrowth defects and susceptible to Debye-Scherrer type peak broadening where periodicity is disturbed within the thin film [256]. **Figure 4.2**, illustrates the impact of inserting just one *m* = 6 fault, equivalent to an intergrowth of one half of an Aurivillius phase, as it moves through a 24 unit cell from layer 0 at one end of the film, towards layer 23 the opposite end of the film. With insertion of this *m* = 6 intergrowth in **Figure 4.2**, there is an overall change to the XRD pattern background in all of the simulated patterns, in comparison to the pure *m* = 5 simulation. While some reflections do not change much, such as the *m* = 5 (00$\underline{12}$) reflections, it is possible that for this position the inclusion of intergrowths in DIFFaX simulations and other structural defects such as OPBs in real thin films, which are caused by the *m* = 4 (00$\underline{10}$) and *m* = 6 (00$\underline{14}$) reflections don't have an impact on *m* = 5 (00$\underline{12}$) 2θ position as the they all have a similar 2θ value. There is also a slight shoulder to the right of the (00$\underline{18}$) reflection and to a lesser extent the (00$\underline{16}$) reflection when compared to the intergrowth free, *m* = 5 pattern (pattern represented by the black plot). This indicates that the (00$\underline{18}$) reflection is highly sensitive to the inclusion of intergrowths and structural defects within the *m* = 5 Aurivillius phase films. For the case where the intergrowth is at the centre of the film (pattern represented by the green plot, where the *m* = 6 intergrowth is present at layer 12), there is very little change to the pattern with the shoulders on the (00$\underline{16}$) and (00$\underline{18}$) reflections. When the intergrowths are about

30 nm away from the start or end of the stacking sequence, small additional oscillations within the XRD pattern can be observed, as seen in **Figure 4.2** for the pattern represented by the blue plot (where the $m = 6$ intergrowth is present at layer 6) and for the pattern represented by the purple plot (where the $m = 6$ intergrowth is present at layer 18). The DIFFaX simulated XRD patterns demonstrate that when the intergrowth is very near the film interface, either at a distance of 0.5 unit cells (in the pattern represented by the red plot (where the $m = 6$ intergrowth is present at layer 0)) or 1.5 unit cells (in the pattern represented by the yellow plot (where the $m = 6$ intergrowth is present at layer 22)) away, this appears to have the greatest impact on the DIFFaX simulated XRD pattern when compared to the film with no intergrowth included. In the pattern represented by the red plot in **Figure 4.2**, extra peaks to the left of the (006) and (008) reflections and to the right of the (00$\underline{2}$0) and (00$\underline{2}$4) peaks are present in addition to those found close to the (00$\underline{1}$6) and (00$\underline{1}$8) reflection. While for the pattern represented by the yellow plot, there is nearly an extra reflection or shoulder on or between every $m = 5$ reflection. Note that the 2θ positions of the observed shoulders and additional Bragg peaks cannot be attributed as to belonging to any periodic Aurivillius phase structure. Rather, these features represent the recursive property of crystals containing defects and X-ray scattering from partially disordered epitaxial films containing a finite number of layers of different structures and thicknesses [256], [310]. **Figure 4.2** clearly demonstrates the positioning of the intergrowth within the film does influence how the DIFFaX simulated XRD pattern changes from the phase pure, defect-free $m = 5$ pattern. Based on these simulations, it would be expected that for films synthesised with a high density of intergrowths and defects, reflections such as the (006), (008), (00$\underline{1}$6) and (00$\underline{1}$8) would be most susceptible to experiencing Debye-Scherrer type peak broadening where periodicity is disturbed and would have large asymmetric shoulders.

### 4.3.2 Experimental Investigations of Crystallographic Properties of Non-periodic Layered Aurivillius Phase Thin Films

In order to deliberately encourage the formation of OPB defects and associated intergrowths and stacking faults, B6TFMO thin films were synthesised on sapphire substrates with varying angles of mis-cut as shown in **Figure 4.3**. The term mis-cut refers to the degree at which the substrate is cut away from the *c*-plane toward the *m*-plane. A variation in mis-cut angle leads to a change in the size of the step heights and terrace widths on the sapphire substrate surface, whereupon with increase in mis-cut angle of the substrate, the terrace width of the steps tends to decrease [311]. In this work, B6TFMO is deposited on substrates with mis-cut angles of 0.2 °, 0.5 ° and 10 °. The roughness of the substrate surfaces increases with mis-cut angle, where RMS roughness values are 0.196 nm, 0.218 nm and 0.321 nm for angles of 0.2 °, 0.5 ° and 10 °, respectively. The terrace width for the 0.2 ° mis-cut sapphire substrate was ~70 ± 20 nm with step heights of ~0.6 ± 0.1 nm. The 0.5 ° mis-cut sapphire substrate had similar terrace widths (~67 ± 16 nm) that were less jagged than the 0.2 ° mis-cut substrate and had slightly deeper step height (~0.8 ± 0.1 nm). When inspecting the 1 µm x 1 µm AFM image of the 10 ° mis-cut sample, no clear steps could be seen, however when examining TEM images, a step-like interface could be observed with approximate step widths and step heights of ~7.4 ± 2.9 nm and ~1.3 ± 0.5 nm as shown later in **Figure 4.2**.

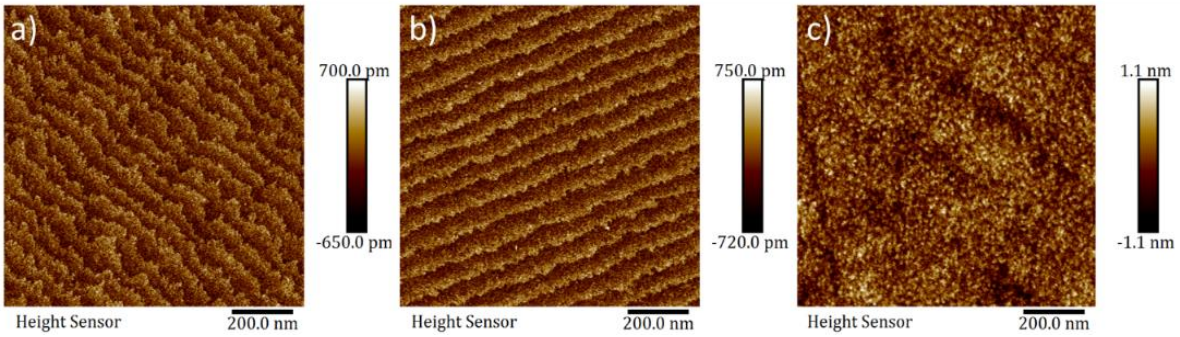


**Figure 4.3** AFM images of bare sapphire surfaces with differing degrees of surface angle mis-cut. a) 0.2 °, b) 0.5 °, c) 10 °.

The atomic-scale topography of the surface, on which a film nucleates, can lead to the nucleation of OPB defects via a steric mechanism during thin film deposition [166]. The nucleation events introduce a phase shift along the layering axis and OPB faults associated

with this shift can propagate through an entire film of half a micron, or more, in thickness. Here, OPB formation by step-flow growth [312] of B6TFMO is encouraged onto the above-described vicinal substrates with a slightly off-axis (0.2 °, 0.5 ° and 10 °) substrate cut and with a controlled density of atomic steps, designed to introduce OPBs into the growing layer. Nuclei on different terraces of the substrate will be out-of-phase along *c*, with an offset determined by the substrate step height, enabling an OPB to be created where they meet. Use of differing surface steps has been shown to impact the growth of perovskite and Aurivillius phases when they are epitaxial matched and have been used to tune structural and ferroelectric properties [190], [216], [217], [313]. Note that although B6TFMO (pseudo cubic lattice parameter of $a$ = 3.89 Å) is not epitaxially matched to sapphire, (hexagonal lattice parameter of $a$ = 4.758 Å (+22.31 % mismatch)), sapphire has been proven to be a suitable substrate to act as a mechanical support for the Aurivillius phase thin films and it is chemically stable at the processing temperatures used to crystallize the Aurivillius phases. The influence of the differing mis-cuts of sapphire on the nucleation and growth of B6TFMO thin films and sub-unit cell structural defects is described below.

DIFFaX simulations of $m$ = 5 Aurivillius phases containing $m$ = 4 and $m$ = 6 intergrowth layers in **Figure 4.4 (a)** are compared with experimentally observed X-ray diffraction patterns of non-periodic $m$ = 5 Aurivillius phases in **Figure 4.4 (b).** Examination of the experimental data in **Figure 4.4 (b)** shows that a significant change in the peaks can be observed depending on the underlying substrate utilised in thin film deposition. As the degree of mis-cut angle of the sapphire substrate increases, macroscopically it appears from XRD as though there is an increase in the defect density within the thin films. For the B6TFMO film on the 0.5 ° mis-cut substrate (XRD plot shown in red), the (006) and (00<u>18</u>) reflections have increased peak broadening in comparison to the B6TFMO film grown on 0.2 ° mis-cut sapphire. This broadening of the (006) and (00<u>18</u>) reflections in the XRD patterns of B6TFMO on higher mis-cut substrates is expected in accordance with the DIFFaX simulations which indicate that these reflections become broader when intergrowths are present (**Figure 4.2 (a)** and **Figure 4.4 (a)**). As displayed in **Table 4.1**, in general the FWHM values also increase with increase in substrate mis-cut. An XRD rocking curve measurement of the (006) peak shown in **Figure 4.5** further demonstrates that a change in the peak width can be observed. The FWHM value increases from a value of 0.22 for the B6TFMO film on 0.2 ° mis-cut sapphire to a value of 0.40

for the film on 0.5 º mis-cut sapphire. This peak broadening could be attributed to an increase in defects within the film as DIFFaX simulations indicate that if more defects are present within the film the (006) peak would experience broadening. From the XRD patterns it does appear that there is an increase in defect density within B6TFMO films when grown on higher mis-cut sapphire surfaces. Here reflections such as the (006) and (00$\underline{18}$) experience broadening as predicted by DIFFaX simulations when there is a half-unit cell intergrowth present. The FWHM values could be affected by the increase in structural disorder within the films, but also by factors such as film thickness and grain size. However, the average film thickness for the three samples is similar. Thickness measurements taken from 4 µm long film sections of the samples are 94 ± 26 nm, 112 ± 22 nm and 94 ± 11 nm for the B6TFMO films on 0.2 °, 0.5 ° and 10 ° mis-cut sapphire, respectively. Thus, it does not appear film thickness is the main contributor to the change in FWHM. Using Gwyddion software [314] to analyse the surface of the films, approximate average grain size values were measured, using the images as later shown for the average RMS values in **Figure 4.6**. The average size of the crystal grains do appear to be decreasing as mis-cut angle of the substrate increases, where the average grains size is 0.49 $\mu m^2$, 0.30 $\mu m^2$ and 0.26 $\mu m^2$ for the B6TFMO films grown on 0.2 °, 0.5 ° and 10 ° mis-cut sapphire respectively. Thus, it is possible that the crystal grain size within the B6TFMO films does contribute to the broadening of the observed FWHM values. Overall, the increase of the FWHM values for the films is also likely due to a combination of smaller grains in the B6TFMO films synthesised on higher mis-cut substrates and the higher number of defects contributing to deviations from periodicity within the films.

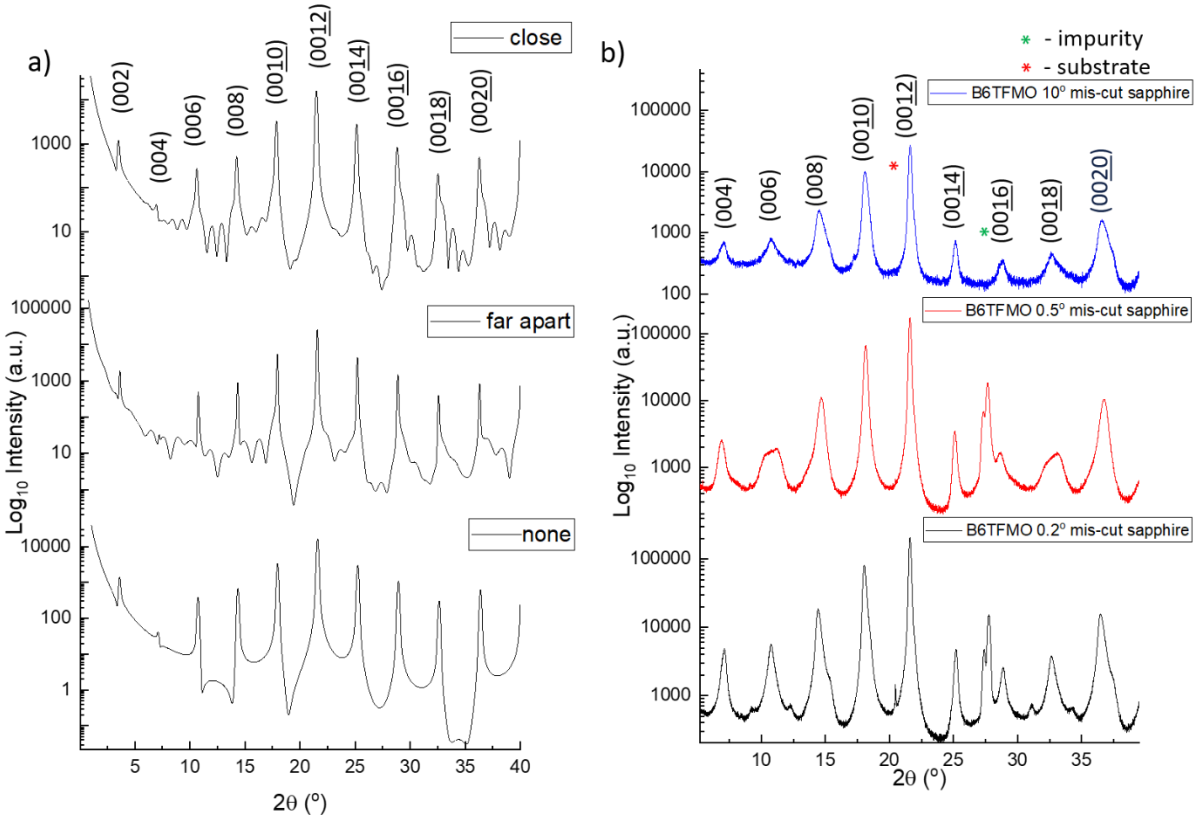


**Figure 4.4** a) Simulated XRD patterns with the instrumental broadening set to Gaussian 0.18 °. The bottom plot is simulated for an $m = 5$ phase with no intergrowths. The middle plot labelled "far apart" simulates a structure with two intergrowths, one $m = 4$ and one $m = 6$. One of the intergrowths is near the top of the film and the other near the bottom of the film, 19.5 unit cells apart. The top plot labelled "close" simulates one $m = 4$ and one $m = 6$ intergrowth near the centre of the film, 1.5 unit cells apart. A schematic with the positions of these intergrowths in an overall $m = 5$ Aurivillius structure is provided in **Appendix II Figure II.2**. b) Experimentally acquired X-ray diffraction patterns of B6TFMO films deposited on sapphire substrates with vicinal surfaces having mis-cut angles of 0.2 ° (XRD plot shown in black), 0.5 ° (XRD plot shown in red) and 10 ° (XRD plot shown in blue).

| Reflection | FWHM | | |
|---|---|---|---|
| | 0.2 ° | 0.5 ° | 10 ° |
| (004) | 0.371 ± 0.003 | 0.504 ± 0.005 | 0.554 ± 0.011 |
| (006) | 0.466 ± 0.002 | 1.303 ± 0.013 | 0.876± 0.012 |
| (008) | 0.399 ± 0.004 | 0.489 ± 0.003 | 0.667 ± 0.006 |
| (0010) | 0.262 ± 0.002 | 0.243 ± 0.001 | 0.354 ± 0.003 |
| (0012) | 0.169 ± 0.001 | 0.169 ± 0.001 | 0.201 ± 0.002 |
| (0014) | 0.263 ± 0.002 | 0.272 ± 0.003 | 0.325 ± 0.004 |
| (0018) | 0.521 ± 0.004 | 1.227 ± 0.011 | 0.945 ± 0.019 |
| (0020) | 0.572 ± 0.003 | 0.491 ± 0.005 | 0.810 ± 0.009 |

**Table 4.1** FWHM values of experimentally acquired XRD patterns from **Figure 4.4 (b)**.

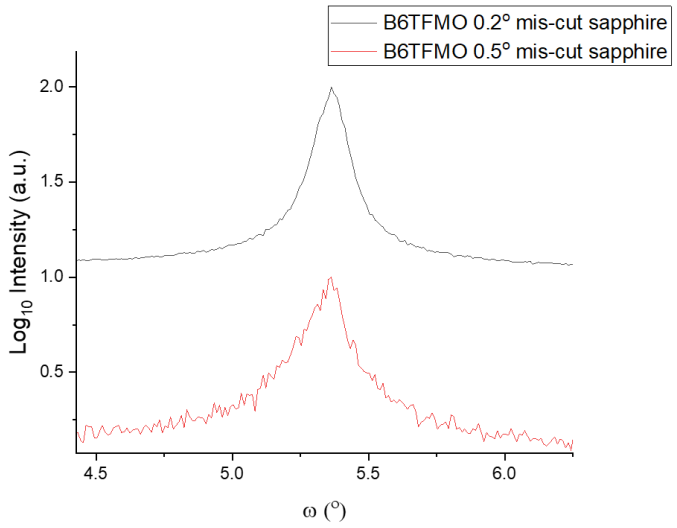


**Figure 4.5** Normalised rocking curve measurement of the (006) reflection for a B6TFMO thin film deposited on 0.2 ° (plot shown in black) and 0.5 ° (plot shown in red) mis-cut sapphire.

While the presence of OPBs and short-range lateral stacking faults within B6TFMO cannot be perfectly replicated, DIFFaX provides insight into how stacking-fault defects across a proportion of the sample might affect the non-periodic material structure. **Figure 4.2**, illustrates how the inclusion of a half-unit cell $m$ = 6 stacking fault impacts the XRD pattern of an $m$ = 5 Aurivillius phase material. However, to create a more complex structure that might produce an XRD pattern more similar to those collected experimentally, a second stacking

fault was included in the DIFFaX structure file to include a half-unit cell $m = 4$ intergrowth. Simulated XRD patterns produced by DIFFaX with one half-unit cell intergrowth of an $m = 4$ phase and one half-unit cell intergrowth of an $m = 6$ phase within the same structure are plotted in **Figure 4.4 (a)**. When one intergrowth is near the top of the film and the other is at the bottom of the film, 19.5 unit cells apart ("far apart"), slight broadening can be observed at the base of some of the peaks, which appear as shoulders on the $m = 5$ reflections. For the simulation labelled "close", where the intergrowths are now inserted towards the centre of the film with a distance of 1.5 unit cells (three half unit cells) apart, the broadening on the $m = 5$ reflections is much more significant. This is most evident in peaks such as those associated with the (006) and (00$\underline{1}$8) reflections. This correlates with the experimental XRD patterns of B6TFMO on the 0.5 ° mis-cut sapphire substrate, where the experimental data (shown in the XRD plot in red in **Figure 4.4 (b)**) shows a relatively large proportion of broadening. Here the FWHM values of the (006) and (00$\underline{1}$8) reflections increase by 179.82 % (0.47 to 1.30) and 141.40% (0.52 to 1.23) respectively from the film deposited on 0.2 ° mis-cut sapphire to the film on 0.5 ° mis-cut sapphire. It is also clear from the DIFFaX simulations that the (00$\underline{1}$0), (00$\underline{1}$2) and (00$\underline{1}$4) reflections experience very little change with the inclusion of $m = 4/6$ intergrowths. This correlates with the experimental data where those three peaks, belonging to B6TFMO films on all three types of substrate mis-cut substrates show no evidence of further broadening or shoulders on their peaks (**Figure 4.4**) and possess the lowest FWHM values, as displayed in **Table 4.1**.

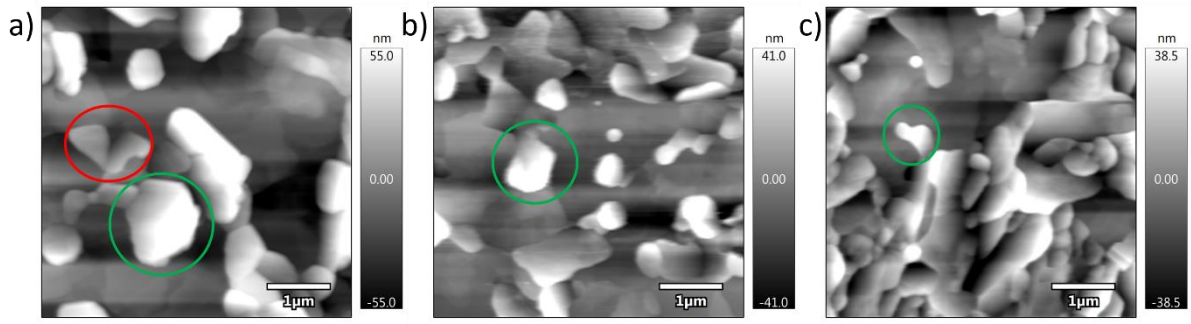


**Figure 4.6** AFM images of B6TFMO films deposited on sapphire substrates with differing degree of surface angle mis-cut, a) 0.2 °, b) 0.5 °, c) 10 °.

### 4.3.3 Experimental Investigations of Thin Film Morphology of Non-periodic Layered Aurivillius Phase Thin Films

The use of differing vicinal substrates appears to have an overall impact on the nucleation and growth of the Aurivillius phase. **Figure 4.6** shows the surface topography of the B6TFMO thin films imaged by AFM in contact mode. The figure demonstrates how the surface changes with increasing substrate mis-cut angle, with the crystal grain size appearing to decrease as the substrate mis-cut increases. The average RMS roughness values for the B6TFMO films on 0.2 °, 0.5 ° and 10 ° mis-cut sapphire substrates each taken from 5 separate 10 x 10 $\mu m^2$ scans are 32.00 ± 2.71 nm, 19.64 ± 0.91 nm and 21.83 ± 1.27 nm, respectively. Through AFM and TEM imaging, the relatively rough nature of the non-epitaxially grown films can be observed. **Figure 4.7** displays STEM images of the cross-section lamellae of the B6TFMO films grown on 0.2 ° and 10 ° mis-cut sapphire, where it appears as though the surface roughness arises from two different mechanisms: i) microcrystallites and ii) crystal grain orientation, as is discussed below. Microcrystallites are found on the surface of all the B6TFMO thin films presented in this work. It is inferred that the microcrystallites are formed during cooling after the 850 °C post deposition-annealing step and electron microscopy analysis shows that they are comprised of a bismuth based layered phase. They have smaller lateral dimensions than the underlying B6TFMO film and can differ from the underlying film by having either a different crystal orientation or by having a different bismuth layering structure. The film on 0.2 ° mis-cut sapphire shown in **Figure 4.6 (a)** has two types of surface crystallites, those that are 20 nm in height (shown within the red circle) and those that are between 100 to 150 nm in height (shown within the green circle). For the B6TFMO films on 0.5 ° and 10 ° mis-cut sapphire, the surface crystallites are approximately 50 to 80 nm in height as seen in **Figure 4.6 (b)** and **(c)**. However, for the B6TFMO thin films on the 10 ° mis-cut sapphire, surface crystallites are not the only contribution to the surface roughness. **Figure 4.7** and **Figure 4.8** depicts STEM and HAADF images of the B6TFMO film grown on 10 ° mis-cut sapphire. It can be observed that there are two types of grain growth within the film. Grains that lie flat at a 0 ° angle to the surface and those that lie at an angle approximately 10 ° to the surface. The grains that grow at a ~10 ° angle do not have an equal thickness throughout the grain. In the grain circled in yellow in **Figure 4.8 (b)**, one area of the grain has a thickness of 48 nm. Towards the left of

the same grain, the crystallite increases in height to a thickness of 104 nm. This unequal/non-equivalent thickness in grains that grow at an angle of ~10 ° demonstrates that the direction of the grain growth also contributes towards to the surface roughness of the B6TFMO film. The density of the Aurivillius phase surface crystallites increase as the substrate mis-cut angle increases while the surface crystallite size decreases, where the average number of surface crystallites are 0.5, 1.3 and 1.5 per $\mu m^2$ and the average lateral dimensions of the surface crystallites are 0.28 $\mu m^2$, 0.11 $\mu m^2$ and 0.12 $\mu m^2$ for the films grown on the 0.2 °, 0.5 ° and 10 ° mis-cut substrates, respectively.

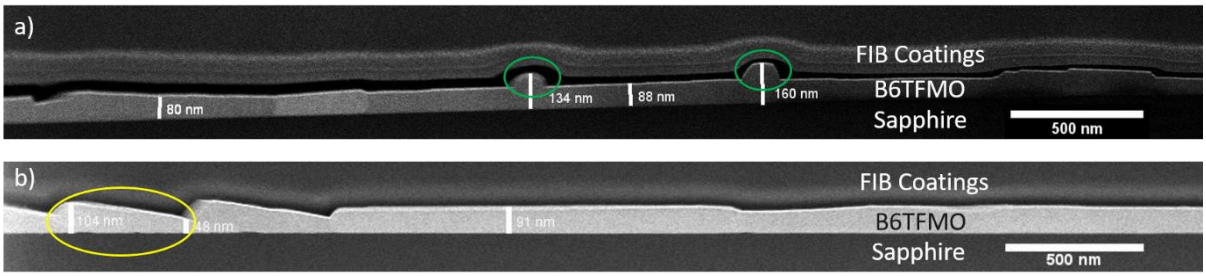


**Figure 4.7** STEM images of B6TFMO films on a) 0.2 ° and b) 10 ° mis-cut sapphire substrates. a) An intermediate stage in the layer-by-layer growth mode shown on top of the film within the green circle while in b) sections of the film are grown at different angles, 0 ° and ~10 ° to the underlying substrate.

Looking more closely at the grains within the B6TFMO film on 10 ° mis-cut sapphire (**Figure 4.8**), areas can be compared where the crystal grains grow at 0 ° vs. 10 ° and it can be observed that the orientation of the grains differ. From the inset in **Figure 4.8 (a)**, it is seen that the as-grown film does not follow the surface steps and the grain is oriented in the (100) direction. In this area the initial $[Bi_2O_2]^{2+}$ interlayer at the substrate/thin film interface ignores the ~10 ° substrate steps and grows parallel (flat) to the overall substrate. In **Figure 4.8 (b)**, the orientation of the grain that grows at a ~10 ° angle with the mis-cut surface steps is (110) orientated, with the initial $[Bi_2O_2]^{2+}$ interlayer at the substrate/thin film interface growing along the ~10 ° surface steps. Further imaging needs to be carried out in B6TFMO thin films on 10 ° mis-cut sapphire in order to ensure that this change in orientation is experienced for all grains that are grown at a 0 ° vs. 10 ° angle. This observation indicates there is a possibility

that the ~10 ° step edge may help nucleate grains within the B6TFMO thin film in a particular crystal orientation.

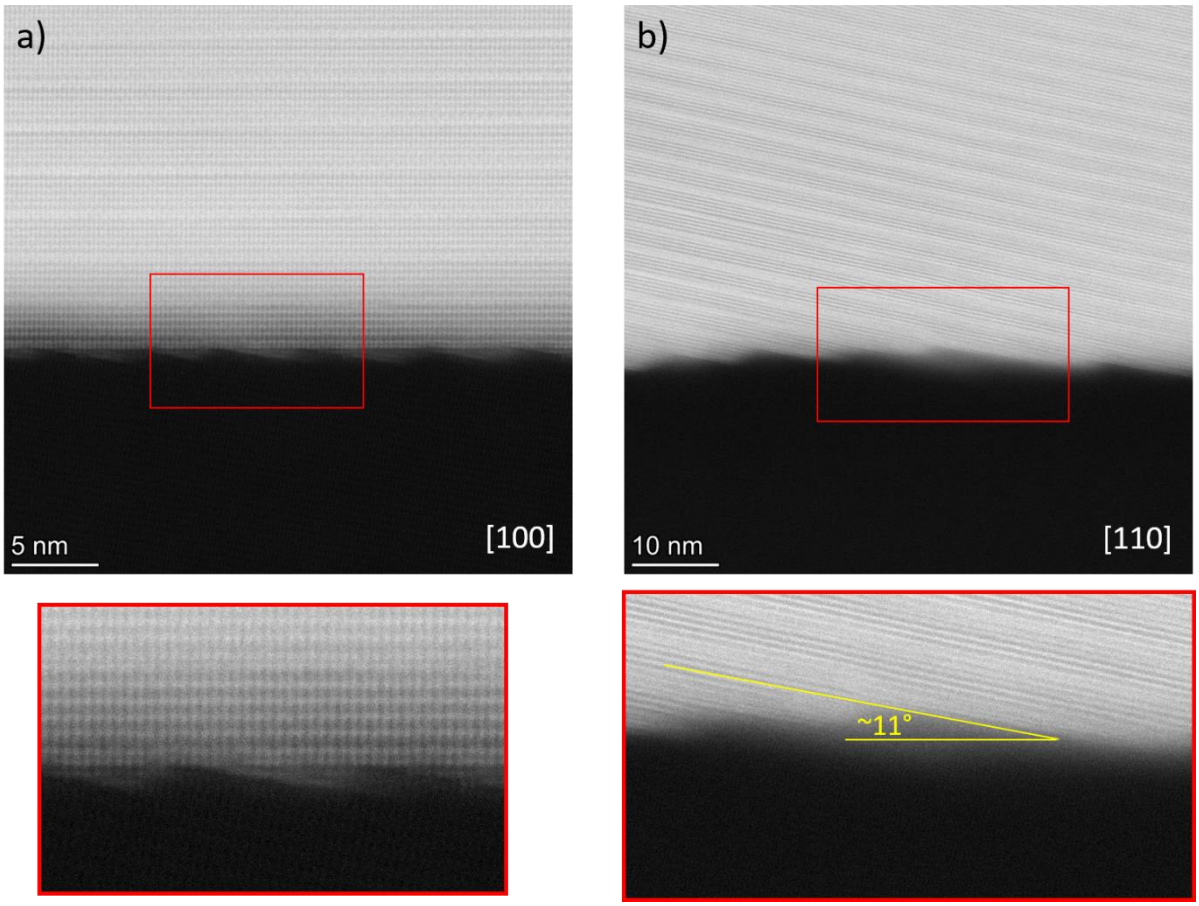


**Figure 4.8** STEM images of B6TFMO films on a 10 ° mis-cut sapphire. The surface of the substrate is made of up steps that are at an approximate 10 ° angle to the surface normal. However, some sections of the film have grown at different angles, a) at 0 ° and b) at ~ 11 ° to the substrate surface. In this figure, the grains lying at a 0 ° angle have a (100) orientation while the grains lying at an angle of ~11 ° are (110) oriented.

### 4.3.4 Visualisation of Sub-unit-cell Structural Defects in Non-periodic Layered Aurivillius Phase Thin Films

Atomic-scale cross-section STEM imaging of the three films on the vicinal sapphire surfaces allowed for the visualisation of sub-unit cell defects such as OPB defects and stacking fault defects within in all of the films, as seen in **Figure 4.9**. Unlike in XRD where the full sample can be analysed and a comparison of defect density can be made between samples, a statistical

comparison of defect density as a function of mis-cut angle cannot be determined by STEM imaging due to the local nature of the technique and given the fact that there is regional variability within the films. However, because the defect dimensions are at the sub-unit cell scale, HAADF-STEM imaging is required to probe their unique characteristics with atomic-scale spatial resolution. Herein, it is revealed that HAADF-STEM imaging reveals other types of unique defects in addition to commonly observed OPB defects and stacking faults.

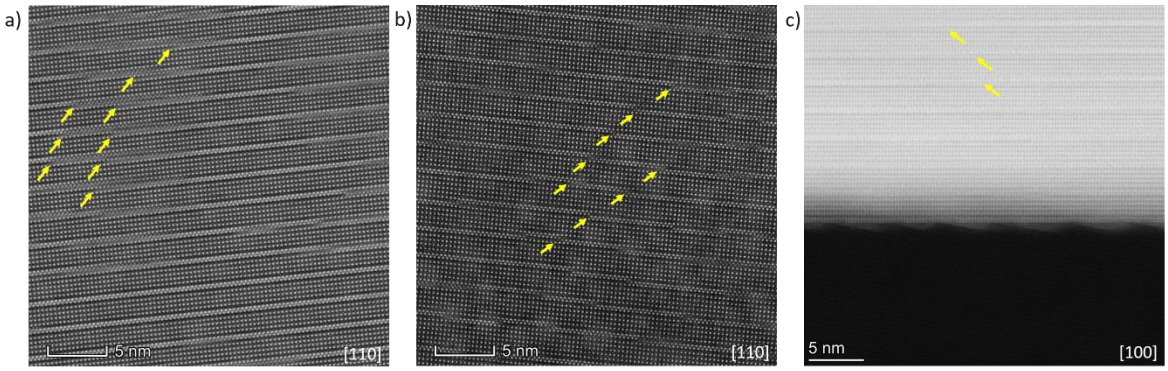


**Figure 4.9** STEM images of the B6TFMO films on a) 0.2 °, b) 0.5 ° and c) 10 ° mis-cut sapphire. OPB defects are observed in all films. The yellow arrows point to some examples of these defects within the images.

For the imaging of defects within the B6TFMO films, STEM was initially used to investigate the possibility of correlating different types of defects within the B6TFMO films to the influence of differing types of mis-cut sapphire substrates and to see how the steps of the mis-cut substrates impacted the formation of defects within B6TFMO. However, STEM imaging does not clarify how the steps of the sapphire substrate contribute to the formation of structural defects within the B6TFMO films. What is seen is that alongside expected defects such as OPBs defects, further structural defects such as 'anatase'-type planar defects and nanorod precipitates are present. In **Figure 4.10**, different crystallographic grains are observed, with a low angle grain boundary (a grain boundary with a mis-orientation of < 15 ° [315]) in inset b) and a surface microcrystallite within the inset in c). To the right of the grain boundary in **Figure 4.10** (shown with lighter colour contrast), there is a grain mostly comprised of the Aurivillius phase $m$ = 5 phase, where the atomic columns of the structure can clearly be identified. To the left of the grain boundary (shown with darker colour contrast), the projected angle of the grain makes the atomic columns more difficult to see due to the slight change in orientation. However, at either side of the grain boundary as seen in **Figure 4.10 (a)** and **(b)**, there are sections where the $[Bi_2O_2]^{2+}$ interlayer has been replaced

with an ‘anatase’- type planar defect, described previously in **Section 1.6.3**. These are bismuth poor interfaces, made up of edge-sharing $BO_6$ octahedra with double columns of $Bi^{3+}$ cations and most likely the $Ti^{4+}$ cation. Batuk *et al.* [175], [176] deliberately synthesised layered materials of the formula $Bi_{3n+1}Ti_7Fe_{3n-3}O_{9n+11}$, containing these ‘anatase’-type chains via a solid state reaction in air at temperatures between 800 to 1000 °C. The ‘anatase’-type chains are interleaved between perovskite blocks where the chains are considered as planar ‘anatase’-like intergrowths that are polysynthetically twinned fragments of the $Bi_2Ti_4O_{11}$ structure. In the region in **Figure 4.10 (c)** which is a surface microcrystallite above the main film, the structure has fully deviated away from the Aurivillius phase structure and the dielectric $[Bi_2O_2]^{2+}$ interlayers are completely replaced by ‘anatase’- type planar defects. This region above the film likely corresponds to one of the surface crystallites as observed **Figure 4.6 (a)** and **Figure 4.7 (a)**, circled in green. One hypothesis for the formation of ‘anatase’- type interlayers within these films could be that there is diffusion of bismuth at the low angle grain boundaries during the 850 °C post anneal step. It has been observed that the loss of bismuth through evaporation leads to the secondary generation of defects such as OPBs through crystal shear [166]. It could be possible here, that the low angle grain boundaries, which are comprised of multiple OPB defects behave as a fast diffusion path for the volatile bismuth and thus as a result, the locally bismuth poor ‘anatase’- type defects form.

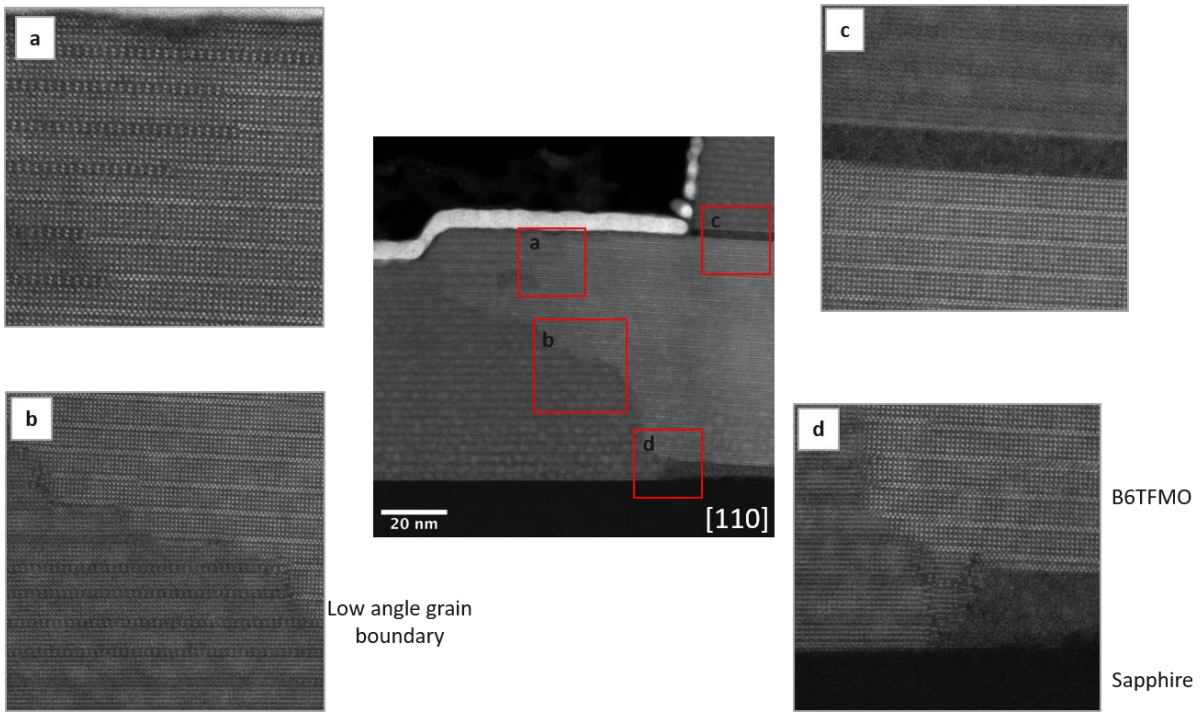


**Figure 4.10** Cross-section STEM images of B6TFMO on 0.5 ° mis-cut sapphire substrate. Within this lamella, there are a number of different regions. a) is a region where planar 'anatase'-like $BO_6$ interlayers replaces some of the fluorite $[Bi_2O_2]^{2+}$ layers at points and *m*, the number of perovskite-like unit cells between the interlayers varies. These 'anatase'- like $BO_6$ interlayers can also be seen at low angle grain boundaries as in b) and d). In c) the interface between the main (continuous) *m* = 5 Aurivillius phase film grown on sapphire and a surface microcrystallite, which appears to also have 'anatase'-like $BO_6$ interlayers instead of the expected $[Bi_2O_2]^{2+}$ fluorite layers, is observed.

In the areas where the $[Bi_2O_2]^{2+}$ interlayer is replaced by the 'anatase'-like interlayer, as seen in **Figure 4.11**, the number of perovskite blocks between the planar 'anatase'-like interlayer is not uniform and varies from 4 to 8 perovskite blocks. In regions where there are 6 perovskite blocks or more, a further chemical defect can be observed as displayed in **Figure 4.11**. Here, there are bismuth deficient nanorod type precipitates that form through the perovskite region of the layer, which can also be observed in the $Bi_9Ti_3Fe_5O_{27}$, *m* = 8, Aurivillius system prepared by other research groups [200], [316]. These defects are made up of a centre comprising of two central bismuth atoms, and have been previously considered by MacLaren *et al.* [317] to be "nanorods". Research on similar defects found in Nd (*A*-site) and Ti (*B*-site) doped $BiFeO_3$ reported that these structures do not travel the full way through the

film, but rather have lengths varying from approximately 1.2 nm to over 10 nm [317]. The precipitates found in the doped $BiFeO_3$ films were also accompanied by the presence of planar 'anatase´-like defects [173], [318]. Imaging of the nanorod precipitates as seen in **Figure 4.11** agree with MacLaren *et al.'s* assessment that these defects do not travel though the entirety of the film. At the far sides of the inset in **Figure 4.11** (circled in purple) distinct precipitates having two central bismuth atoms can be observed, however other defects in the inset (circled in blue) appear like a mixture of the precipitate with the Aurivillius structure. This indicates that the defects do not run fully through the lamella. It is likely in this sample that the central atoms at the precipitate have a $Bi_2O_3$ structure with highly strained Ti rich columns next to the precipitate. EELS work by MacLaren *et al.* [317] from the Nd/Ti doped $BiFeO_3$ indicated that there is an $Nd_2O_3$ structure at the core of their precipitates. Density Functional Theory (DFT) calculations predicted that to the sides of the precipitate, the $BO_6$ octahedra move to $BO_5$ square pyramids. This change could be due to the internal strain imparted by the nanorod core. It is possible that the $Bi^{3+}$ poor planar 'anatase'-like defects and nanorod precipitates are a result of $Bi^{3+}$ diffusion along low angle grain boundaries. The defects could also potentially be a result of the reorganisation of the layered structure in order to accommodate intergrowths with $m$ = 6, 7 or 8. For example, the nanorod precipitates are only found in regions where $m$ is greater than 7, these defects could form in order to compensate for the extra $Bi^{3+}$ required to stabilise these intergrowths.

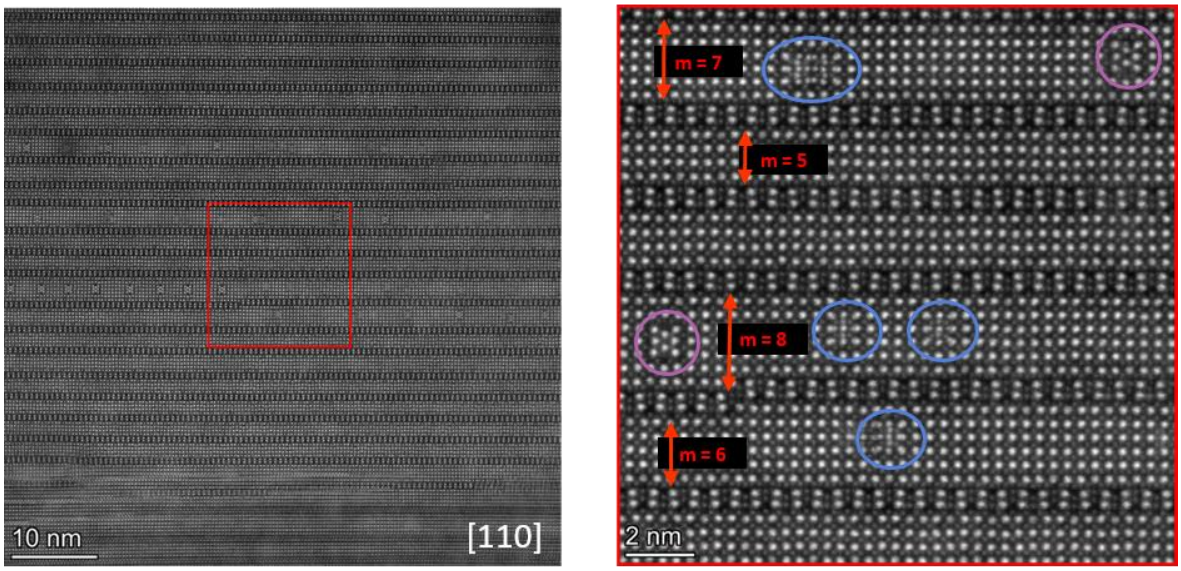


**Figure 4.11** HAADF STEM images showing planar 'anatase' rich regions in a B6TFMO film on 0.2 ° mis-cut sapphire substrate near the top of the B6TFMO film. Within this region, the number of *m* perovskite-like unit cells between the dielectric interlayers varies from 4 to 8. When there are 7 or more perovskite unit cells, a nanorod-type precipitate (blue and purple circles) is also observed.

### 4.3.5 Local PFM In-plane and Out-of-plane Ferroelectric Investigations of Non-periodic Layered Aurivillius Phase Thin Films

DART-PFM [234] was used to measure the piezoresponse of the B6TFMO samples in order to investigate how the substrate mis-cut angle impacted the ferroelectric domains. It should be noted that for B6TFMO grown on sapphire the films are preferentially c-axis orientated due to natural layering, but there is no preferred in-plane orientation, as the films are not epitaxially matched to the sapphire substrate. It has been observed for very thin films (1 unit cell) on NGO, that B6TFMO can have ferroelectric stripe domains [171] and that substrate steps can influence the formation of ferroelectric domains within other Aurivillius phases [190]. While such distinct domain ordering would not be expected to be observed in relatively thick (90 to 100 nm) Aurivillius phase films, due to the high electrostatic costs associated with charged domain walls, in this work the influence of the mis-cut sapphire substrate steps on the formation of ferroelectric domains and domain wall structure within B6TFMO was investigated. For even-layered Aurivillius phases, the spontaneous polarisation within the material is confined to the in-plane (*b*-axis) direction, due to the presence of the horizontal mirror symmetry [284]. However for odd-layered phases, e.g. $m = 5$ B6TFMO, the mirror

symmetry is broken and the resulting two-fold rotation symmetry allows for a minor out-of-plane component to be present in the out-of-plane (*c*-axis) direction [196].
PFM imaging in **Figure 4.12** reveals that the three B6TFMO samples studied are all naturally self-polarised, demonstrating a clear lateral piezoresponse (LPFM) and a weaker vertical piezoresponse (VPFM). In **Figure 4.12**, it is evident how the size of the ferroelectric domains within the films varies with the substrate mis-cut angle, where the size of the ferroelectric domains decrease with increased mis-cut angle. For example, the average ferroelectric domain size from the in-plane LPFM measurements were calculated to be 0.233 ± 0.025 $\mu m^2$, 0.210 ± 0.004 $\mu m^2$ and 0.139 ± 0.012 $\mu m^2$ for the B6TFMO films on 0.2 °, 0.5 ° and 10 ° mis-cut sapphire substrates respectively.

The higher degree of structural disorder within the B6TFMO films grown on higher angles of mis-cut sapphire is the most likely contributor to the increased number of ferroelectric domains observed. In a thin film that is comprised of mostly small grains (as is the case when comparing the B6TFMO film for example on 0.2 ° vs 10 ° mis-cut sapphire) there is a higher level of structural disorder due to an increased number of grain boundaries within that film, compared to a thin film with very few, large-sized grains. The greater degree of grain boundaries within these types of films would mean that defects such as OPBs are much more prevalent, given that grain boundaries can act as fast diffusion paths for volatizing bismuth (See **Figure 4.10** [166]). While the inclusion of a single OPB within a ferroelectric does not necessarily create a domain wall, it has been shown in previous work that a defect such as an OPB can cause local polar discontinuities [192] and can potentially act as a nucleation site for ferroelectric domains [319]. In structures where there are a large prevalence of structural defects, the polar discontinuities can result in a higher likelihood of interesting polar topologies such as domain walls. It appears from **Figure 4.12,** that increase in substrate mis-cut leads to an increase the number of ferroelectric domains within the material.

**Figure 4.13** demonstrates that both vertical and lateral ferroelectric domains within all the B6TFMO films studied were switchable with the application of a DC voltage ($V_{DC}$) to the surfaces. Direct application of voltage from the vertical PFM probe enabled switching of domains in the out-of-plane (vertical) direction. As the PFM tip scans a material surface with an applied DC bias, it creates a trailing field that can generate an in-plane electric

field [320], [321], which enabled switching of the underlying domains in the lateral direction. PFM poling experiments of B6TFMO films on sapphire are displayed in **Figure 4.13** and **Figure 4.14**, where it can be observed that the out-of-plane response can be switched for all films after ±15 $V_{DC}$ is applied. It is noted that the film on the 10 ° mis-cut substrate switches more easily after ±5 $V_{DC}$ is applied, compared to films synthesised on the other two substrates. The in-plane component does not switch as easily, possibly due to the method by which the poling occurs. In practice, the in-plane electric field generated by the scanning trailing field used to switch the in-plane component will be lower than the direct field generated in the vertical direction. Looking more closely at the poled in-plane regions in **Figure 4.14**, full switching of domains in the out-of-plane (vertical) direction (**Figure 4.14 (b)**) is observed. Some, but not complete, switching of the domains in the lateral direction from the naturally self-polarised state, to a lateral switching of polarisation towards the right direction is present. In **Figure 4.14 (c)**, before a bias of ± 45 $V_{DC}$ was applied, the average ferroelectric domain size was 0.46 $\mu m^2$. 51.6 % (purple) of the domains were polarised to the left and 48.2 % of the domains were polarised to the right (yellow). Whereas after poling, while the domains were not completely switched to the right, with 46.3 % polarised to the left (purple) and 53.3 % polarised to the right (yellow), there is an overall increase in domains polarised to the right. The average ferroelectric domain size increases to 0.99 $\mu m^2$.

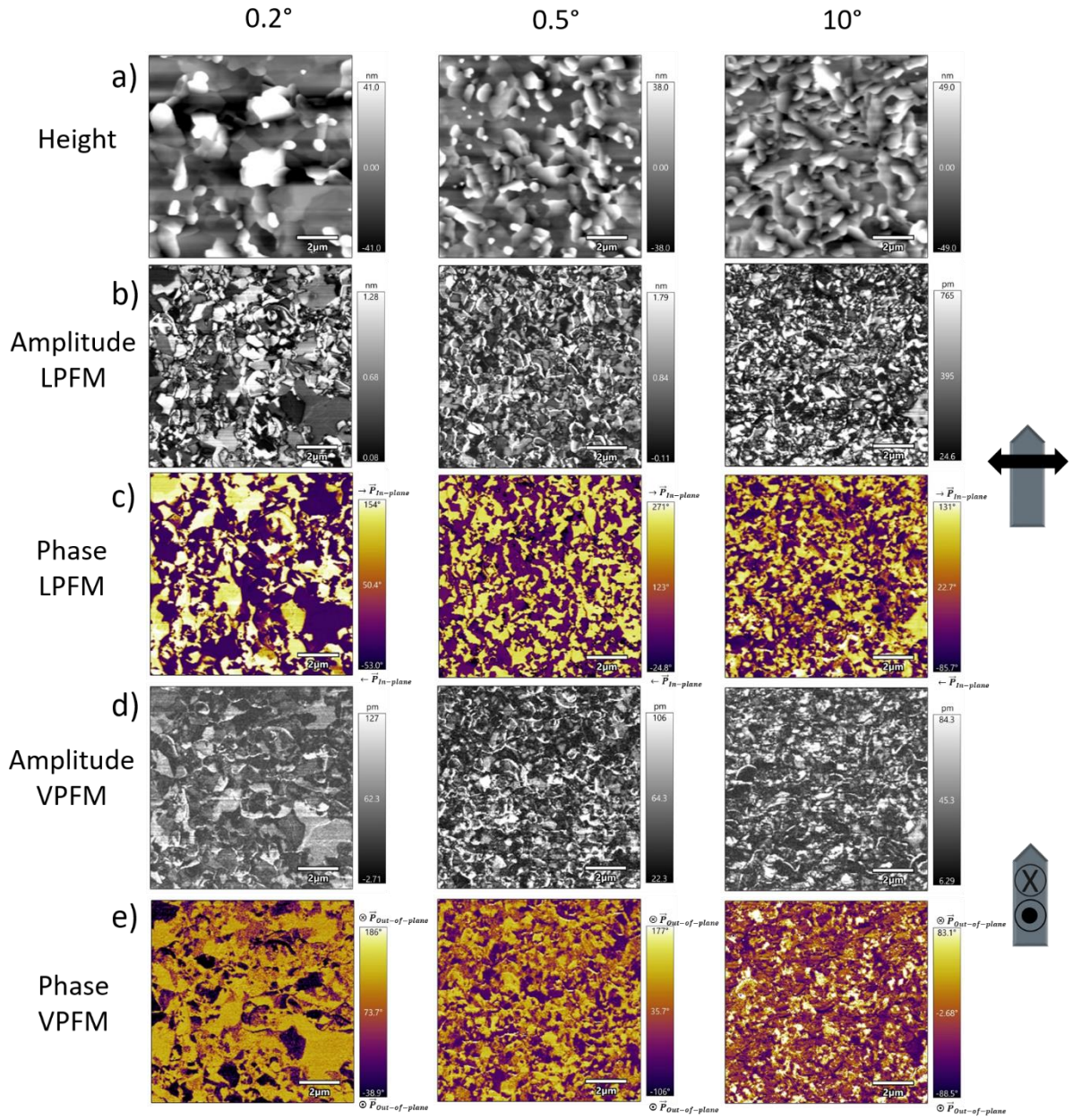


**Figure 4.12** In–plane LPFM and out-of-plane VPFM images of B6TFMO thin films on 0.2 °, 0.5 ° and 10 ° mis-cut sapphire substrates probed at 2 $V_{AC}$.

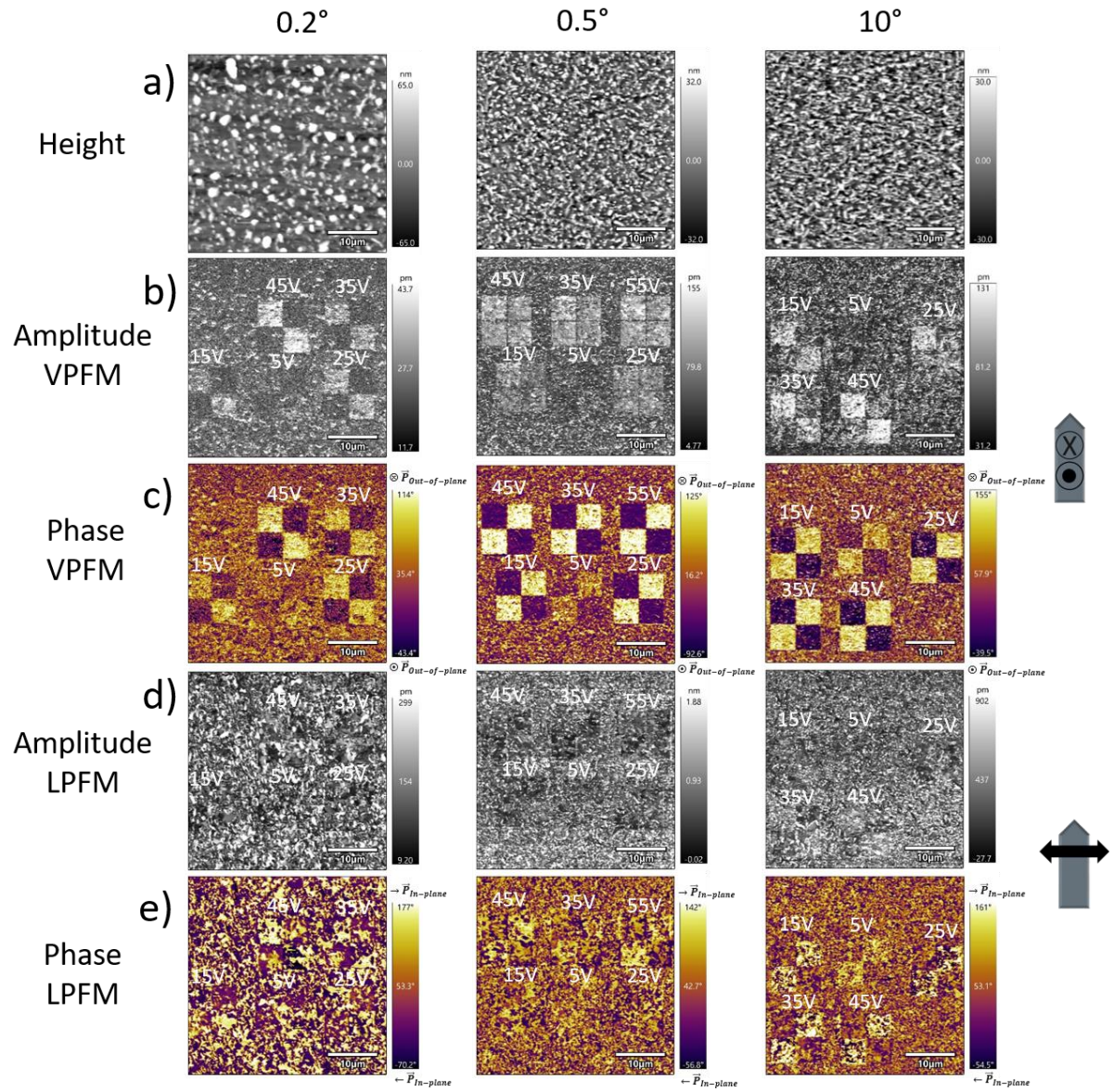


**Figure 4.13** Ferroelectric poling of B6TFMO on 0.2 °, 0.5 °and 10 ° mis-cut sapphire substrates using applied biases of ±5 $V_{DC}$ to ±55 $V_{DC}$ over 10 x 10 µm$^2$ regions.

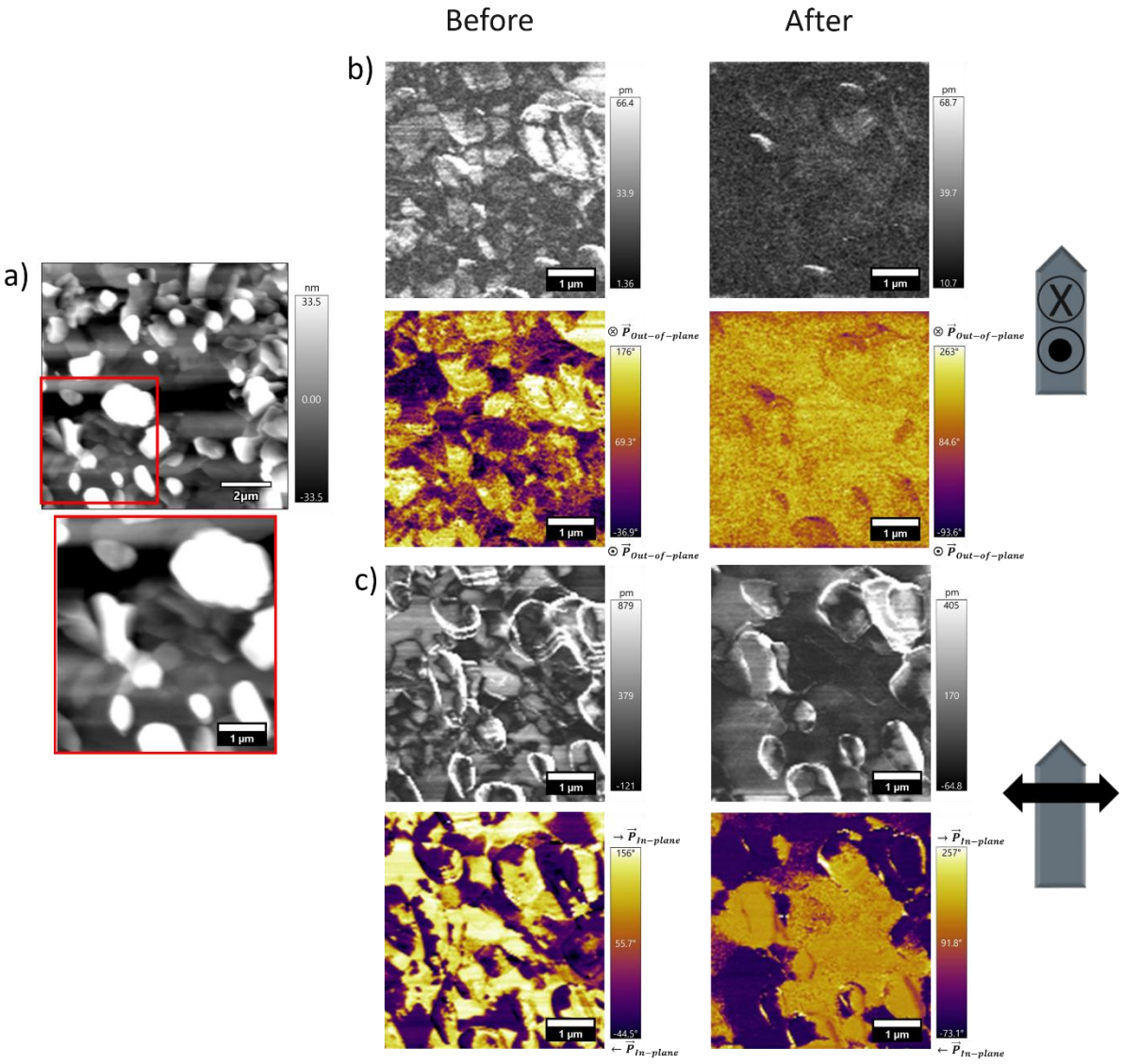


**Figure 4.14** B6TFMO region on 0.2 ° mis-cut sapphire substrate where ±45 $V_{DC}$ was applied over a total 10 x 10 µm$^2$ area for ferroelectric poling studies. a) Height image with inset (4.8 x 5.2 µm$^2$ area). The corresponding amplitude and phase images of the inset area b) before and after poling imaged using a 2 V vertical $V_{AC}$ and c) before and after poling imaged using a 2 V lateral $V_{AC}$.

### 4.3.6 Atomic Resolution Mapping of Polar Topologies of Non-periodic Layered Aurivillius Phase Thin Films

Disruptions to the periodic Aurivillius phase lattice by OPBs and stacking-faults have a marked influence on the internal elastic strain and electrostatic energy gradients within the structure [192]. The local polarisation component within the perovskite unit cells can be measured via quantification of the displacement of the *B*-site cation through local polarisation mapping within B6TFMO. Atomic resolution polarisation vector mapping is used to further investigate the affect that defect positioning, distance and density has on the formation of exotic charged domain walls and polar vortices within B6TFMO. What is apparent from polarisation mapping of HAADF-STEM images (**Figure 4.15** and **Appendix II Figure II.5**) is that defects such as OPBs encourage the formation of nominally 180 $^{o}$ charged domain walls going through multiple perovskite layers. Within this section, the aim was to utilise polarisation mapping of HAADF-STEM images to visualise how the strain induced by the structural defects impacts the polarisation within the B6TFMO system. In the centre of **Figure 4.15,** where a dashed yellow line indicates the approximate position of a changed domain wall, the domain wall seems to be facilitated by the OPB defects passing through the film. The presence of OPB defects and the resulting change in the elastic strain and electrostatic energies can cause the magnitude and the orientation of the local polarisation vectors to be altered. This polar discontinuity can aid in the nucleation of a charged domain wall. At sites where charged domain walls are present, a large bound charge accumulates, and a compensating mechanism is required in order for the domain wall to be stabilised. In B6TFMO, it is not yet known what fundamental mechanism is compensating this bound charge. For different ferroelectric systems, different compensation mechanisms have so far been postulated [88], [91]. One possibility is the presence of point charges, such as $Bi^{3+}$ or $O^{2-}$ vacancies in the proximity the bismuth deficient OPB defect. While vacancy sites within perovskites are common and oxygen vacancies are present in other systems at domain walls where strain gradients are relieved [322], [323], previous work by Snedden *et al.* [324] describes how reports of oxygen deficient Aurivillius phases should be treated with caution. Their work illustrating the difficulty of replacing similarly sized $Ti^{4+}$ by $Ga^{3+}$ in both $Bi_2Sr_2Nb_2TiO_{12}$ ($m$ = 3) and $BaBi_4Ti_4O_{15}$ ($m$ = 4) indicates the intolerance of the Aurivillius phases (with $m$ > 1) towards oxide ion vacancies.

McCabe and Greaves [325] also describe the difficulty in formation of an oxygen deficient $Bi_2Sr_2Nb_2MnO_{12-\delta}$ ($m$ = 3) Aurivillius phase containing $Mn^{3+}$. Whereas the synthesis of the $Mn^{3.4+}$ Aurivillius phase, $Bi_2Sr_{1.4}La_{0.6}Nb_2MnO_{12}$ ($m$ = 3), in which charge compensation required no oxygen vacancies, was successful. Zurbuchen *et al*. [326] likewise describe that oxide ion vacancies are not favourable for the $m$ = 6 Aurivillius phase $Bi_7Mn_{3.75}Ti_{2.25}O_{21}$. Some preliminary EELS mapping of the B6TFMO system [192] does show that at domain walls there is a depletion of oxygen, however further chemical mapping needs to be carried out to confirm these findings and further investigations on B6TFMO Aurivillius phases need to be undertaken to see how favourable it is for vacancies to be present within these systems. In work by Gradauskaite *et al.* [190] on $m$ = 4 $Bi_5FeTi_3O_{15}$ epitaxial thin films, they suggest through DFT calculations that Head-to-Head and Tail-to-Tail domain walls are created at OPB sites through $Bi^{3+}$ vacancies. Conversely, given that there is a clear augmentation of cation partitioning near OPB defects in B6TFMO [164], [192] this might lead to local (site specific) bandgap changes between the DW and bulk material, signifying that intrinsic mechanisms may support domain wall conduction [88], [91]. High resolution EELS analysis would be required to confirm this.

In previous work [192], it has been shown that within B6TFMO regions disrupted by OPB steps, the internal elastic strain and electrostatic energy gradients are altered in such a way that non-trivial rotations of the polarisation must occur, facilitating the formation of extraordinary polar vortex type topologies. In a true vortex state, polarisation is continuously changing about a vortex core, giving rise to an inhomogeneous polarisation distribution. Within these topological structures, both the change in magnitude of polarisation and rotation angle are observed, therefore they cannot be considered as prototypical Ising (axis of polarisation is fixed), Néel or Bloch-type (polarisation magnitude is fixed) domain walls. Given there is continuous rotation of the local polarisation vector, these topological structures resemble vortex domain walls rather than flux-closure architectures (where segregation into uniform domains occurs in the latter). Results so far indicate that these polar vortex topologies are present at charged domain wall regions where OPB defects are spaced 3 to 4 nm apart (equivalent to between 5 to 8 perovskite unit cells) and which are 2.4 to 2.8 nm in height (corresponding to half-unit-cell thick $m$ = 5 and $m$ = 6 structures).

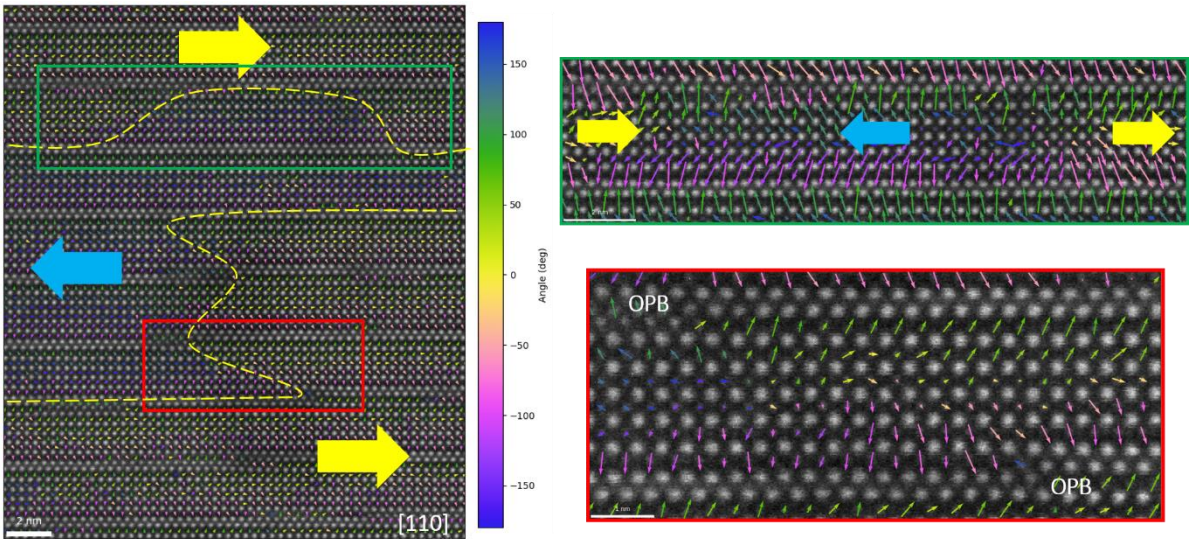


**Figure 4.15** HAADF-STEM images of B6TFMO thin film on 0.2 ° mis-cut sapphire where polarisation displacement vectors of the *B*-site cation are mapped using TEMUL toolkit [55]. In this figure, the colour of the arrow indicates the direction that polarisation is pointing in, with yellow arrows (orientated 0 °) indicating that polarisation is pointing towards the right and with blue arrows (orientated 180 °) indicating that polarisation is pointing towards the left. In the insets, the size of the arrow correlates to the magnitude of the displacement of the *B*-site cation. The dashed yellow curved line gives an approximate location of charged domain walls within the image. The large arrows indicate an approximate overall direction of polarisation within the ferroelectric domains present. Green Inset: shows an enlarged region of nominally charged 180 ° Head-to-Head and Tail-to-Tail domain walls. Red Inset: shows that a polar vortex is present in a region containing a nominal 180 ° Tail-to-Tail charged domain wall between two OPB defects.

Further evidence for polar vortex formations were observed within the newly synthesised films in this work. Interestingly, as **Figure 4.15** demonstrates, the polar vortex observed is created and stabilised between two OPBs that are spaced at a further 12 perovskite unit cells apart (~5 nm apart). Although it can be noted that from 8 perovskite unit cells to the right of the top OPB, the in-plane polarisation is now distinctly going in one direction and that the size of the completely rotated polar vortex is comparable to those observed in B6TFMO before.

## 4.4 Conclusions

The synthesis of B6TFMO films on vicinal sapphire surfaces were examined and the impact of the substrate surface on thin film growth has been assessed. DIFFaX XRD θ/2θ simulations show that (00*l*) reflections such as the (00$\underline{10}$), (00$\underline{12}$) and (00$\underline{14}$) are not as impacted by the inclusion of intergrowths within the 5 layer Aurivillius phase structure in comparison to the other reflections such as the (006), (008), (00$\underline{18}$) and (00$\underline{20}$) reflections. Macroscopically through experimental XRD measurements, there is broadening of the FWHM for reflections corresponding to films grown on higher mis-cut sapphire, particularly the (006), (008), (00$\underline{18}$) and (00$\underline{20}$) indicating a higher defect density is present in the films when grown on higher mis-cut substrates.

The substrate surface on which the B6TFMO films are grown on and disruptions to the periodicity of the Aurivillius phases by the inclusion of sub-unit-cell defects has a marked effect on the film morphology and ferroelectric properties. PFM measurements of the films reveal that the density of the ferroelectric domains increase with the increase of defect density through increasing the substrate mis-cut angle. As the substrate mis-cut angle increases, the grain size within the B6TFMO films decrease. This could be caused by the decrease in the size of the step terrace widths as mis-cut angle increases, where the step width is ~70 ± 20 nm for 0.2 ° mis-cut sapphire compared to ~7.4 ± 2.9 nm for 10 ° mis-cut sapphire. As step terraces can often act as nucleation sites during thin film deposition, the smaller steps associated with the 10 ° mis-cut substrates create films with a smaller crystal grains and thus smaller ferroelectric domains. It is very common for structural defects such as OPBs to be present along grain boundaries, therefore the smaller grain size within the B6TFMO films on 10 ° mis-cut sapphire also contributes to the increase of structural defects with the films.

Through cross-section STEM imaging, it is observed that the substrate mis-cut angle can affect the direction of the film growth. In the B6TFMO film on 10 ° mis-cut sapphire, some crystal grains lie at a ~10 ° angle, following the orientation of the substrate steps, but this is not seen in the B6TFMO film on 0.2 ° mis-cut sapphire. For the B6TFMO film on 10 ° mis-cut sapphire it was shown that the crystal grain is oriented in the (100) direction the as-grown film does not follow the surface steps while when the crystal grain is oriented in the (110)

direction the grain that grows at a ~10 ° angle, however further imaging in needed to be conclusive of this finding.

Looking more closely at the grains within the B6TFMO film on 10 ° mis-cut sapphire (**Figure 4.8**), comparisons between areas where the crystal grains grow at 0 ° vs. 10 ° can be drawn and show that the orientation of the grains differ. From the inset in **Figure 4.8 (a)**,it is shown that the as-grown film does not follow the surface steps and the grain is oriented in the (100) direction. In this area the initial $[Bi_2O_2]^{2+}$ interlayer at the substrate/thin film interface ignores the ~10 ° substrate steps and grows parallel (flat) to the overall substrate. In **Figure 4.8 (b)**, the orientation of the grain that grows at a ~10 ° angle with the mis-cut surface steps is (110) orientated, with the initial $[Bi_2O_2]^{2+}$ interlayer at the substrate/thin film interface growing along the ~10 ° surface steps. Further imaging needs to be carried out in B6TFMO thin films on 10 ° mis-cut sapphire to ensure that this change in orientation is experienced for all grains that are grown at a 0 ° vs. 10 ° angle. This observation indicates there is a possibility that the ~10 ° step edge may help nucleate grains within the B6TFMO thin film in a particular crystal orientation.

HAADF-STEM imaging enabled a closer examination of defects and revealed that OPB defects were present within all the thin films examined. Charged domain walls alongside exotic polar vortices facilitated by OPBs are also observed. In this work, the conditions for the formation of polar vortices appear to be more relaxed than initially thought. These vortex topologies are present at charged domain wall regions where OPBs are present and while initial reports indicated that it was required to have OPB defects spaced between 3 to 4 nm apart, in this contribution it is shown that a polar vortex can form between two OPB defects that are ~5 nm apart.

This work offers valuable insight into the role of mis-cut sapphire substrates on the growth of B6TFMO thin films which demonstrate that increasing mis-cut provides a method for increasing and controlling the density of structural defects, ferroelectric domains, ferroelectric domain walls and the associated emergent properties within the films.

# 5 Influence of Patterned Sapphire Substrates on the Multiferroic Properties of Aurivillius Phase Thin Films

In this chapter, all research is the work of the author, with the exception of the following contributions from collaborators: B. Sheehan (Tyndall-UCC) prepared cross-section lamella of the samples. S. Stock and J. Peters (Trinity College Dublin) carried out scanning transmission electron microscopy and aided in the interpretation of the analysis. L. Keeney (Tyndall-UCC) acquired the atomic force microscopy images using the Bruker Dimension Icon tool. M. Bansal and T. Maity (Indian Institute of Science Education and Research, Thiruvananthapuram) acquired and aided in the interpretation of the magnetic measurements.

## 5.1 Introduction

$Bi_6Ti_xFe_yMn_zO_{18}$ (B6TFMO), is an example of an odd-layered Aurivillius phase room temperature (RT) magnetoelectric multiferroic, where '*m*', the number of perovskite units per half-cell, is equal to five [162], [163]. The origin of ferroelectricity within the Aurivillius phases (through stereo-chemical activity of the $Bi^{3+}$ lone pair electrons at the *A*-site and through $Ti^{4+}$ distortion at the *B*-site caused by the pseudo/second order Jahn-Teller effect) is well established. Crystal symmetry of B6TFMO dictates that the major polarization (~40 $\mu C/cm^2$) arises spontaneously along the *a*-axis, typically lying along the in-plane, lateral direction in conventional B6TFMO films coming from grains where the long *c*-axis is perpendicular to the substrate [154], [161], [196], [275], [327]. In even layered-Aurivillius phases, the out-of-plane polarisation components have an anti-polar ordering, where the polarisation faces towards the $[Bi_2O_2]^{2+}$ dielectric interlayers and this polarisation cancels out due to the presence of a horizontal mirror plane [154], [160]. However, a weak (~0.4 $\mu C/cm^2$) out-of-plane polarisation can be measured for the odd, five-layered phase due to the breaking of its horizontal mirror plane and retention of the two-fold rotation axis [328]. Due to this breaking of the horizontal mirror plane within the odd layered Aurivillius systems, areas in B6TFMO have either a minor net-up or net-down out-of-plane polarisation resulting from the displacement of the *B*-site cation in the *c*-axis direction. Improving the accessibility of the *a*-plane and major polarization vector in vertical architectures employing B6TFMO could improve its ability to be utilised in circuit designs for device applications with 3-*D* stacks. In contemporary ferroelectric random

access memories, the most common device design utilises a metal-insulator-metal geometry, where the ferroelectric material is sandwiched between a top and bottom electrode. In these device architectures, the electric field is perpendicular to the film plane. Therefore, materials with a vertical polarisation are optimal for effective domain switching. In lead zirconate titanate (PZT) thin films, it has been found that application of either a tensile or compressive stress by utilising an appropriate underlying substrate can tailor the presence of either a majority lateral or majority vertical polarisation in the film [329]–[331]. For hysteresis loop measurements in the vertical direction using capacitor type electrodes in metal-insulator-metal based devices, it has been demonstrated that PZT samples with predominant in-plane polarisation have reduced polarisation in the ferroelectric hysteresis when compared to PZT samples having predominant out-of-plane polarisation [332], [333]. Subsequently, one manner in which the ferroelectric switching of B6TFMO could be optimised in metal-insulator-metal based devices is through accessing the major in-plane polarisation by orientating it towards a vertical direction. Watanabe *et al.* [196] investigated the impact of orientation of individual anisotropic crystals on ferroelectric device performance utilising Aurivillius phase thin films, $SrBi_2Ta_2O_9$ ($m$ = 2) and $Bi_4Ti_3O_{12}$ ($m$ = 3). Films were grown via metalorganic chemical vapour deposition (MOCVD) on (100)$SrTiO_3$, (110)$SrTiO_3$ and (111)$SrTiO_3$ single crystal substrates to orient the deposited Aurivillius phase films along particular crystal planes. It was observed that the out-of-plane polarisation-electric field hysteresis loops for the Aurivillius phase films grown on the (110)$SrTiO_3$ substrates exhibited a larger polarisation compared to the Aurivillius phase films on the (100)$SrTiO_3$ substrates, due to the change in orientation of the major spontaneous polarisation vector towards the vertical direction.

The epitaxial growth of impurity free B6TFMO has not yet been well established [171]. Hence the aim of this work was to reorient the crystal grains of the B6TFMO Aurivillius phase by using a different approach to Watanabe *et al.* [196]. Sapphire is proven as a suitable substrate for the phase-pure growth of non-epitaxial B6TFMO films [162], [163], therefore in this research, sapphire substrates that have been micro-patterned with sapphire domes are used to encourage the reorientation of the B6TFMO films grains towards the vertical direction. Patterned substrates with domed features have previously been found to enhance the properties of other material systems, such as GaN based ultra violet light emitting diodes

(LED), through the reduction of dislocations within the material [334], [335]. Moreover, the LED lifetime and light extraction efficiency of GaN based LED devices are improved through the use of patterned sapphire substrates when compared to devices made using un-patterned sapphire. For example, in work by Wang *et al*. [336] who used patterned sapphire substrates where the central angle of the dome was 10 °, the efficiency of the LED increased by 19 % compared to using un-patterned sapphire substrates, without a decrease in crystalline quality.

Increasing levels of integration of ferroelectric thin films into devices requires the ability to conformally coat miniature features having challenging aspect ratios at sub-micron scales and ultimately at the nanoscale. Chemical vapour deposition (CVD) offers the capability to deposit uniform and conformal thin films of high crystallinity over three-dimensional structures and within trenches using scalable growth processes [337]. Liquid delivery direct liquid injection chemical vapour deposition (DLI-CVD) involves transporting vaporised precursors over a substrate, such that a solid film forms on the substrate through a variety of mechanisms such as thermal, decomposition, reduction and exchange reactions. This deposition method allows for the well-controlled growth of thin films on substrates with uniform thickness and low porosity. The technique is ideal for potential emerging technologies where non-standard substrates e.g. curved, patterned or stretchable, may be used, but where uniform thin films with controlled surface morphologies are still required [197]. In this work, DLI-CVD is utilised with the objective of synthesising conformal B6TFMO thin films that follow the surface features of patterned sapphire substrates.

In this chapter, substrates patterned with dome-type structures are investigated to encourage inclination of the *a*-axis of B6TFMO towards an upright geometry in order to access the major ferroelectric polarisation in the vertical direction.

## 5.2 Methods

Aurivillius phase thin films, $Bi_6Ti_xFe_yMn_zO_{18}$ (B6TFMO; x = 2.93 to 3.14; y = 1.38 to 1.59; z = 0.48 to 0.50), were synthesised by DLI-CVD via a horizontal flow AIXTRON AIX 200/4FE AVD (atomic vapour deposition) system [284], [285]. $Bi(thd)_3$, $Fe(thd)_3$ and $Ti(O\text{-}iPr)_2(thd)_2$ (where thd = 2,2,6,6-tetramethyl 3,5-heptanedionate and O-iPr = isopropoxide) dissolved in toluene were used as bismuth, iron and titanium precursor solutions, respectively and are

commercially available from Epivalence Ltd. [284], [285]. The manganese precursor was prepared by dissolving $Mn(thd)_3$ (99 %, STREM chemicals) in anhydrous toluene (99.8 %, Sigma-Aldrich) under $N_2$ in a glovebox. The thin films were grown over a series of growth runs using a two-step process [162] on *c-m* sapphire (un-patterned) and patterned sapphire substrates. Step One involved deposition at 630 °C and Step Two involved crystallisation using a post-deposition anneal at 850 °C. The patterned substrates had one polished side where the surface is fabricated with micro-patterned domes (height= 1.6 µm, base = 2.5 µm, pitch = 2.9 µm), as shown in **Figure 5.1**. All substrates were cleaned by first sonicating in acetone for five minutes, then rinsing with isopropyl alcohol followed by deionised water and subsequently dried using $N_2$ gas. Both a patterned and an un-patterned sapphire substrate were loaded into the reaction chamber for each deposition run, such that a direct comparison utilising the same deposition conditions could be made. The reactor chamber was set at a pressure of 10 mbar while the temperature of the rotating susceptor-heated sample holder was set to 630 °C (Step One). These conditions were maintained for the entirety of the deposition process. The low vapour pressure precursors were then injected using nitrogen pulses into the Trijet Vaporizer of the DLI-CVD system, where they entered a reactor (growth) chamber via lines maintained at 220 °C. Precursors were mixed with reactive $O_2$ gas during the growth run. A total gas flow of 3000 sccm (standard cubic centimetres per minute) was maintained in the growth chamber comprised of $O_2$ run gas and $N_2$ carrier gas where the $O_2$ flow was 1000 sccm. The precursor volumes were controlled electronically by setting the opening time for each injection between 1.3 and 15.3 ms, depending on the relevant precursor. A continuous injection mode was employed where the injections pulsed at a frequency of 1 Hz. A set number of injections of each precursor were selected and pulsed, depending on the requirements of the deposition run. For this study, the number of injections used for a deposition run was varied from 100 to 800 injections. The net precursor flow was monitored using liquid flow meters. An excess (11 to 19 %) of $Bi(thd)_3$ was used in order to circumvent the volatile nature of bismuth [287], [288] and to promote crystallisation of phase pure B6TFMO samples after the post-deposition anneal step of 850 °C (1 hr in atmosphere, Step Two).

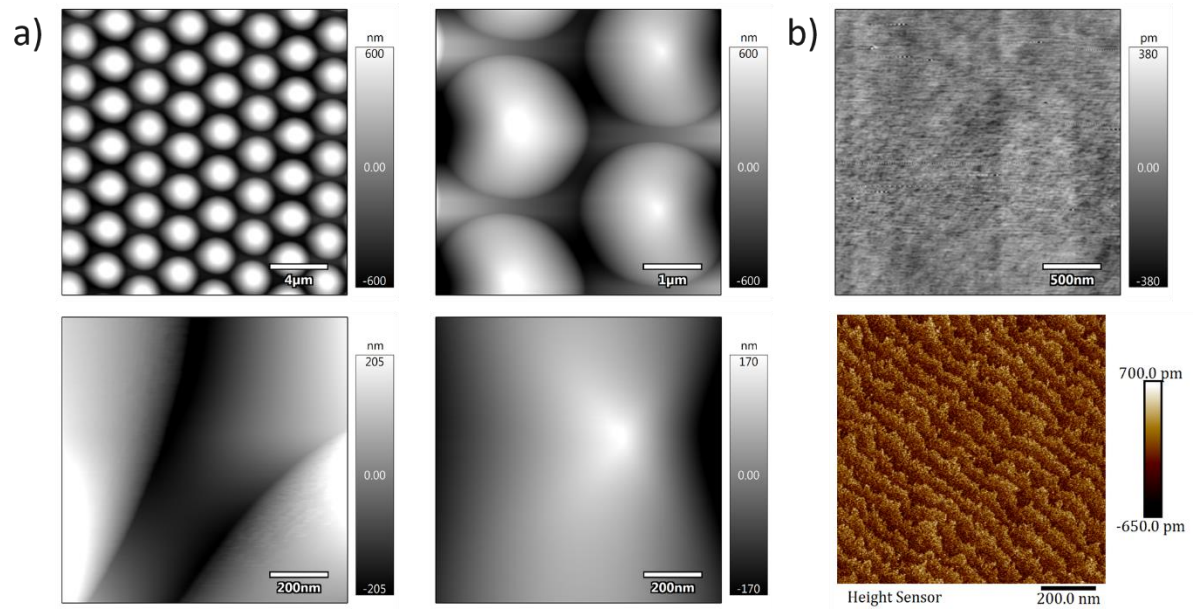


**Figure 5.1** AFM images of surfaces of bare sapphire substrates. a) (four images on the left) has a patterned sapphire surface made up of domes (height = 1.6 µm, base = 2.5 µm, pitch = 2.9 µm) and b) (two images on the right) is un-patterned sapphire displaying surface steps, where the terrace widths are ~70 ± 20 nm and the step heights are ~0.6 ± 0.1 nm.

Atomic Force Microscopy (AFM) and Piezoresponse Force Microscopy (PFM) were performed using an MFP-3D$^{TM}$ Asylum Research instrument. AFM on this instrument was carried out using AC mode with Olympus AC240TS probes (Al reflex coated, 15 nm tip radius, 70 kHz resonant frequency). PFM was conducted in lateral (LPFM) and vertical (VPFM) Dual AC Resonance Tracking (DART-PFM) mode [234]. The DART-PFM mode was used to boost the piezo signal while minimising instrumental crosstalk. Drive amplitudes of 1 to 2 $V_{AC}$ and 2 to 3 $V_{AC}$ were used for measurement of the piezoresponse in LPFM and VPFM modes respectively. Centre drive frequencies in the range of 742 to 792 kHz were used for the LPFM measurements and 258 to 282 kHz were used for the VPFM measurements. A frequency width of 10 kHz was used for all the measurements. The probes used were Oxford Instruments AC240TM-R3 electrilevers (Ti/Pt coated silicon probes, Al reflex coated, 25 nm tip radius, 70 kHz resonant frequency)).

Atomic Force Microscopy (AFM) of the bare sapphire substrates was carried out to obtain topographical profiles of the surface steps. A commercial Bruker Dimension Icon in PeakForce Tapping mode (with Bruker SCANASYST-AIR probes, Al reflex coated, 2 nm tip radius, 70 kHz resonant frequency), was used.

X-ray diffraction (XRD) measurements were performed using an X'pert Diffractometer (Cu Kα radiation λ = 0.1541876 nm) (45 kV, 40 mA). The typical 2θ scan range was from 5 ° to 50 ° with a step size of 0.005 °. In this chapter, the XRD diffraction patterns were indexed using reference data from García-Guaderrama *et al.* [258] for the *m* = 5 phase.

The B6TFMO lamella cross sections were prepared initially using the TESCAN Solaris. The lift-out of the lamella and the final polishing were performed using the FEI Helios (FEI DualBeam Helios NanoLab 600i). STEM imaging in Tyndall was carried out using an Oxford EDX detector at 20 kV. Further STEM-HAADF imaging was acquired in Trinity College Dublin using the FEI Titan FEG (S)TEM at 300 kV.

The magnetic measurements were performed in a Quantum Design MPMS3 magnetometer with maximum temperature range of between 2 to 350 K and applied magnetic field range of ±7 T. The sample was demagnetized at RT by an appropriate demagnetization protocol and the magnet was reset before starting the measurement. This removes any stray field present in the sample or the superconducting coils of the magnetometer [338]. Temperature dependent magnetization (*MT*) measurements were performed for three protocols; field cooling (FC), zero field cooling (ZFC) and remanence (REM) to locate possible phase transitions in the sample. For ZFC *MT* measurements, the sample was first demagnetized at RT, then cooled down from 350 K to 2 K with zero bias field. A field of 100 Oe was then applied and the moment was measured as a function of temperature while ramping from 2 K up to 350 K. Next, similar measurements were performed immediately to acquire FC *MT* measurement while cooling from 350 K to 2 K under 100 Oe bias field. Afterwards, the applied field was removed and magnetization was measured while heating from 2 K to 350 K to get REM *MT*. Magnetization versus field (*MH*) measurements were carried out at different temperatures to understand the effect of temperature on the ferromagnetism of the sample.

## 5.3 Results and Discussion

### 5.3.1 Investigations of Thin Film Conformality

Initial approaches to the growth of bismuth-based Aurivillius phase thin films investigated the use of low-cost substrates such as silicon, quartz and sapphire. For films on silicon and quartz substrates, it was found that a reaction occurred during the anneal step between bismuth and silicon at the film-substrate interface, resulting in an amorphous $Bi_2O_3$-$SiO_2$ impurity phase [339]. On the other hand, sapphire substrates were found to be chemically stable with respect to growth of the bismuth-based Aurivillius phases at the high temperatures required for Aurivillius phase crystallisation. In this work, both un-patterned and patterned sapphire substrates were used as they were cost effective and readily available commercially. The thin films that were initially deposited at 630 °C onto the patterned sapphire substrates by DLI-CVD were conformal to the substrate topography and were amorphous, as shown in **Figure 5.2**. To obtain the crystalline *m* = 5 B6TFMO phase, a post-deposition anneal step at 850 °C was carried out. The 850 °C post-deposition anneal is required to crystallise B6TFMO due to the limitations of the DLI-CVD kit, where the maximum temperature it can operate safely at is 710 °C. Therefore, a two-step process is required to form crystalline B6TFMO. First a deposition step at 630 °C, where an amorphous film is deposited, followed by a subsequent anneal step at 850 °C to crystallise the material. Since sapphire (hexagonal lattice parameter of $a$ = 4.758 Å (+22.31 % mismatch)) does not allow for epitaxial matching with B6TFMO (pseudo cubic lattice parameter of $a_p$ = 3.89 Å), polycrystalline grains of B6TFMO crystallised in their natural layer-by-layer fashion. While the underlying substrate steers the orientation of film growth, there is a tendency for the polycrystalline Aurivillius phase grains to crystallise independently from both the underlying un-patterned and patterned sapphire substrates, discussed in more detail below.

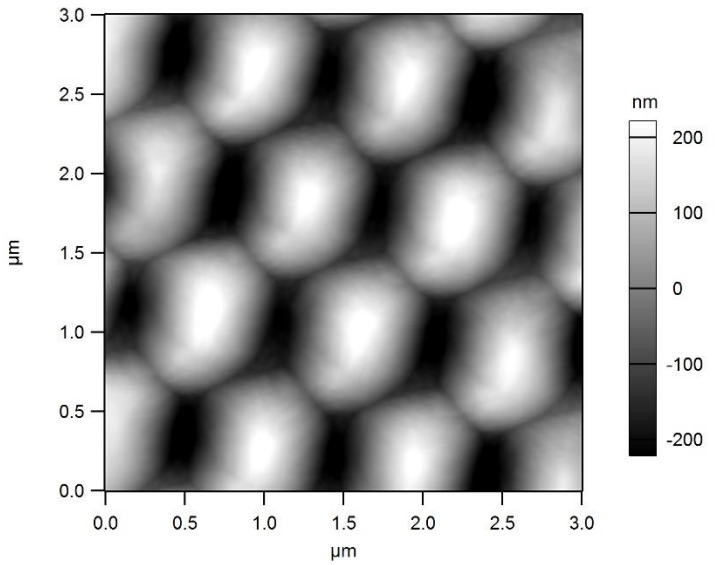


**Figure 5.2** AFM image of an amorphous B6TFMO thin film on patterned sapphire deposited via DLI-CVD with 100 injections at a process temperature of 630 °C.

In **Figure 5.3 (a)** and **(c)**, as expected, similar film characteristics for B6TFMO grown on un-patterned sapphire substrates are observed, when compared to those observed for the 800-injection deposited B6TFMO films in **Chapter 4**. In this study, the films had an average thickness of 88 ± 16 nm, as determined from measurements of nineteen STEM image data points over a ~9 µm long lamella section. An average RMS roughness value of 20.9 ± 2.9 nm was measured from five 5 µm x 5 µm AFM scans of the film surface. A typical area is shown in **Appendix II Figure III.1 (e)**. The B6TFMO films deposited on un-patterned sapphire also show the same surface features contributing to the thin film surface roughness previously discussed in **Section 4.3**, such as the Aurivillius phase micro-crystallites. An example of these features can be seen in **Figure 5.3 (a) and (c)**. In this case, the Aurivillius phase micro-crystallites are approximately 30 nm thick, lying on top of a ~75 nm section of the Aurivillius phase B6TFMO film. From an approximately 9 µm long lamella section taken from the B6TFMO grown on un-patterned sapphire, seven micro-crystallites were present ranging in height from between 20 to 50 nm. No clear micro-crystallites can be observed on the B6TFMO films deposited on the patterned sapphire. The B6TFMO film deposited on the patterned substrate is less uniform than those on the un-patterned sapphire. The plate-like B6TFMO grains can be observed in certain locations overlapping each other in **Figure 5.3 (b)** and do not strictly follow the orientation of the patterned sapphire substrate underneath. In other areas, such as at the top of Dome 3 in **Figure 5.5**, the substrate is not fully covered by the

B6TFMO film; the film thickness over the substrate varies from areas with no B6TFMO film present, to areas with a thickness of over 100 nm. Analysis of the 800-injection lamella section shown in **Appendix III Figure III.2**, reveals that ~11 % of the substrate had no B6TFMO coverage, while for the thinner 700-injection lamella shown in **Figure 5.4**, the extent of regions without B6TFMO coverage increases to ~16 %. Conversely, for the region shown in **Figure 5.3 (d)**, the entire sapphire dome surface is covered with a B6TFMO film. Here, the B6TFMO sample deposited via DLI-CVD with 800 injections has a film thickness along the side of the dome between ~70 to 85 nm thick. The B6TFMO film is measured to be much thinner at the flat region in between the domes, having a thickness of ~40 nm. From a 9 µm long lamella of the 800 injection deposited B6TFMO, where there are three domes (**Figure 5.4**), the average thickness of the film was 58 ± 31 nm. This indicates that the films on patterned substrates are overall thinner compared to films on un-patterned sapphire. This difference in the thickness between the films on patterned vs un-patterned sapphire could be related to the presence of surface steps on the un-patterned substrates shown in **Figure 5.1 (b)**, which would aid the nucleation and subsequent crystallisation of B6TFMO. In similar AFM images of the patterned substrates, steps on the sapphire surface are not visible, **Figure 5.1 (a)**.

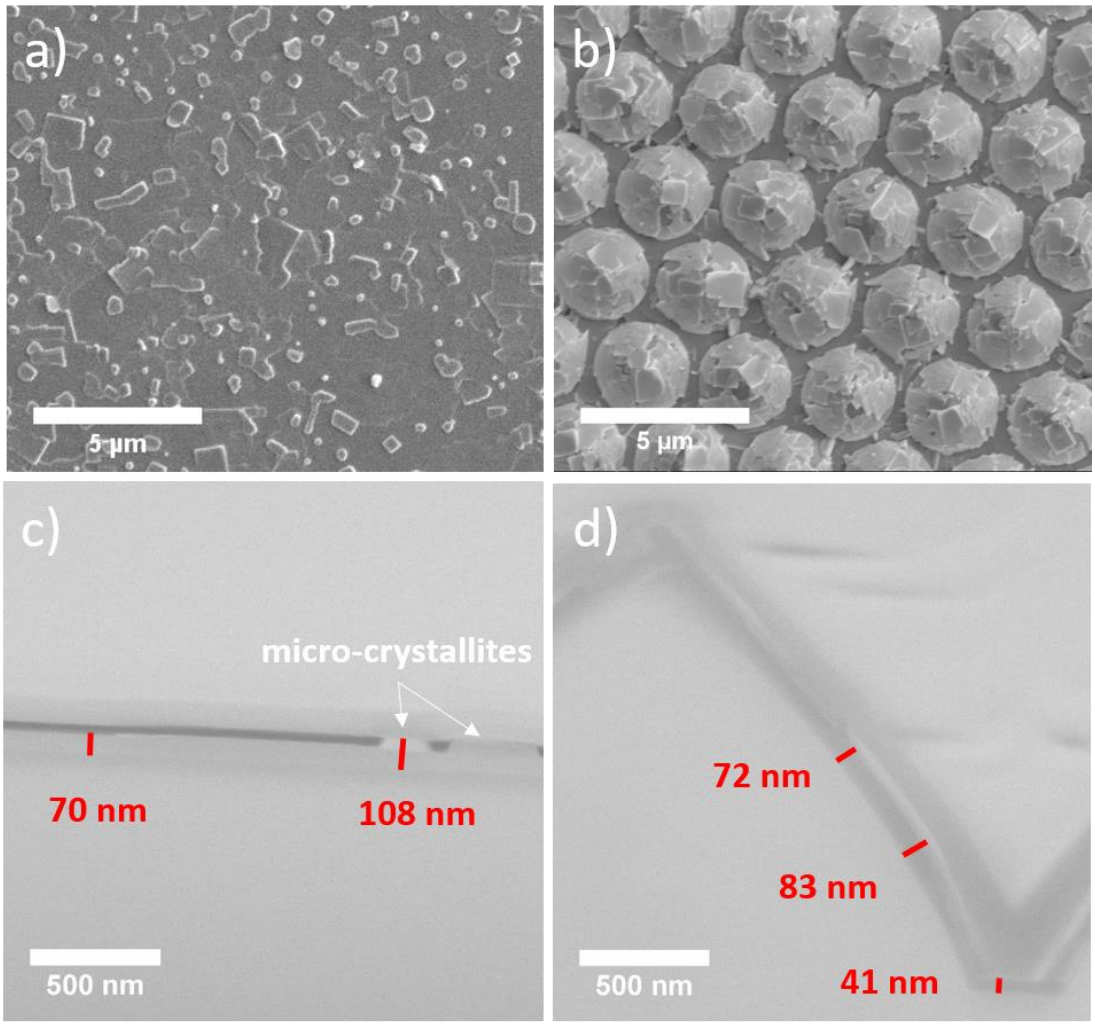


**Figure 5.3** SEM images of 800 injection B6TFMO on a) un-patterned, b) patterned sapphire. Cross-section STEM image of B6TFMO on c) un-patterned and d) patterned sapphire.

By inspecting the cross-section STEM image of the domes on the patterned sapphire shown in **Figure 5.4**, it can be observed that the domes are hemispherical and that the incline on which the B6TFMO crystallises is not linear over the patterned surface. In-between the domes and at the very top (summit) of the dome, the film can crystallise parallel to the overall substrate at 0 ° (e.g. Dome 1 in **Figure 5.5**). Moving from the base of the dome towards the dome summit, the slope of the incline decreases. For example, as shown in **Appendix III Figure III.3**, the slope near the base of the dome was calculated to be approximately 1.9, while near the top of the dome the slope was calculated to be 0.4. From examination of the cross-section STEM image of the sample in **Appendix III Figure III.3**, a comparison of the B6TFMO crystals that grow in between the sapphire domes to those that grow on top of the sapphire domes, reveals that there is up to a 60 ° difference in the angle at which the crystals orientate.

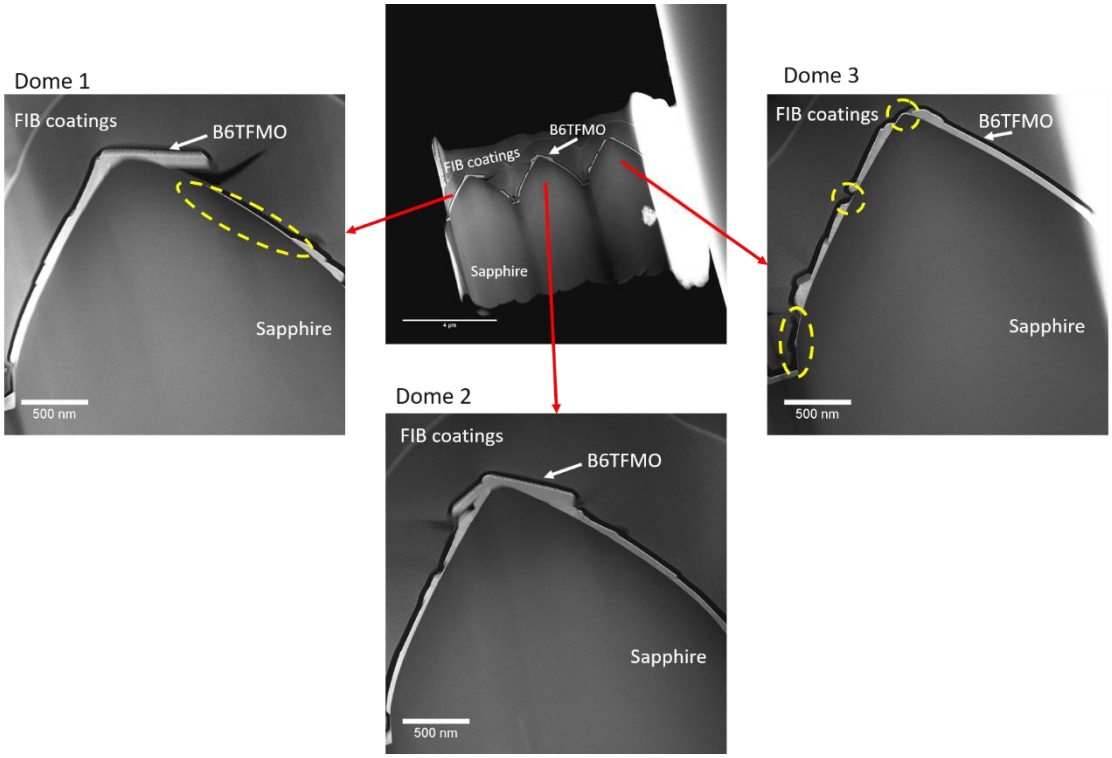


**Figure 5.4** STEM images of a FIB lamella of a B6TFMO film deposited with 700 injections on patterned sapphire domes.

Segments of a cross section of a 700-injection B6TFMO film on sapphire are viewed via HAADF-STEM imaging in **Figure 5.5**, where the full lamella is shown in **Figure 5.4.** Within **Figure 5.5**, it can be observed that, similarly to the 800-injection B6TFMO film in **Figure 5.3**, the material does not uniformly coat the substrate surface. In **Figure 5.5**, it is evident that due to the nature of the layer-by-layer crystallisation process, the Aurivillius phase poly-crystals find difficulty in fully conforming with the curvature of the domes and the more complex geometries at the top of the domes. As shown for the areas marked with dashed yellow circles in **Figure 5.4** and **Figure 5.5** on Dome 1 and Dome 3, there are gaps in the film where no B6TFMO is present.

While the initial DLI-CVD deposition at 630 °C (Step One) allows for a thin film to conformally coat the patterned sapphire substrate (demonstrated by the AFM image in **Figure 5.2**), this conformal coat is disrupted during the post-deposition anneal step (Step Two). The post-deposition anneal step at 850 °C is required to provide energy to the system to crystallise. However, this annealing step also gives energy that allows for the reformation of the thin film and changes the coverage of the film over the sapphire substrate as the

polycrystalline grains are formed. The layered structure of the Aurivillius phases determines the nature of the crystallisation mechanism for the material. The layered structure promotes preferential crystallisation of grains in directions perpendicular to the stacking axis of the layers, resulting in crystals with plate-like characteristics. When annealed at temperatures above 800 °C on non-epitaxial substrates, the *m* = 5 Aurivillius phase tends to have unevenly distributed plate-like grains, with relatively large lateral dimensions and minor dimension parallel to the *c*-axis [275], [287], [340]. This type of crystallisation can be advantageous for yielding anisotropic, preferentially *c*-axis grain-orientated Aurivillius phase films. However, in the absence of an epitaxial template on a complex and curved surface, such as the domes patterned on the sapphire substrate, the crystallisation process yields independent poly-crystallites with a thin elongated rectangle plate-like morphology that crystallise at different *a*/*b* orientations and can result in gaps appearing within the film. In Dome 1 and 2 (**Figure 5.5**), some Aurivillius grains on the patterned sapphire substrate continue to elongate independently without any substrate underneath, rather than bending with the curve of the sapphire domes. At the top of Dome 1 (shown in **Figure 5.5** and marked with a dashed green box), the crystal grain extends approximately 300 nm beyond the top of the patterned sapphire substrate. This grain is fixed only at one end, with the remainder of the grain to the right unsupported by the substrate underneath. The patterned sapphire substrate underneath is bare, with no B6TFMO film evident. While for the example shown in the dashed red circle for Dome 2 in **Figure 5.5**, the patterned substrate is covered by more than one Aurivillius phase grain. The tendency for the Aurivillius phase to crystallise as independent plate-like grains allows for sections of the Aurivillius phase film to crystallise independently of the substrate during the grain-growth step of crystallisation. Once the Aurivillius phase grain nucleates and starts growing at a particular angle, the drive to continue to crystallise in a plate-like manner is strong and the ceramic can maintain the grain growth direction without an underlying substrate. This horizontal lamellar-type crystallisation of the grain is preferred by the system over a situation where the grain would curve over the curved surface at the top of the patterned dome.

While several of the crystal grains making up the film do not follow the underlying substrate as discussed above, it can be seen for most regions of the domes (with the exception of the summit) that the Aurivillius phase follows the substrate. For example, to the right of

Dome 3 shown in **Figure 5.4** and **Figure 5.5** , it can be observed that the film follows the orientation of the patterned sapphire substrate. Within the orange inset in Dome 3, the crystal domain boundaries appear similar to those observed in films on un-patterned sapphire, for example to that observed in **Chapter 4, Figure 4.7 and Figure 4.10***,* where two poly-crystalline grains meet, separated by a grain boundary.

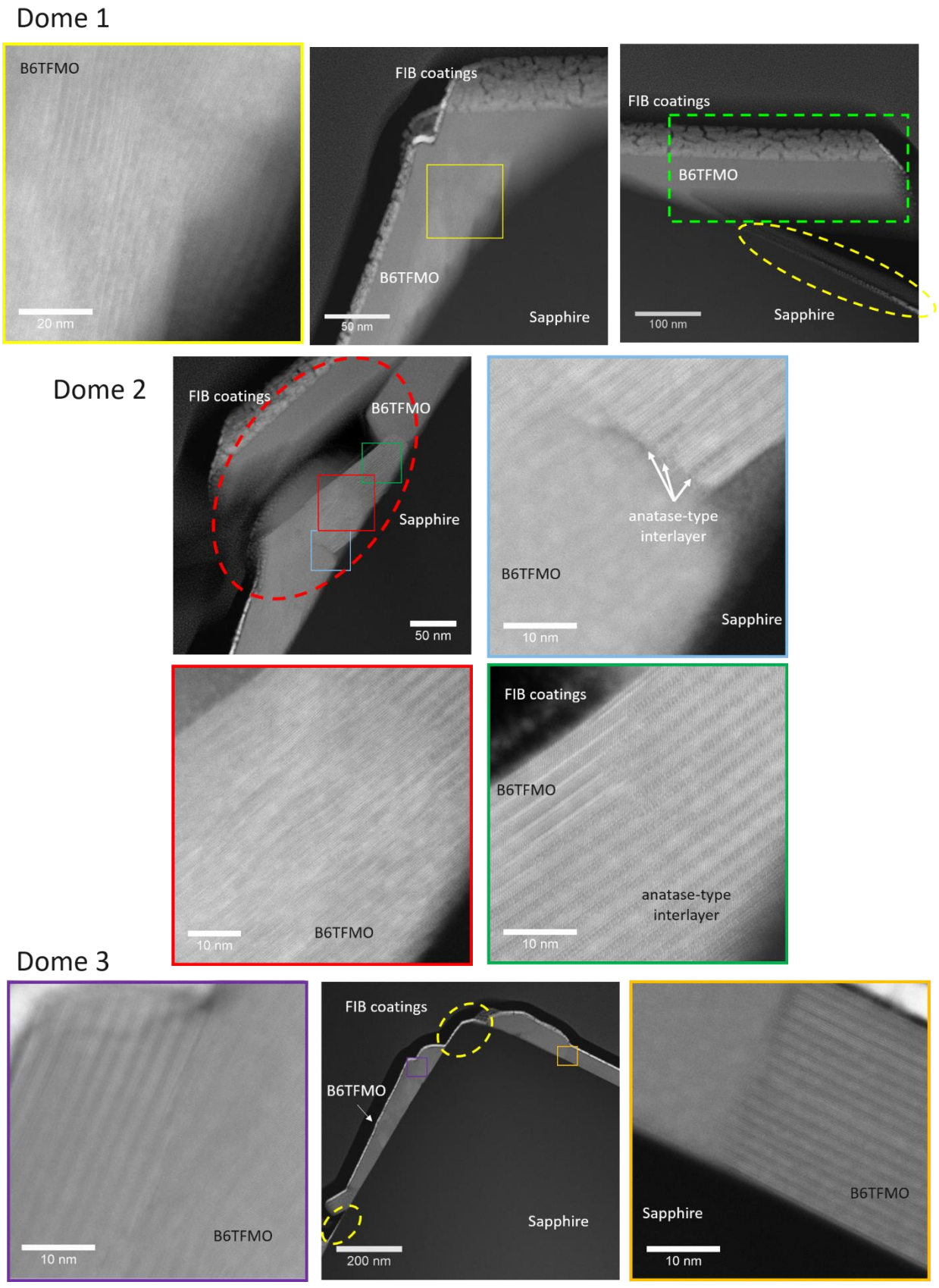


**Figure 5.5** Representative cross-section STEM images of 700 injection B6TFMO on a patterned sapphire substrate.

### 5.3.2 Investigations of Influence of Substrate on Thin Film Orientation

In the following section, differences in thin film orientation between B6TFMO films grown on patterned versus un-patterned sapphire substrates are compared. The Lotgering factor (f) [341] gives a measure of the distribution of the crystallite orientation of a particular sample. This factor can indicate if the crystallites within a material prefer any one orientation. For the B6TFMO system, the thin film samples on sapphire typically prefer the (00*l*) orientation. In this work the Lotgering factor is calculated by equation 5.1:

$$f = \frac{P - P_0}{1 - P_0} \qquad 5.1$$

where

$$P = \frac{\Sigma I(00l)}{\Sigma I(hkl)} \qquad and \qquad P_0 = \frac{\Sigma I(00l)_0}{\Sigma I(hkl)_0} \qquad 5.2$$

*P* describes the experimental sample being analysed, where ΣI(*hkl*) is the sum of the intensities from all the peak reflections present in the XRD pattern and ΣI(00*l*) is the sum of the intensities of all (00*l*) reflections present (as shown in **Figure 5.6**). $P_0$ is representative of a randomly orientated sample, where ΣI(*hkl*)$_0$ and ΣI(00*l*)$_0$ are the sum of all the reflections and the (00*l*) reflections respectively. In this work, the values used for the randomly orientated sample were obtained from data provided by García-Guaderrama *et al.* [258] and extracted using Vesta [296]. For the sample on un-patterned sapphire, *f* has a value of 0.932, while for the sample on patterned sapphire, the value of *f* decreased to 0.828. This indicates that the B6TFMO grown on patterned sapphire substrates have more crystallites orientated in different (*hkl*) directions than compared to growth on un-patterned sapphire. From analysis of the data used to generate a randomly orientated sample [258], the most intense (*hkl*) reflections that might be expected to emerge in the XRD pattern of the B6TFMO on patterned sapphire, outside of the (00*l*) reflections, would be the (111) ~22.9 °, the (11$\underline{1}$1) ~30.5 °, (020) ~33.7 °, (02$\underline{1}$2) ~39.3 ° and the (220) ~46.8 ° reflections.

From the XRD plots shown in **Figure 5.6**, it is evident that the *m* = 5 phase is dominant in both thin films. There are clear differences between the XRD patterns, with the B6TFMO film on un-patterned sapphire (XRD plot shown in red) having more of the (00*l*) reflections present, e.g. with the (004) and (006). Alongside this, all the (*00l)* reflections for the B6TFMO film on the un-patterned sapphire substrate have an increased intensity in comparison to the

XRD pattern for the B6TFMO film on patterned sapphire (XRD plot shown in black). While intensity is in arbitrary units, the XRD data in **Figure 5.6** was acquired under the same conditions and on the same day of analysis, thus both intensities are comparable. It is shown in **Table 5.1** that the FWHM (full width at half maximum) values for the peaks shown for the (00*l*) orientated reflections present in the B6TFMO film on patterned sapphire are larger than that for the film on the un-patterned sapphire substrate. There are a number of factors that can contribute to the broadening of the peaks measured for the film on patterned sapphire, one being the thickness non-uniformity of the film (e.g. in some areas there is no film coverage while on other areas the film is over 100 nm thick). Inclusion of intergrowths of Aurivillius phases having different *m* numbers, as observed by STEM imaging within the film on patterned sapphire (shown later in **Figure 5.7**), could further contribute to the larger FWHM values obtained for the XRD peaks compared to the film on un-patterned sapphire.

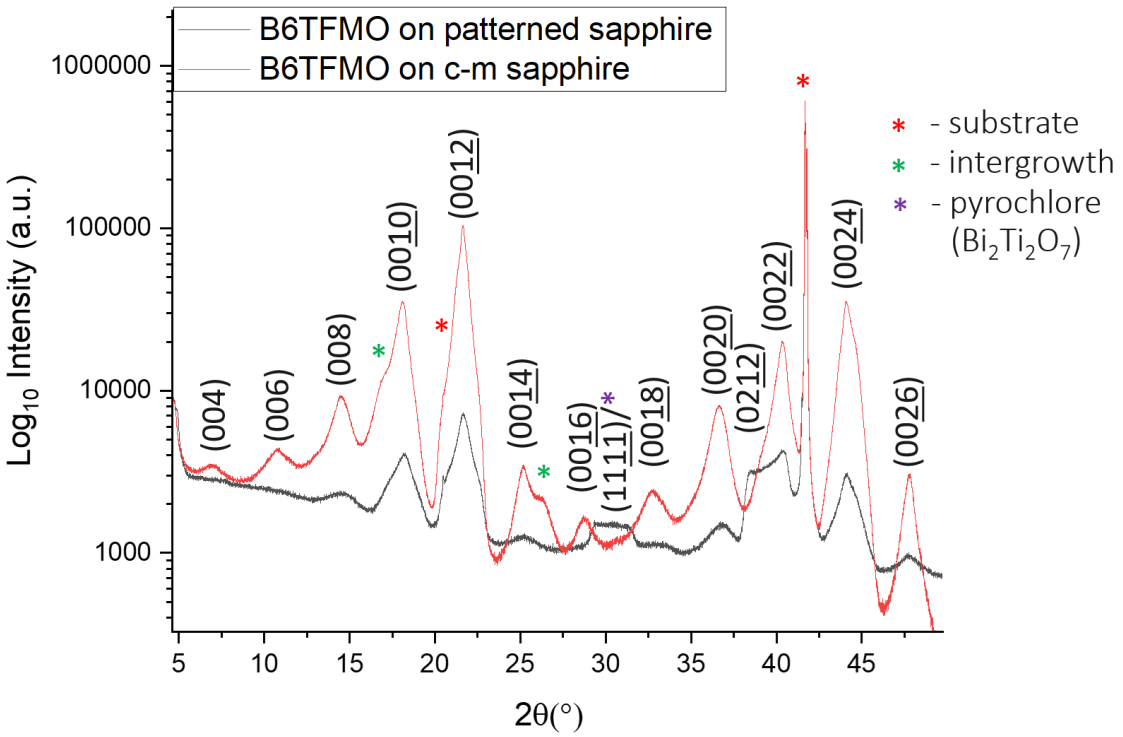


**Figure 5.6** X-ray diffraction patterns of 800 injection B6TFMO films deposited on a patterned sapphire substrate (plot in black) and an un-patterned sapphire substrate (plot in red).

The peak shoulders observed at 2θ angles of ~17.1 °, to the left of the (00$\underline{10}$) peak and at ~26.1 °, to the right of the (00$\underline{14}$) peaks within the XRD pattern of B6TFMO on un-patterned

sapphire (XRD plot in red in **Figure 5.6**) indicate the presence of *m* = 4 intergrowth phases. This is deduced from reference data from Hervoches *et al.* [150] for the $Bi_5Ti_3FeO_{15}$ system, which demonstrates that the (008) reflection for *m* = 4 appears at a 2θ angle of ~17.1 °, whereas the (00$\underline{12}$) reflection is expected at ~25.9 °. While some of the lower intensity lower angle reflections (e.g. (004) and (006)) are not evident in the XRD patterns for B6TFMO on patterned sapphire, two broad peaks are present which are additional to the (00*l*) peaks observed for B6TFMO on un-patterned sapphire. The first additional peak has a 2θ peak centre at ~30.4 ° (the peak position ranges from 2θ angles of 28.8 ° to 32.1 °) which could potentially be due to a (11$\underline{11}$) reflection of the *m* = 5 B6TFMO Aurivillius phase. A second broadened peak is observed between ~38.5 and 40 °. This peak could originate from both the (00$\underline{22}$) and (02$\underline{12}$) reflection of the *m* = 5 Aurivillius phase. The presence of secondary phase inclusions is also considered within these XRD patterns. A possible impurity phase present in the B6TFMO film on patterned sapphire is pyrochlore, $Bi_2Ti_2O_7$. The large broad peak at ~30 ° present in the black pattern in **Figure 5.6** corresponds to the intense (444) reflection at 29.6 ° of the pyrochlore phase (JCPDS 32-0118) and further reflections such as the (222) at 14.6 ° could be present, hidden by the (008) reflection of the *m* = 5 B6TFMO phase. However, from STEM imaging of B6TFMO films on patterned sapphire, no clear evidence for the pyrochlore phase can be observed. STEM analysis shown in the green inset in **Figure 5.5** (Dome 2), reveals 'anatase'-type defects (discussed further in **Section 5.3.3**) within the B6TFMO films on patterned sapphire. Examining the literature data of the *m* = 3 to 6 'anatase'-type structures as collected from X-ray and neutron diffraction by Batuk *et al.* [175], [176], the most intense (00*l*) reflections overlap with Aurivillius phase reflections, possibly contributing to their broadening. When searching for possible contributions to the signal at the 30 ° peak position, potentially very intense reflections from the 'anatase-type' phase ($Bi_{3m+1}Ti_7Fe_{3m-3}O_{9m+11}$), such as the (017) *m* = 3 reflection at ~29.9 °, the (01$\underline{10}$) *m* = 4 reflection at ~31.6 °, the (01$\underline{11}$) *m* = 5 reflection at ~30.5 ° and the (01$\underline{13}$) *m* = 6 refection at ~30.7 ° could be responsible. There is no clear evidence for any magnetic impurities in the films using XRD analysis, however it should be noted that the noise level in any XRD scan places a limit on detectability, meaning that the method is intrinsically unable to detect impurity levels below 1 to 3 vol. %.

| Reflection | FWHM | |
|---|---|---|
| | un-patterned | patterned |
| (0 0 4) | 6.918 ± 0.008 | - |
| (0 0 6) | 2.163 ± 0.073 | - |
| (0 0 8) | 1.182 ± 0.006 | 9.594 ± 1.898 |
| (0 0 10) | 0.978 ± 0.019 | 1.694 ± 0.030 |
| (0 0 12) | 0.700 ± 0.004 | 1.299 ± 0.014 |
| (0 0 14) | * | 2.147 ± 0.068 |
| (0 0 16) | 0.896 ± 0.021 | - |
| (0 0 18) | 1.842 ± 0.051 | - |
| (0 0 20) | 1.109 ± 0.007 | 1.955 ± 0.033 |
| (0 0 22) | 0.787 ± 0.007 | * |
| (0 0 24) | 1.009 ± 0.008 | 1.505 ± 0.012 |
| (0 0 26) | 0.830 ± 0.005 | 1.638 ± 0.039 |

**Table 5.1** FWHM values acquired from XRD patterns shown in **Figure 5.6**. The FWHM was not calculated for reflections marked with an * due to the peaks exhibiting additional shoulders, thus potentially yielding inaccurate FWHM values.

### 5.3.3 Investigations of Boundary Defects, Stacking Fault Defects and Intergrowth Phases

The curved nature of the sapphire dome surfaces, together with the preference for the Aurivillius phase grains to grow in a plate-like manner, leads to the poly-crystalline B6TFMO grains crystallising at a variety of orientations over the substrate. The poly-crystalline grains at these curved regions, both along the incline of the dome and when meeting at the summit of the dome, can result in many grain boundaries meeting within the films. On the left-hand side of Dome 1 (yellow inset within **Figure 5.5**), there is a point at which multiple poly-crystalline grains meet. On the domes where different orientated grains meet, low-angle domain boundaries are present. These low angle domain boundaries are potentially regions where increased migration of volatile $Bi^{3+}$ out of the film has occurred during the high

temperature anneal step. Within the green and blue insets of Dome 2, there are different defects associated with a local decency in $Bi^{3+}$. One type, called 'anatase'-type planar defects [175], [176] are shown in **Figure 5.5** and another type, called of out-of-phase boundary (OPB) defects [166] are shown in **Figure 5.5** and **Figure 5.7**. These types of defects have been previously described in **Sections 1.6.3** and **4.3.4** and are common near low-angle grain boundaries of layered structured materials. In the blue inset, along the grain boundary, the 'anatase'- type planar defect has replaced small segments of the $[Bi_2O_2]^{2+}$ interlayer. However, for the region highlighted by the green inset, nearly the entire crystal grain appears to be made up of perovskite unit cells interleaved between bismuth poor 'anatase'- type interfaces, instead of the fluorite–type $[Bi_2O_2]^{2+}$ interlayer.

Examples of OPB defects can be observed in **Figure 5.7 (b).** The yellow arrows mark the positions where OPB defects have propagated next to a low angle domain boundary (shown within the orange dashed box). OPB defects most commonly occur at the $[Bi_2O_2]^{2+}$ layer in the Aurivillius phases, sometimes associated with stacking-faults within the perovskite layers. Within the region inside the dashed navy box in **Figure 5.7**, projected down a (110) orientation, an example of a very brief stacking fault defect (two to three perovskite unit cells in width)can be seen, where the crystal phase changes from an $m = 4$ structure to an $m = 3$ structure, back to the $m = 4$ phase. The stacking fault here arises at the meeting between two of the perovskite layers. There is bending down of the $[Bi_2O_2]^{2+}$ layer above the fault and two perovskite layers (from an $m = 4$ section) meeting one another and merging into a single perovskite layer (changing to an $m = 3$ section), then an OPB defect brings this section of the material back to the $m = 4$ phase.

STEM and TEM imaging indicates that the type of Aurivillius phase varies considerably throughout the B6TFMO film on patterned sapphire. In some regions, such as orange box from of Dome 3 in **Figure 5.5**, the Aurivillius phase is made up of mainly $m = 5$ perovskite layers with occasional $m = 4$ or 6 intergrowths. However, in other regions such as the B6TFMO region shown in **Figure 5.7 (b)**, large deviations from the $m = 5$ phase are present. Where the material seems to be mainly be comprised of the $m = 3$ or $m = 4$ phase, with $m = 2$ and $m = 5$ intergrowths also present. It is well established that the Aurivillius phases are inclined towards nanoscale structural disorder due to their complex layered nature and small thermodynamic driving force for formation of any individual phase [146]. Some reports have utilised this in

order to deliberately form mixed Aurivillius phase superlattices [145], [342]. For example, the composition $Bi_9Ti_6FeO_{27}$, where the overall phase is $m$ = 3.5 due to the structure being made up of alternating $m$ = 3 and $m$ = 4 perovskite blocks. However in general, these intergrowths are often not well controlled and veer towards structural disorder rather than ordered systems [343]–[345]. Often this disorder can be instigated and tuned via parameters such as stoichiometric ratio control and appropriate selection of the *A* or *B*-site cation [165], [344], [346] or the substrate [166] selected for deposition. While the films of B6TFMO are not epitaxially matched to the underlying sapphire substrates, the continuously changing angle at which the B6TFMO crystallites orientate over the patterned substrate leads to an increase in grain boundaries where more than two grains meet, as shown in **Figure 5.5** e.g. within the yellow inset in Dome 1. It is possible that extra disorder is created in the film on patterned substrates from these grain boundaries, resulting in regions with more structural defects and intergrowths.

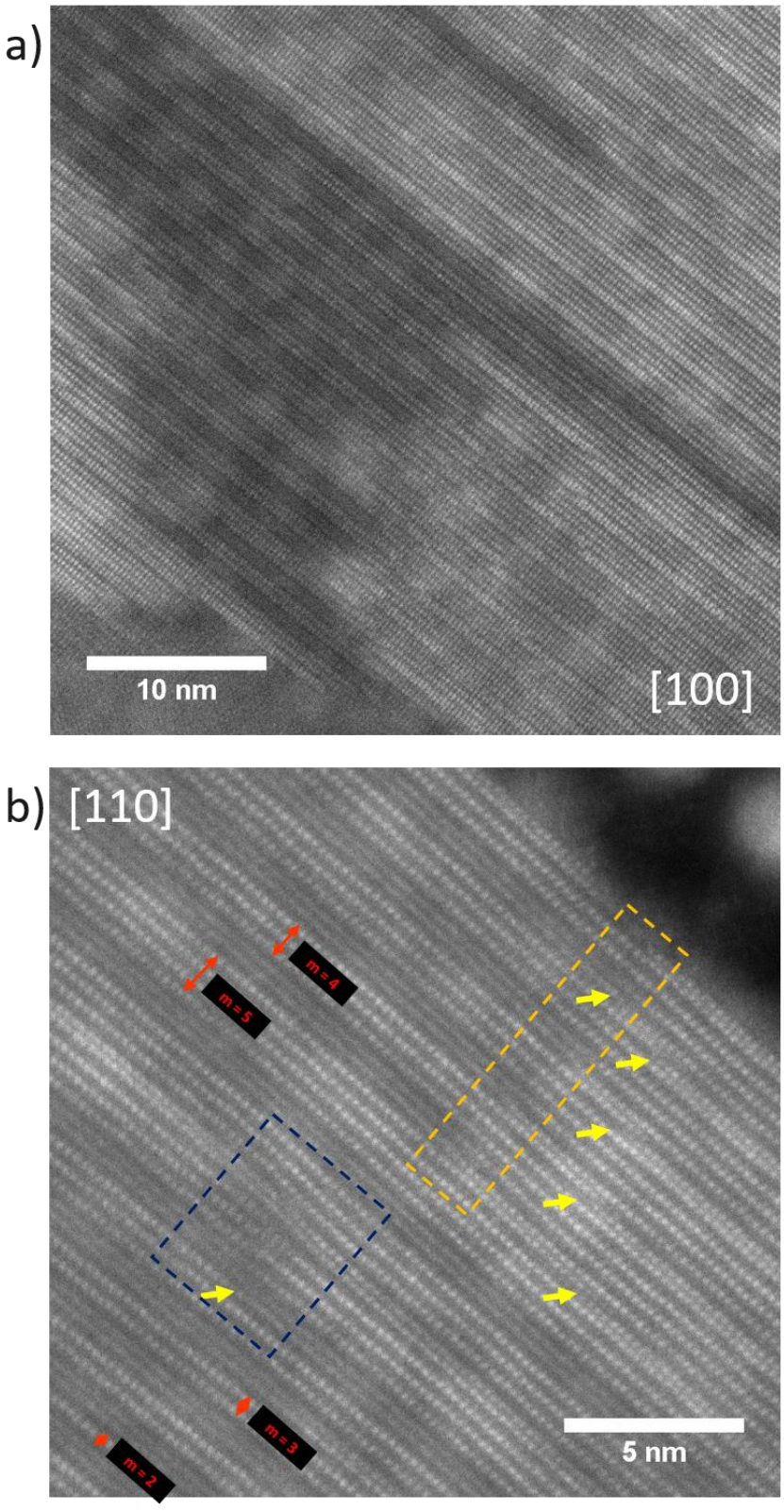


**Figure 5.7** Representative cross-section STEM images of 500 injection B6TFMO thin film on patterned sapphire substrate projected down (100) (a) and down (110) (b).

### 5.3.4 Investigations of Nano-scale Ferroelectric Behaviour

In this section the use of DART-PFM to investigate how the patterned sapphire substrate influences the orientation of the B6TFMO grains and the characteristics of ferroelectric domains within B6TFMO [234], is described. It should be noted that for B6TFMO on sapphire the films are preferentially *c*-axis orientated due to natural layering, there is no preferred in-plane orientation, as the films are not epitaxially matched to the sapphire substrate. The objective of this work was to investigate whether deposition of B6TFMO films along an inclined surface could enable major polarisation, (which is typically within the plane, parallel to a flat substrate surface), to be orientated towards the vertical direction. The studies demonstrate that the samples are all naturally self-polarised, with both films having a clear lateral piezoresponse (LPFM) and a vertical piezoresponse (VPFM).

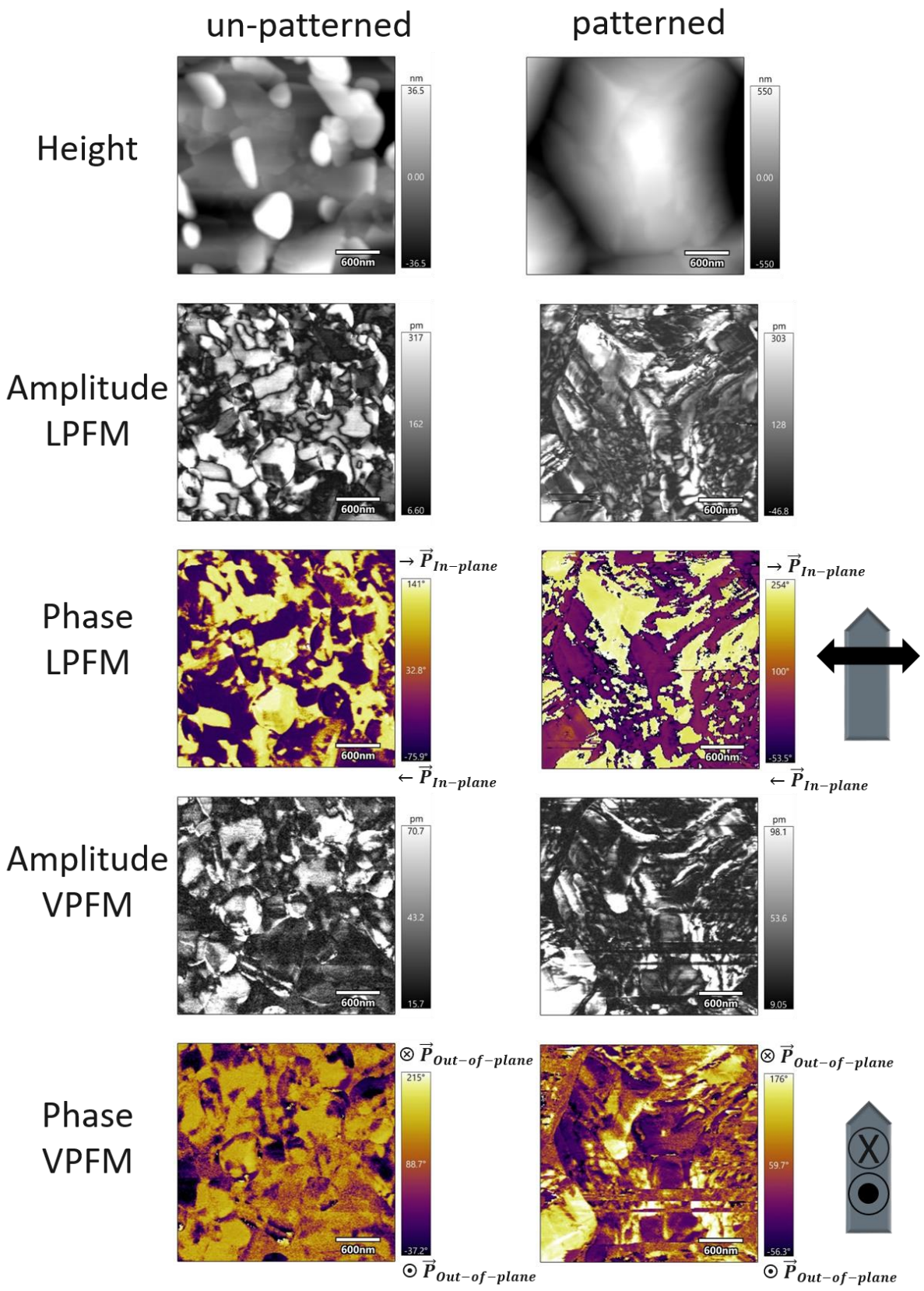


**Figure 5.8** Representative LPFM and VPFM images of 800 injection B6TFMO thin films on patterned and un-patterned sapphire substrates probed at 2 $V_{AC}$.

As intended by employing patterned sapphire, B6TFMO grains are inclined towards an upright geometry on the domes, therefore apart from regions between the domes, the grains do not lie parallel to the substrate. On the patterned sapphire however, many of the poly-crystals do not fully conform with the dome architecture. Some grains are orientated up to ~60 ° away from the substrate as shown near the base of the dome in **Appendix III Figure III.3,** while other crystallites, for example close to the top of the dome, are orientated ~25 ° away from the substrate. In work on even-layered $m$ = 4 $Bi_5Ti_3Fe_{0.5}Co_{0.5}O_{15}$ flakes [328], tilting of the flakes resulted in a polarisation being measured in the out-of-plane direction, which would not be expected for perfectly flat flakes. By taking the laterally measured polarisation as 40 μC/cm$^2$ when the film is parallel to the substrate i.e. 0 °, if the crystal grain was moved to be perpendicular to the substrate i.e. 90 °, now the vertically measured polarisation would appear to be 40 μC/cm$^2$. Considering this, an estimate indicates that for a crystallite tilted at a ~25 ° angle, there could be an out-of-plane response of ~11 μC/cm$^2$ measured. While for a crystallite tilted at ~60 °, an out-of-plane response of up to ~27 μC/cm$^2$ could be expected. However, while the patterned sapphire substrate is successful for enabling the majority deposition of Aurivillius phase B6TFMO poly-crystallites at angles of up to 60 ° tilted vertically away from the sapphire substrate plane, the VPFM response nevertheless still appears weaker than the LPFM response in all cases investigated. Representative LPFM and VPFM measurements shown in **Figure 5.8**, taken at a 2 $V_{AC}$ probing voltage and at the same location on the film, demonstrate that the lateral response still appears as the dominant response in the film. Due to large differences in the topography of the unpatterned and patterned B6TFMO films, as caused by the substrate surface (shown in **Figure 5.1**) and given the difference in the thickness of the films, (58 ± 31 nm and 88 ± 16 nm for B6TFMO on patterned and un-patterned sapphire respectively), it would not be fair to compare relative piezoresponse values between B6TFMO films on the un-patterned and patterned sapphire substrates. Another factor to take into consideration is the difficulty the PFM probe experienced in accessing deeper recesses in the sample and the sides of the domes when tracking over the B6TFMO surface on patterned sapphire. This could also contribute to the lower piezoresponses observed for the film on the patterned substrate. This PFM tracking issue is discussed in more detail below.

As demonstrated via the SEM and cross-section STEM imaging of the B6TFMO films on patterned sapphire (**Figure 5.3**), the B6TFMO film does not perfectly conform to the surface of the substrate. The angle at which the B6TFMO crystallises can vary unpredictably over the sapphire substrate. In **Figure 5.9** , the ferroelectric grains of the B6TFMO films at different regions of the sapphire domes are examined in more detail. In the red inset **Figure 5.9 (f)**, an area between two domes is imaged. At the centre of the image (darker region), the substrate is horizontal (flat). At either side (brighter regions), the thin film grows up along the sides of the domes. In the LPFM amplitude and phase scans for the red inset, **Figure 5.9 (g)** and **(h)**, the ferroelectric grains appear to be going up along the incline of the dome in columnar shaped grains. Comparing the area within the red inset (**Figure 5.9 (f)**) to the area within the green inset shown in **Figure 5.9 (k)**, (which scans the top (summit) of the dome) fewer distinct domains within the corresponding PFM images shown in **Figure 5.9 (l)** and **(m)** are obseved. The domains at the summit of the dome are overall larger than those in the red inset and the elongated character of the ferroelectric domains is not present for domains within the green inset. For both regions, VPFM imaging using a probing voltage of 3 $V_{AC}$ shows a relatively weak piezoresponse, further indicating that the patterned sapphire does not improve the measured vertical PFM response. Consequently, while the domes on the patterned sapphire substrate have an impact on the direction of B6TFMO film deposition, with grains tending to follow the incline of the domes, the results demonstrate that the overall dominant piezoresponse for B6TFMO lies within the lateral plane.

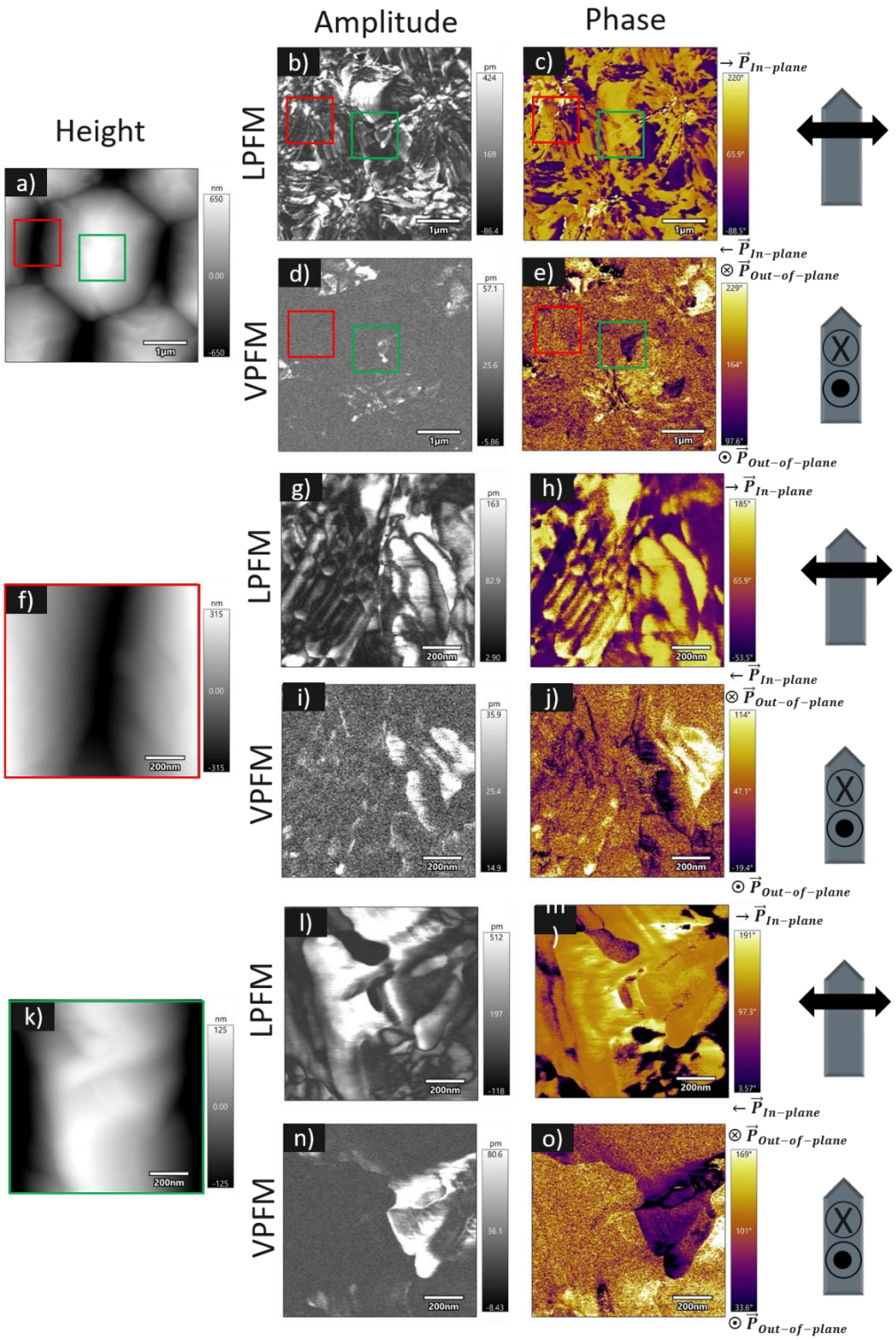


**Figure 5.9** LPFM and VPFM images of 800 injection B6TFMO thin films on patterned sapphire substrates. Here the LPFM images were probed at 1 $V_{AC}$ while the VPFM images were probed at 3 $V_{AC}$. Red Inset: Demonstrates the LPFM and VPFM response at a region in between two of the sapphire domes. Green Inset: Demonstrates the LPFM and VPFM response at a region at the summit/centre of a dome.

Due to the high resolution of scanning probe techniques in the z direction (typically capable of measuring height differences of less than 0.1 nm) [347] they are very useful at detecting nanoscale topography height variations. However, given that the dimensions of the domes have a height equal to 1.6 µm and a base width equal to 2.5 µm, it is more difficult for the PFM probe to track the surface of the films on the patterned sapphire compared with the flatter surface of the films on the un-patterned substrates. Precautions were taken to try and improve the image quality, such as slowing the scan speed. However, evidence of how the probe struggled to maintain proper sample tracking when imaging down the sloped sides of the dome and between the domes can be observed in the VPFM amplitude and phase images in **Figure 5.8**, and can been seen more closely in **Appendix III Figure III.4**. The difficulty experienced by the PFM probe while tracking and measuring the B6TFMO features on the patterned sapphire domes could be a contributing factor to the overall lower piezoresponse measured using both LPFM and VPFM for the B6TFMO on patterned sapphire.

### 5.3.5 Investigations of Ferromagnetic Behaviour

Previous studies demonstrate that partitioning of the magnetic cations towards the central perovskite layers in B6TFMO is key to driving long-range ferromagnetic order in B6TFMO [164]. The ferromagnetic properties can potentially arise from superexchange and double-exchange interactions through $Fe^{3+}$ (hs) −O−$Mn^{4+}$ or $Mn^{3+}$ (hs) −O−$Mn^{4+}$ respectively (where hs stands for high-spin). B6TFMO films on patterned and un-patterned sapphire substrates were investigated within this contribution to assess how the orientation of the B6TFMO poly-crystalline grains influences the measured magnetic properties.

Magnetic hysteresis loops (MH curves) were obtained for the 800 injection B6TFMO films on un-patterned sapphire and patterned sapphire by performing magnetisation versus magnetic field measurements at temperatures between 2 K and 300 K, as shown in **Figure 5.10 (a)** and **(b)**. Both films depict clear ferromagnetic hysteresis through the MH curves over the entire temperature series (2 K to 300 K), indicative of clear ferromagnetic behaviour, which perseveres for both types of B6TFMO film at RT. MH curves of the two types of thin film before normalising for the volume of the B6TFMO present are shown in

**Appendix III Figure III.5.** The B6TFMO sample on the patterned sapphire substrate appears to have an increased ferromagnetic signal before normalising for B6TFMO sample volume. The increased magnetisation can be attributed to the patterned sapphire substrate having a greater surface area for the thin film to grow on in comparison to the un-patterned sapphire substrate and thus has a larger volume of B6TFMO film on its surface. 10 mm x 10 mm substrate pieces were used for the magnetic measurements yielding a surface area of 100 $mm^2$ for the un-patterned substrate. However, for the patterned sapphire substrate, the surface area is calculated to be 252 $mm^2$. Average thicknesses were calculated from ~9 µm long cross-section STEM images of both types of films, taking into consideration that the film on the patterned sapphire is not completely conformal and the film on un-patterned sapphire has additional B6TFMO micro-crystallites across its surface (these micro-crystallites were not evident in the B6TFMO films on patterned sapphire). For the B6TFMO film on patterned sapphire, an average thickness of 58 ± 31 nm was calculated using 26 points along 3 domes, while an average thickness of 88 ± 16 nm was calculated for the B6TFMO on un-patterned sapphire using 19 points. Thickness in conjunction with the width and length of the sample piece was used to calculate film volume. This corrected value was used to allow for an accurate comparison of the magnetic properties of the B6TFMO films in emu/$cm^3$, shown in **Figure 5.10**.

As is characteristic of the expected ferromagnetic behaviour from B6TFMO, the remanent magnetisation ($M_R$) values of the B6TFMO films on un-patterned sapphire and patterned sapphire substrates decrease as the temperature increases in both cases. As seen in **Appendix III Table III.1** at 2 K the $M_R$ values were 1.63 emu/$cm^3$ and 1.87 emu/$cm^3$ for the thin films un-patterned and patterned sapphire respectively. At 300 K, these values decreased to 0.40 emu/$cm^3$ and 0.43 emu/$cm^3$ for the films on un-patterned and patterned sapphire respectively. These values are quite similar, but a potential factor that could contribute to the slight difference in the measurements could be the directionality of the magnetic response of the material and the inclined geometry of the B6TFMO films on un-patterned sapphire. It is not yet known if the magnetisation measured in B6TFMO systems is anisotropic or isotropic.

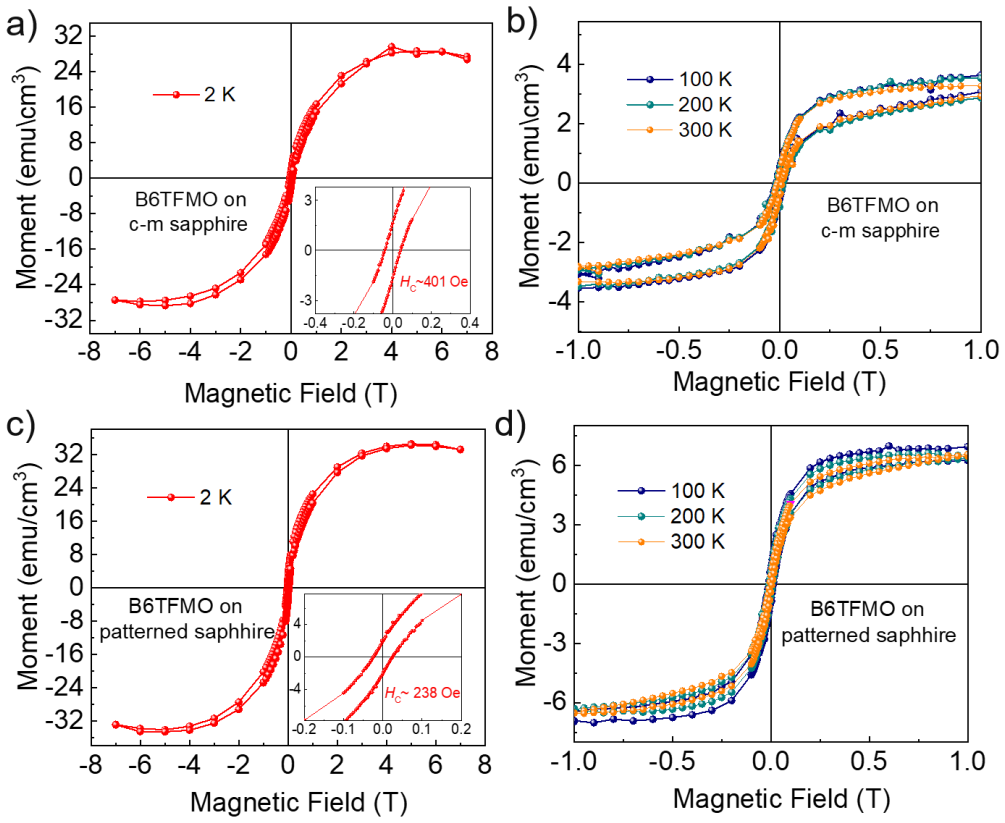


**Figure 5.10** Magnetisation versus magnetic field (MH) measurements of B6TFMO thin films measured at 2 K on a) un-patterned and b) patterned sapphire substrate. MH at different temperatures ranging from 100 K to 300 K on c) un-patterned and d) patterned sapphire substrate.

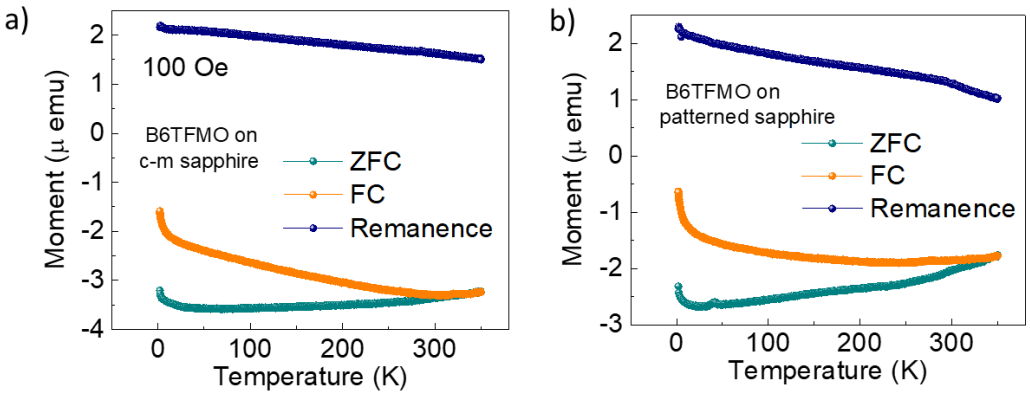


**Figure 5.11** Magnetization versus temperature (MT) measurements for zero field cooled (ZFC), field cooled (FC) and remanence (REM) B6TFMO films on a) un-patterned and b) patterned sapphire substrates.

Considering that the $M_R$ and $H_C$ values of magnetic materials are extrinsic properties, they can be readily influenced by many factors, for examples, the surface roughness, grain size and orientation. Thus, one must be careful when comparing $M_R$ measurement values from films with similar compositions but different methods of deposition. Often the saturation magnetisation ($M_S$) value of a material can offer a more reliable value for comparison. The $M_S$ values from the unsaturated MH loops for both B6TFMO films on un-patterned sapphire and patterned substrates at 100, 200 and 300 K could not be accurately calculated for comparison due to the relatively high diamagnetic contribution from the underlying substrate and the sample holder used for SQUID measurements. Accurate subtraction of the diamagnetic contribution from the ferromagnetic contribution can be challenging for relatively low moment samples, such as the B6TFMO samples in this work. A slight inaccuracy in subtraction of the diamagnetic contribution, necessary to observe the ferromagnetic characteristics of the B6TFMO film, could lead to unsaturated loop characteristics at high magnetic fields and can result in the value of $M_s$ changing significantly. However, the $M_s$ values for the two films from the saturated loops at 2 K can be accurately extracted and compared where they were measured to be 28.0 emu/cm$^3$ and 32.0 emu/cm$^3$ on un-patterned and patterned sapphire respectively. Previous studies [162], [163] on $Bi_6Ti_{2.8}Fe_{1.52}Mn_{0.68}O_{18}$ deposited by CSD had a 2 K $M_S$ value equal to 18 emu/cm$^3$. The CVD-grown B6TFMO samples in this study on patterned and un-patterned sapphire both have higher $M_s$ values at this temperature. Then again, a previous $Bi_6Ti_{2.99}Fe_{1.46}Mn_{0.55}O_{18}$ thin film deposited via a similar DLI-CVD process by Faraz *et al.* [163] showed significantly enhanced magnetic properties, with a RT magnetisation value of $M_S$ equal to 215 emu/cm$^3$. Note that while the $M_s$ values in this contribution are measured at 2 K, compared to Faraz *et al.'s* [163] RT measurements, typically $M_s$ does not increase with temperature (it usually decreases with increased temperature). Therefore, it can be considered that the films in this work have lower magnetisation. The high $M_S$ values reported from Faraz *et al.* [163] were considered to be a result of the structural homogeneity of the thin films deposited via DLI-CVD. For those previous samples, XRD and TEM data demonstrate the thin film is mainly comprised of the $m$ = 5 Aurivillius structure.

The inclusion of $m < 5$ Aurivillius phases in the thin films within this contribution could play a role in the origin of lower $M_S$ values within this work. Another factor to consider is the

concentration of Mn in the thin film, which is discussed below. From previous high-resolution atomic scale characterisation of B6TFMO films, it has been established that the presence of Mn is crucial for the ferromagnetic properties observed in the material [164]. Keeney *et al*. [164] have demonstrated that Mn cations have a preference to position towards the centre of the perovskite layers, where there is a 17 to 20 % increase in the *B*-site proportion of Mn cations going from the outer perovskite layers to the centre perovskite layers. Nearest-neighbour (NN) and next-nearest-neighbour (NNN) coupling interactions between magnetic cations above the percolation threshold is necessary for a material to demonstrate long-range magnetic order. When NN and NNN interactions are permitted between particular magnetic cations, Density Functional Theory (DFT) studies show that the NN interaction provides a much larger magnetic contribution *vs*. a contribution from NNN interactions [159]. The *B*-site magnetic cation concentration (Fe and Mn) for all the films discussed is between 40 to 45 %, which is higher than the predicted percolation threshold of 31 % that permits NN coupling interactions [348], [349]. However, even at the percolation threshold sometimes there are not enough NN superexchange reactions to allow ferromagnetism to be present at RT in the material. The preference for Mn and to a lesser extent the Fe cations (3 to 5 %) to partition to the centre perovskite layers means that there is increased potential for NN coupling between the magnetic cations. Calculations by Birenbaum *et al.* [350] have also indicated that the magnetic Curie temperature increases when the concentration of magnetic ions increases, thus increased magnetic cation concentration within the central layer above the percolation threshold would lead to an increase in the magnetic ordering temperature [351]. Therefore, the increased percentage of magnetic cations at the centre of the perovskite layers can lead to an increased RT ferromagnetic response in B6TFMO. The composition of the B6TFMO films in the previous studies [162], [163] was calculated via elemental analysis using STEM-EDX over a number of different grains in the films, where the percentage of Mn at the *B*-site is calculated to be 13.6 % for the CSD sample and 11 % for the DLI-CVD sample. In this work, the predicted concentration of Mn at the *B*-site from the DLI-CVD 800 injection deposition is 9.6 %. The percentage of Mn predicted to be at the *B*-site for this work is lower than previous reports and considering the large impact that the Mn cations have on the RT magnetic properties of B6TFMO, this lower Mn *B*-site contribution could be a contributing factor to the lower $M_S$ values reported in this work compared to some previous B6TFMO samples. Moreover,

previous experimental work [352] on $m = 4$, $Bi_5Ti_{2.8}Fe_{1.1}M_{0.1}O_{15}$ and $Bi_5T_{2.9}Fe_{1.1}O_{15}$ epitaxial films has demonstrated that a decrease in the concentration of magnetic cations can lead to magnetisation only existing below RT.

The magnetisation versus temperature measurements shown in **Figure 5.10 (a-b)**, further confirm the clear ferromagnetic behaviour of the B6TFMO films grown on both un-patterned sapphire and patterned sapphire substrates. ZFC-FC measurements were carried out, where a relatively low field of 100 Oe was applied for the measurements. The ZFC-FC curves separate below 280 K and 310 K for B6TFMO on un-patterned and pattered sapphire respectively, indicating the point at which the ferromagnetic to paramagnetic phase transition occurs [162]. The ZFC-FC curve splitting is 30 K higher for the B6TFMO films on patterned sapphire compared to films on un-patterned sapphire, since the magnetic moment is higher for the B6TFMO films on patterned sapphire (**Appendix III Figure III.5**). Therefore, the ferromagnetic phase can persist and be measured at higher temperatures. The clear splitting of the ZFC-FC curves confirms that both types of film are ferromagnetic at RT. The positive remanence value measured for the films is shown in **Appendix III Table III.1**, which decreases with increasing temperature. These results further confirm the ferromagnetic character of the B6TFMO thin films.

## 5.4 Conclusions

The initial DLI-CVD procedure at 630 °C enabled the conformal deposition of amorphous films onto the domed structures of the patterned sapphire. However, the preference for the Aurivillius phase to crystallise in a plate-like manner hindered the fully conformal formation of an Aurivillius phase thin film over the patterned sapphire substrate after the 850 $^{o}$C post-deposition anneal step required for the formation of the crystalline $m = 5$ phase. The dome-shaped features on the patterned sapphire substrates have an overall impact on the B6TFMO film orientation, with most of the grains tending to follow the incline of the domes. The Lotgering factor, used to describe the texture of materials, decreases from 0.993 for the B6TFMO film on un-patterned sapphire to 0.828 on patterned sapphire. XRD analysis of the samples revealed that non-(00*l*) reflections were present in the film on patterned sapphire,

which could be attributed to reflections of inclined *a*-*b* polycrystals such as the *m* = 5 (11$\underline{11}$) reflection. STEM imaging of the B6TFMO films showed that regions comprised of structural defects and intergrowths of Aurivillius phases having lower number of perovskite layers were abundant in the films on patterned sapphire. These intergrowth regions and 'anatase'-type defects could also contribute to the broader peaks and additional XRD reflections shown for the B6TFMO film on the patterned sapphire substrate.

Given the geometry of the PFM cantilever, it was found difficult to gain access to the inclined grains and to fully probe the piezoresponse of the B6TFMO films on patterned sapphire. From the PFM studies using DART LPFM and VPFM, the out-of-plane piezoresponse still appears weaker than the in-plane piezoresponse. Consistent with the samples grown on un-patterned sapphire substrates, the B6TFMO films on patterned sapphire substrates were shown to demonstrate RT ferromagnetic / ferroelectric multiferroic behaviour. The magnetisation values for both films were very similar with the values for B6TFMO on patterned sapphire being slighter higher compared to B6TFMO on un-patterned sapphire. This research further supports the findings that B6TFMO has RT ferromagnetic properties and that even when changing the topography of the underlying substrate, B6TFMO still maintains its RT multiferroic properties.

# 6 Optimisation of Sub-50 nm Epitaxial B6TFMO Thin Films Grown by DLI-CVD

In this chapter, all research is the work of the author, with the exception of the following contributions from collaborators: M. Schmidt (Tyndall-UCC) prepared cross-section lamella of the samples and carried out the scanning transmission electron microscopy. D. Dutta (Tyndall-UCC) acquired the atomic force microscopy images using the Bruker Dimension Icon tool.

## 6.1 Introduction

Future memory storage devices utilising room temperature, non-volatile magnetoelectric multiferroic materials have been road-mapped [353] as promising architectures for memory scaling beyond current technologies. Aurivillius phase $Bi_6Ti_xFe_yMn_zO_{18}$ (B6TFMO), with a general formula $(Bi_2O_2)(A_{m-1}B_mO_{3m+1})$ circumnavigates fundamental contra-indications for multiferroic conditions by combining the chemistries required for ferroelectricity ( *A*-site ($Bi^{3+}$) and *B*-site ($Ti^{4+}$)) and ferromagnetism (*B*-site $Fe^{3+}$, $Mn^{3+/4+}$) [163], as shown in **Chapter 5** of this thesis. B6TFMO films that are 100 nm thick have shown promising room temperature ferroelectric and ferromagnetic properties with saturation magnetization ($M_S$) values of up to 215 emu/cm$^3$ and in-plane saturation polarization ($P_S$) values of > 26 μC/cm$^2$ [163]. These impurity free, room temperature multiferroic B6TFMO films have been successfully grown using direct liquid injection chemical vapour deposition (DLI-CVD) on non-epitaxial, sapphire substrates [162], [163] however due to the non-epitaxial nature of the films there is a lack of control over the film orientation. Furthermore, the two-step (deposition and post-anneal) process for film growth on sapphire does not allow for the synthesis of continuous B6TFMO films that are less than 80 nm.

To grow thinner, conformal and continuous films of B6TFMO required for integration into commercial memory devices, epitaxial substrates must be employed. Epitaxial substrates often help extend the range of crystal growth conditions through what is known as epitaxial stabilisation [354], where the physical constraints imposed by epitaxy alters the thermodynamic and kinetic energies needed for crystal nucleation and growth [166]. The

introduction of epitaxial strain into a material system can also aid in tuning different functional properties of a material. For example, ferromagnetism has been reported for $Bi_9Ti_3Fe_5O_{27}$ (*m* = 8) thin films grown on epitaxial $SrTiO_3$ substrates [200], where it is believed that the compressive strain (0.3 %) and modification of the lattice symmetry imparted by the substrate influences Dzyaloshinskii–Moriya (DM) exchange interactions, leading to a large enhancement of the ferromagnetic order within the system. It has also been predicted by Birenbaum *et al*. [348] that epitaxial strain tuning of Aurivillius phase thin films can tailor ferroelectric polarisation and aid in controlling the magnetic cation distributions through the perovskite layers of the structure. A further example of this can be found in earlier work on sub-10 nm films of B6TFMO, where the piezoresponse was found to increase with an increase in tensile epitaxial strain [171] .

The epitaxy imposed by perovskite substrates such as $SrTiO_3$ (100) (STO), $La_{0.26}Sr_{0.76}Al_{0.61}Ta_{0.37}O_3$ (100) (LSAT) and $NdGaO_3$ (001) (NGO), enables the growth of conformal sub-10 nm films of B6TFMO [171], [191]. However, epitaxial growth tends to be confounded by the presence of impurity phases, not present in films deposited on non-epitaxially matched sapphire substrates. Initial work by Keeney *et al.* [171] used both a two-step deposition and anneal method and a single-step DLI-CVD deposition (at 700 to 710 °C), to produce continuous (5 to 20 nm thick) B6TFMO thin films over the substrate surface. Use of this single-step process delivered B6TFMO films having a significantly reduced volume fraction of surface impurities to (3 to 4 vol. %) compared with films prepared by a two-step process involving deposition and a high temperature (850 °C) post-anneal (11 to 12 vol. %).

During the development of a new deposition process for B6TFMO, it is obviously important to try to reduce and eliminate impurity phases and carry out careful evaluations of the material composition when synthesised via a new method. Impurity phase inclusions can greatly impact material properties. For example, even trace levels (<0.1 vol. %) of magnetic impurity phases would greatly alter the measured magnetic properties associated with the B6TFMO phase [273]. In this work, the impact of growth process, substrate strain and bismuth excess on the B6TFMO film growth was explored in order to ascertain parameters important for the reduction of impurity phases in sub-50 nm B6TFMO films.

In this chapter, initially, the single step growth is compared to the two-step process as used in previous chapters of this thesis. Then there are investigations on how the strain

imparted by the underlying substrate affects the properties of B6TFMO thin films deposited during a single step DLI-CVD deposition at 700 °C. Next, how changing the bismuth excess during deposition influences the synthesis and growth of Aurivillius thin films on a single substrate, LSAT (100) is addressed. Finally, the ferroelectric properties of the ~45 nm thick B6TFMO thin films are characterised. By switching to epitaxial substrates, B6TFMO films can be grown with a controlled orientation. Furthermore, use of epitaxial substrates allows for potential strain-induced enhancement of the material's multiferroic properties, as utilised for other materials for example $BiFeO_3$ [136] and $(Ca_ySr_{1-y})_{1.15}Tb_{1.85}Fe_2O_7$ [272]. In this work sub-50 nm epitaxial B6TFMO films are developed, at thicknesses relevant to applications as piezoelectric actuators, sensors and energy harvesters [355]–[358].

## 6.2 Methods

Aurivillius phase thin films, $Bi_6Ti_xFe_YMn_zO_{18}$ (B6TFMO; x = 2.84 to 2.98; Y = 1.42 to 1.50; Z = 0.59 to 0.68) were synthesised by DLI-CVD via a horizontal flow AIXTRON AIX 200/4FE AVD (atomic vapour deposition) system [284], [285]. The films were deposited using conditions with a variable bismuth excess to investigate the influence on thin film purity and crystallinity.

Substrates with an epitaxial match to B6TFMO ($SrTiO_3$ (100), $La_{0.26}Sr_{0.76}Al_{0.61}Ta_{0.37}O_3$ (100), $NdGaO_3$ (001)) along with sapphire (*c-m* (0001)) which is not epitaxially matched to B6TFMO were used for deposition. Substrates were cleaned via a sonication with acetone, rinse with isopropyl alcohol followed by a rinse with deionised water and were dried using $N_2$ gas.

The majority of the samples were deposited using a single step process, where for each bismuth excess, the substrates were loaded together into the reactor chamber during the same growth run. Therefore, for each bismuth excess run, the films discussed were synthesised under the exact same growth conditions and the underlying substrate was the varying factor. In this study, four different bismuth excess values were used for the single step process, 50.6 %, 17.7 %, 5.0 % and 1.8 %. The 0.100 mol $dm^{-3}$ bismuth, iron and titanium precursors in toluene solution, $Bi(thd)_3$, $Fe(thd)_3$ and $Ti(O\text{-}iPr)_2(thd)_2$ (where thd = 2,2,6,6-tetramethyl 3,5-heptanedionate and O-iPr = isopropoxide), were purchased from Epivalence

Ltd. The 0.025 mol $dm^{-3}$ manganese precursor was prepared by dissolving $Mn(thd)_3$ (99 %, STREM chemicals) in anhydrous toluene (99.8 %, Sigma-Aldrich) under $N_2$ in a glovebox. The low vapour pressure precursors were injected using nitrogen pulses into the Trijet Vaporizer of the DLI-CVD system, where they entered the reactor growth chamber via lines maintained at 220 °C. The precursor volumes were controlled electronically by setting the opening time for each injection to be between 1.8 and 11.2 ms, depending on the relevant precursor. A continuous injection mode was employed where the injections were pulsed at a frequency of 1 Hz. 400 injections of each precursor were pulsed. Precursors were mixed with reactive $O_2$ gas during the growth run. A total gas flow of 3000 sccm (standard cubic centimetres per minute) was maintained in the growth chamber comprised $O_2$ run gas and $N_2$ carrier gas where the $O_2$ flow was 1000 sccm. The reactor chamber was set at a pressure of 10 mbar while the temperature of the rotating susceptor-heated sample holder was heated to 700 °C using infra-red lamps. These conditions were maintained for the entirety of the deposition process.

The second type of growth process was carried out using a two-step deposition and anneal in a similar procedure to that used in **Chapters 3, 4** and **5** of this thesis. Here, the thin film deposition via DLI-CVD in Step One was carried out similarly to what is described above but at a temperature of 630 °C with a 19.3 % bismuth excess. In Step Two, the samples were post-annealed in atmosphere for 1 hr at 850 °C to produce crystalline Aurivillius phase films via the two-step growth process.

A commercial Bruker Dimension Icon with the PeakForce Tunnelling AMF (PF-TUNA) module was used for conductive atomic force microscopy (C-AFM) measurements. Conductive single crystal diamond (Adama Innovation AD-40-AS) probes were used to scan the sample.

Piezoresponse Force Microscopy (PFM) was performed using an MFP-3D$^{TM}$ Asylum Research instrument. PFM was conducted in lateral (LPFM) and vertical (VPFM) Dual AC Resonance Tracking (DART-PFM) modes [234]. The DART-PFM method of measuring boosts the measured signal while reducing instrumental crosstalk. Drive amplitudes of 1.0 $V_{AC}$ and 1.0 to 2.0 $V_{AC}$ were used for measurement of the piezoresponse in LPFM and VPFM modes respectively. Two types of probes were used, the Oxford Instruments AC240TM-R3 electrilevers (Ti/Pt coated silicon probes, Al reflex coated, 25 nm tip radius, 70 kHz resonant

frequency)) and the Adama Innovation AD-2.8-SS super sharp single crystal diamond probes (< 5 nm tip radius, 75 kHz resonant frequency). The AD-2.8-SS probes were used for getting higher resolution images of the smoothest B6TFMO films in this work due to the small tip radius. The drive frequencies used for the Oxford Instruments probes were in the range of 552 to 646 kHz for the LPFM measurements and 194 to 237 kHz for the VPFM measurements. The drive frequencies used for the AD-2.8-SS probes were in the range of 479 to 655 kHz for the LPFM measurements and 255 to 331 kHz for the VPFM measurements. A frequency width of between 6 and 10 kHz was used for the measurements, depending on the thin film type.

X-ray diffraction (XRD) measurements were performed using an X'pert Diffractometer (Cu Kα radiation λ = 0.1541876 nm) (45 kV, 40 mA). The typical 2θ scan range was from 5 ° to 50 ° with a step size of 0.006 °. In this chapter, the XRD diffraction patterns were indexed using reference data from García-Guaderrama *et al.* [258] for the *m* = 5 Aurivillius phase.

A FEI DualBeam Helios NanoLab 600i Focused Ion Beam instrument was used to prepare the lamella cross sections of the B6TFMO films. Transition electron microscopy (TEM) cross sections were prepared by depositing C and Pt as electron-beam induced layers, followed by an ion-beam induced C layer for protection. The lamellas were thinned at 0.28 nA/30 kV with final polish at 47 pA/5 kV. TEM imaging was carried out using a JEOL JEM 2100 in bright field mode at 200 kV.

## 6.3 Results and Discussion

### 6.3.1 Comparison of a Two-step Thin Film Deposition and Anneal Process to Single-step Deposition for B6TFMO Film Growth on Epitaxially-matched Substrates

Previous chapters employed a two-step process for B6TFMO synthesis with thicknesses of ~90 nm, involving deposition and a post-anneal on sapphire substrates that are not epitaxially matched to B6TFMO. In order for thin film growth by DLI-CVD on substrates that are not epitaxially matched to B6TFMO, initial deposition of an amorphous phase at a temperature of 630 °C is needed, followed by a post-deposition high temperature anneal step at 850 °C to avoid the formation of phases such as pyrochlore. By depositing at temperatures lower than

the crystallisation temperature, the resultant amorphous film can be transformed into an impurity free Aurivillius phase films during the post-deposition crystallisation anneal step. While this two-step procedure utilising non-epitaxially matched substrates provides impurity free B6TFMO samples (as shown in **Chapters 4** and **5** e.g. **Figure 5.6**), without an epitaxial underlying template, the production of continuous films is limited to thicker samples (~90 nm). As is shown in **Appendix IV Figure IV.1**, continuous B6TFMO films with a target thickness of 45 nm (400 DLICVD injections) are not formed. Rather, using non-epitaxial substrates, islands of B6TFMO layers are formed where gaps to the underlying substrate can be observed.

Converse to the above bulk crystallisation of amorphous films on non-epitaxial substrates, crystallisation of epitaxial films during growth occurs as material is deposited on the surface. Given the large differences in surface diffusion coefficients compared with bulk diffusion coefficients, temperatures for the crystallisation of epitaxial thin films are often lower than those needed for crystallisation of their bulk counterparts [166]. Therefore, a target for the current chapter is to examine the effectiveness of epitaxially matched substrates using deposition processes that enables production of continuous B6TFMO films at crystallisation temperatures lower than 850 °C.

Herein, a comparison of the two-step technique (630 °C deposition and 850 °C anneal) to the single-step process (700 °C) is performed to determine which deposition technique produces the best quality B6TFMO thin films on epitaxially-matched LSAT substrates. For both the deposition methods, 400 injections were used to synthesise ~45 nm films. Three thin films on LSAT are compared to each other in **Figure 6.1**. The XRD patterns for B6TFMO synthesised using the two-step technique (red line) and single-step methods (blue and black lines) on LSAT in **Figure 6.1 (a)** reveal that the $m$ = 5 structure is the dominant phase. Further analyses of the XRD pattern for the B6TFMO films using the modified Scherrer equation [359] applicable for orthorhombic structures, indicates that the crystalline quality is lower for the film grown via the two-step technique compared to films grown via the single-step technique. The Scherrer equation calculates a quality factor, Q, of 2.47 ± 1.88 for B6TFMO on LSAT synthesised using the two-step technique, which is lower than Q calculated for the films deposited using the single-step method on LSAT with 1.8 % and 17.7 % bismuth excess (the blue and black lines in **Figure 6.1**), where Q is 3.69 ± 1.48 and 3.12 ± 1.60, respectively.

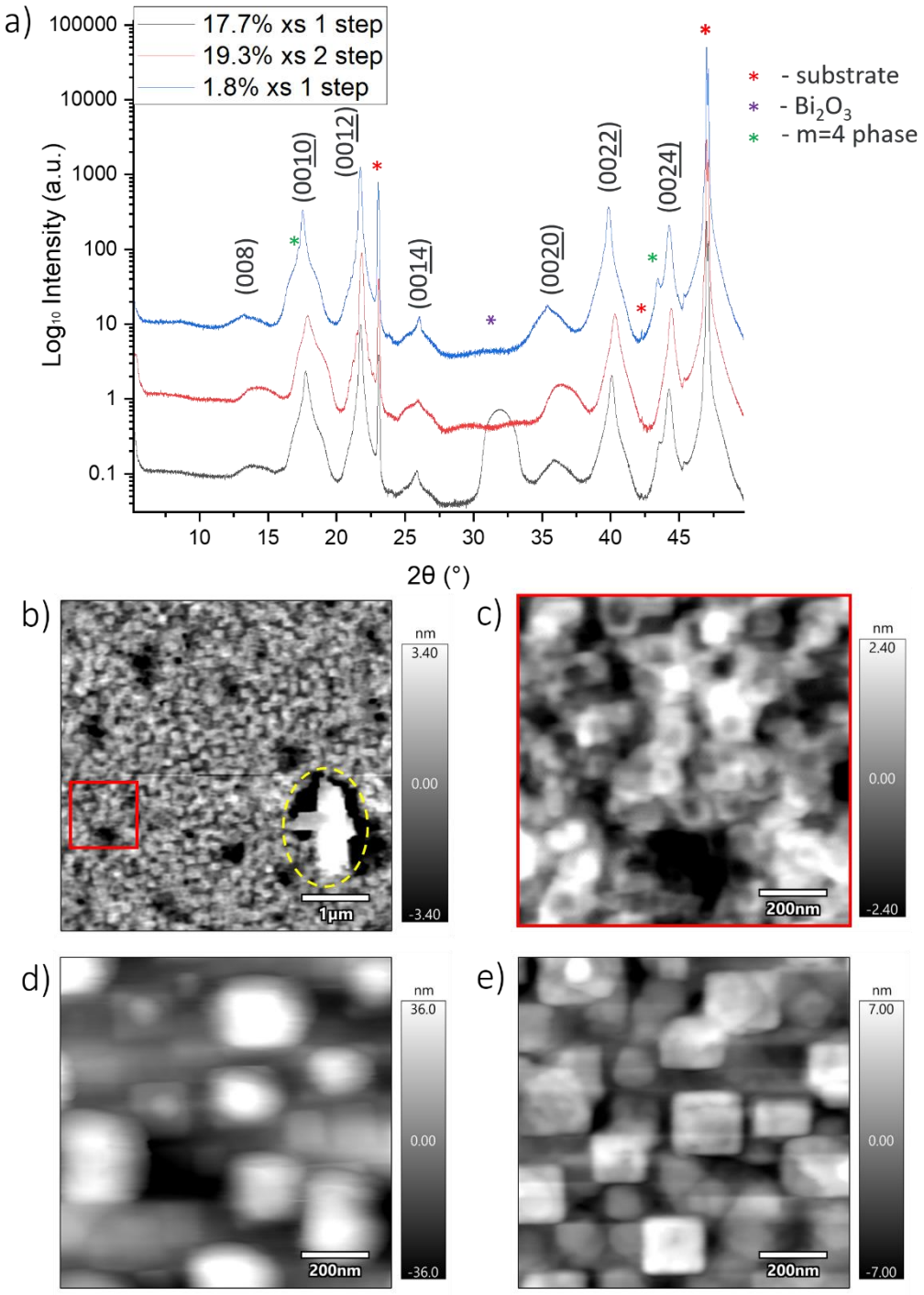


**Figure 6.1** Results for B6TFMO thin films on LSAT. a) XRD patterns comparing the two-step process with a 19.3 % bismuth excess (xs) (red line) to films prepared by a one-step growth process at 700 °C where bismuth excess of 17.7 % (black line) and 1.8 % (blue line) were used. b) 5 x 5 $\mu m^2$ AFM image of the B6TFMO surface on LSAT after two-step deposition and c) 1 x 1 $\mu m^2$ image from the same sample. 1 x 1 $\mu m^2$ AFM images of the films synthesised using a single-step process are shown in d) with 17.7 % bismuth excess and e) with 1.8 % bismuth excess.

Five factors could potentially contribute to the decreased Q factor and the XRD peak broadening observed for the samples prepared by the two-step process: 1) reduced crystallite size, 2) reduced film thickness, 3) sub-unit cell structural defects, 4) the inclusion of intergrowths of differing *m*-numbered Aurivillius phases, or 5) the inclusion of secondary phase impurities. Using Gwyddion software [314], lateral dimensions for the crystallites were approximated from 2 x 2 $\mu m^2$ AFM images (**Appendix IV Figure IV.2**) of the B6TFMO film deposited via the two-step method and compared with the film deposited using the single-step method with a 1.8 % bismuth excess. The lateral dimensions of the crystallites within the B6TFMO film grown via the two-step method were found to be smaller with values of 0.0104 ± 0.0096 $\mu m^2$ when compared to the crystallites within the films grown by the single-step process, where the crystallite size is on average 0.0216 ± 0.0158 $\mu m^2$. Furthermore, results from thirty thickness measurements across a ~5 µm TEM cross-section of the B6TFMO film deposited via the two-step method and a comparison with measurements with the deposited via the single-step method with 5.0 % bismuth excess determined that the film prepared by the two-step method is slightly thinner on average (37 ± 6 nm) compared to the film prepared by the single step method (44 ± 6 nm). Combination of effects from the smaller crystallites and thinner film would contribute to the broader peaks observed for the B6TFMO deposited via the two-step method. TEM images shown in **Figure 6.2** reveal that B6TFMO films deposited by the two-step method contain areas with structural out-of-phases boundary (OPB) defects as marked in the yellow inset in **Figure 6.2 (b)**. Associated with the OPB defects are intergrowths of differing *m*-numbered Aurivillius phases where the number of perovskite layers between bismuth oxide layers can vary between $m = 4$ to 6. The presence of these defects and thus the disorder in the periodic structure of the crystal could further contribute to peak broadening with the material. In **Figure 6.2 (c),** there two different regions, one area (green box) lasting 2 to 4 Aurivillius phase unit cells in thickness in the *c*-axis direction, at the substrate film interface and a second region (red box) which is lighter in colour and makes up the rest of the film in the image. The lighter region at the top of the film does not appear to be made up completely of Aurivillius phase material. In this region, the layers where $[Bi_2O_2]^{2+}$ is usually present for the Aurivillius phase appears to be thicker than would be expected, indicating that possibly here the 'anatase'-type interlayer defects (as discussed previously in **Section 1.6.3** and **4.3.4**), are present instead. From comparing a variety of TEM images acquired for approximately 8 µm long thin film-sections for samples deposited via the single-

step and two-step methods, there appears to be more structural disorder to the thin film grown via the two-step method as seen in **Figure 6.2**. While faults such as OPBs were present for both single-step and two-step deposited films, in this study the only areas where the 'anatase'-type defects were observed were in the films deposited via the two-step method. It is expected that at the higher temperatures needed for the two-step deposition, e.g. the 850 °C anneal, there would be a higher tendency for bismuth migration than for the single-step deposition which uses temperatures as high as 700 °C, due to the enhancement in bismuths diffusion coefficient above 710 °C [360]. However, it should be noted that this is just a preliminary finding and due to the localised manner of imaging TEM cross-sections, more sample sections would need to be examined to confirm this.

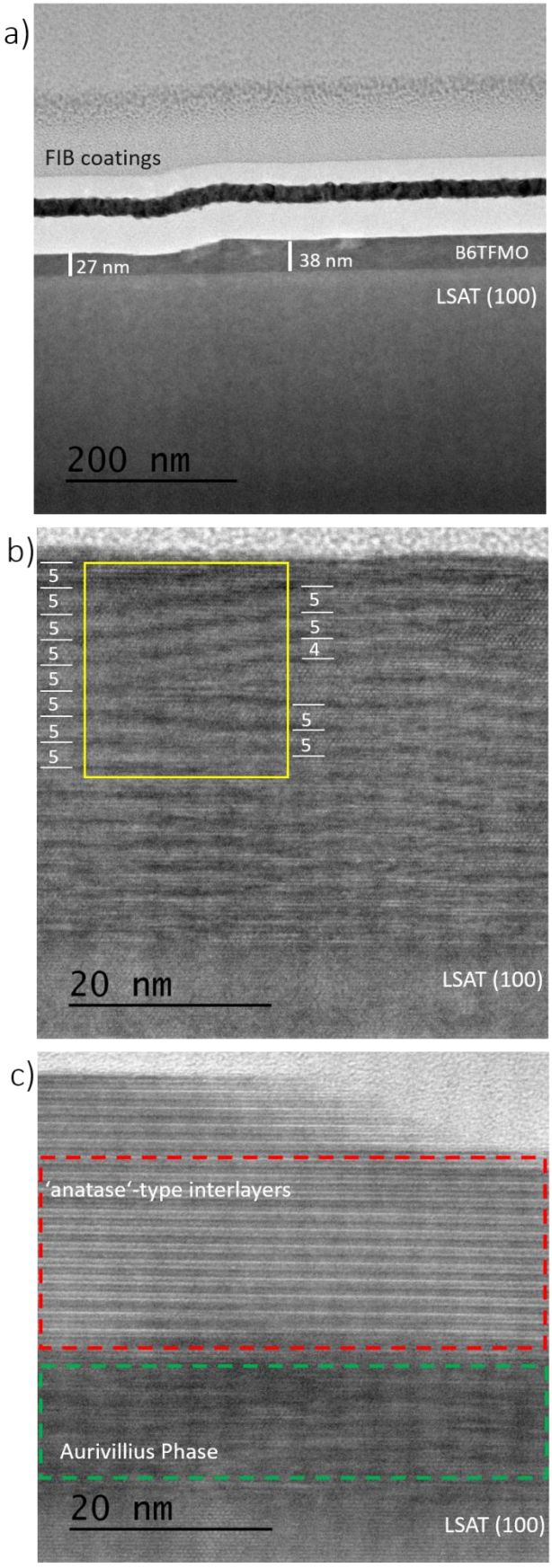


**Figure 6.2** Representative TEM images of a B6TFMO thin film on LSAT synthesised via a two-step process.

The surface of the B6TFMO film grown on LSAT via the two-step method is relatively smooth with a RMS roughness value of 1.714 nm compared to the smoothest film (1.8 % bismuth excess) from the single-step samples which has an RMS roughness value of 3.236 nm as measured from **Figure 6.1**. However, while the samples grown via the two-step method have overall smoother surfaces, it should be noted the surface of these films are not consistent over the entire sample. In **Figure 6.1 (b),** a random surface particle (possibly an impurity) can be seen in the right hand of the image in the dashed yellow circle, with a height of ~10 nm above the rest of the film. Examples of the non-uniform surface resulting from the two-step deposition and anneal can be observed for B6TFMO on STO and NGO substrates shown in **Appendix IV Figure IV.3**. The inclusion of secondary phase impurities could also potentially contribute to the decreased Q factor and the XRD peak broadening observed for the samples prepared by the two-step process. Further discussion on possible impurity phases within the films will be discussed later in **Section 6.3.3**.

Overall, it appears as though the single-step deposition method for B6TFMO allows for the synthesis of epitaxial films with less structural disorder and more consistent surfaces when compared to those grown via the two-step method. Furthermore, the single-step deposition method can be considered advantageous over the two-step deposition and anneal method for synthesising B6TFMO, due to the simplified procedure and the 150 °C reduction in the temperature required for thin film crystallisation. Therefore, the single-step process is the focus of the remainder of this chapter.

### 6.3.2 Impact of Substrate-induced Biaxial strain on B6TFMO Thin Film Growth

**Figure 6.3 (a)** shows that deposition at 700 °C using the single-step method on sapphire substrates leads to the formation of impurity pyrochlore phases, $Bi_2Ti_2O_7$, with the (444) peak evident at a 2θ value of 29.8 ° (JCPDS 32-0118) [361]. Therefore, non-epitaxial sapphire substrates are clearly not amenable with the single-step process. To optimise the single-step deposition process, the suitability of differing types of epitaxially matched substrates were tested. Three types of perovskite substrates were chosen for the epitaxial growth of sub-50 nm thick B6TFMO, namely (100) STO, (100) LSAT and $(001)_p$ NGO. To calculate the lattice mismatch between the Aurivillius phase and the epitaxial substrates, the pseudo-cubic lattice

parameter ($a_p$) of B6TFMO was calculated. A method to calculate this parameter was developed by Newnham and Armstrong [149] using the below formula,

$$a_p = 1.33r_B + 0.6r_A + 2.36\ \text{Å} \qquad 6.1$$

where $r_A$ is the eight-fold coordinate radius value of the *A*-site cation ($Bi^{3+}$) and $r_B$ is the six-fold coordinate radii values of the *B*-site ions ($Ti^{4+}$, $Mn^{3+}$ and $Fe^{3+}$). The radii values used to calculate the pseudo-cubic lattice parameter were acquired from Shannon's work [277]. A comparison of the lattice parameters of these substrates to the pseudo-cubic lattice parameter of B6TFMO ($a_p$ = 3.89 Å) reveals that STO ($a$ = 3.905 Å) is the substrate which has the closest lattice matching along the *a*-direction. Between STO and B6TFMO the strain is tensile, and the mismatch is +0.39 %, while LSAT ($a$ = 3.868 Å) and NGO ($a_p'$ = 3.858 Å) provide compressive strains of -0.57 % and -0.82 % respectively. Tensile strain would cause B6TFMO to expand laterally, hence, to maintain the total volume of the unit-cell, the lattice would shrink along the *c*-axis. For substrates imparting a compressive strain, the opposite effect would occur, with the lattice stretching along the *c*-axis to compensate and maintain unit-cell volume. Within this study, all the XRD peaks were calibrated using the substrate peaks. Examination of the XRD patterns for the thin films grown on epitaxial substrates in **Figure 6.3 (a)**, determined that an $m$ = 5 Aurivillius phase is present. There is also evidence for epitaxial strain within each of the films. Inspection of the (00<u>12</u>) reflection shows that the peak position shifts slightly depending on the substrate used. The (00<u>12</u>) reflection of B6TFMO on STO has the highest position at a 2θ value of 21.99 °. The reflection is positioned at 21.76 ° for B6TFMO on LSAT and at 21.64 ° for B6TFMO on NGO. The increase in the (00<u>12</u>) position from NGO to LSAT to STO correlates with the strain imparted on the B6TFMO film as it experiences compressive stress to tensile stress.

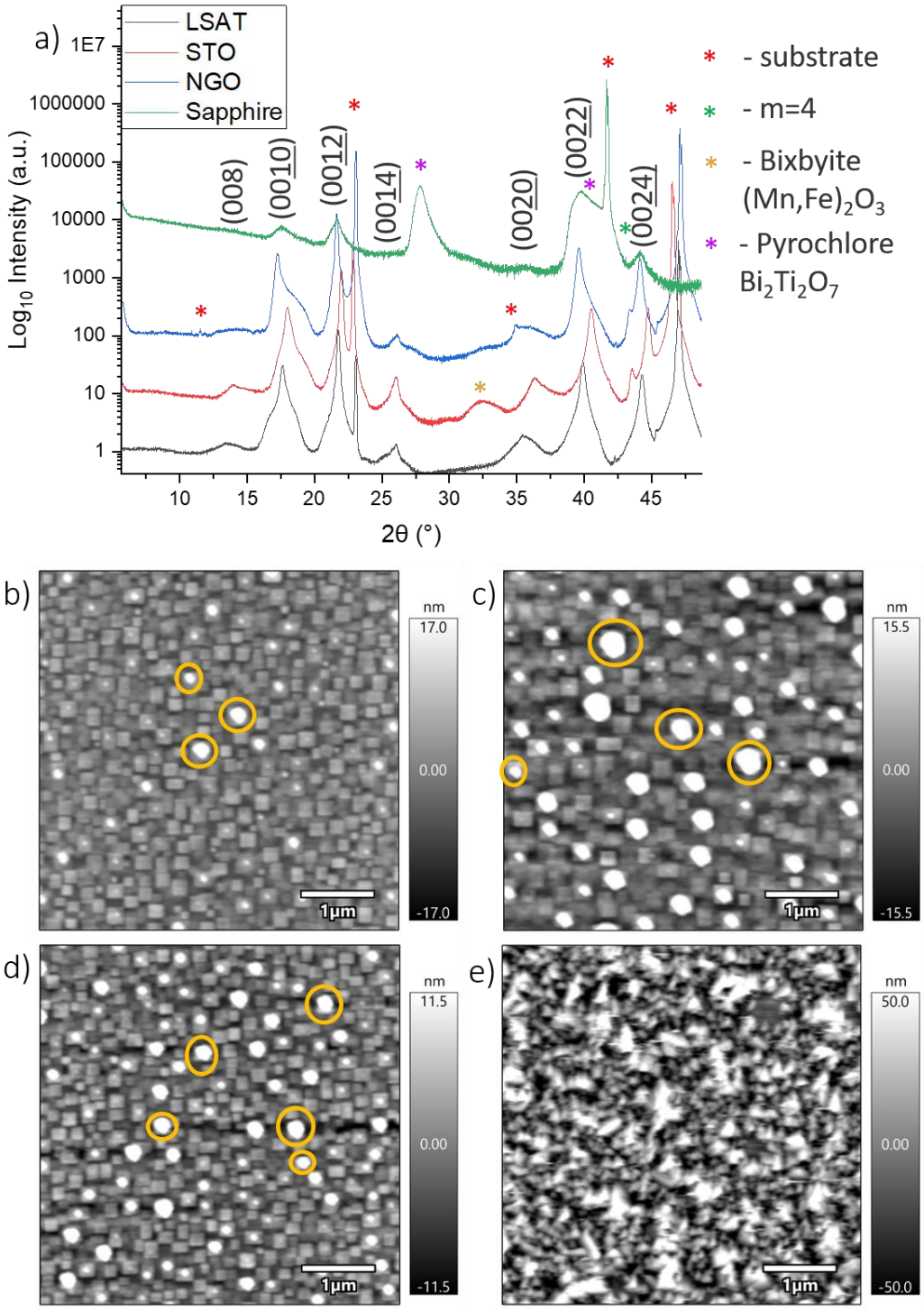


**Figure 6.3** a) XRD patterns of B6TFMO films deposited on differing substrates (indicated within the legend) during the same deposition run where a 5.0 % bismuth excess was used with a process temperature of 700 °C. AFM images of B6TFMO thin films with a 5.0 % bismuth excess on different substrates, b) LSAT, c) STO, d) NGO and e) sapphire. Orange circles show examples of impurity phases on surface.

Thin film deposition is generally considered to occur by three main growth modes: Volmer-Weber (island growth), Stranski-Krastanov (island-by-layer growth) [362] and Frank van der Merwe (layer-by-layer growth) [363]. The Frank van der Merwe/layer-by-layer growth is highly desired for deposition of epitaxial films, as it can allow for the deposition of thin films with a controlled and uniform thickness along with atomically smooth surfaces. Layer-by-layer growth occurs when the bonding between the deposited atoms is weaker than their bonding to the substrate surface. Thus, when nucleation occurs, a single layer (e.g. for a simple perovskite this corresponds to a single unit cell) coalesces laterally as the surface coverage increases and the film continues to grow in this layer-by-layer fashion. However, for more complex layered materials, such as the Aurivillius phases, the material may coalesce laterally as surface coverage increases for a fraction of the unit cell rather than the full unit cell and grow via a layer-by-layer fashion via partial unit cell layers [193], [364].

CVD studies of the lower order ($m$ = 3) Aurivillius phase, $Bi_4Ti_3O_{12}$ , on epitaxial STO deemed that growth occurred via the Stranski-Krastanov mode [165], [365]. However, Deepak *et al*. [165] discovered that with the addition of Fe to the $m$ = 3 Aurivillius phase, the layer-by-layer mode takes command for $Bi_4Ti_{2.5}Fe_{0.5}O_{12}$ films. The $m$ = 3 Aurivillius phases grow on perovskite substrates with epitaxial relation (001) [001] BTO, BTFO ‖ (001) [001] STO and (100) [010] BTO, BTFO ‖ [110] STO. In the $m$ = 3 system, the addition of Fe increases the $a$ and $b$ parameters of the unit cell [150], [366], thus decreasing the lattice mismatch between the Aurivillius phase structure and underlying substrate, and promoting the layer-by-layer growth mechanism. It therefore follows, that by tweaking the composition or phase of an Aurivillius material, the growth mechanism may be tuned by altering the lattice parameters of the material. The growth of even $m$ = 4, 6 and 8 layered Aurivillius phases on NGO and STO grown via pulsed laser deposition [199], [200] further show the that Aurivillius phases can have a preference to grow via the 2$D$ layer-by-layer mechanism when equilibrium conditions are satisfied.

Previous CVD approaches for $m$ = 3 Aurivillius phases used a sequential growth mechanism (each precursor is injected separately in sequence, mimicking the Aurivillius structure [165], [308]) in order to achieve layer-by-layer growth. The films in this work were deposited using a concurrent injection method (all the precursors are injected into the chamber at the sample time as a mixture) under high supersaturation conditions. Analysis of

the surface morphology of the B6TFMO films deposited under 5.0 % bismuth excess in **Figure 6.3 (b-d)** and examination of the cross-section of the 5.0 % bismuth excess film, as shown later in **Figure 6.5 (a)**, clearly demonstrates that the epitaxial growth mode for $m$ = 5 films under high supersaturation conditions proceeds via 2*D* nucleation and a layer-by-layer growth mechanism [363] without the need for the more complex sequential deposition method. Multiples of laterally grown half unit-cell B6TFMO building blocks progressively unite with increased lateral coverage to form a flat film prior to the growth of subsequent layers. AFM images of B6TFMO films deposited during the same growth run are shown in **Figure 6.3 (b) to (d)**, where *2D* islands are visible on the film surface. These 2*D* islands are similar to those shown before by Gradauskaite *et al*. [193] and Keeney *et al*. [191], [367] for other Aurivillius phase samples and indicate an intermediary stage in the growth of B6TFMO. Overall, it appears as though epitaxial substrate strain does not have a large impact on the size of the crystal grains or the 2D islands observed in **Figure 6.3 (b)** to **(d)**, given that there is no significant difference between the morphologies of the Aurivillius grains for the B6TFMO films on STO, LSAT or NGO. However, in **Figure 6.3 (e)**, it is shown that when a non-epitaxial substrate is used, continuous B6TFMO films cannot be grown, nor are any *2D* island features present.

The impact of substrate strain on the formation of secondary phase impurities was also investigated. AFM images indicate that substrate strain influences the levels of secondary phases. This is evident on the B6TFMO surfaces for samples prepared under these growth conditions utilising a 5.0 % excess bismuth. Examples of these second phase impurities can be seen in the orange circles in **Figure 6.3**. They typically appear on top of Aurivillius phase *2D* islands, where their diameter can be seen to vary between ~0.05 to 0.4 um with heights of about 5 to 10 nm above the *2D* islands. The XRD pattern for the film with the highest percentage of surface impurities, B6TFMO on STO (red line), is shown in **Figure 6.3 (a)** and demonstrates a broad peak at a 2θ value of ~32.4 °. This peak potentially corresponds to the (222) cubic *Ia*-3 bixbyite reflection (JCPDS 08-0010) [368]. This secondary-phase magnetic impurity has been observed previously in Keeney *et al.*'s [171] thinner, sub-10 nm films that were grown via a two-step deposition and anneal process. The density of secondary phase impurities on the surface varies significantly, depending on the substrate used. For these films, the volume percentage (vol. %) of the surface covered by impurities is the lowest for

B6TFMO on LSAT at 1.7 vol. %, while for B6TFMO on NGO and STO, surface impurity levels are 5.5 vol. % and 6.7 vol. %, respectively. RMS roughness values for the images of the films shown in **Figure 6.3** are 4.351 nm for B6TFMO on LSAT, 5.981 nm for B6TFMO on NGO and 9.559 nm for B6TFMO on STO. The decreased RMS roughness value for the B6TFMO thin film on LSAT is attributed to the lower volume of impurities on the film surface.

To comprehend why strain has an impact on the formation of the surface impurities as shown in **Figure 6.3**, the bi-axial epitaxial relationship between B6TFMO and the underlying substrates must be considered. In this study, epitaxial growth of the B6TFMO films on LSAT, NGO and STO, was confirmed by the shift observed in the (00*l*) reflection positions. When investigating which epitaxial substrate used is the best match for B6TFMO, it should be considered that orthorhombic B6TFMO grows on the substrates with an epitaxial relation (001) [001] B6TFMO||(001) [001] substrate and (100) [010] B6TFMO||[110] substrate [165]. By theoretically calculating the length of the (110) *a*-*b* parameter of the substrates, it is predicted that LSAT would have the smallest lattice mismatch to the B6TFMO substrate at approx. -0.2 % where STO and NGO would have larger lattice mismatches of approx. 0.8 % and approx. -0.5 % in the *a*-*b* direction respectively. While investigating the bi-axial relationship between B6TFMO and its underlying substrate reveals that LSAT is the most lattice matched (compared to STO if just the parameter is considered). The trend of the strain for the substrates remains the same with STO leading to tensile strain in B6TFMO and LSAT and NGO causing compressive strain. Thus, it is possible that the lattice matching between the LSAT substrate and the B6TFMO film promotes the growth of the Aurivillius phase more favourably compared to growth on the STO and NGO substrates. It follows that this may help reduce the formation of surface impurities in B6TFMO and explain why the B6TFMO film on LSAT had the lowest volume of surface impurities (1.7 vol. %) compared to the films on STO and NGO.

### 6.3.3 Influence of Utilising a Bismuth Excess during Aurivillius Phase Thin Film Growth via DLI-CVD

The above section explored the influence of substrate-induced biaxial strain on B6TFMO growth and it was determined that LSAT (100) substrates were optimal for growing ~45 nm thick B6TFMO films using a single step DLI-CVD deposition at 700 °C. In this section, the influence of bismuth excess on B6TFMO film growth is investigated.

XRD patterns of Aurivillius phase thin films deposited via DLI-CVD at 700 °C with between 1.8 to 50.6 % bismuth excesses employed during deposition are shown in **Figure *6.4* (a)**. For all the films synthesised, the desired *m* = 5 Aurivillius phase was the main crystal phase identified. However, there is evidence for lower phase *m* = 4 intergrowths as shown through broadening of the base of the (00$\underline{1}$0) and (00$\underline{2}$4) reflections, along with the appearance of prominent shoulder peaks as marked by the green asterisk [150], [258].

From AFM images (**Figure 6.4 (d) and (e)**) of B6TFMO films deposited with 5.0 % and 1.8 % excess bismuth**,** it is shown that the surface is mainly made up of Aurivillius phase 2*D* islands. From the line profile analysis performed in **Appendix IV Figure IV.4 (c-d)** and the regions marked with red rectangles within the TEM image in **Figure 6.5 (b)**, it is determined the Aurivillius phase 2*D* islands are typically between 2.5 to 10 nm in height. This corresponds to Aurivillius phase structures of between 0.5 and 2 unit cells (u.c.) in thickness. TEM images demonstrate that step heights at the edge of the Aurivillius 2*D* islands can originate from differing multiples of half-unit cell and are not always equal in thickness. For example, the Aurivillius phase 2*D* islands on the left of **Figure 6.5 (b)** demonstrate a step height equivalent to 0.5 u.c. thick structures above the underlying film. However, the edge at the right side of the 2*D* island has a step height of 1 u.c. above the thickness of the underlying film.

For films deposited under a higher bismuth excess, for example 50.6 % (black line in XRD plot) and 17.7 % (red line in XRD plot) excess, a large, broad peak within the XRD pattern (**Figure 6.4 (a)**) is observed at a 2θ value of ~32 °. In both films, this peak has a broad base (with a width of ~3 °) and the peak becomes less intense as the bismuth excess decreases. For the B6TFMO films with 50.6 % bismuth excess, this peak has a FWHM value of ~1.67 ± 0.01. The broad peak within the B6TFMO film with 17.7 % bismuth excess has a FWHM value of

~1.60 ± 0.01. For the films with 5.0 % and 1.8 % bismuth excess, the reflection is no longer present. The position of this peak, its broad nature, and its disappearance when a lower bismuth excess is used indicates the presence of a $Bi_2O_3$ impurity phase. $Bi_2O_3$ demonstrates peaks at 2θ positions of 31.6 ° for the (200) reflection of the cubic *Fm*-3*m* cubic δ-$Bi_2O_3$ phase (JCPDS 77-2008) [369]. Inspection of the films with 50.6 % and 17.7 % bismuth excess by AFM imaging (**Figure 6.4 (b) and (c)**), exposes large cubic features which dominate the film surface topography. These resemble the δ-$Bi_2O_3$ impurity features (Impurity 1) seen in work by Alexe *et al.* [288]. From AFM analysis of the films shown in **Appendix IV Figure IV.4**, these features can reach thicknesses of up to 100 nm high on the sample with a 50.6 % bismuth excess. The AFM images of the films with lower bismuth excess presented in **Figure 6.4 (d)** and **(e)**, show that the large cubic surface features indicative of the $Bi_2O_3$ impurities are not present. A second type of impurity phase (Impurity 2) can be observed in the films with bismuth excess of 17.7 %, 5.0 % and to a lesser extent with 1.8 % excess. From an area analysis of both types of impurities shown in **Figure 6.4**, the impurities cover approximately 36 % ($Bi_2O_3$), 21 vol. % (a combination of $Bi_2O_3$ and smaller impurity phase), 1.7 vol. % and 1.0 vol. % of the B6TFMO film surface for the samples prepared with 50.6 %, 17.7 %, 5.0 % and 1.8 % bismuth excess, respectively. This clearly shows that as the bismuth excess decreases, overall volumes of impurity phases on the material surface decrease.

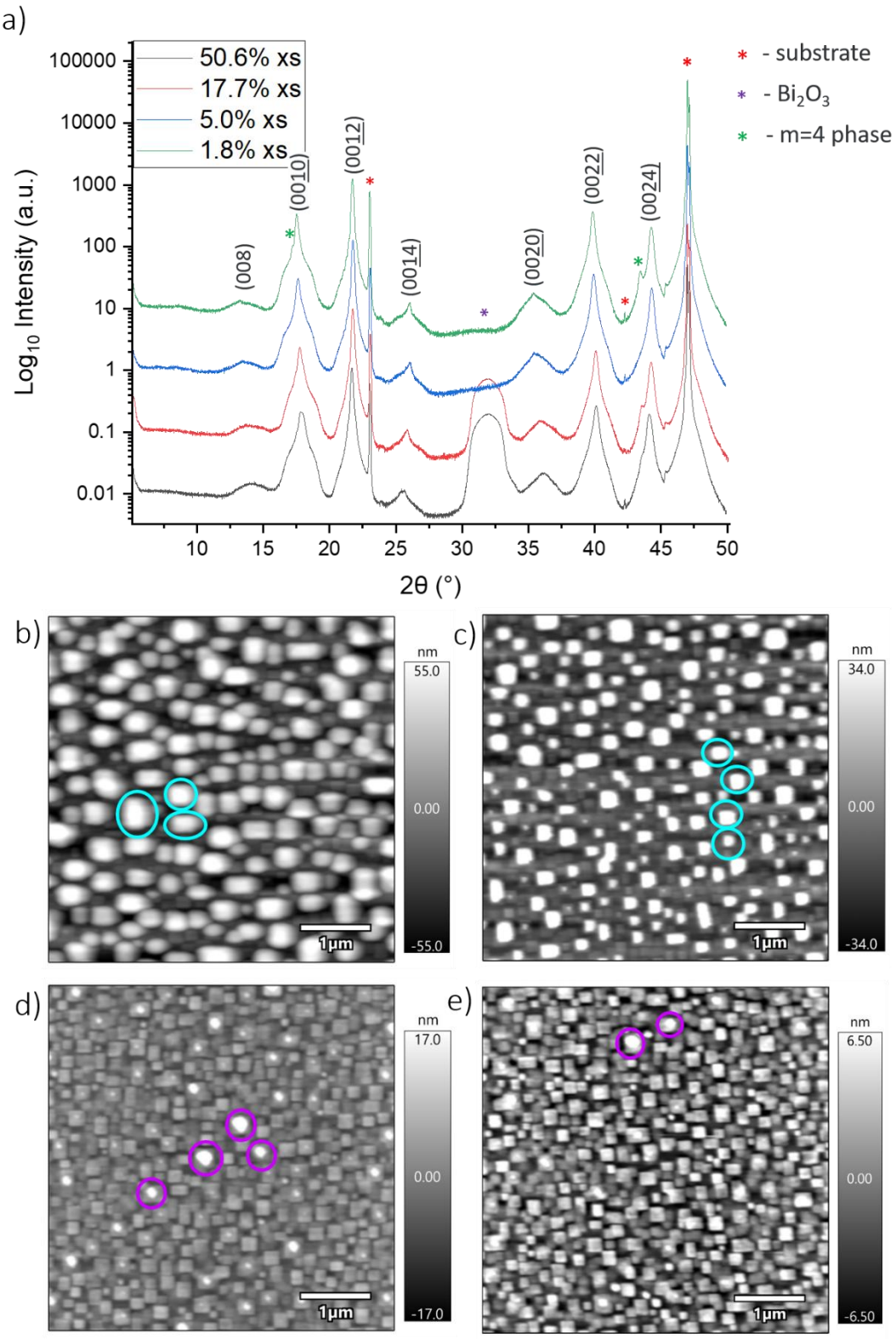


**Figure 6.4** a) XRD plots of B6TFMO films on LSAT with varied bismuth excess (xs) used during deposition. b) to e) AFM images of the four films where the bismuth precursor excess used was 50.6 % (b), 17.7 % (c), 5.0 % (d) and 1.8 % (e). Here examples of Impurity 1 are in blue circles in (b) and (c), while examples of Impurity 2 are in purple circles in (d) and (e).

TEM imaging of a cross section of the film deposited with a 17.7 % bismuth excess (presented in **Figure 6.6 (a)** and **(b)**), shows a large $Bi_2O_3$ impurity (green inset), alongside smaller impurity phases (red inset). From the images of the cross sections, it is shown that the impurities lie only on the surface of the material and not within the main Aurivillius phase film. The impurities tend to form on top of the Aurivillius phase 2*D* islands. As indicated by the TEM images of the film lamella, the $Bi_2O_3$ impurities (Impurity 1) appear to have an average height of 61 ± 14 nm, while the smaller impurities (Impurity 2) have an average height of 22 ± 7 nm. From higher resolution AFM scanning (**Figure 6.6 (c)**) of the sample with a 5.0 % bismuth excess, it appears as though the second smaller impurity is comprised of two components. One segment (Impurity 2a), which tends to be positioned at the centre of the Aurivillius phase 2*D* island, is accompanied by a second component (Impurity 2b) that is situated diagonally from the centre of the Impurity 2a. From the height profiles taken of these features and shown in **Appendix IV Figure IV.4** and ***Figure IV.5***, it is shown that Impurity 2a at the centre of the Aurivillius 2*D* island is taller than the Impurity 2b component to the corner. XRD analysis (**Figure 6.3 (a)**) of the B6TFMO film deposited with 5.0 % bismuth excess, where only Impurity 2 type is present in the film, reveals a peak at 32.4 °. This indicates the centre impurity phase (Impurity 2a) potentially corresponds to the (222) cubic *Ia*-3 bixbyite reflection (JCPDS 08-0010) [368]. In previous work by Keeney *et al.* [171] on thinner B6TFMO films, when the bixbyite impurity was detected, it was accompanied by a smaller amorphous $Bi_xTi_yO_z$ material, which appears similar to Impurity 2b in **Figure 6.6 (c)**.

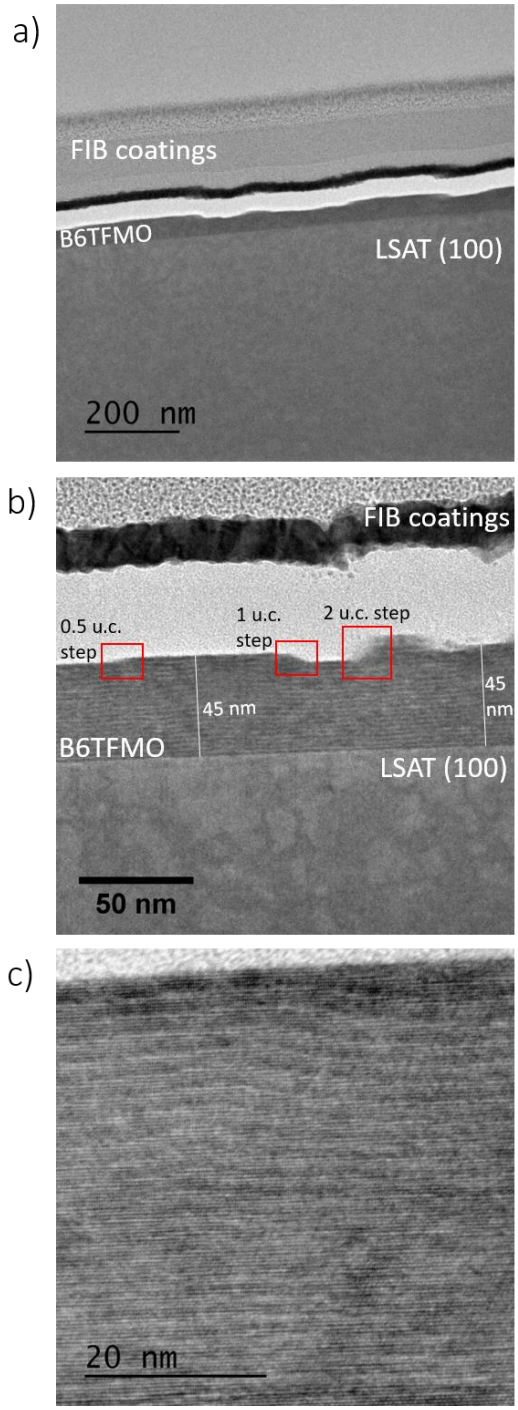


**Figure 6.5** TEM images of the B6TFMO film deposited on LSAT using a 5.0 % bismuth excess. The Aurivillius 2*D* islands that make up the surface topography are clearly seen in a) and b). The differing heights of the surface features within the red rectangles were measured. These heights are typically between 2.5 nm and 10 nm, corresponding to the thickness of 0.5 to 2 B6TFMO unit cells. c) Impurity free section of the Aurivillius film (overall $m = 5$) with out-of-phase boundary defects present.

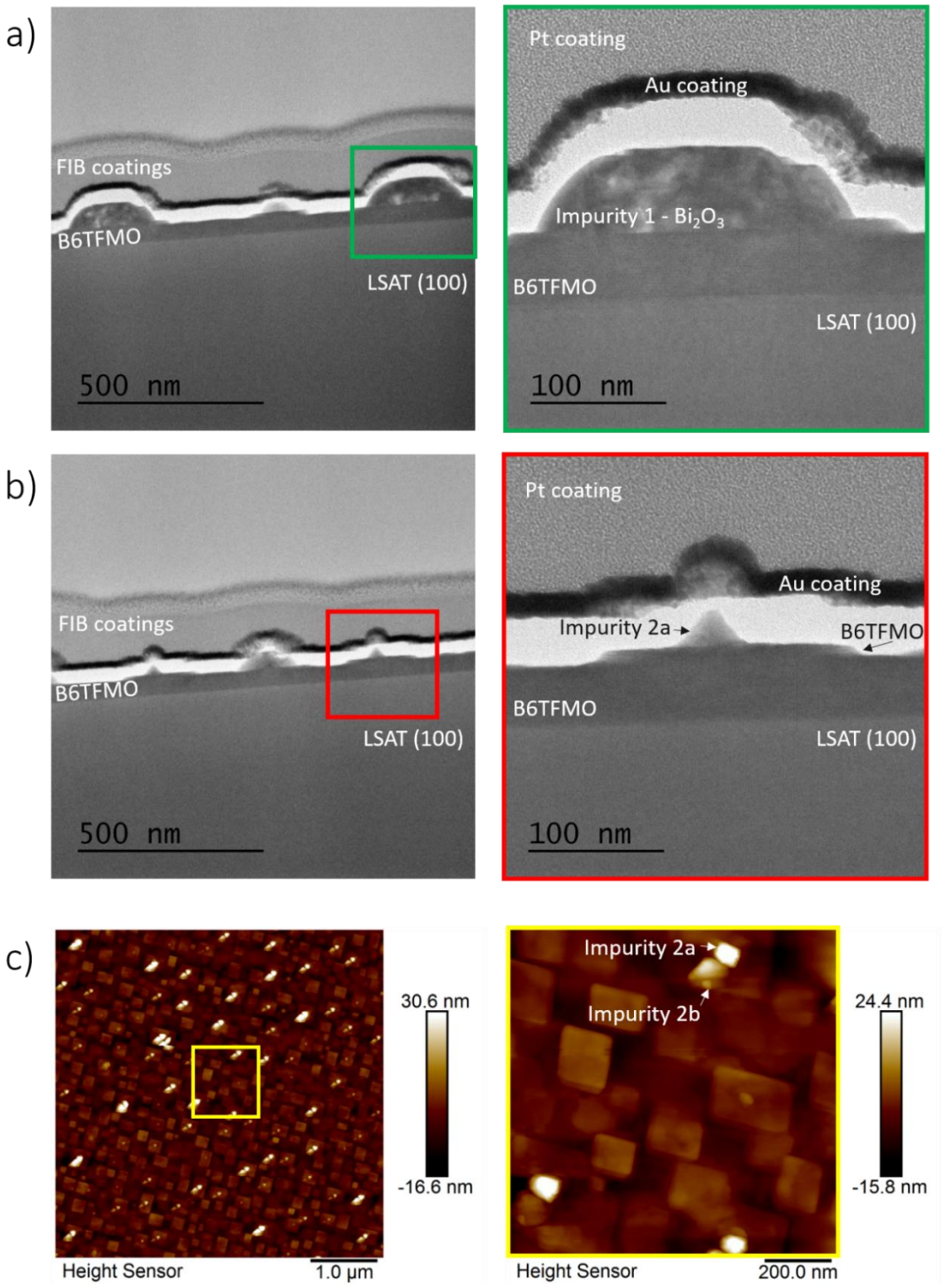


**Figure 6.6** a) and b) TEM images of a B6TFMO film deposited with 17.7 % bismuth excess. Two types of surface impurities can be observed. In the green inset in a) a large $Bi_2O_3$ impurity (impurity 1) that is ~70 nm in height is visible, while within the red inset in b) a smaller triangular shaped impurity about ~25 nm high is present (impurity 2). High resolution AFM imaging in c) of B6TFMO film deposited with 5.0 % bismuth excess shows the smaller impurity is made up of two components (Impurity 2a and Impurity 2b).

For B6TFMO thin films grown using the single step deposition process with 400 injections at 700 °C on LSAT, it is evident that as the bismuth excess is lowered and becomes close to the actual stoichiometric value, the volume of impurities on the thin film surface decreases. The films deposited using a 1.8 % bismuth excess are the smoothest, with an RMS roughness value of 3.2 nm as taken from **Figure 6.4 (e)** compared to 4.4 nm, 18.5 nm and 29.1 nm for the 5.0 %, 17.7 % and 50.6 % bismuth excess films respectively (**Figure 6.4 (b)** to **(d)**).

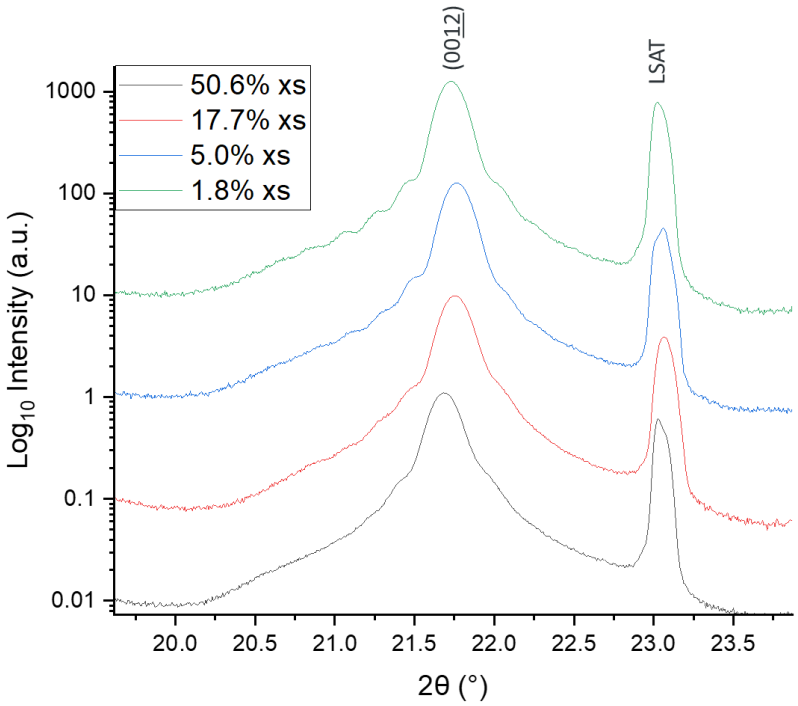


**Figure 6.7** XRD plot showing peaks corresponding to the (00$\underline{12}$) reflection and the LSAT substrate taken from B6TFMO films on LSAT with varied bismuth excess.

Focusing more closely on the (00$\underline{12}$) reflection of the *m* = 5 B6TFMO phase in **Figure 6.7**, it is shown that superlattice reflections become clearer as the bismuth excess percentage is lowered. This indicates that for the thin films deposited with a lower bismuth excess of 1.8 % and 5.0 %, there is a periodic arrangement of alternating *m* phases crystallographically aligned within the B6TFMO film [309] (visually evident in the TEM image in **Figure 6.5 (c)**). The fact that superlattice reflections are observed for the films with lower bismuth excess could be a result of the reduced number of secondary phase surface impurities. This is further investigated using the modified Scherrer equation [359] applicable for orthorhombic structures, which is useful for assessing the crystalline quality of a material. In this work, the

quality factor was calculated using the (00$\underline{10}$), (00$\underline{12}$) and (00$\underline{22}$) reflections. The quality factor, Q, is 3.69 ± 1.48, 3.41 ± 1.68, 3.12 ± 1.60 and 2.78 ± 1.76 for the B6TFMO films deposited with 1.8 %, 5.0 %, 17.7 % and the 50.6 % bismuth excess films respectively. This indicates that the quality factor increases as the bismuth excess decreases.

In this work, it is observed that for a single step deposition via DLI-CVD at 700 $^{o}$C, a bismuth precursor value that matches the requirements of a stoichiometric B6TFMO composition produces films with the lowest volume of impurity phases. This is in contrast to previous works using a two-step deposition and anneal method [163] or the single step deposition of thinner sub-10 nm films [171], where large 20 to 50 % bismuth excesses were employed. Perhaps the different bismuth requirements for the deposition of different thicknesses of B6TFMO films is affected by the surface area of the films. Bismuth desorbs from the surface of materials during growth and considering that the surface of the sub-10 nm films is a much larger component of the film than the sub-50 nm films, the thinner films may need a higher bismuth excess to compensate for this. The fact that bismuth desorbs from the surface of B6TFMO at high deposition temperatures (above 710 °C [360]) indicates that the amount of bismuth used in a deposition run can often be critical to the successful growth of B6TFMO and its material properties. When growing B6TFMO, the role of the surface becomes more and more important as film thickness decreases. The larger relative surface area of the sub-10 nm films compared to the relative surface area of the sub-50 nm films mean a higher percentage of the bismuth in the underlying film can escape compared to the sub-10 nm films [370].

### 6.3.4 Investigations of Ferroelectric Properties at the Nanoscale

DART-PFM was performed on the B6TFMO films to investigate the nano-scale piezoelectric properties of the B6TFMO thin films grown by the one-step deposition process. From the PFM images in **Figure 6.8 (a)** to **(f),** it is determined that the large impurity phases found on the film deposited with 17.7 % bismuth excess (and found similarly in the films deposited with 50.6 % bismuth excess) do not demonstrate a piezo-response, although but the underlying B6TFMO film is piezoelectric. While previous studies from Alexe *et al*. [288] showed that

similar impurities demonstrated conductive characteristics, electrical conductivity could not be measured from conductive AFM (C-AFM) measurements (**Appendix IV *Figure IV.6***) of the B6TFMO film deposited using a 50.6 % bismuth excess (the film with the highest surface density of $Bi_2O_3$ impurities). Note however that the lack of conductive response for the C-AFM measurements could be associated with the insulating nature of the underlying substrate.

A strong in-plane PFM response is measured using lateral piezorespose force microscopy (LPFM) of the smooth impurity free region, as shown in **Figure 6.8 (g** to **l)** for the B6TFMO film deposited with 1.8 % bismuth excess. A much weaker vertical piezoresponse was measured by PFM in the vertical direction (VPFM). The clear in-plane response obtained is expected for an Aurivillius phase material due to crystal symmetry considerations [154]. The ferroelectric domains measured on these films appear relatively small compared to those found on films synthesised by the two-step method on *c-m* sapphire (0.23 ± 0.03 $\mu m^2$), **Chapter 4, Section 4.3.5**. For the B6TFMO film grown on LSAT using a 1.8 % bismuth excess, the average ferroelectric domain size was 0.0031 ± 0.0026 $\mu m^2$ (calculation from two 1 x 1 $\mu m^2$ images). From a closer inspection of the surface features of the film shown in **Figure 6.9 (b** and **c)**, it can be observed that there are multiple configurations of ferroelectric domains on the surface of the B6TFMO film. It is possible that due to the thin nature of the Aurivillius phase surface 2*D* islands, which are often between 2.5 to 10 nm in height, in some areas the piezoresponse measured could be complicated by the mixing of different piezo signals coming from both the Aurivillius phase 2*D* island and the underlying Aurivillius phase film. One possible route that could be taken to investigate the underlying domain structure would be to perform AFM-based nano-milling followed by PFM measurements. AFM-based nano-milling (sometimes called AFM-based nano-machining) is a technique, which uses a sufficiently hard and stiff probe combined with an appropriate loading force to shave away the top surface of a thin film in a controlled manner. It is proposed that this technique could be used to gently remove the Aurivillius surface 2*D* islands to investigate domain configurations of an even and smooth material surface [367], [371], [372].

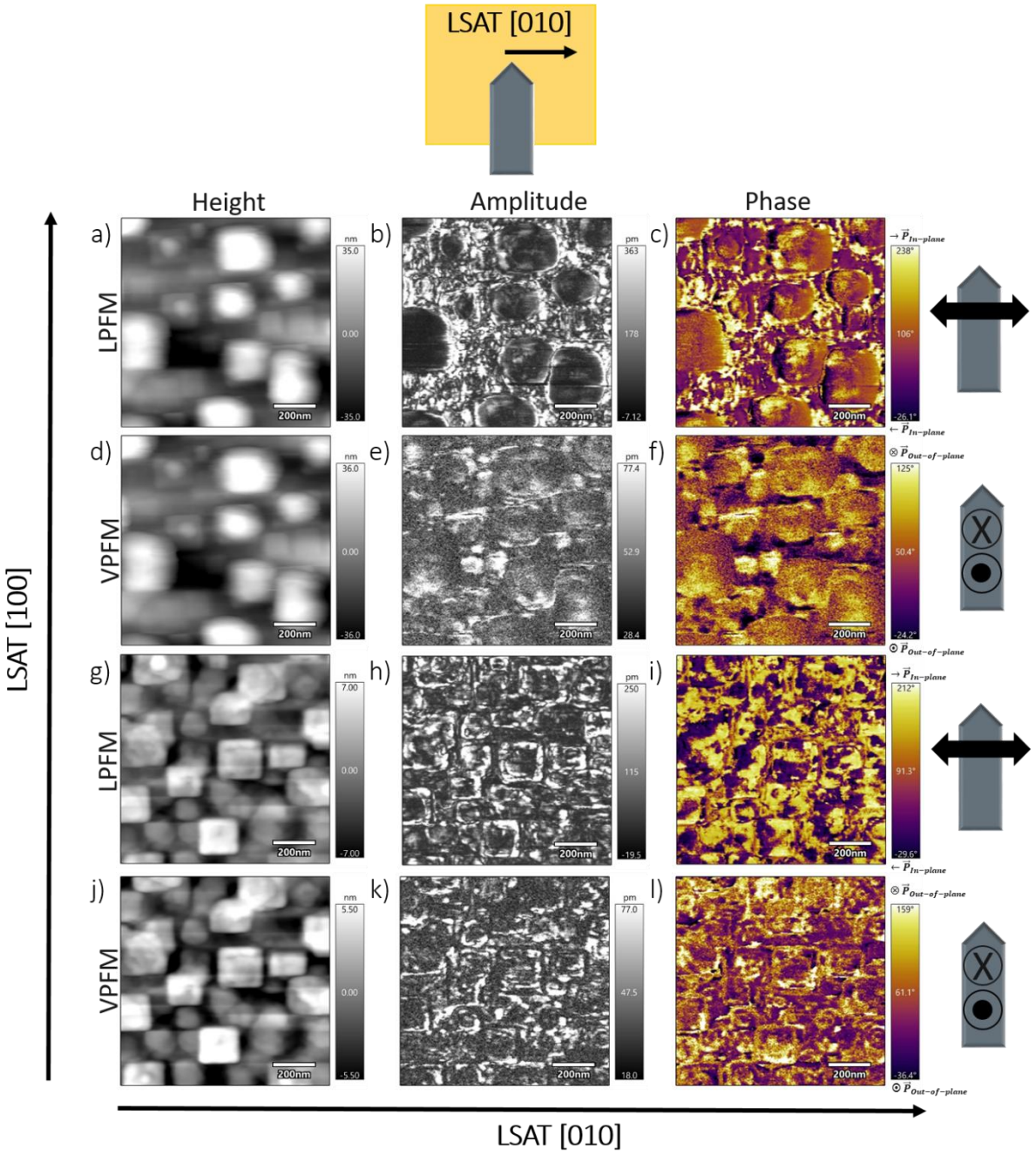


**Figure 6.8** In–plane LPFM and out-of-plane VPFM images of B6TFMO thin films on LSAT deposited with a) to f) 17.7 % and g) to l) 1.8 % bismuth excess. The probing voltage ($V_{AC}$) is 1.0 V.

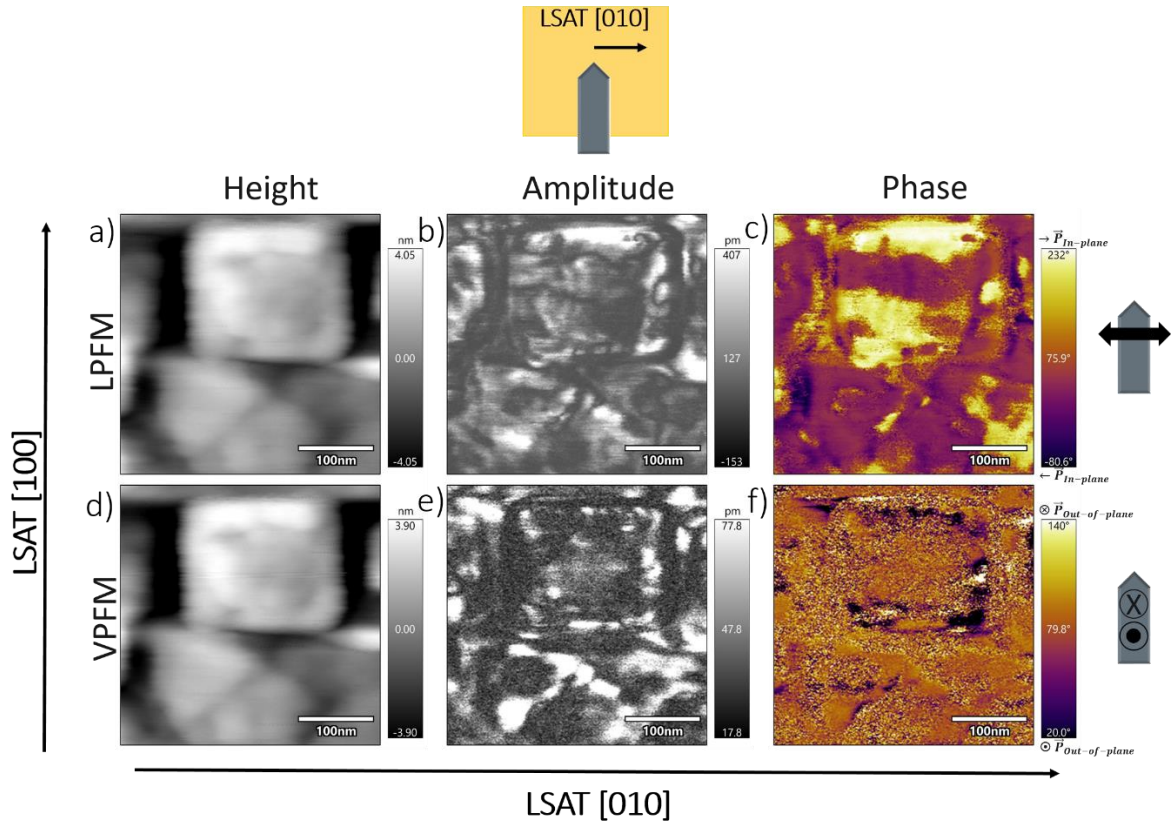


**Figure 6.9** (a to c) In–plane LPFM and (d to f) out-of-plane VPFM images over 350 x 350 nm$^2$ areas of a B6TFMO thin film on LSAT deposited with a 1.8 % bismuth excess. The probing voltage ($V_{AC}$) is 1.0 V.

Previous studies by Gradauskaite *et al*. [193] on 0.5 u.c. bismuth based Aurivillius films deposited on NGO have displayed anisotropic in-plane ferroelectric domain patterns. However, above these thicknesses, uniaxial ferroelectric anisotropy is lost, attributed to the weak interlayer coupling between the perovskite layers in the Aurivillius scaffold [158]. In Aurivillius structures which display ferroelectric anisotropy, this is stabilised by a latticed mismatch. However, as the film increases in thickness, the strain imparted by the substrate lessens and anisotropic ferroelectric domains are eventually lost. While the films in this study are considerably thicker ~45 nm (9 u.c.), PFM experiments were performed on the B6TFMO films to investigate whether ferroelectricity is anisotropic within the thin films. These experiments were carried out with the cantilever aligned parallel to the [010] substrate direction, as shown for the film deposited with 1.8 % bismuth excess on NGO in **Figure 6.10 (a** to **f)**. The PFM measurements were then immediately repeated on the same sample after it was rotated by 90 °, such that the cantilever was aligned parallel to the [100] substrate

direction as shown in **Figure 6.10 (g** to **l).** As would be expected for films of this thickness, ferroelectric anisotropy is not present, and this is also the case for films on LSAT and STO as observed in **Appendix IV Figure IV.7** and ***Figure IV.8***.

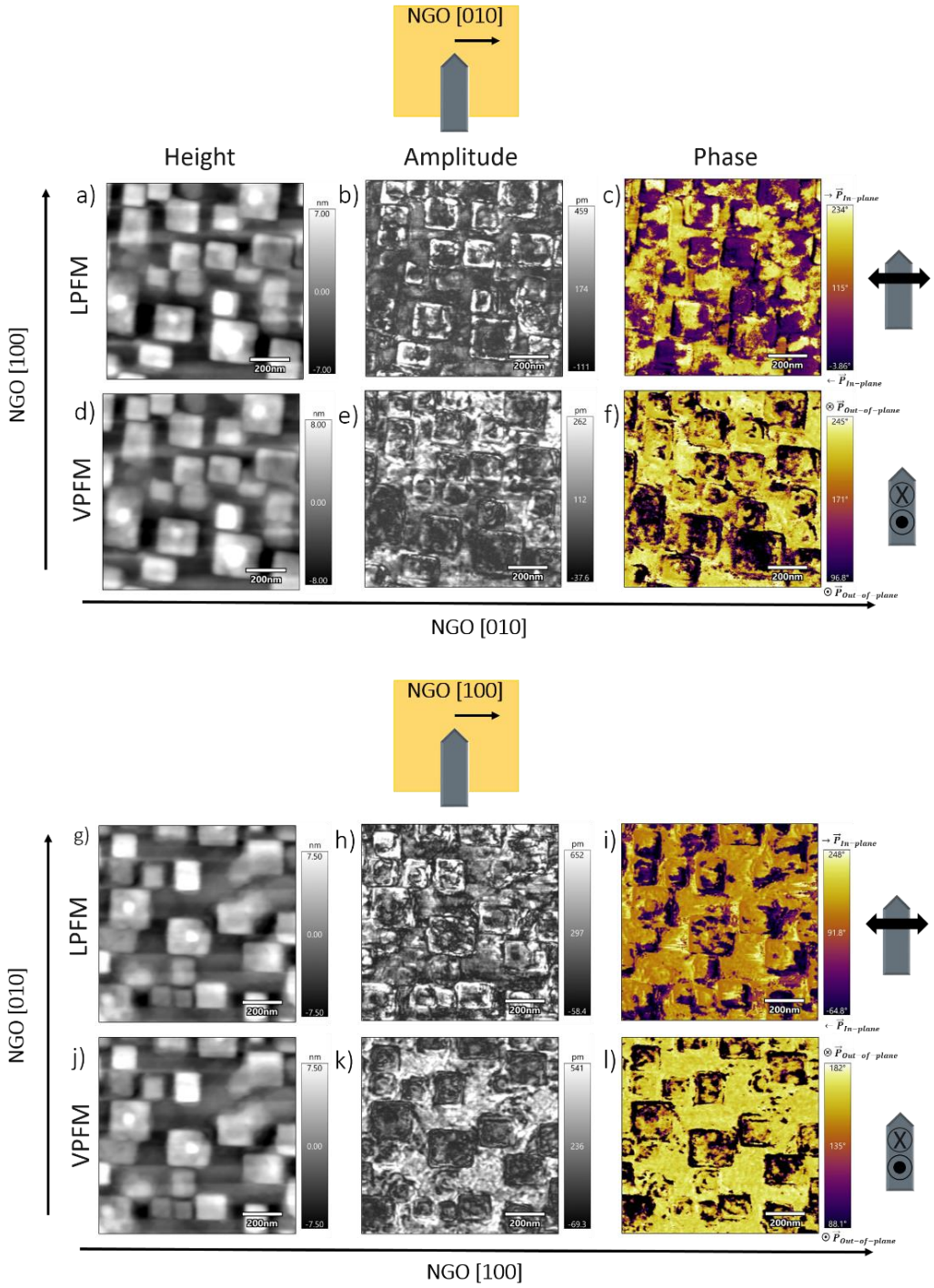


**Figure 6.10** LPFM and VPFM, DART-PFM height, amplitude and phase images of B6TFMO films on NGO (100) deposited with a 1.8 % bismuth excess and probed at 1 $V_{AC}$ and 2 $V_{AC}$, for LPFM and VPFM measurements respectively. Images (a) to (f) were performed with the cantilever scanning direction parallel to the [010] NGO axis. The samples were subsequently rotated 90 ° for images (g) to (l), where the cantilever scanning direction was parallel to the [100] NGO axis. These images demonstrate the isotropic distribution of in-plane and out-of-plane domains in films ~ 45 nm thick for B6TFMO on LSAT (100).

## 6.4 Conclusions

The influence of deposition method, substrate and percentage bismuth excess were investigated to optimise the growth of B6TFMO films with a thickness of ~45 nm. Epitaxial substrates were needed to grow continuous B6TFMO films at sub-50 nm thickness.

The two-step deposition and anneal of B6TFMO using a 630 °C deposition temperature and a post-anneal at 850 °C requires a bismuth excess of ~20 % to mitigate bismuth loss at the post anneal stage. However, using the two-step deposition and anneal resulted in thin films that had a non-uniform surface.

During a single-step deposition process at 700 °C, the Aurivillius phase grows via a *2D* nucleation and layer-by-layer Frank van der Merwe growth mode. Due to the lattice matching of the (010) plane of the underlying substrate with either the *a* or *b* lattice parameter of B6TFMO, it was found in this study that LSAT was the optimum candidate of substrate to grow B6TFMO films with minimum levels of impurities, when compared to NGO or STO. A 5.0 % decrease in surface impurities was found for films grown on LSAT when compared to STO.

For films grown via a single-step process at 700 °C, lowering of the bismuth excess used and keeping it closer to the quantity required for compositional stoichiometry appears to be optimal for reducing impurities. For B6TFMO films deposited with 17.7 % and higher bismuth excess, $Bi_2O_3$ secondary phase impurities were abundant. For the B6TFMO films prepared by the single-step process in this study, those deposited with 1.8 % bismuth excess on LSAT substrates displayed the lowest volume of surface impurities, at 1.7 % vol. PFM measurements demonstrate the films have a strong in-plane ferroelectric response with isotropic domains, where surface Aurivillius phase 2*D* islands, formed during an intermediary step during 2D layer-by-layer growth, appear to complicate the measured surface piezoresponse.

Further optimisation is required on these films to completely eliminate the impurity phases, perhaps by lowering the deposition temperature, altering the magnetic cation concentrations or moving towards a sequential, layer-by-layer chemical vapour deposition approach. Nonetheless, this work progresses the understanding of the parameters required

to optimise the epitaxial growth of B6TFMO via DLI-CVD and their ferroelectric behaviour at nanoscale.

# 7 Conclusions and Outlook

The research within this thesis delves into a deeper understanding of the fundamental mechanisms driving the multiferroic behaviour within Aurivillius phase B6TFMO using atomic and nano-scale characterisation techniques in conjunction with DFT calculations. Alongside this, further knowledge into how substrate and deposition conditions influence the growth and ferroelectric and ferromagnetic properties at the macro- and nano-scale was accomplished.

B6TFMO is an intriguing, yet not fully understood material. First synthesised in 2013 [162], it has been proven to be a true single phase room-temperature magnetoelectric multiferroic [163], [273]. While previous EDX studies [164] revealed the importance of magnetic cation partitioning towards the centre of the perovskite layers within the Aurivillius structure, in this thesis, atomic resolution electron microscopy in conjunction with DFT calculations are used to correlate the fundamental electronic structure of *B*-site cations with local chemical bonding environments in B6TFMO. Discrete changes in the crystal field splitting of the $Ti^{4+}$ cations were detected using HAADF-STEM EELS, where the $e_g$-$t_{2g}$ splitting, $\Delta$, was found to increase going from the outer to the centre perovskite layers of the Aurivillius structure. The atom resolved projected density of states produced via DFT calculations elucidated that this splitting is driven by the distortion of the perovskite unit cells created by the $[Bi_2O_2]^{2+}$ interlayer and is felt more strongly in octahedra which situate closest to the outer $[Bi_2O_2]^{2+}$ layers. Further imaging revealed the complicated nature of the $BO_6$ perovskite octahedra through the material. Through iDPC imaging, the competition between the tilting of the $BO_6$ octahedra and the extent of the tetragonal distortion felt by the perovskite unit cells can be appreciated, with DFT indicating that the tilting of the octahedra helps to minimise electrostatic potential and stabilise B6TFMO. The findings from the first results chapter, **Chapter 3**, on naturally layered B6TFMO, indicate that tilting of the perovskites is required to allow the magnetic iron and manganese cations to locate next to each other within the centre perovskite layers and thus could be necessary to enable long-range magnetic interactions and subsequent multiferroic behaviour in B6TFMO. The learnings from this work could be applied more widely to the development of heterostructure materials and

layered perovskites, where tilt engineering has been shown to enhance multiferroic properties [272].

Recent studies [192] have demonstrated the presence of unusual polar topologies within B6TFMO close to regions where structural defects, such as out-of-phase boundaries (OPBs), occur. Tantalisingly, this could open up B6TFMO to a host of new applications, such as energy-efficient nanoelectronics, ultrahigh speed data processing, ultra-compact memory storage applications and domain wall-based memory devices. While polar topologies can be observed naturally in B6TFMO without the need for an artificial interface or external strain engineering, for the topologies to become useful for future technologies, a greater understanding and control of them is needed. The use of substrates with differing mis-cut angles was employed in **Chapter 4** to deliberately introduce structural defects in the B6TFMO growing layers to examine whether there was enhancement in the formation of nominally charged 180 ° domain walls and polar vortices. Through both macroscopic (XRD) and microscopic (HAADF-STEM and PFM) measurements, it was found that increasing the mis-cut of the sapphire substrate was successful for impacting the structural and ferroelectric properties of B6TFMO. Broadening of the FWHM for reflections such as (006), (008), (00$\underline{18}$) and (00$\underline{20}$) occurred as the substrate mis-cut increased from 0.2 ° to 10 °, indicating a higher defect density within the B6TFMO films grown on higher mis-cut substrates. PFM measurements show the density of the ferroelectric domains increase with an increase in defect density due to increase in the substrate mis-cut angle. HAADF-STEM imaging also uncovered examples of charged domain walls and exotic polar vortices facilitated by OPBs within the samples when two OPB defects are spaced ~5 nm apart. This work successfully demonstrates that polar vortex domain walls and charged domain walls are promoted within layered multiferroics by tailoring the underlying substrate that the film is grown on. This work provides insight into methods for controlling defect levels and demonstrates how topological defects within B6TFMO can be tailored. Future work would build on the knowledge gained on mis-cut sapphire substrates and apply to the tailoring of novel topologies within B6TFMO films grown on epitaxial substrates with an off-axis substrate mis-cut. By employing step-flow growth across a vicinal substrate series with a controlled density of atomic steps, terrace width and step height, designed to introduce OPBs into the growing layer, could in turn enable regulation of the density and inclination of charged DWs within epitaxial B6TFMO films.

Furthermore, while the results here concern a naturally layered multiferroic, the learnings gained from using substrates with a slightly off-axis substrate cut and with a controlled density of atomic steps, could also be applied to enhancing polar vortex domain walls and polar skyrmions in artificial heterostructured materials.

In **Chapter 5**, the growth and properties of B6TFMO films on patterned sapphire were explored, with the aims of encouraging inclination of the *a*-axis of B6TFMO towards an upright geometry to increase access to the major *a*-axis polarisation. While initially the DLI-CVD deposited films were conformal, the preference for the Aurivillius phase to crystallise in a plate-like manner meant that after annealing, the B6TFMO was not fully conformal over the substrate. However, the majority of the B6TFMO grains followed the incline of the dome-shaped features on the patterned sapphire substrates. An XRD comparison of the B6TFMO films on patterned sapphire with those on un-patterned *c-m* sapphire, revealed that increased levels of non-(00*l*) reflections were present in the film on patterned sapphire. This indicated an increase in inclined *a-b* polycrystals present for B6TFMO deposited on the patterned sapphire substrate. Due to the inclined nature of the B6TFMO grains on patterned sapphire, it was challenging to fully probe the piezoresponse. Nevertheless, it was concluded that the out-of-plane piezoresponse of the samples is weaker than the in-plane piezoresponse. Studies of the magnetic properties of the films demonstrated that the B6TFMO samples were ferromagnetic at room temperature. It was found that the B6TFMO film on patterned sapphire had comparable magnetic properties to the films deposited on un-patterned sapphire in this study. These findings support B6TFMO's status as a room temperature multiferroic and indicates that the topography of the underlying substrate does not have a significant impact on the measured magnetic signal. While a two-step deposition on non-epitaxial substrates did not support the conformal growth of B6TFMO on patterned substrates, utilising epitaxial patterned substrates could provide a route to deposit conformal films. Epitaxial substrates can allow for the use of lower temperatures [166], [354] to grow conformal crystalline BTFMO thin films via a single-step DLI-CVD method. Investigating a wider range of shapes/sizes for the *3D* features on the surface of the patterned substrate in future work, along with a single-step method for film growth on epitaxial substrates could encourage vertically accessible out-of-plane polarisation in B6TFMO films.

Finally, in **Chapter 6** research on B6TFMO in this body of work moves onto optimising a process for the deposition of sub-50 nm films on epitaxial substrates. The deposition process was altered from a two-step to a single-step method to grow continuous films via a *2D* layer-by-layer growth mechanism. Two parameters within the single-step deposition were varied to improve the purity of the B6TFMO films: bismuth excess and substrate strain. It was discovered that for films deposited via the single-step deposition, maintaining the amount of bismuth used during the deposition process to that required stoichiometrically helps to avoid $Bi_2O_3$ impurities. Lattice matching B6TFMO's *a* or *b* lattice parameter to the (010) plane of the underlying epitaxial substrate also aided in reducing surface impurities on the epitaxially grown films. While the films were not optimised to be completely impurity free, PFM measurements demonstrate the films have a strong in-plane ferroelectric response with isotropic domains. Further optimisation of the B6TFMO films could perhaps be achieved through means such as lowering deposition temperature, altering the magnetic cation concentrations or moving towards a sequential, layer-by-layer chemical vapour deposition approach. Another possible route to be explored for the growth of thinner B6TFMO films could be via van der Waals epitaxy. While traditional epitaxial growth has enabled the development of thin film growth, ensuring a lattice match between the substrate and a proposed film has limited the number of heterostructures that can be fabricated. Van der Waals epitaxy involves the use of a *2D* material as the substrate and/or the epitaxial layer. The materials used in van der Waals epitaxy have no dangling bonds, therefore when growth occurs, no covalent bonds are formed between the substrate and the epitaxial layer. The layers are bound by the much weaker van der Waals forces. This weaker bond at the beginning of the film growth could allow for strain free growth of Aurivillius phases and potentially navigate the formation of impurity phases within the thin film growth that can be observed when using traditional epitaxial substrates [171].

To summarise, this thesis demonstrates that the appropriate combination of chemistry, internal strain and octahedral tilting is key to generating room temperature multiferroic properties within B6TFMO and that its room temperature multiferroic properties persist with changing substrate topographies. The wider technological potential of multiferroic B6TFMO has been demonstrated by showing that control of structural defects can facilitate unusual polar topologies, which will be useful for nanoelectronic device

applications. Moreover, progress has also been made with optimisation of the epitaxial growth of B6TFMO via DLI-CVD, which is necessary for its integration into commercial memory devices and potential use in a variety of other applications such as piezoelectric actuators, sensors and energy harvesters.

# I. Appendix - Supporting Information for Chapter 3

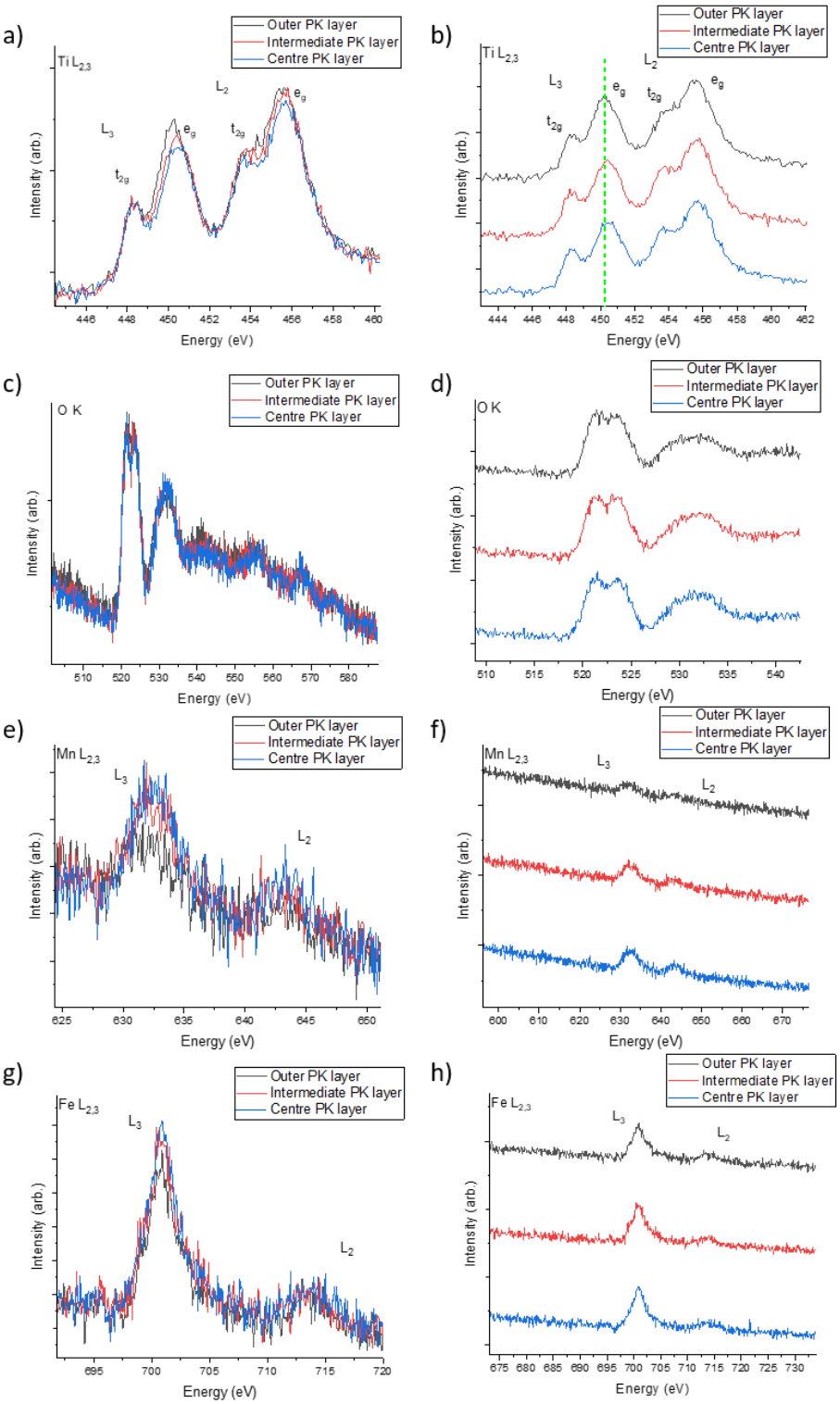

**Figure I.1** Atomic resolution STEM EELS spectra of outer, intermediate and centre perovskite regions of 5 layer B6TFMO. a) and b) Ti $L_{2,3}$-edge, c) and d) O K-edge, e) and f) Mn $L_{2,3}$-edge, g) and h) Fe $L_{2,3}$-edge.

The most intense component of the O K-edge in the data collected in **Figure I.1 (c-d)**, which is not zero-loss aligned, is at an energy of ~522 eV and gives information on the unoccupied O 2*p* states, which hybridise with the *B*-site metal cation 3*d* states. First, an energy splitting of ~2 eV in the O K-edge is observed. This is due to the weak hybridisation between the transition metal cation 3*d* $t_{2g}$ orbitals (lower peak) with the O 2*p* orbitals, and the more strongly hybridised 3*d* $e_g$ orbitals (higher peak) with the O 2*p* orbitals. This splitting could also have a contribution from the interactions between the O 2*p* and Bi 5*d*/*p* states [373], [374]. The second broad feature at ~532 eV in the spectra of the O K-edge is attributed to the O 2*p* hybridisation with the 4*s* and 4*p* states in the metal cations along with covalent bonding in Bi. This analysis did not differentiate any significant changes to the O K-edge structure in the EELS spectra as measured from the outer, intermediate or centre perovskite layers and taking into account that B6TFMO is a complex multi-cation oxide, it would be difficult to deconvolute the individual contributions of Ti, Mn and Fe to the O K-edge structure. In previous works [162], [164], [192], it has been demonstrated that the presence of Mn is key to the ferromagnetic behaviour observed within B6TFMO. EELS analysis in this work (**Figure I.1 (e-f)**) confirms the previous EDX observations of the partitioning of Mn cations towards the centre perovskite layers. Previous Density Functional Theory (DFT) calculations [192] indicate that magnetization values in B6TFMO are highly dependent on the increased nearest neighbour magnetic interactions resulting from this Mn partitioning. Considering the Goodenough−Kanamari rules, [75], [375], [376] ferromagnetic coupling could be created through $Fe^{3+}$–O–$Mn^{4+}$ ($d^5/d^3$ configurations) superexchange or $Mn^{3+}$–O–$Mn^{4+}$ ($d^4/d^3$ configurations) double-exchange interactions. Ferromagnetic coupling is also possible via semicovalent exchange interactions of $Mn^{3+}$–O–$Mn^{3+}$ ($d^4/d^4$ configurations). Ideally, EELS analysis would enable determination of the oxidation state of Mn within B6TFMO in order to determine the precise mechanism for ferromagnetism [377], [378]. However, due to the low concentration of Mn (~1.7 %) within B6TFMO's total composition, the Mn $L_{2,3}$-edge had a relatively low intensity compared to Ti, Fe and O signals within the data sets. The low signal to noise ratio within the Mn $L_{2,3}$-edge meant that the structural features characteristic of the

different Mn oxidation states could not be observed and it was not possible to determine the exact oxidation state of the Mn cation. The Fe cation oxidation state was confirmed by the presence of a shoulder at ~699 eV just after the edge onset in the $L_3$ signal. This initial feature is ~1 eV before the maximum peak, at ~700eV, and the shape seen in **Figure I.1 (g-h)** is characteristic of $Fe^{3+}$ and is consistent with the literature [379]–[382].

| Data Set Label | Outer Ti4+ L3 eg Peak (eV) | Centre Ti4+ L3 eg Peak (eV) | Change in Δ (eV) |
|---|---|---|---|
| 210610 K2 11 i | 453.77 | 453.87 | 0.1 |
| 210610 K2 11 ii | 453.8 | 453.87 | 0.07 |
| 210520 K2 7 i | 450.24 | 450.44 | 0.2 |
| 210520 K2 7 ii | 450.36 | 450.44 | 0.08 |
| 210520 K2 8 i | 450.65 | 450.88 | 0.23 |
| 210520 K2 8 ii | 450.61 | 450.88 | 0.27 |
| 210520 K2 12 i | 458.06 | 458.15 | 0.09 |
| 210520 K2 12 ii | 458.06 | 458.15 | 0.09 |
| 211002 K2 12 i | 458.44 | 458.51 | 0.07 |
| 211002 K2 12 ii | 458.33 | 458.51 | 0.18 |
| 211002 K2 16 i | 458.75 | 458.83 | 0.08 |
| 211002 K2 16 ii | 458.71 | 458.83 | 0.12 |
| 211201 K2 2.5 32 i | 458.35 | 458.38 | 0.03 |
| 211201 K2 2.5 32 ii | 458.26 | 458.38 | 0.12 |
| 211201 K2 5 29 i | 457.86 | 458.00 | 0.14 |
| 211201 K2 5 29 ii | 457.83 | 458.00 | 0.17 |
| 211201 K2 5 31 i | 458.14 | 458.24 | 0.1 |
| 211201 K2 5 31 ii | 458.14 | 458.24 | 0.1 |
| US100 2.5 13 A i | 460.12 | 460.26 | 0.14 |
| US100 2.5 13 A ii | 460.04 | 460.26 | 0.22 |
| US100 2.5 13 B i | 460.2 | 460.28 | 0.08 |
| US100 2.5 13 B ii | 460.14 | 460.28 | 0.14 |
| | | Average | 0.13 eV |
| | | St. Dev | 0.06 eV |

**Table I.1** Data from which the average change in crystal field splitting (Δ) for the $Ti^{4+}$ $L_3$-edge is calculated. Eleven EELS data sets were used to calculate the average Δ value. Each data set had two $e_g$ values for the outer perovskite layer and one $e_g$ value for the centre layer, therefore for each data set, two Δ values were obtained (twenty two data sets were obtained in total). The $t_{2g}$ peak value remains the same for the EELS spectra moving from the outer to the centre perovskite layers while the $e_g$ peak value changes. The change in Δ moving from the outer to the centre perovskite layers for the $Ti^{4+}$ $L_3$ peak was calculated by subtracting the outer perovskite layer $Ti^{4+}$ $L_3$ $e_g$ peak value from the centre perovskite $Ti^{4+}$ $L_3$ $e_g$ layer value.

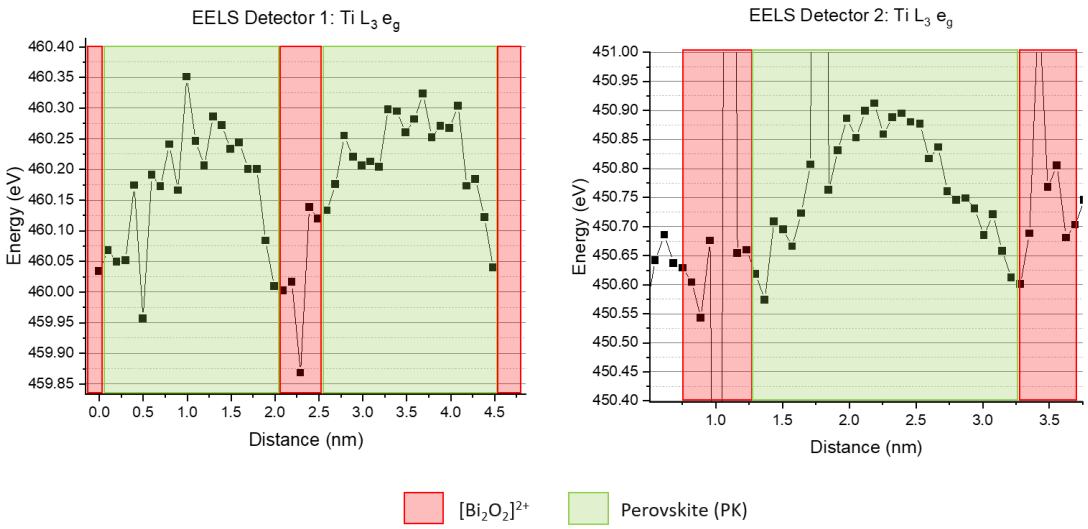


**Figure I.2** Further examples of plots from EELS data sets to support **Figure 3.2 (d)** in the main text. These plots demonstrate the change in peak energy of the Ti $L_3$ $e_g$ peak from re-binned EELS spectra as a function of distance through the perovskite layers of B6TFMO.

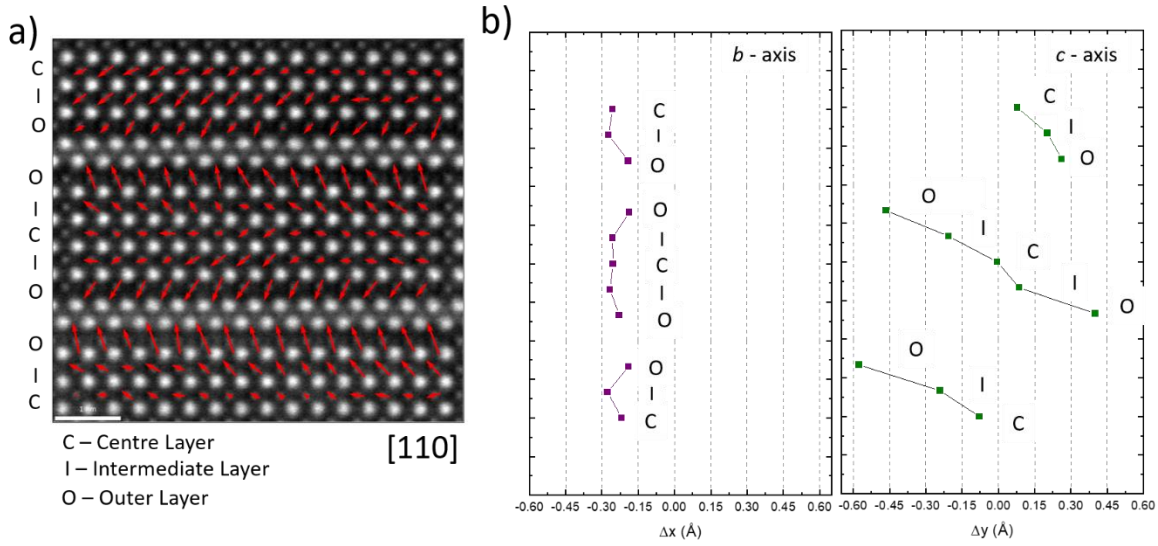


**Figure I.3** a) STEM-HAADF image of five-layered B6TFMO overlaid with polarisation vector mapping represented by the red arrows. Once the *A*- and *B*- site positions of the atoms are determined, the polarisation vectors (red) were obtained from the reverse of the *B*-site cation displacements using TEMUL toolkit [254]. The average *B*-site displacement within a perovskite cell for ''outer'', ''intermediate'' and ''centre'' *B*-sites were calculated along the *b*-axis (Δx) and *c*-axis (Δy) direction and are plotted in b). The overall average magnitude from each type of perovskite layer (outer, intermediate, centre) for the *B*-site cations displacements in the *c*-axis (Δy) direction were outer: 0.426 ± 0.142 Å, intermediate: 0.184 ± 0.095 Å and centre: 0.054 ± 0.062 Å. Average values for *B*-site cation displacements along the *b*-axis (Δx) were outer: 0.199 ± 0.006 Å, intermediate: 0.268 ± 0.009 Å and centre: 0.243 ± 0.009 Å.

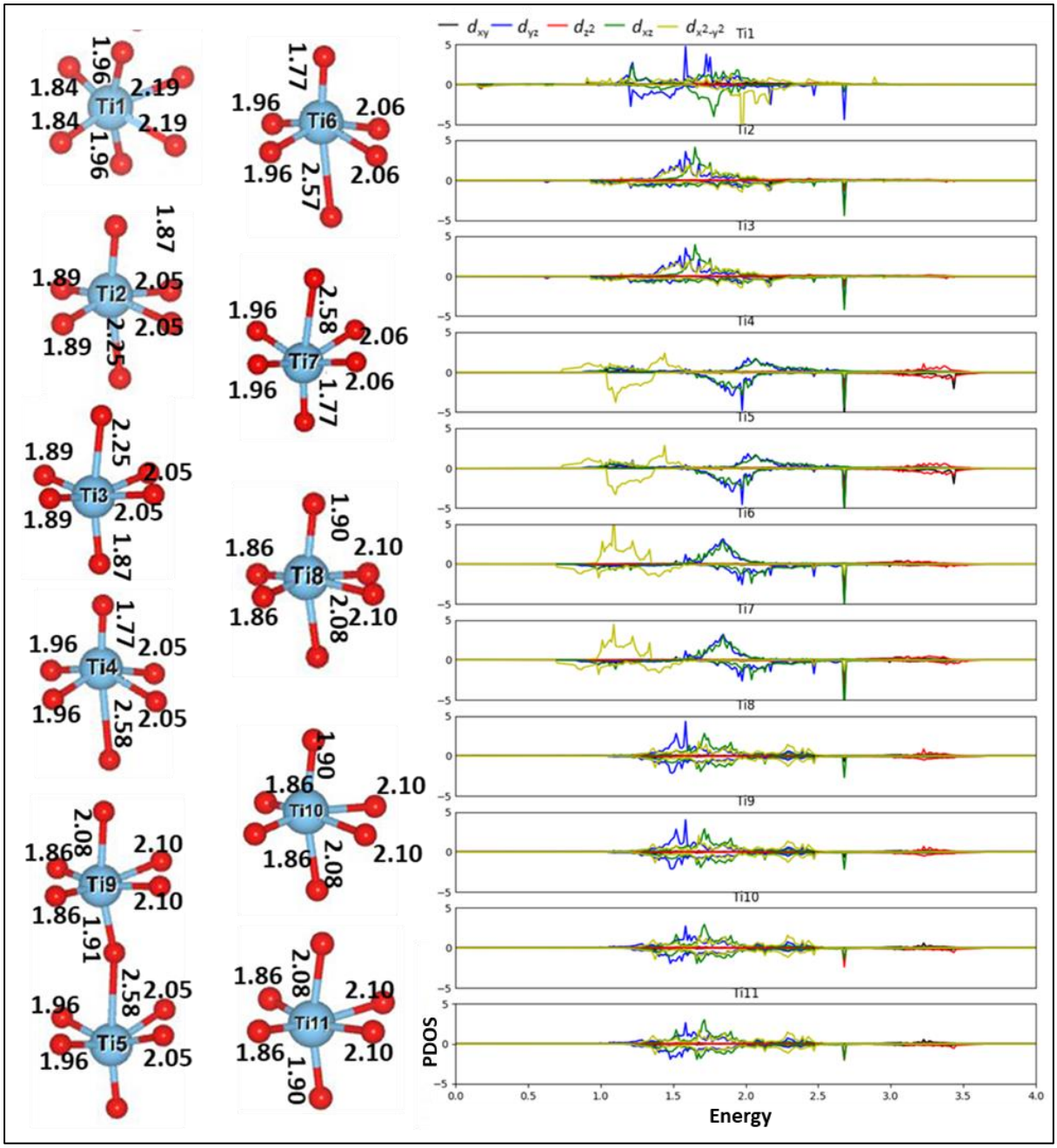


**Figure I.4** This is supplementary information to **Figure 3.3** in the main text (Configuration: *a*). All of the Ti-O bond lengths in Å and PDOS calculations for all of the Ti atoms of the $Bi_{24}Ti_{11}Fe_6Mn_3O_{72}$ configuration are shown.

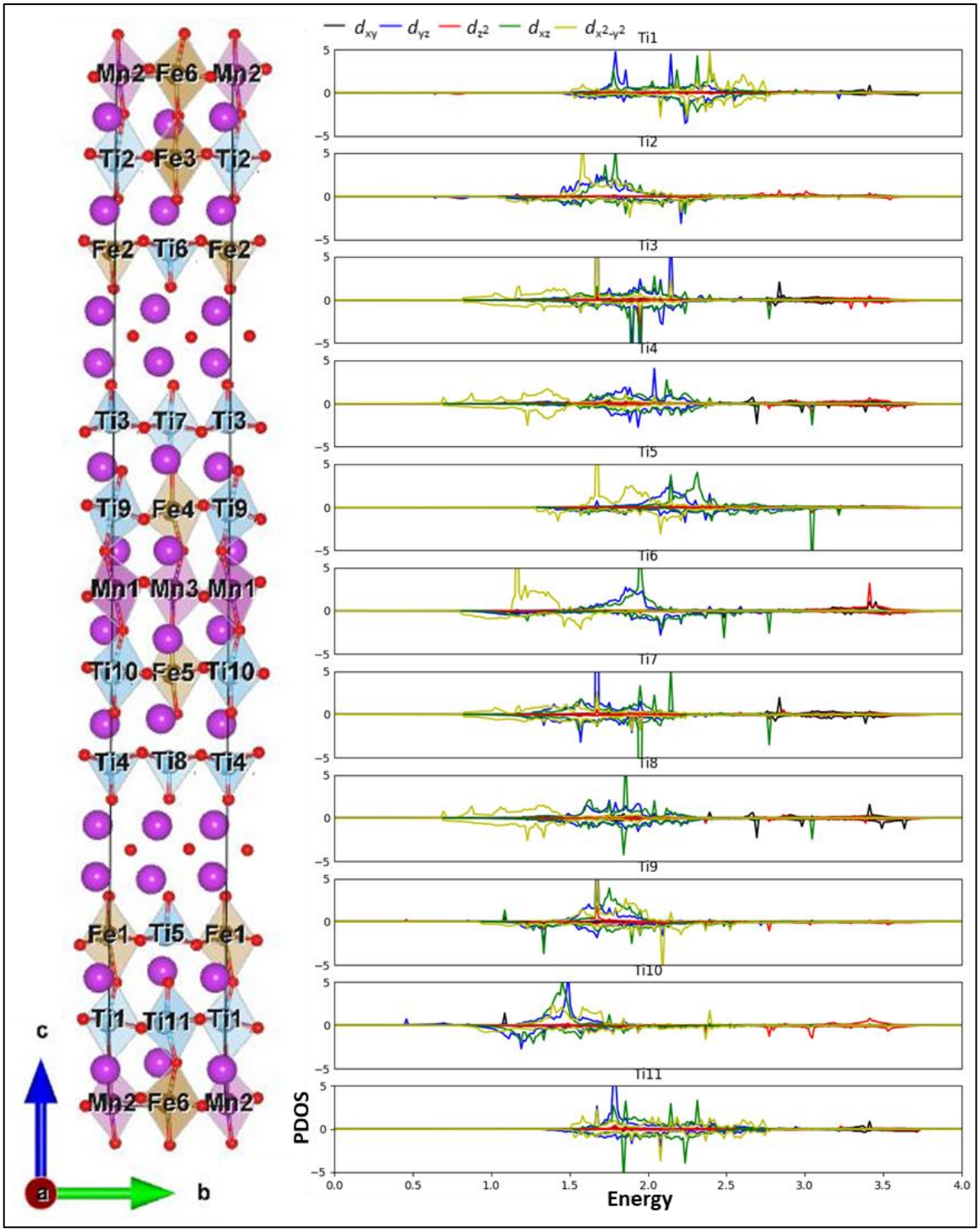


**Figure I.5** Another configuration (Configuration: *b*) of atoms and magnetic moments with differing locations for the *B*-site cations to that shown for the configuration (Configuration: *a*) in **Figure 3.3**/**Figure I.4**. The fully optimized structure (both lattice parameters and atomic positions) calculated for this configuration of $Bi_{24}Ti_{11}Fe_6Mn_3O_{72}$ is shown. The calculated lattice parameters for *a*, *b*, and *c* are 5.53 Å, 5.63 Å, and 49.93 Å, respectively. Similar to the previous configuration, it is observed that Ti/Fe/Mn atoms are displaced along the negative

*b*-axis, producing a dipole moment, thus net ferroelectric polarization lies along the *b*-axis. It is noticed that Ti/Fe/Mn atoms move along the *c*-direction upward and downward (significant displacement of the Outer Ti atoms) in an antipolar arrangement toward the $[Bi_2O_2]^{2+}$ layers, which would result in a net zero dipole along the *c*-direction if the horizontal mirror plane was allowed to persist. (Right) The atom resolved PDOS are shown, where positive (negative) PDOS represents up (down) spin channels. The Fermi energy ($E_F$) is set at 0 eV. The configuration is in a ferrimagnetic state with net magnetic moment of 33.892 $\mu_B$ per unit cell, where Fe1, Fe2, Fe3, Fe4, Fe5, Fe6, Mn1, Mn2, and Mn3 atoms contribute 4.341 $\mu_B$, 4.322 $\mu_B$, 4.365 $\mu_B$, 4.351 $\mu_B$, 4.348 $\mu_B$, 4.306 $\mu_B$, 3.596 $\mu_B$, -3.348 $\mu_B$, 3.809 $\mu_B$, respectively. Positive (negative) signs of the magnetic moment represent up (down) spin states. Other atoms contribute very little to the overall magnetic moment. Note that Configuration *b* is slightly (0.18 meV/atom) lower in energy relative to Configuration *a*. In fact, there are many possible atomic and magnetic configurations for Mn and Fe atoms to be placed in real samples. While there are two possible configurations presented within this study, it is proposed that the antipolar Ti displacement along *c*-direction within each perovskite block will be observed irrespective of the atomic and magnetic configurations of Mn and Fe atoms.

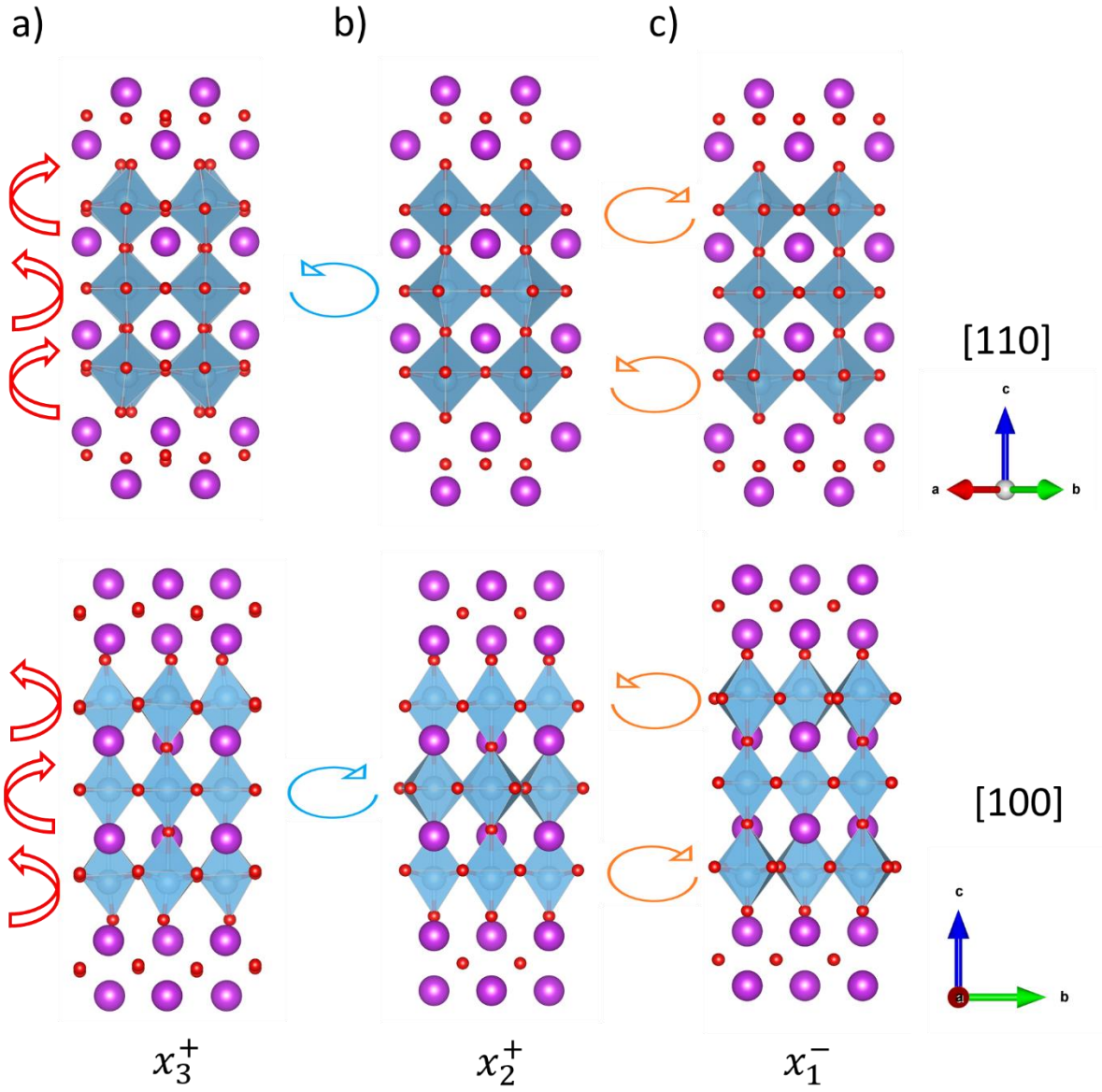


**Figure I.6** Illustration of individual tilt modes found in three-layered Aurivillius phases. Structures from Guo *et al.* [16] are used to visualise these octahedral tilt modes. a) *P4/ncm* structure demonstrating the out-of-plane anti-phase tilting in the *a-b* plane, associated with the *irrep* $X_3^+$ mode. b) *Cmce* space group, where the *irrep* $X_2^+$ mode provides a rotation around *c* at the centre perovskite layer. c) *P4/nbm* space group, where the *irrep* $X_1^-$ mode has an anti-phase rotation around c, in the outer perovskite layers next to $[Bi_2O_2]^{2+}$.

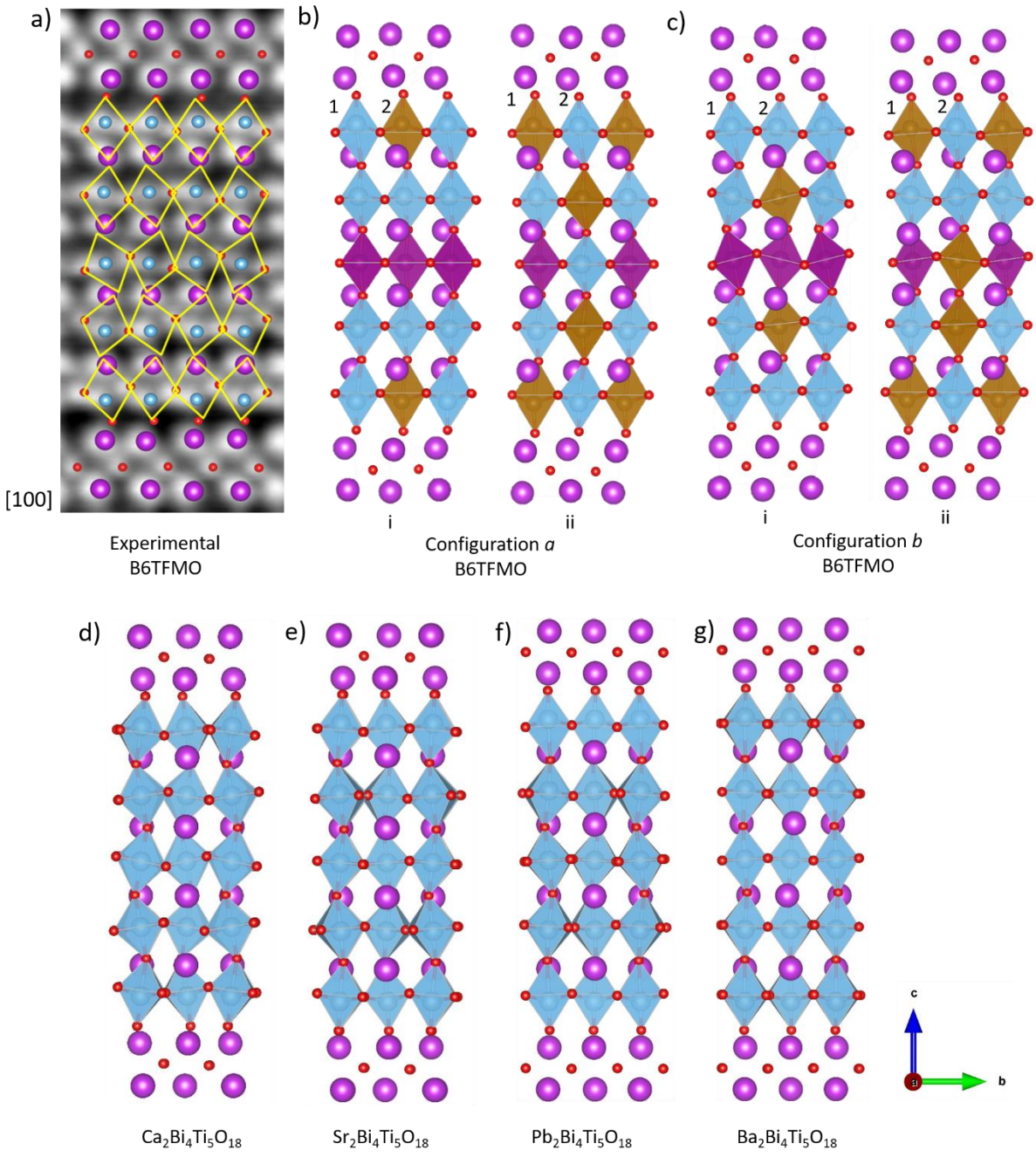


**Figure I.7** Images used to approximate tilt angles associated with out-of-plane anti-phase tilting of perovskite octahedra, correlated with the *irrep* $X_3^+$ mode. Given that positions of the perovskite *A*-site bismuth atoms coincide with positions of apex oxygen atoms, accurate O-*B*-O (*B*-site to oxygen) bond angles could not be determined from the 2*D* iDPC images. To approximate tilt angles for the perovskite octahedra, a 2*D* diamond shape (yellow) shown in (a) was created to match the positions determined for the apex and equatorial oxygen atoms of the $BO_6$ octahedra (when viewed down the [100] projection). To allow a comparison of tilt angles from experimental and theoretical data, the yellow diamond was overlaid onto iDPC

images (a), atomistic structures simulated by DFT ((b), (c)) and atomistic structures determined from neutron diffraction data from literature ((d) to (g)) [156]. One Aurivillius unit cell is comprised of two five-layered perovskite blocks. In order to enable the desired $Bi_{24}Ti_{11}Fe_6Mn_3O_{72}$ stoichiometry, two different half-unit cell arrangements of the Ti, Fe and Mn cations are required for the DFT structures simulated in (b) and (c). These two different arrangements are represented by the half-unit cell blocks labelled (i) and (ii). A manual fit to the underlying octahedra was applied using the position of the oxygen atoms as a guide. The yellow diamond is considered to be at a 0 ° tilt angle when equatorial oxygen atoms lie along the same horizontal plane. Octahedral tilting results in deviations from 0 ° and values determined for the outer, intermediate and centre perovskite layers are displayed in **Table I.2**.

| Layer | Tilt (°) | | | | | | | | | | | | | |
|---|---|---|---|---|---|---|---|---|---|---|---|---|---|---|
| | Experimental B6TFMO [100] | $Ca_2Bi_4Ti_3O_{18}$ [100] | $Sr_2Bi_4Ti_3O_{18}$ [100] | $Pb_2Bi_4Ti_3O_{18}$ [100] | $Ba_2Bi_4Ti_3O_{18}$ [100] | Layer | DFT Configuration: *a* | | | | DFT Configuration: *b* | | | |
| | | | | | | | B6TFMO [100] i | | B6TFMO [100] ii | | B6TFMO [100] i | | B6TFMO [100] ii | |
| | | | | | | | Column 1 | Column 2 | Column 1 | Column 2 | Column 1 | Column 2 | Column 1 | Column 2 |
| Outer | ±5 | ±7 | ±4 | ±2 | ±1 | Outer (top) | -4 | -2 | -3 | -4 | -6 | 2 | -5 | 1 |
| Intermediate | ±11 | ±10 | ±5 | ±4 | ±2 | Intermediate (top) | -1 | -1 | -2 | -2 | 13 | -11 | 8 | -8 |
| Centre | ±16 | ±11 | ±4 | ±6 | ±2 | Centre | 0 | 0 | 1 | 1 | -14 | 11 | -6 | 6 |
| | | | | | | Intermediate (bottom) | 1 | 1 | 2 | 2 | 6 | -4 | 4 | 1 |
| | | | | | | Outer (bottom) | 4 | 2 | 3 | 4 | 2 | 6 | 3 | 3 |

**Table I.2** Octahedral tilt angles along the <010> direction for experimental B6TFMO are approximated from iDPC images in **Figure I.7 (a)**, and compared to structures of five-layered Aurivillius phases $A_2Bi_4Ti_5O_{18}$ determined from literature neutron diffraction data [156] (**Figure I.7 (d** to **g)**) and DFT simulated configurations (**Figure I.7 (b)** and **(c)**). This table shows the degree of tilt for the $BO_6$ octahedra away from 0 ° for the *irrep* $X_3^+$ tilt mode (out-of-plane (parallel to *c*) anti-phase tilting of the octahedra with respect to each other in the *a*-*b* plane). Values for the experimental B6TFMO [100] are averaged as measured from **Figure I.7 (a)** which can be also seen in **Figure 3.4 (g)** of the main text. The average was calculated from the four columns as observed in **Figure I.7 (a)**, where the value for the outer and intermediate layers were each averaged over eight values (four from the top layer and four from the bottom layer). In this table, a minus value (–) indicates a tilt towards the left while a plus value (+) indicates a tilt towards the right. With the exception of **Figure I.7 (b)** and **(c)** (Configuration: *a* and Configuration: *b*), the tilting direction alternates between right and left (+/-) for the structures shown in **Figure I.7** as one moves through the perovskite layer in both the *c*-axis and *b*-axis direction. The DFT configurations which include Mn, Fe and Ti at the *B*-sites are more complex than the neutron diffraction crystallographic file structures from Ismunander *et al.* [156] (having only Ti at the *B*-sites) and have two distinct columns (marked 1 and 2 in **Figure I.7 (b)** and **(c)**), where the tilt angles differ due to the differing arrangement of the *B*-site cations within the Aurivillius half-unit cell. DFT Configuration: *a* and the neutron diffraction data have perovskite blocks where there are only three unique layers across the five perovskite sites. The two outer layers (top and bottom) have an equivalent arrangement of *B*-cations and the two intermediate layers (top and bottom) have an equivalent arrangement of *B*-cations. Therefore, the two outer and two intermediate octahedra in the five-layered perovskite block have the same degree of tilt, but with differing direction, as

indicated by the +/- sign. In DFT Configuration: *b* there are five unique layers in the perovskite block at the centre of the unit cell (**Figure I.7(c) ii, Figure I.8** and **Figure I.9**). The two outer layers (top and bottom) are not equivalent nor are the two intermediate layers (top and bottom), therefore five tilt values are obtained for this structure.

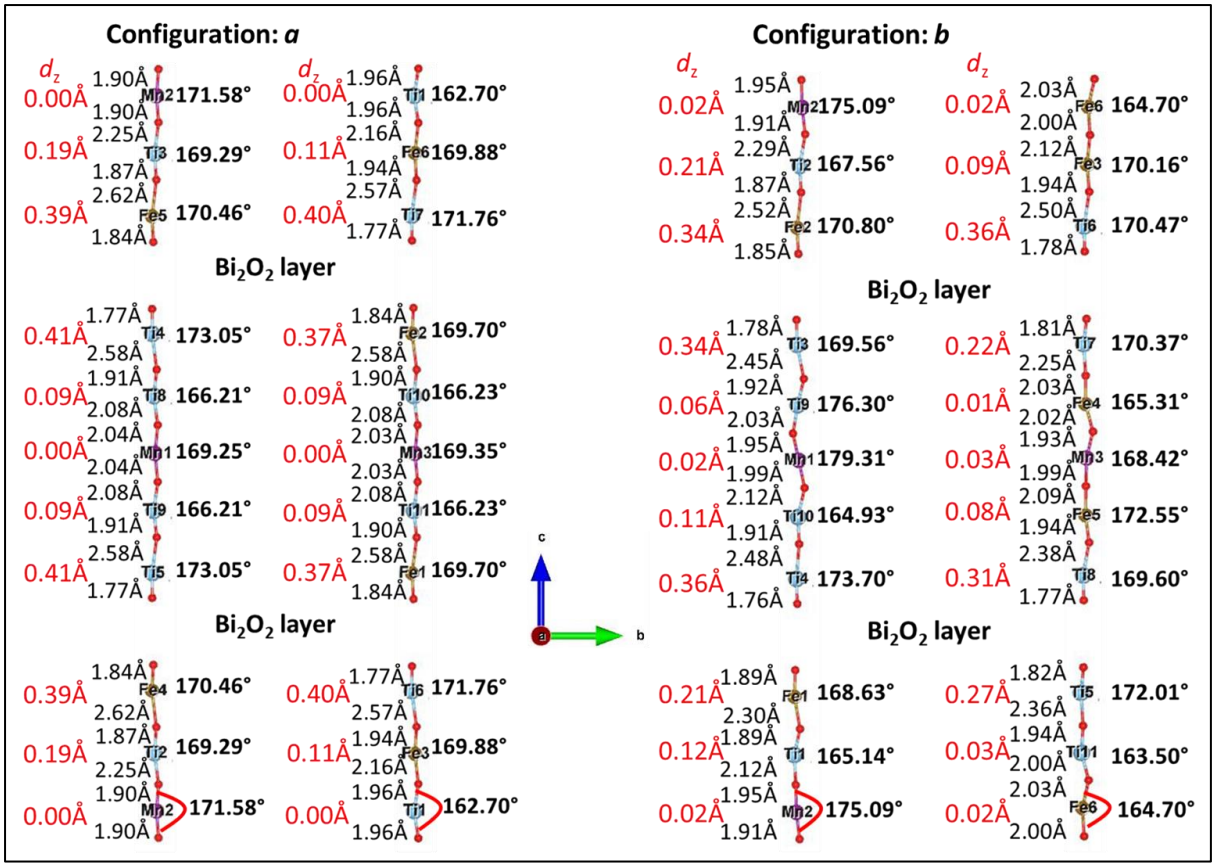


**Figure I.8** The positions of all oxygen and *B*-site atoms can be accurately measured from the DFT simulated structures. This figure displays bond angles at each *B*-site cation (Ti/Fe/Mn) between two *B*-*O* bonds along the *c*-direction for both calculated atomic configurations. In general, the bond angle deviates from 180 ° due to displacement of Ti/Fe/Mn atoms as well as octahedral tilting along the a-direction. The Ti/Fe/Mn-O bond lengths are shown. As discussed in the main text, short ($l_s$) and long ($l_l$) bonds along the *c*-direction are observed going from the centre layer to the outer layer. The displacement ($d_z$) of Ti/Fe/Mn is defined along the *c*-direction as ($l_l$ - $l_s$)/2, shown in red text in the figure. In agreement with experimental STEM data, $d_z$ of Ti/Fe/Mn increases going from the centre layer to the outer layer.

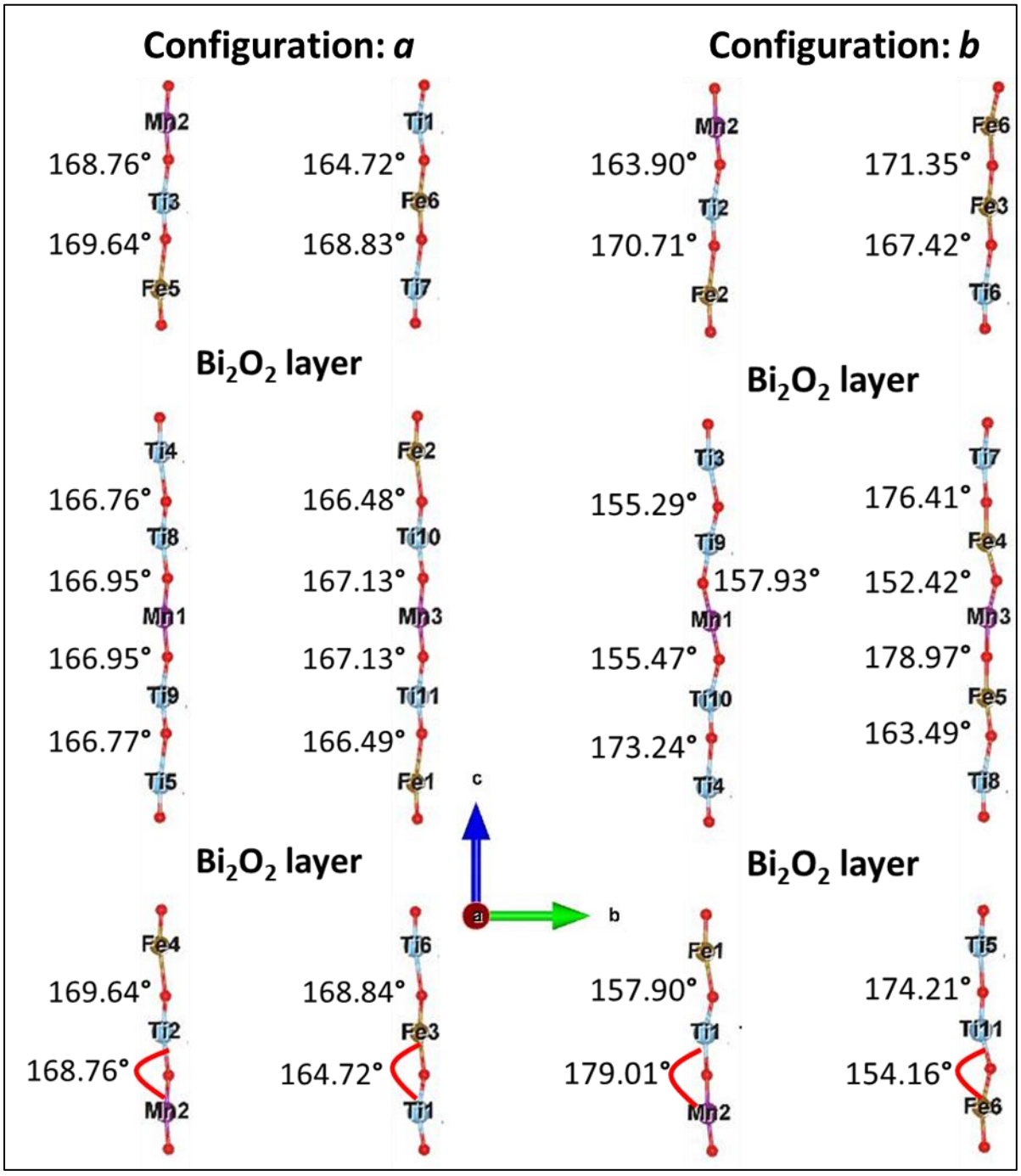


**Figure I.9** The positions of all oxygen and *B*-site atoms can be accurately measured from the DFT simulated structures. This figure displays bond angles at each oxygen (O)-site between two *B*-O bonds along the *c*-direction for both calculated atomic configuration. Without any distortion or tilting, the angle should be 180 °. Overall, the angles deviate from 180 ° significantly (by 12.87 ° to 27.58 °) along the *b*-direction at the centre layer. Note that

Configuration: *a* and Configuration: *b* have different atomic arrangements of Ti/Fe/Mn atoms, which results in different magnitudes for the tilt angles.

# II. Appendix - Supporting Information for Chapter 4

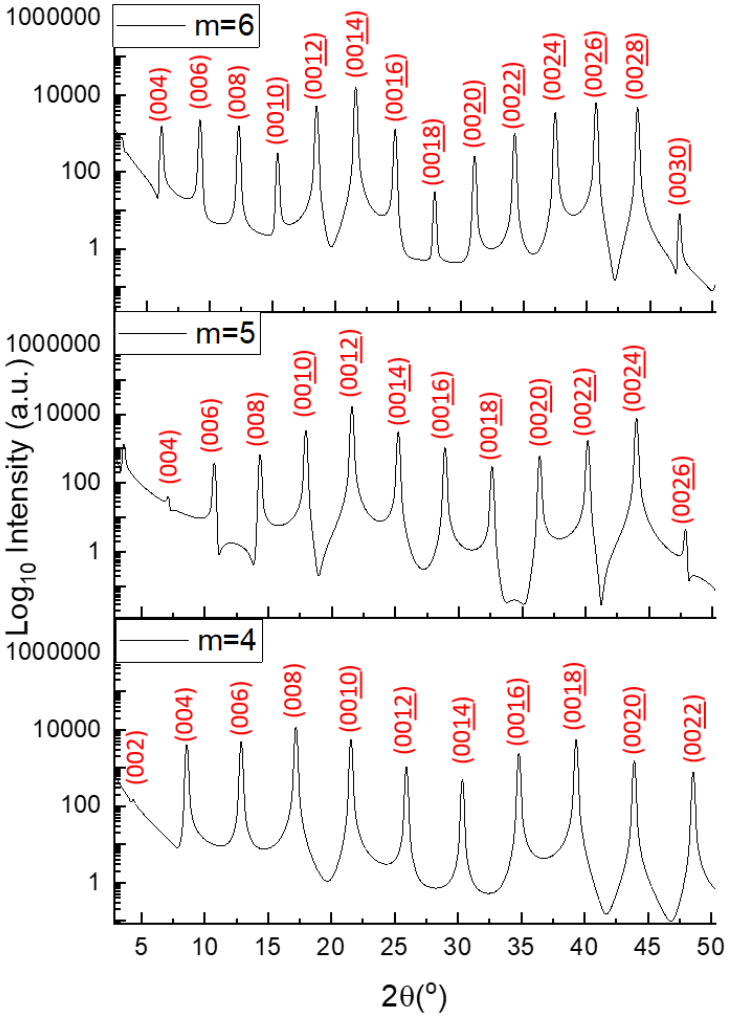


**Figure II.1** Simulated XRD patterns showing the (00*l*) reflections, produced for *m* = 4, 5 and 6 Aurivillius phases using DIFFaX software package [1].

| Reflection | 2θ peak position simulated from DIFFaX | 2θ peak position projected from VESTA |
|---|---|---|
| *m* = 5 | ° | ° |
| (002) | 3.5785 | 3.5785 |
| (004) | 7.1604 | 7.1604 |
| (006) | 10.749 | 10.749 |
| (008) | 14.349 | 14.349 |
| (00$\underline{10}$) | 17.963 | 17.963 |
| (00$\underline{12}$) | 21.595 | 21.595 |
| (00$\underline{14}$) | 25.249 | 25.249 |
| (00$\underline{16}$) | 28.929 | 28.929 |
| (00$\underline{18}$) | 32.640 | 32.640 |
| (00$\underline{20}$) | 36.387 | 36.387 |
| (00$\underline{22}$) | 40.175 | 40.175 |
| (00$\underline{24}$) | 44.008 | 44.008 |
| (00$\underline{26}$) | 47.895 | 47.895 |

**Table II.1** Peak positions of reflection values for the *m* = 5 Aurivillius phase structure as displayed in **Appendix II Figure II.1** A comparison is shown between peak position values simulated using DIFFaX vs reflections obtained from a VESTA projection of the experimental CIF data file from XRD data from Garcia-Guaderrama *et al.* [258]

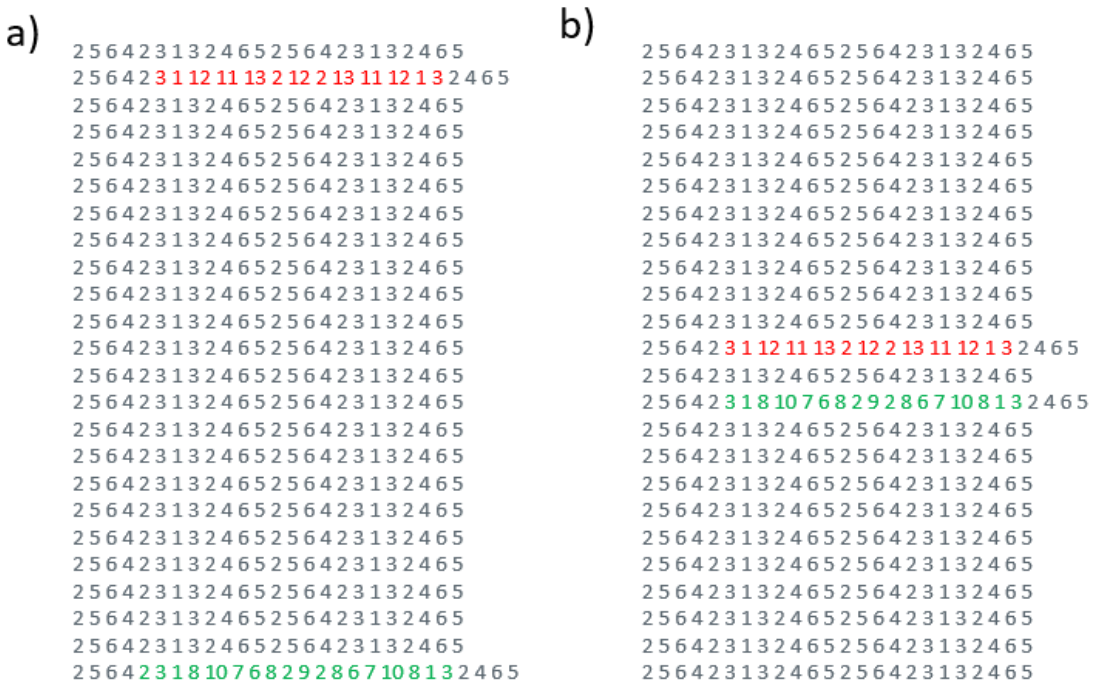


**Figure II.2** Schematic showing positions of $m = 4$ and $m = 6$ intergrowth within an $m = 5$ Aurivillius structure as simulated in **Figure 4.4 (a)** in the main text. Here a) represents structure corresponding to the plot "far apart" where the intergrowths are 19.5 unit cells apart. b) represents the structure which corresponds to the plot "close" with the intergrowths 1.5 unit cells apart.

The outputs in **Figure 4.2 (b)** and **Figure II.2** represent how the stacking of the layers are ordered when simulating XRD patterns using DIFFaX. A unique, fixed sequence of layers can be defined and in this work a variety of stacking orders were calculated. Each row in **Figure 4.2 (b)** and **Figure II.2** represent a unit cell of the structure.

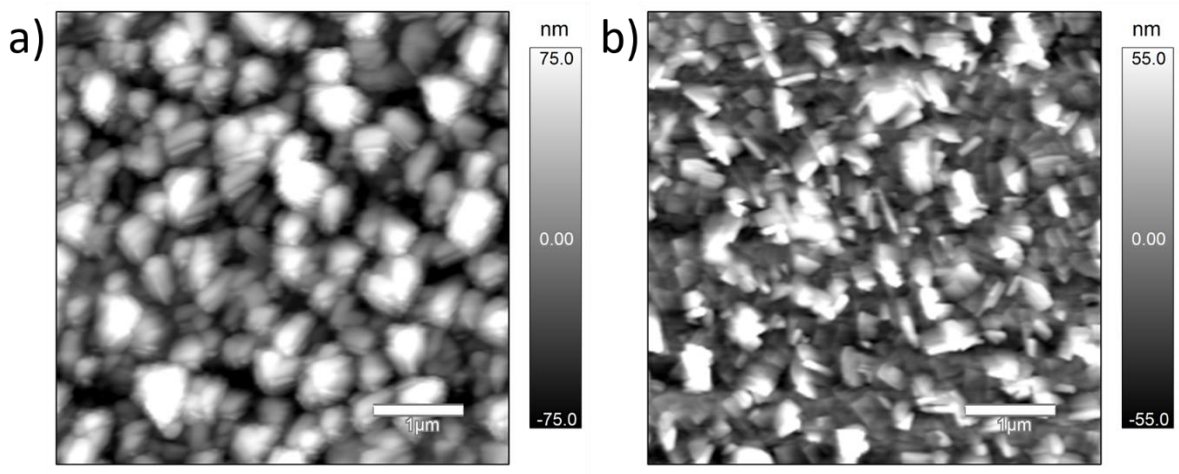


**Figure II.3** 5 µm x 5 µm AFM images of the bismuth based films after the initial DLI-CVD deposition at 630 °C but before the post anneal at 850 °C on a) 0.2 °, b) 10 ° mis-cut sapphire substrates with RMS values of 42.92 nm and 32.32 nm respectively.

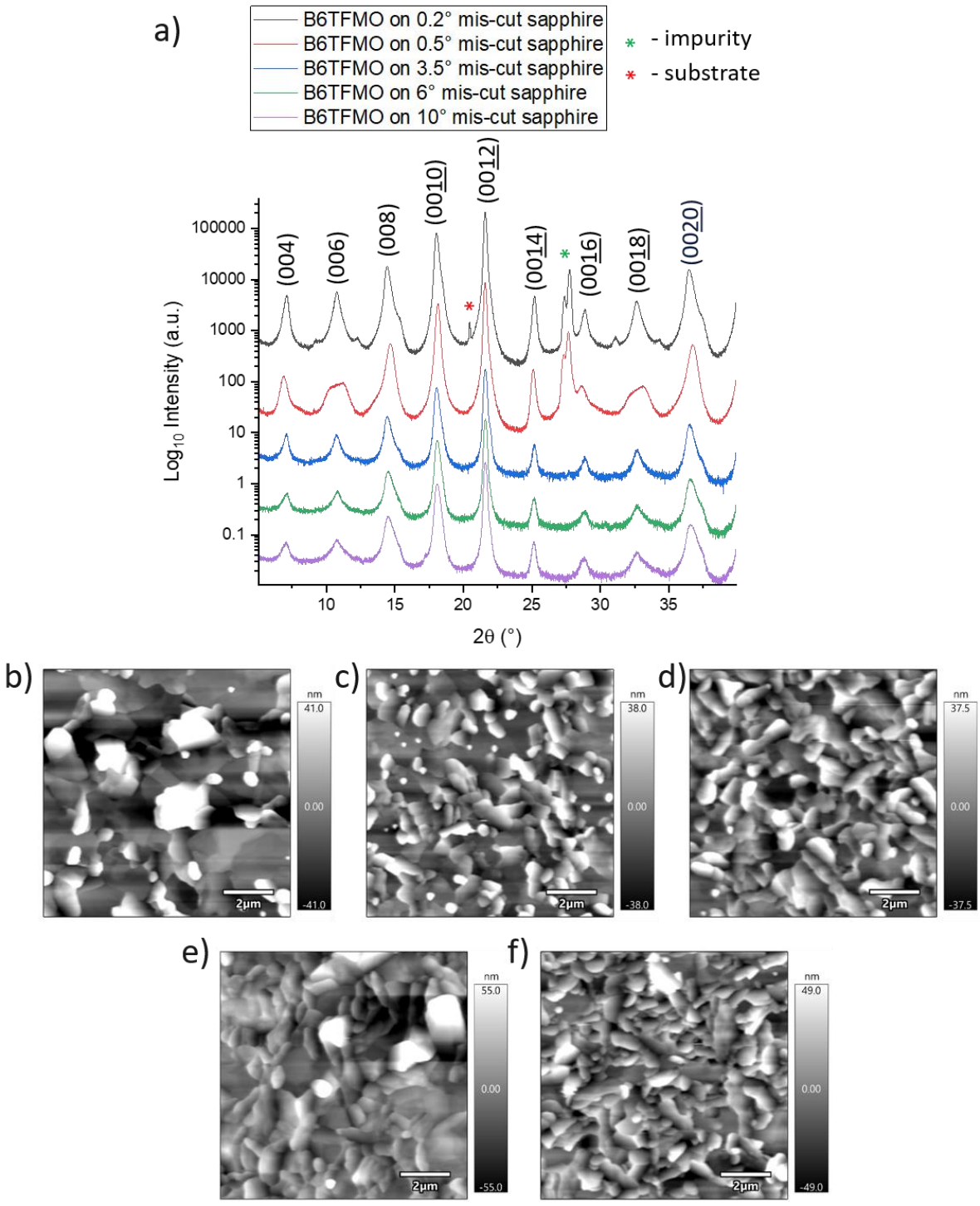


**Figure II.4** a) X-ray diffraction patterns of B6TFMO films deposited on sapphire substrates with vicinal surfaces having mis-cut angles of 0.2 ° (plot shown in black), 0.5 ° (plot shown in red), 3.5 ° (plot shown in blue), 6 ° (plot shown in green) and 10 ° (plot shown in purple). 10 µm x 10 µm AFM images of the B6TFMO films on b) 0.2 °, c) 0.5 °, d) 3.5 °, e) 6 ° and f) 10 ° mis-cut sapphire substrates.

B6TFMO thin films were also grown on 3.5 ° and 6 ° mis-cut sapphire substrates under the same conditions as described in **Chapter 4 Section 4.2**. After XRD analysis the patterns from the 3.5 °, 6 ° and 10 ° sample were found to be very similar and just one (the B6TFMO film on 10 ° mis-cut sapphire) was selected alongside the B6TFMO films on 0.2 ° and 0.5 ° sapphire substrates for STEM analysis.

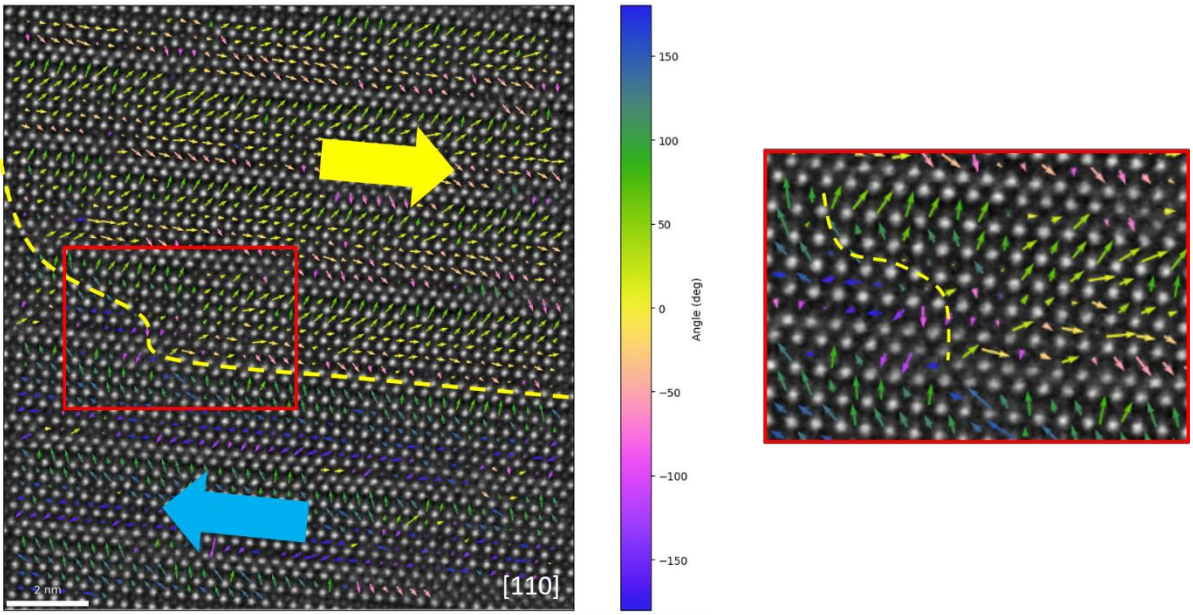


**Figure II.5** HAADF STEM images of B6TFMO thin film on 0.5 ° mis-cut sapphire where polarisation displacement vectors of the *B*-site cation are mapped using TEMUL toolkit [2]. In this figure, the colour of the arrow indicates the direction polarisation is pointing in, with yellow (orientated 0 °) pointing towards the right and blue (orientated 180 °) pointing towards the left. In the inset to the right, the size of the arrow correlates to the magnitude of the displacement of the *B*-site cation. The dashed yellow line gives an approximate location of charged domain walls within the image and the large arrows indicate an approximate overall direction for the ferroelectric domains present. Inset: enlarged image of a nominally charged 180 ° Tail-to-Tail domain wall.

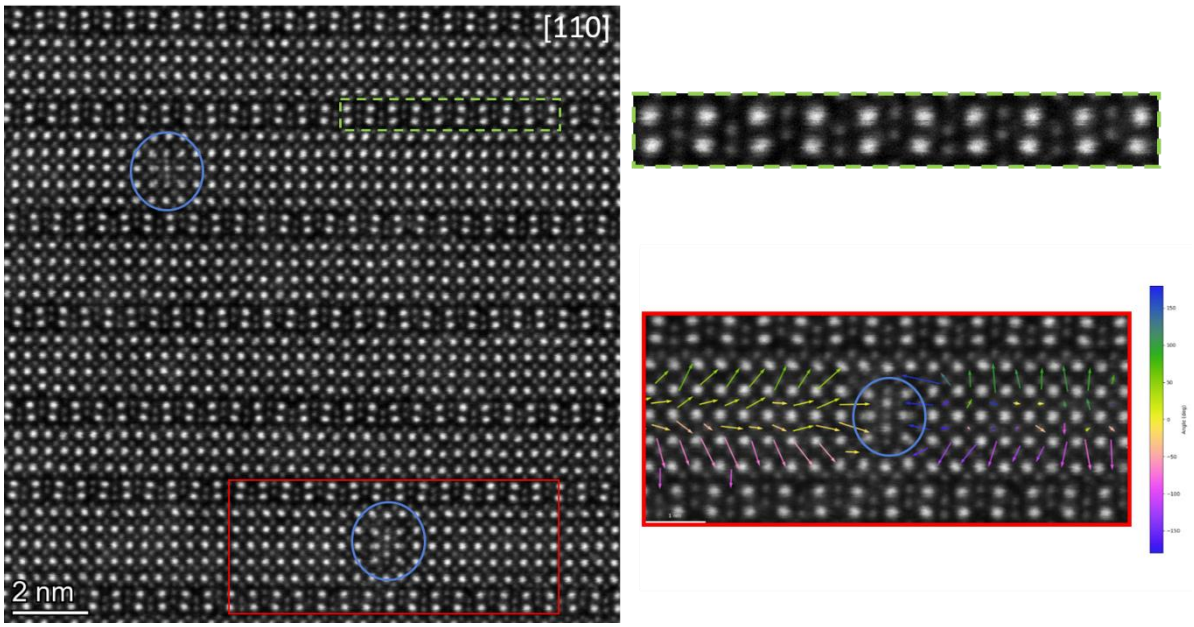


**Figure II.6** HAADF STEM imaging of an area with 'anatase'- type planar defects replacing the $[Bi_2O_2]^{2+}$ interlayer within a B6TFMO thin film on 0.2 ° sapphire. The 'anatase'- type defect can be seen in more closely in the green dashed inset. In the red inset the polarisation displacement vectors of the *B*-site cation are mapped using TEMUL toolkit [254]. In the red inset, the colour of the arrow indicates the direction it is pointing in, with yellow (0 °) pointing towards right and blue (180 °) pointing towards the left, while the size of the arrow correlates to the magnitude of the displacement of the *B*-site cation. Within this image 'anatase'-like interlayers made up of stabilised by $BO_6$ octahedral forming "s"-shaped tunnels are interleaved between perovskite unit cells. Further nanorod precipitates, circled in blue are also present within the perovskite blocks where the *B*-site cations next to the precipitates are highly strained with the polarisation vectors pointing towards the defect.

Using polarisation vector mapping of the *B*-site cations around the nanorod precipitate shown in **Appendix II Figure II.6**, the polarisation vectors of the *B*-site cations do appear to be displaced away from the nanorod participate. With the polarisation vectors at either side of the precipitate pointing towards its core. These nonstoichiometric nanoregion defects resemble the type described by Li *et al*. [383] which promote hedgehog and anti-hedgehog states of the types seen in polar and magnetic skyrmions. This indicates that defect engineering can potentially tailor the creation of future multiferroic skyrmions in B6TFMO.

# III. Appendix - Supporting Information for Chapter 5

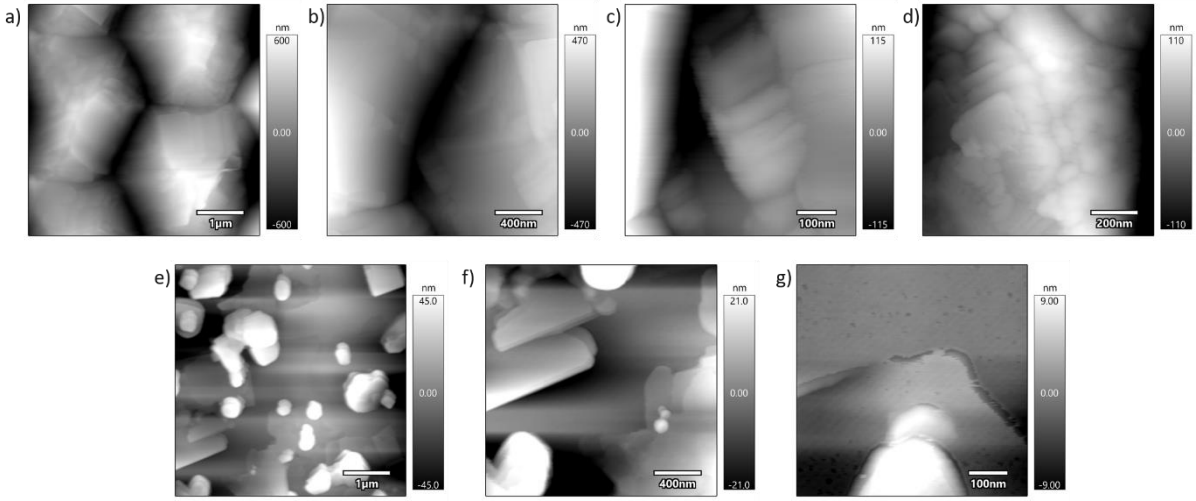


**Figure III.1** Representative tapping mode AFM images of 800 injection B6TFMO films after deposition at 630 °C via DLI-CVD and post anneal at 850 °C. (a) to (d) are images of the film on a patterned sapphire substrate with domes and (e) to (g) are images of a B6TFMO film deposited on an un-patterned *c-m* sapphire substrate.

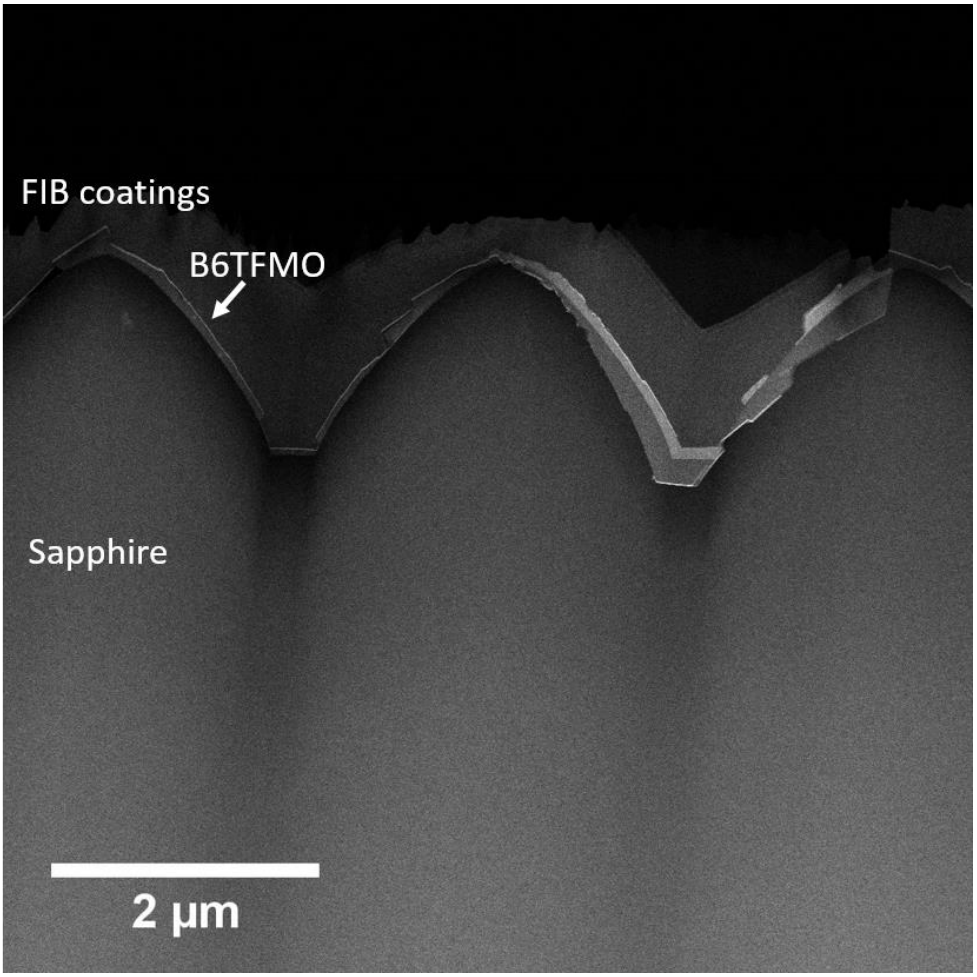


**Figure III.2** STEM image of a FIB lamella of a B6TFMO film deposited with 800 injections on patterned sapphire domes.

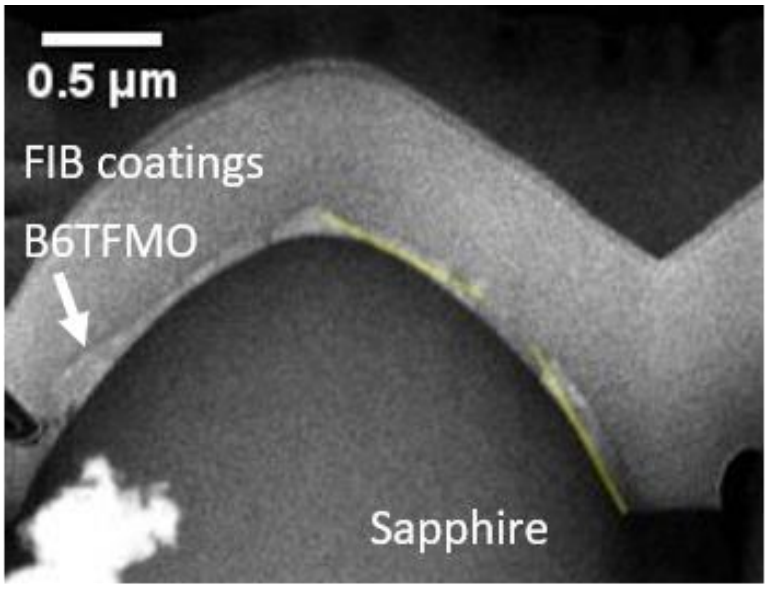


**Figure III.3** STEM image of a 500 injection B6TFMO film on a patterned sapphire dome, showing an example of two angles at which B6TFMO can crystallise at. Near the bottom of the dome, the growth angle to the substrate (demonstrated by the yellow line) is ~60 °. Here the slope of the line is 1.9. Near the top of the dome, the angle to the substrate is ~25 °, where the yellow line has a slope of 0.4.

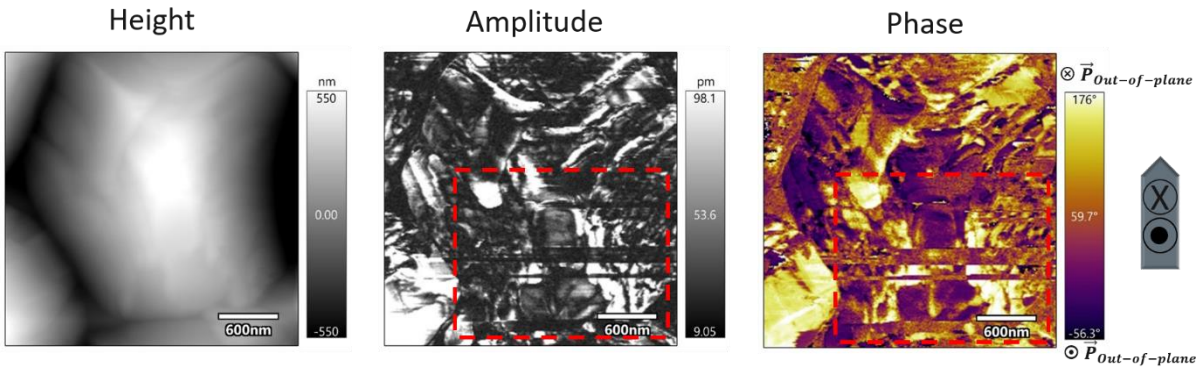


**Figure III.4** Vertical mode PFM (VPFM) images of 800 injection B6TFMO thin films on patterned sapphire substrates probed at 2 $V_{AC}$. Within the dashed red inset is an area where the tip was unable to track the piezo response properly, as indicated by horizontal scanning artefacts.

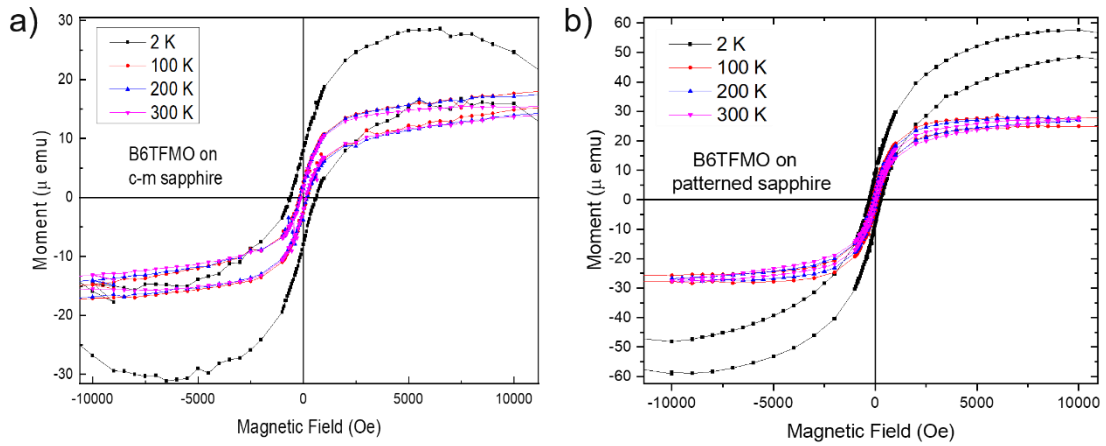


**Figure III.5** Magnetisation versus magnetic field (MH) measurements of B6TFMO on a) un-patterned *c-m* and b) patterned sapphire substrates before the thin film volume has been considered for the magnetisation values.

| B6TFMO on un-patterned *c-m* sapphire | | | B6TFMO on patterned sapphire | | |
|---|---|---|---|---|---|
| Temperature K | $M_R$ emu/cm$^3$ | $H_C$ Oe | Temperature K | $M_R$ emu/cm$^3$ | $H_C$ Oe |
| 2 | 1.63 | 401 | 2 | 1.87 | 238 |
| 100 | 0.54 | 173 | 100 | 0.74 | 105 |
| 200 | 0.55 | 163 | 200 | 0.60 | 89 |
| 300 | 0.40 | 111 | 300 | 0.43 | 62 |

**Table III.1** Magnetic parameters for 800 injection B6TFMO thin films on un-patterned *c-m* sapphire and patterned sapphire substrates.

# IV. Appendix - Supporting Information for Chapter 6

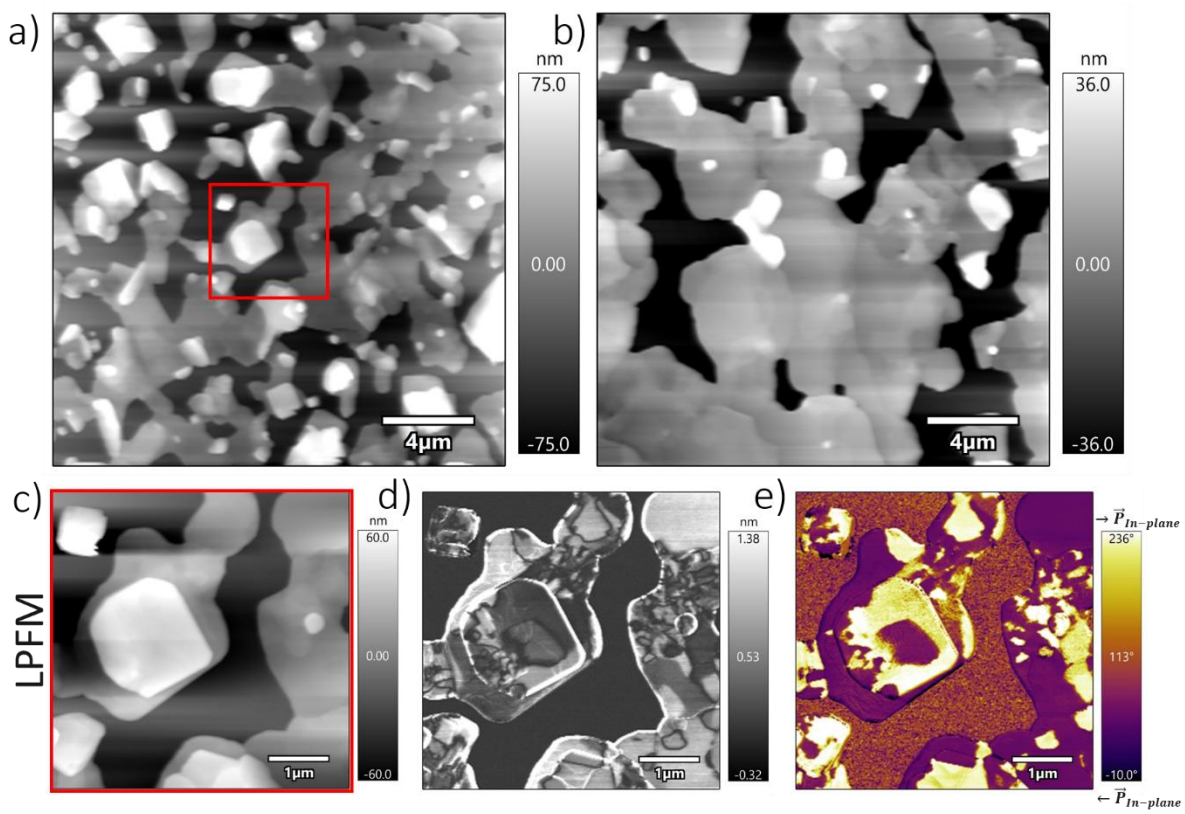


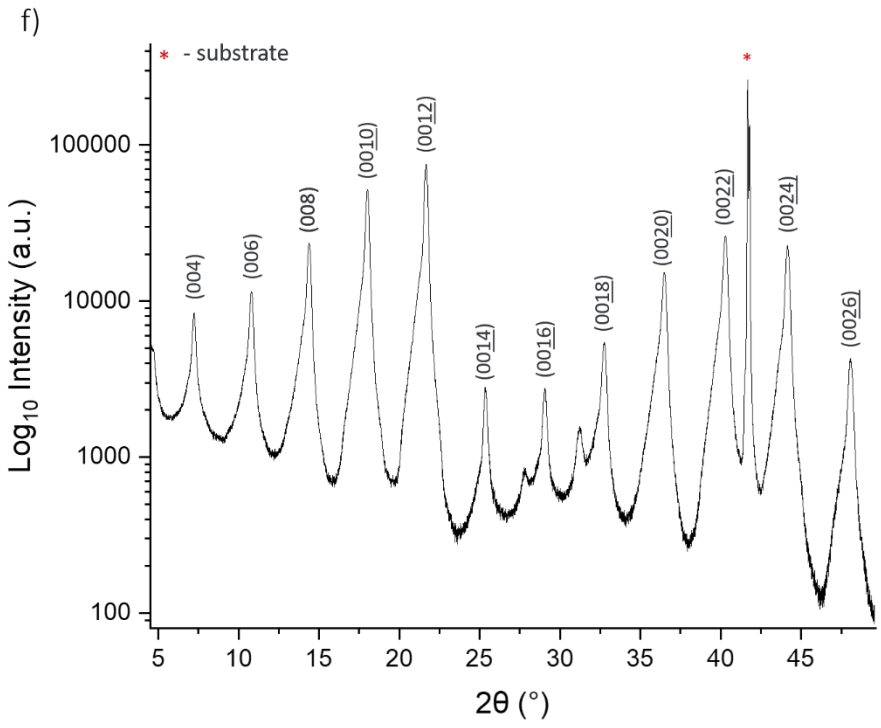

**Figure IV.1** a) and b) 20 x 20 $\mu m^2$ AFM images of two different regions of a non-continuous B6TFMO film on sapphire deposited at 630 °C and post annealed at 850 °C for 1 hr. c) to e) LPFM measurement using a probe voltage ($V_{AC}$) of 1.0 V over a 5 x 5 $\mu m^2$ region from the same sample. c) topography, d) amplitude and e) phase images. The in-plane piezo response can be visualised in d) and c) and the non-responsive substrate can also be identified by the dark amplitude response and noisy phase signal in between the grains. f) XRD pattern of the non-continuous B6TFMO film on sapphire, indicating the overall *m* = 5 phase of the material.

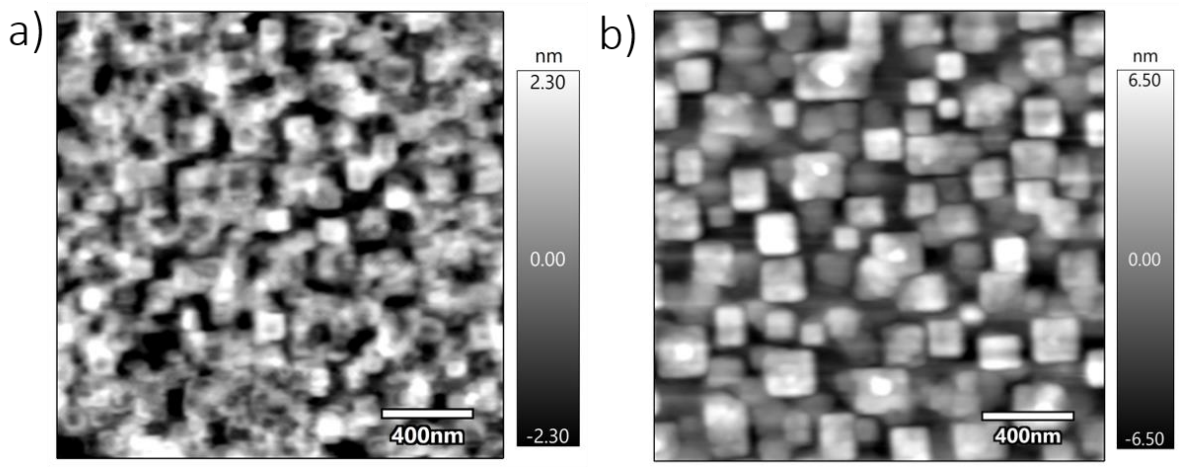


**Figure IV.2** Gwydion software was utilised to approximate the lateral dimensions for B6TFMO crystallite from AFM images such as the ones shown above, where a) represents the B6TFMO film grown via a two-step deposition method on LSAT while b) represents a B6TFMO grown via a single-step deposition method, where for a) and b) the bismuth excess used was 19.3 % and 1.8 % respectively.

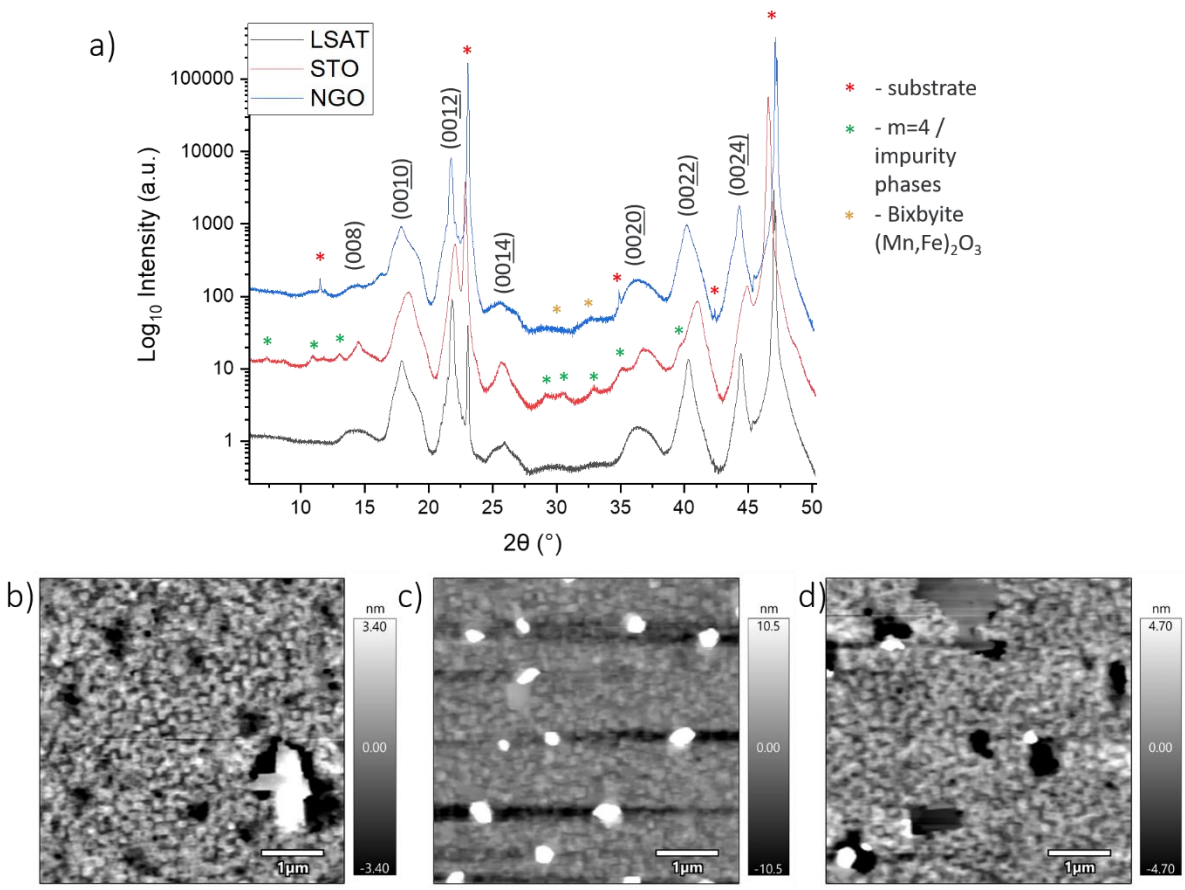


**Figure IV.3** B6TFMO films on epitaxial substrates synthesised via the two-step method. The XRD pattern of the thin films are shown in a), where the patterns correspond to B6TFMO on LSAT (black line), STO (red line) and NGO (blue line). AFM images of the film surfaces on b) LSAT, c) STO and d) NGO.

AFM measurements of the B6TFMO thin films on LSAT, STO and NGO show that similarly to the single-step technique, LSAT appears be the optimum candidate of substrate for epitaxial growth of B6TFMO, given that film coverage is the most continuous of the three substrates investigated. The RMS roughness of the B6TFMO films from **Appendix IV Figure IV.3** were measured to be 1.71 nm, 5.92 nm and 2.31 nm for growth on LSAT, STO and NGO respectively.

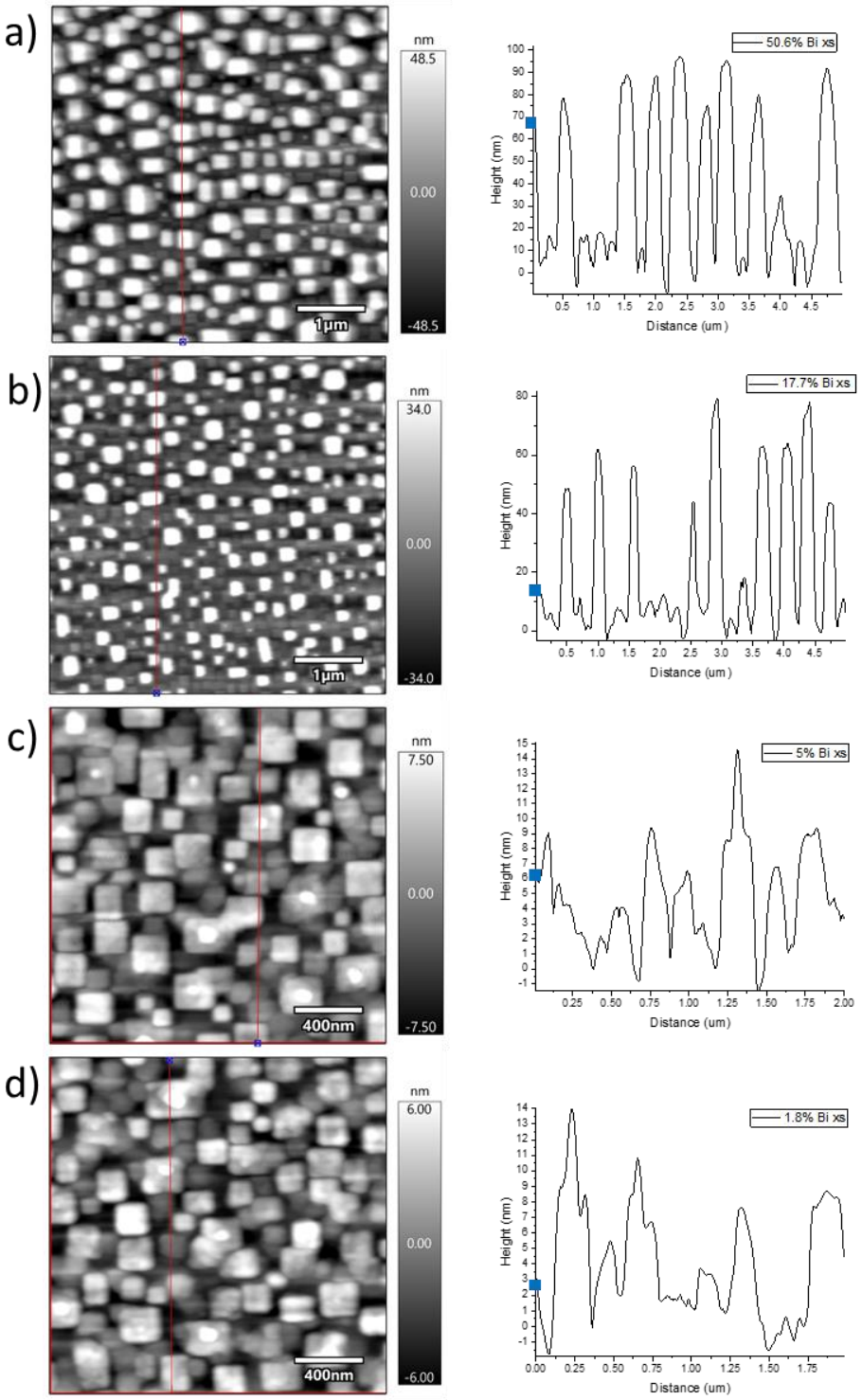


**Figure IV.4** Topography images along with line profiles of the surface features on B6TFMO thin films on LSAT with different percent bismuth excess used during deposition. a) and b) 5 x 5 µm$^2$ scans of B6TFMO films deposited with 50.6 % and 17.7 % bismuth excess, respectively, where large $Bi_2O_3$ impurities dominate the surface topography. c) and d) 2 x 2 µm$^2$ scans of B6TFMO films deposited with 5 % and 1.8 % bismuth excess where the Aurivillius phase dominates the surface topography with much smaller volumes of impurities visible.

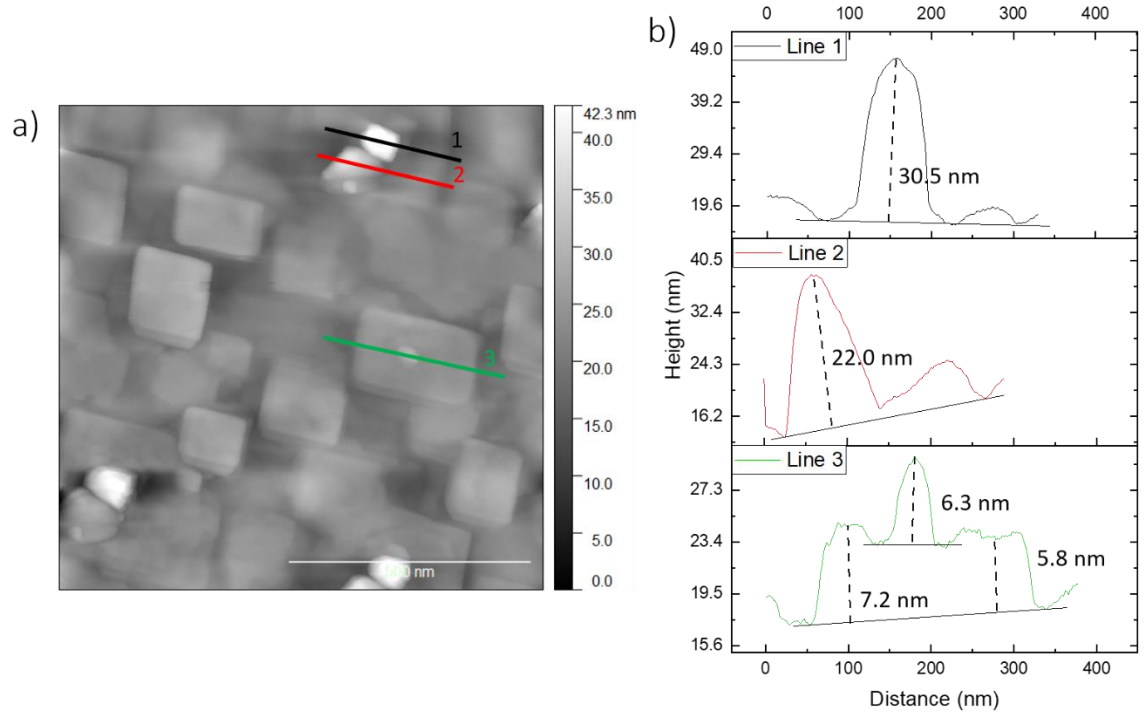


**Figure IV.5** AFM image of B6TFMO deposited with a 5 % bismuth excess. b) Line profiles of the heights of three features on the thin films surface from image a) Where line 1 represents Impurity 2a and line 2 represents Impurity 2b as in the main text. Line 3 could represent the initial stages of Impurity 2a or potentially the start of another Aurivillius *2D* Island.

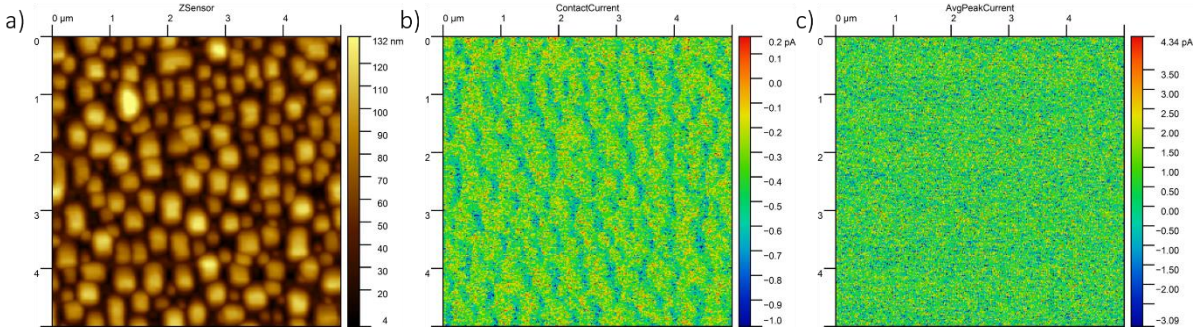


**Figure IV.6** Conductive AFM images of the 50.6 % bismuth excess film on LSAT where a) is the height topography, b) is the contact current and c) is the average peak current.

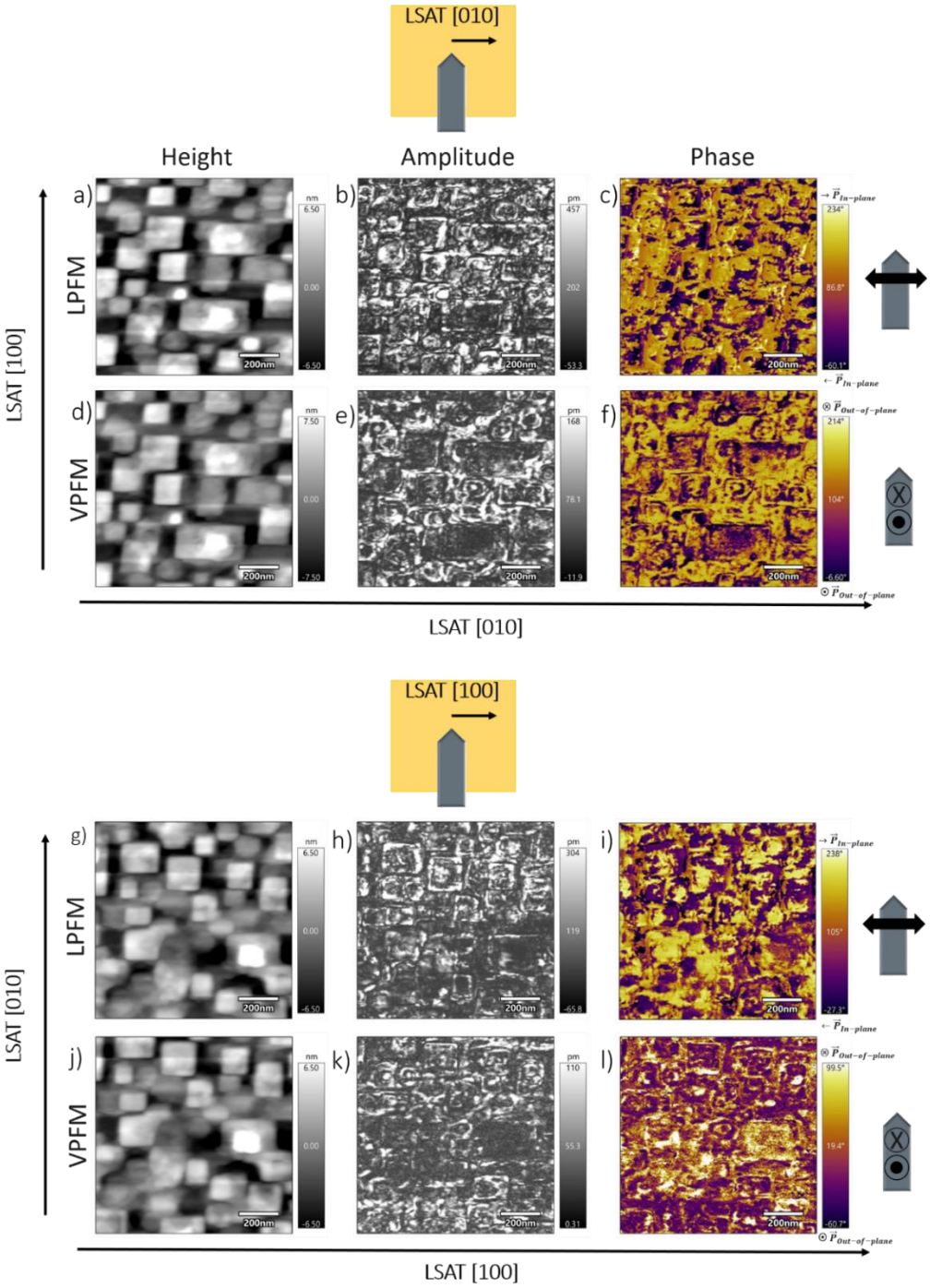


**Figure IV.7** Lateral LPFM and vertical VPFM , DART-PFM height, amplitude and phase images of B6TFMO films on LSAT (100) with a 5 % bismuth excess probed at 1 $V_{AC}$ and 2 $V_{AC}$, for LPFM and VPFM measurements respectively. Images (a) to (f) were performed with the cantilever scanning direction parallel to the [010] LSAT axis. The samples were rotated 90 ° for images (g) to (l) where the cantilever scanning direction was parallel to the [100] LSAT axis. These images demonstrate the isotropic random distribution of in-plane and out-of-plane domains in films ~45 nm thick for B6TFMO on LSAT (100).

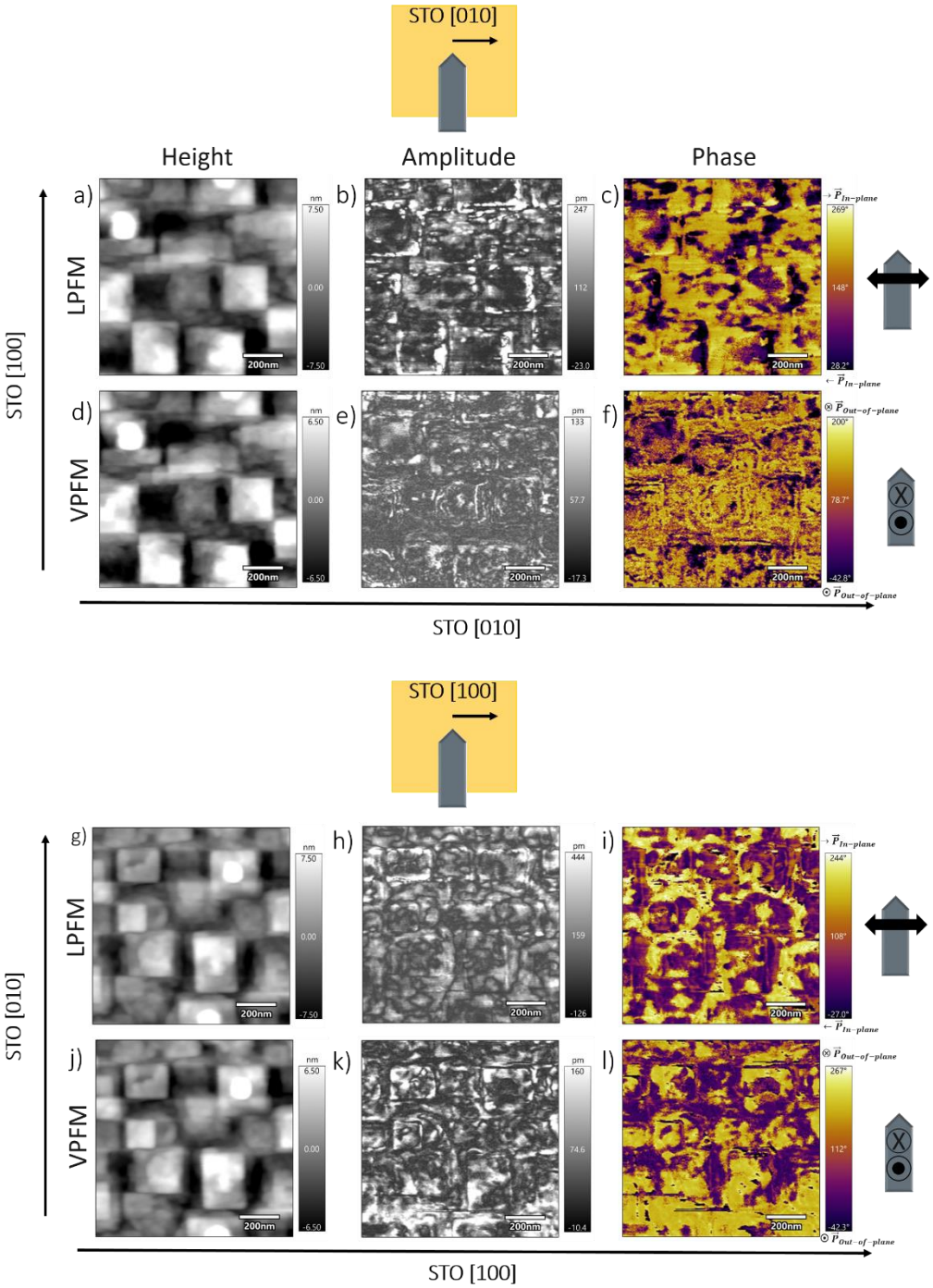


**Figure IV.8** Lateral LPFM and vertical VPFM , DART-PFM height, amplitude and phase images of B6TFMO films on STOT (100) with a 5 % bismuth excess probed at 1 $V_{AC}$ and 2 $V_{AC}$, for LPFM and VPFM measurements respectively. Images (a) to (f) were performed with the cantilever scanning direction parallel to the [010] STO axis. The samples were rotated 90 ° for images (g) to (l) where the cantilever scanning direction was parallel to the [100] STO axis. These images demonstrate the isotropic random distribution of in-plane and out-of-plane domains in films ~45 nm thick for B6TFMO on STO (100).

# References


[1] K. Moharm, 'State of the art in big data applications in microgrid: A review', *Adv. Eng. Inform.*, vol. 42, p. 100945, Oct. 2019, doi: 10.1016/j.aei.2019.100945.

[2] D. Reinsel, J. Gantz, and J. Rydning, 'The Digitization of the World From Edge to Core'. Seagate, 2018. Accessed: Mar. 24, 2023. [Online]. Available: https://www.seagate.com/files/www-content/our-story/trends/files/idc-seagate-dataage-whitepaper.pdf

[3] H. H. Radamson *et al.*, 'Miniaturization of CMOS', *Micromachines*, vol. 10, no. 5, 2019, doi: 10.3390/mi10050293.

[4] H. Saini, A. Upadhyaya, and M. K. Khandelwal, 'Benefits of Cloud Computing for Business Enterprises: A Review', *Proc. Int. Conf. Adv. Comput. Manag. ICACM*, Oct. 2019, doi: http://dx.doi.org/10.2139/ssrn.3463631.

[5] A. Syed, K. Purushotham, and G. Shidaganti, 'Cloud Storage Security Risks, Practices and Measures: A Review', in *2020 IEEE International Conference for Innovation in Technology (INOCON)*, Nov. 2020, pp. 1–4. doi: 10.1109/INOCON50539.2020.9298281.

[6] 'Data Centres Metered Electricity Consumption 2022'. Accessed: Sep. 13, 2023. [Online]. Available: https://www.cso.ie/en/releasesandpublications/ep/p-dcmec/datacentresmeteredelectricityconsumption2022/keyfindings/

[7] 'All-Island Generation Capacity Statement 2019-2028'. Accessed: Sep. 13, 2023. [Online]. Available: https://www.eirgridgroup.com/site-files/library/EirGrid/EirGrid-Group-All-Island-Generation-Capacity-Statement-2019-2028.pdf

[8] 'ReRAM Overview', Fujitsu Semiconductor Memory Solution Limited, White Paper, Mar. 2023. Accessed: Jun. 09, 2023. [Online]. Available: https://www.fujitsu.com/jp/group/fsm/en/products/reram/ReRAM_whitepaper_2023e.pdf

[9] D. C. Gilmer, T. Rueckes, and L. Cleveland, 'NRAM: a disruptive carbon-nanotube resistance-change memory', *Nanotechnology*, vol. 29, no. 13, p. 134003, Feb. 2018, doi: 10.1088/1361-6528/aaaacb.

[10] B. Gervasi, 'Will Carbon Nanotube Memory Replace DRAM?', *IEEE Micro*, vol. 39, no. 2, pp. 45–51, 2019, doi: 10.1109/MM.2019.2897560.

[11] E. Bichoutskaia, A. M. Popov, and Y. E. Lozovik, 'Nanotube-based data storage devices', *Mater. Today*, vol. 11, no. 6, pp. 38–43, Jun. 2008, doi: 10.1016/S1369-7021(08)70120-2.

[12] 'FeRAM Overview', Fujitsu Semiconductor Memory Solution Limited, White Paper, Feb. 2023. Accessed: Jun. 09, 2023. [Online]. Available: https://www.fujitsu.com/jp/group/fsm/en/documents/products/feram/features/FeRAM_whitepaper_2023e.pdf

[13] M. Fiebig, Th. Lottermoser, M. K. Kneip, and M. Bayer, 'Correlations between magnetic and electrical orderings in multiferroic manganites (invited)', *J. Appl. Phys.*, vol. 99, no. 8, p. 08E302, Apr. 2006, doi: 10.1063/1.2172198.

[14] M. Gajek *et al.*, 'Tunnel junctions with multiferroic barriers', *Nat. Mater.*, vol. 6, no. 4, pp. 296–302, Apr. 2007, doi: 10.1038/nmat1860.

[15] E. Y. Tsymbal, A. Gruverman, V. Garcia, M. Bibes, and A. Barthélémy, 'Ferroelectric and multiferroic tunnel junctions', *MRS Bull.*, vol. 37, no. 2, pp. 138–143, 2012, doi: 10.1557/mrs.2011.358.

[16] Y. W. Yin *et al.*, 'Multiferroic tunnel junctions and ferroelectric control of magnetic state at interface (invited)', *J. Appl. Phys.*, vol. 117, no. 17, p. 172601, Mar. 2015, doi: 10.1063/1.4913753.

[17] J. F. Scott, 'Multiferroic memories', *Nat. Mater.*, vol. 6, no. 4, pp. 256–257, Apr. 2007, doi: 10.1038/nmat1868.

[18] F. Yang *et al.*, 'Eight-logic memory cell based on multiferroic junctions', *J. Phys. Appl. Phys.*, vol. 42, no. 7, p. 072004, Mar. 2009, doi: 10.1088/0022-3727/42/7/072004.
[19] S. Boyn *et al.*, 'Learning through ferroelectric domain dynamics in solid-state synapses', *Nat. Commun.*, vol. 8, no. 1, p. 14736, Apr. 2017, doi: 10.1038/ncomms14736.
[20] Z.-D. Luo, G. Apachitei, M.-M. Yang, J. J. P. Peters, A. M. Sanchez, and M. Alexe, 'Bi-ferroic memristive properties of multiferroic tunnel junctions', *Appl. Phys. Lett.*, vol. 112, no. 10, p. 102905, Mar. 2018, doi: 10.1063/1.5023877.
[21] N. A. Hill, 'Why Are There so Few Magnetic Ferroelectrics?', *J. Phys. Chem. B*, vol. 104, no. 29, pp. 6694–6709, 2000, doi: 10.1021/jp000114x.
[22] N. A. Spaldin, 'Multiferroics beyond electric-field control of magnetism', *Proc. R. Soc. Math. Phys. Eng. Sci.*, vol. 476, no. 2233, p. 20190542, 2020, doi: 10.1098/rspa.2019.0542.
[23] D. Brewster, *Observations on the pyro-electricity of minerals*. in Landmarks of science II. Edinburgh: William Blackwood, 1824.
[24] J. Curie and P. Curie, 'Développement par compression de l'électricité polaire dans les cristaux hémièdres à faces inclinées', *Bull. Soc. Minerol. Fr.*, vol. 3, pp. 90–93, 1880.
[25] J. Unsworth, 'Piezoelectricity and piezoelectric materials', presented at the Key Engineering Materials, Trans Tech Publ, 1992, pp. 273–310.
[26] C. Borel, 'Recherches des constantes diélectriques principales de quelques substances cristallisées biaxes (orthorhombiques et clinorhombiques) suivies d'une notice relative a des phénomènes dynamiques dus a l'electrisation résiduelle des diélectriques: Dissertation présentée à la Faculté des Sciences de l'Université de Genève pour obtenir le grade de Docteur ès Sciences', 1893.
[27] F. Pockels, 'On the Effect of an Electrostatic Field on Optical the Behavior of Piezoelectric Crystals', *Abh. Gott.*, vol. 39, pp. 1–7, 1894.
[28] K. C. Kao, '4 - Ferroelectrics, Piezoelectrics, and Pyroelectrics', in *Dielectric Phenomena in Solids*, K. C. Kao, Ed., San Diego: Academic Press, 2004, pp. 213–282. doi: https://doi.org/10.1016/B978-012396561-5/50014-1.
[29] J. Valasek, 'Piezo-Electric and Allied Phenomena in Rochelle Salt', *Phys Rev*, vol. 17, no. 4, pp. 475–481, Apr. 1921, doi: 10.1103/PhysRev.17.475.
[30] G. Busch and P. Scherrer, 'A new seignette-electric substance', *Naturwiss*, vol. 23, no. 1, pp. 737–738, 1935, doi: 10.1080/00150198708224825.
[31] A. von Hippel, R. G. Breckenridge, F. G. Chesley, and L. Tisza, 'High dielectric constant ceramics', *Ind. Eng. Chem.*, vol. 38, no. 11, pp. 1097–1109, 1946, doi: 10.1021/ie50443a009.
[32] B. M. Wul and I. M. Goldman, 'Dielectric Constants of Titanates of Metals of the Second Group', *SecDokl. Akad. Nauk. SSSR*, vol. 46, p. 154, 1945.
[33] J. C. Slater, 'Theory of the Transition in $KH_2PO_4$', *J. Chem. Phys.*, vol. 9, no. 1, pp. 16–33, 1941, doi: 10.1063/1.1750821.
[34] B. Grey, 'Transducer and Method of Making Same', 2 486 560
[35] V. K. Wadhawan, 'Towards a rigorous definition of ferroic phase transitions', *Phase Transit.*, vol. 64, no. 3, pp. 165–177, 1998, doi: 10.1080/01411599808220645.
[36] L. Landau, 'The Theory of Phase Transitions', *Nature*, vol. 138, no. 3498, pp. 840–841, Nov. 1936, doi: 10.1038/138840a0.
[37] V. Ginzburg, 'On the dielectric properties of ferroelectric (seignetteelectric) crystals and barium titanate', *Zh Eksp Teor Fiz*, vol. 15, p. 739, 1945.
[38] V. Ginzburg, 'On polarization and piezoelectric effect of barium titanate near the point of ferroelectric transition', *Zh Eksp Teor Fiz*, vol. 19, p. 36, 1949.
[39] A. F. Devonshire, 'Theory of ferroelectrics', *Adv. Phys.*, vol. 3, no. 10, pp. 85–130, 1954, doi: 10.1080/00018735400101173.
[40] A. K. Bain and P. Chand, *Ferroelectrics: Principles and applications*. John Wiley & Sons, 2017.

[41] E. K. Akdogğan and A. Safari, 'Thermodynamics of Ferroelectricity', in *Piezoelectric and Acoustic Materials for Transducer Applications*, A. Safari and E. K. Akdoğan, Eds., Boston, MA: Springer US, 2008, pp. 3–16. doi: 10.1007/978-0-387-76540-2_1.
[42] C. Kittel, 'Theory of Antiferroelectric Crystals', *Phys Rev*, vol. 82, no. 5, pp. 729–732, Jun. 1951, doi: 10.1103/PhysRev.82.729.
[43] W. Cochran, 'Crystal Stability and the Theory of Ferroelectricity', *Phys Rev Lett*, vol. 3, no. 9, pp. 412–414, Nov. 1959, doi: 10.1103/PhysRevLett.3.412.
[44] P. Anderson, 'Fizika dielektrikov', *Akad Nauk SSSR Mosc.*, 1960.
[45] C. V. RAMAN and T. M. K. NEDUNGADI, 'The α-β Transformation of Quartz', *Nature*, vol. 145, no. 3665, pp. 147–147, Jan. 1940, doi: 10.1038/145147a0.
[46] G. Shirane and A. Takeda, 'Phase Transitions in Solid Solutions of $PbZrO_3$ and $PbTiO_3$ (I) Small Concentrations of $PbTiO_3$', *J. Phys. Soc. Jpn.*, vol. 7, no. 1, pp. 5–11, Jan. 1952, doi: 10.1143/JPSJ.7.5.
[47] E. Sawaguchi, 'Ferroelectricity versus Antiferroelectricity in the Solid Solutions of $PbZrO_3$ and $PbTiO_3$', *J. Phys. Soc. Jpn.*, vol. 8, no. 5, pp. 615–629, Sep. 1953, doi: 10.1143/JPSJ.8.615.
[48] N. A. Spaldin and R. Ramesh, 'Advances in magnetoelectric multiferroics', *Nat. Mater.*, vol. 18, no. 3, pp. 203–212, Mar. 2019, doi: 10.1038/s41563-018-0275-2.
[49] L. L. Hench and J. K. West, *Principles of electronic ceramics*. New York: Wiley-Interscience, 1990.
[50] T. Lottermoser and D. Meier, 'A short history of multiferroics', vol. 6, no. 2, 2021, doi: 10.1515/psr-2020-0032.
[51] J. Wang *et al.*, 'Epitaxial $BiFeO_3$ Multiferroic Thin Film Heterostructures', *Science*, vol. 299, no. 5613, pp. 1719–1722, 2003, doi: 10.1126/science.1080615.
[52] P. B. Jamieson, S. C. Abrahams, and J. L. Bernstein, 'Ferroelectric Tungsten Bronze-Type Crystal Structures. I. Barium Strontium Niobate $Ba_{0.27}Sr_{0.75}Nb_2O_{5.78}$', *J. Chem. Phys.*, vol. 48, no. 11, pp. 5048–5057, Sep. 2003, doi: 10.1063/1.1668176.
[53] B. Aurivillius, 'Mixed Bismuth Oxides with Layer lattices I. The structure type of $CaNb_2$ $Bi_2O_9$', *Ark. Kemi*, vol. 1, no. 54, pp. 463–480, 1949.
[54] S. N. Ruddlesden and P. Popper, 'New compounds of the $K_2NIF_4$ type', *Acta Crystallogr.*, vol. 10, no. 8, pp. 538–539, 1957, doi: https://doi.org/10.1107/S0365110X57001929.
[55] M. Dion, M. Ganne, and M. Tournoux, 'Nouvelles familles de phases $M^{I}M^{II}{}_2Nb_3O_{10}$ a feuillets "perovskites"', *Mater. Res. Bull.*, vol. 16, pp. 1429–1435, 1981.
[56] A. J. Jacobson, J. T. Lewandowski, and J. W. Johnson, 'Ion exchange of the layered perovskite $KCa_2Nb_3O_{10}$ by protons', *J. Common Met.*, vol. 116, no. 1, pp. 137–146, 1986, doi: https://doi.org/10.1016/0022-5088(86)90224-9.
[57] M. Noor-A-Alam, O. Z. Olszewski, and M. Nolan, 'Ferroelectricity and Large Piezoelectric Response of AlN/ScN Superlattice', *ACS Appl. Mater. Interfaces*, vol. 11, no. 22, pp. 20482–20490, Jun. 2019, doi: 10.1021/acsami.8b22602.
[58] M. Akiyama, T. Kamohara, K. Kano, A. Teshigahara, Y. Takeuchi, and N. Kawahara, 'Enhancement of Piezoelectric Response in Scandium Aluminum Nitride Alloy Thin Films Prepared by Dual Reactive Cosputtering', *Adv. Mater.*, vol. 21, no. 5, pp. 593–596, Feb. 2009, doi: 10.1002/adma.200802611.
[59] M. H. Park, Y. H. Lee, T. Mikolajick, U. Schroeder, and C. S. Hwang, 'Review and perspective on ferroelectric $HfO_2$-based thin films for memory applications', *MRS Commun.*, vol. 8, no. 3, pp. 795–808, 2018, doi: 10.1557/mrc.2018.175.
[60] T. S. Böscke, J. Müller, D. Bräuhaus, U. Schröder, and U. Böttger, 'Ferroelectricity in hafnium oxide thin films', *Appl. Phys. Lett.*, vol. 99, no. 10, p. 102903, Sep. 2011, doi: 10.1063/1.3634052.
[61] S. S. Cheema *et al.*, 'Enhanced ferroelectricity in ultrathin films grown directly on silicon', *Nature*, vol. 580, no. 7804, pp. 478–482, Apr. 2020, doi: 10.1038/s41586-020-2208-x.

[62] S. Salahuddin, K. Ni, and S. Datta, 'The era of hyper-scaling in electronics', *Nat. Electron.*, vol. 1, no. 8, pp. 442–450, Aug. 2018, doi: 10.1038/s41928-018-0117-x.
[63] C. Wang, L. You, D. Cobden, and J. Wang, 'Towards two-dimensional van der Waals ferroelectrics', *Nat. Mater.*, vol. 22, no. 5, pp. 542–552, May 2023, doi: 10.1038/s41563-022-01422-y.
[64] S. Barraza-Lopez, B. M. Fregoso, J. W. Villanova, S. S. P. Parkin, and K. Chang, 'Colloquium: Physical properties of group-IV monochalcogenide monolayers', *Rev Mod Phys*, vol. 93, no. 1, p. 011001, Mar. 2021, doi: 10.1103/RevModPhys.93.011001.
[65] K. Chang *et al.*, 'Discovery of robust in-plane ferroelectricity in atomic-thick SnTe', *Science*, vol. 353, no. 6296, pp. 274–278, Jul. 2016, doi: 10.1126/science.aad8609.
[66] Z. Fei *et al.*, 'Ferroelectric switching of a two-dimensional metal', *Nature*, vol. 560, no. 7718, pp. 336–339, Aug. 2018, doi: 10.1038/s41586-018-0336-3.
[67] Q. Yang, M. Wu, and J. Li, 'Origin of Two-Dimensional Vertical Ferroelectricity in $WTe_2$ Bilayer and Multilayer', *J. Phys. Chem. Lett.*, vol. 9, no. 24, pp. 7160–7164, Dec. 2018, doi: 10.1021/acs.jpclett.8b03654.
[68] S. Yuan *et al.*, 'Room-temperature ferroelectricity in $MoTe_2$ down to the atomic monolayer limit', *Nat. Commun.*, vol. 10, no. 1, p. 1775, Apr. 2019, doi: 10.1038/s41467-019-09669-x.
[69] M. Wu and X. C. Zeng, 'Bismuth Oxychalcogenides: A New Class of Ferroelectric/Ferroelastic Materials with Ultra High Mobility', *Nano Lett.*, vol. 17, no. 10, pp. 6309–6314, Oct. 2017, doi: 10.1021/acs.nanolett.7b03020.
[70] F. Liu *et al.*, 'Room-temperature ferroelectricity in $CuInP_2S_6$ ultrathin flakes', *Nat. Commun.*, vol. 7, no. 1, p. 12357, Aug. 2016, doi: 10.1038/ncomms12357.
[71] L. You *et al.*, 'In-Plane Ferroelectricity in Thin Flakes of Van der Waals Hybrid Perovskite', *Adv. Mater.*, vol. 30, no. 51, p. 1803249, Dec. 2018, doi: 10.1002/adma.201803249.
[72] H. C. Oersted, 'Experiments on the Effect of a Current of Electricity on the Magnetic Needle', Annals of Philosophy, 1820, pp. 273–276.
[73] E. C. Stoner, 'LXXX. Atomic moments in ferromagnetic metals and alloys with non-ferromagnetic elements', *Lond. Edinb. Dublin Philos. Mag. J. Sci.*, vol. 15, no. 101, pp. 1018–1034, May 1933, doi: 10.1080/14786443309462241.
[74] C. Kittel, 'Introduction to solid state physics Eighth edition', 2021.
[75] J. B. Goodenough, 'Theory of the Role of Covalence in the Perovskite-Type Manganites [La, M(II)]$MnO_3$', *Phys Rev*, vol. 100, no. 2, pp. 564–573, Oct. 1955, doi: 10.1103/PhysRev.100.564.
[76] J. B. Goodenough, 'An interpretation of the magnetic properties of the perovskite-type mixed crystals $La_{1-x}Sr_xCoO_{3-\lambda}$', *J. Phys. Chem. Solids*, vol. 6, no. 2, pp. 287–297, Aug. 1958, doi: 10.1016/0022-3697(58)90107-0.
[77] J. Kanamori, 'Superexchange interaction and symmetry properties of electron orbitals', *J. Phys. Chem. Solids*, vol. 10, no. 2, pp. 87–98, Jul. 1959, doi: 10.1016/0022-3697(59)90061-7.
[78] H. A. Kramers, 'L'interaction Entre les Atomes Magnétogènes dans un Cristal Paramagnétique', *Physica*, vol. 1, no. 1, pp. 182–192, Jan. 1934, doi: 10.1016/S0031-8914(34)90023-9.
[79] P. W. Anderson, 'Antiferromagnetism. Theory of Superexchange Interaction', *Phys Rev*, vol. 79, no. 2, pp. 350–356, Jul. 1950, doi: 10.1103/PhysRev.79.350.
[80] C. Zener, 'Interaction between the d-Shells in the Transition Metals. II. Ferromagnetic Compounds of Manganese with Perovskite Structure', *Phys Rev*, vol. 82, no. 3, pp. 403–405, May 1951, doi: 10.1103/PhysRev.82.403.
[81] I. Dzyaloshinsky, 'A thermodynamic theory of "weak" ferromagnetism of antiferromagnetics', *J. Phys. Chem. Solids*, vol. 4, no. 4, pp. 241–255, Jan. 1958, doi: 10.1016/0022-3697(58)90076-3.
[82] T. Moriya, 'Anisotropic Superexchange Interaction and Weak Ferromagnetism', *Phys Rev*, vol. 120, no. 1, pp. 91–98, Oct. 1960, doi: 10.1103/PhysRev.120.91.

[83] S.-W. Cheong and M. Mostovoy, 'Multiferroics: a magnetic twist for ferroelectricity', *Nat. Mater.*, vol. 6, no. 1, pp. 13–20, Jan. 2007, doi: 10.1038/nmat1804.
[84] D. M. Evans, V. Garcia, D. Meier, and M. Bibes, 'Domains and domain walls in multiferroics', vol. 5, no. 9, 2020, doi: 10.1515/psr-2019-0067.
[85] C. Kittel, 'Theory of the Structure of Ferromagnetic Domains in Films and Small Particles', *Phys Rev*, vol. 70, no. 11–12, pp. 965–971, Dec. 1946, doi: 10.1103/PhysRev.70.965.
[86] C. Kittel, 'Physical Theory of Ferromagnetic Domains', *Rev Mod Phys*, vol. 21, no. 4, pp. 541–583, Oct. 1949, doi: 10.1103/RevModPhys.21.541.
[87] T. Mitsui and J. Furuichi, 'Domain Structure of Rochelle Salt and $KH_2P\mathrmO_4$', *Phys Rev*, vol. 90, no. 2, pp. 193–202, Apr. 1953, doi: 10.1103/PhysRev.90.193.
[88] G. F. Nataf *et al.*, 'Domain-wall engineering and topological defects in ferroelectric and ferroelastic materials', *Nat. Rev. Phys.*, vol. 2, no. 11, pp. 634–648, Nov. 2020, doi: 10.1038/s42254-020-0235-z.
[89] M. Kläui, 'Head-to-head domain walls in magnetic nanostructures', *J. Phys. Condens. Matter*, vol. 20, no. 31, p. 313001, Jul. 2008, doi: 10.1088/0953-8984/20/31/313001.
[90] D. Meier *et al.*, 'Anisotropic conductance at improper ferroelectric domain walls', *Nat. Mater.*, vol. 11, no. 4, pp. 284–288, Apr. 2012, doi: 10.1038/nmat3249.
[91] D. Meier and S. M. Selbach, 'Ferroelectric domain walls for nanotechnology', *Nat. Rev. Mater.*, vol. 7, no. 3, pp. 157–173, Mar. 2022, doi: 10.1038/s41578-021-00375-z.
[92] J. P. V. McConville *et al.*, 'Ferroelectric Domain Wall Memristor', *Adv. Funct. Mater.*, vol. 30, no. 28, p. 2000109, Jul. 2020, doi: 10.1002/adfm.202000109.
[93] E. K. H. Salje, 'Multiferroic Domain Boundaries as Active Memory Devices: Trajectories Towards Domain Boundary Engineering', *ChemPhysChem*, vol. 11, no. 5, pp. 940–950, Apr. 2010, doi: 10.1002/cphc.200900943.
[94] N. Domingo, S. Farokhipoor, J. Santiso, B. Noheda, and G. Catalan, 'Domain wall magnetoresistance in $BiFeO_3$ thin films measured by scanning probe microscopy', *J. Phys. Condens. Matter*, vol. 29, no. 33, p. 334003, Jul. 2017, doi: 10.1088/1361-648X/aa7a24.
[95] D. Lee *et al.*, 'Mixed Bloch-Néel-Ising character of 180° ferroelectric domain walls', *Phys Rev B*, vol. 80, no. 6, p. 060102, Aug. 2009, doi: 10.1103/PhysRevB.80.060102.
[96] Z. Li *et al.*, 'High-density array of ferroelectric nanodots with robust and reversibly switchable topological domain states', *Sci. Adv.*, vol. 3, no. 8, p. e1700919, doi: 10.1126/sciadv.1700919.
[97] Z. Hong *et al.*, 'Vortex Domain Walls in Ferroelectrics', *Nano Lett.*, vol. 21, no. 8, pp. 3533–3539, 2021, doi: 10.1021/acs.nanolett.1c00404.
[98] S. Das *et al.*, 'Author Correction: Local negative permittivity and topological phase transition in polar skyrmions', *Nat. Mater.*, vol. 20, no. 6, pp. 905–905, Jun. 2021, doi: 10.1038/s41563-021-00962-z.
[99] S. Das *et al.*, 'Local negative permittivity and topological phase transition in polar skyrmions', *Nat. Mater.*, vol. 20, no. 2, pp. 194–201, Feb. 2021, doi: 10.1038/s41563-020-00818-y.
[100] L. D. Landau and E. M. Lifshitz, 'On the Theory of the Dipersion of Magnetic Permeability in Ferromagnetic Bodies', 1935. [Online]. Available: https://api.semanticscholar.org/CorpusID:26634163
[101] T. Shinjo, T. Okuno, R. Hassdorf, † K. Shigeto, and T. Ono, 'Magnetic Vortex Core Observation in Circular Dots of Permalloy', *Science*, vol. 289, no. 5481, pp. 930–932, Aug. 2000, doi: 10.1126/science.289.5481.930.
[102] A. Wachowiak, J. Wiebe, M. Bode, O. Pietzsch, M. Morgenstern, and R. Wiesendanger, 'Direct Observation of Internal Spin Structure of Magnetic Vortex Cores', *Science*, vol. 298, no. 5593, pp. 577–580, Oct. 2002, doi: 10.1126/science.1075302.
[103] H. Fu and L. Bellaiche, 'Ferroelectricity in Barium Titanate Quantum Dots and Wires', *Phys Rev Lett*, vol. 91, no. 25, p. 257601, Dec. 2003, doi: 10.1103/PhysRevLett.91.257601.
[104] I. I. Naumov, L. Bellaiche, and H. Fu, 'Unusual phase transitions in ferroelectric nanodisks and nanorods', *Nature*, vol. 432, no. 7018, pp. 737–740, Dec. 2004, doi: 10.1038/nature03107.

[105] C.-L. Jia, K. W. Urban, M. Alexe, D. Hesse, and I. Vrejoiu, 'Direct Observation of Continuous Electric Dipole Rotation in Flux-Closure Domains in Ferroelectric Pb(Zr,Ti)O3', *Science*, vol. 331, no. 6023, pp. 1420–1423, Mar. 2011, doi: 10.1126/science.1200605.
[106] C. T. Nelson *et al.*, 'Spontaneous Vortex Nanodomain Arrays at Ferroelectric Heterointerfaces', *Nano Lett.*, vol. 11, no. 2, pp. 828–834, Feb. 2011, doi: 10.1021/nl1041808.
[107] A. K. Yadav *et al.*, 'Observation of polar vortices in oxide superlattices', *Nature*, vol. 530, no. 7589, pp. 198–201, Feb. 2016, doi: 10.1038/nature16463.
[108] Z. Hong *et al.*, 'Stability of Polar Vortex Lattice in Ferroelectric Superlattices', *Nano Lett.*, vol. 17, no. 4, pp. 2246–2252, 2017, doi: 10.1021/acs.nanolett.6b04875.
[109] S. Das *et al.*, 'Observation of room-temperature polar skyrmions', *Nature*, vol. 568, no. 7752, pp. 368–372, Apr. 2019, doi: 10.1038/s41586-019-1092-8.
[110] P. Shafer *et al.*, 'Emergent chirality in the electric polarization texture of titanate superlattices', *Proc. Natl. Acad. Sci.*, vol. 115, no. 5, pp. 915–920, 2018, doi: 10.1073/pnas.1711652115.
[111] Y.-T. Shao *et al.*, 'Emergent chirality in a polar meron to skyrmion phase transition', *Nat. Commun.*, vol. 14, no. 1, p. 1355, Mar. 2023, doi: 10.1038/s41467-023-36950-x.
[112] A. K. Yadav *et al.*, 'Spatially resolved steady-state negative capacitance', *Nature*, vol. 565, no. 7740, pp. 468–471, Jan. 2019, doi: 10.1038/s41586-018-0855-y.
[113] G. Tian *et al.*, 'Topological domain states and magnetoelectric properties in multiferroic nanostructures', *Natl. Sci. Rev.*, vol. 6, no. 4, pp. 684–702, Jul. 2019, doi: 10.1093/nsr/nwz100.
[114] B. B. Van Aken, J.-P. Rivera, H. Schmid, and M. Fiebig, 'Observation of ferrotoroidic domains', *Nature*, vol. 449, no. 7163, pp. 702–705, Oct. 2007, doi: 10.1038/nature06139.
[115] S. Gnewuch and E. E. Rodriguez, 'The fourth ferroic order: Current status on ferrotoroidic materials', *J. Solid State Chem.*, vol. 271, pp. 175–190, 2019, doi: https://doi.org/10.1016/j.jssc.2018.12.035.
[116] H. Schmid, 'Multi-ferroic magnetoelectrics', *Ferroelectrics*, vol. 162, pp. 317–338, 1994.
[117] E. Ascher, H. Rieder, H. Schmid, and H. Stössel, 'Some Properties of Ferromagnetoelectric Nickel-Iodine Boracite, $Ni_3B_7O_{13}I$', *J. Appl. Phys.*, vol. 37, no. 3, pp. 1404–1405, Jun. 2004, doi: 10.1063/1.1708493.
[118] G. Smolenskii, V. Isupov, N. Krainik, and A. Agranovskaya, 'The coexistence of the ferroelectric and ferromagnetic states', *Izv Akad Nauk SSSR Seriya Fiz*, vol. 25, pp. 1333–9, 1961.
[119] L. Keeney *et al.*, 'Novel Approaches for Genuine Single-Phase Room Temperature Magnetoelectric Multiferroics', in *Nanoscale Ferroelectrics and Multiferroics*, John Wiley & Sons, Ltd, 2016, pp. 789–829. doi: https://doi.org/10.1002/9781118935743.ch25.
[120] I. E. Dzyaloshinskiĭ, 'On the magneto-electrical effects in antiferromagnets', *Sov. Phys. JETP*, vol. 10, pp. 628–629, 1960.
[121] D. Astrov, 'The magnetoelectric effect in antiferromagnetics', *Sov Phys JETP*, vol. 11, no. 3, pp. 708–709, 1960.
[122] D. Astrov, 'Magnetoelectric effect in chromium oxide', *Sov Phys JETP*, vol. 13, no. 4, pp. 729–733, 1961.
[123] S. Manipatruni *et al.*, 'Scalable energy-efficient magnetoelectric spin–orbit logic', *Nature*, vol. 565, no. 7737, pp. 35–42, Jan. 2019, doi: 10.1038/s41586-018-0770-2.
[124] I. B. Bersuker, 'Origin of Perovskite Multiferroicity and Magnetoelectric-Multiferroic Effects—The Role of Electronic Spin in Spontaneous Polarization of Crystals', *Magnetochemistry*, vol. 8, no. 1, 2022, doi: 10.3390/magnetochemistry8010009.
[125] P. Barone and S. Picozzi, 'Mechanisms and origin of multiferroicity', *Multiferroic Mater. Heterostruct. Matér. Hétérostructures Multiferroïques*, vol. 16, no. 2, pp. 143–152, Mar. 2015, doi: 10.1016/j.crhy.2015.01.009.
[126] T. Günter *et al.*, 'Incipient ferroelectricity in 2.3% tensile-strained $CaMnO_3$ films', *Phys Rev B*, vol. 85, no. 21, p. 214120, Jun. 2012, doi: 10.1103/PhysRevB.85.214120.

[127] H. Sakai *et al.*, 'Displacement-Type Ferroelectricity with Off-Center Magnetic Ions in Perovskite $Sr_{1-x}Ba_xMnO_3$', *Phys Rev Lett*, vol. 107, no. 13, p. 137601, Sep. 2011, doi: 10.1103/PhysRevLett.107.137601.
[128] D. I. Khomskii, 'Classifying multiferroics: Mechanisms and effects', *Physics*, vol. 2, p. 20, 2009.
[129] B. B. Van Aken, T. T. M. Palstra, A. Filippetti, and N. A. Spaldin, 'The origin of ferroelectricity in magnetoelectric $YMnO_3$', *Nat. Mater.*, vol. 3, no. 3, pp. 164–170, Mar. 2004, doi: 10.1038/nmat1080.
[130] B. Lorenz, 'Hexagonal Manganites—($RMnO_3$): Class (I) Multiferroics with Strong Coupling of Magnetism and Ferroelectricity', *ISRN Condens. Matter Phys.*, vol. 2013, p. 497073, Feb. 2013, doi: 10.1155/2013/497073.
[131] A. Roy, R. Gupta, and A. Garg, 'Multiferroic Memories', *Adv. Condens. Matter Phys.*, vol. 2012, p. 926290, Apr. 2012, doi: 10.1155/2012/926290.
[132] H. W. Jang *et al.*, 'Epitaxial (001) $BiFeO_3$ membranes with substantially reduced fatigue and leakage', *Appl. Phys. Lett.*, vol. 92, no. 6, p. 062910, Feb. 2008, doi: 10.1063/1.2842418.
[133] V. Shelke *et al.*, 'Reduced Coercive Field in $BiFeO_3$ Thin Films Through Domain Engineering', *Adv. Mater.*, vol. 23, no. 5, pp. 669–672, Feb. 2011, doi: 10.1002/adma.201000807.
[134] D. H. Kim, H. N. Lee, M. D. Biegalski, and H. M. Christen, 'Effect of epitaxial strain on ferroelectric polarization in multiferroic $BiFeO_3$ films', *Appl. Phys. Lett.*, vol. 92, no. 1, p. 012911, Jan. 2008, doi: 10.1063/1.2830799.
[135] V. M. Goldschmidt, 'Die Gesetze der Krystallochemie', *Naturwissenschaften*, vol. 14, no. 21, pp. 477–485, May 1926, doi: 10.1007/BF01507527.
[136] A. Agbelele *et al.*, 'Strain and Magnetic Field Induced Spin-Structure Transitions in Multiferroic $BiFeO_3$', *Adv. Mater.*, vol. 29, no. 9, p. 1602327, Mar. 2017, doi: 10.1002/adma.201602327.
[137] M. Müller, Y.-L. Huang, S. Vélez, R. Ramesh, M. Fiebig, and M. Trassin, 'Training the Polarization in Integrated $La_{0.15}Bi_{0.85}FeO_3$-Based Devices', *Adv. Mater.*, vol. 33, no. 52, p. 2104688, Dec. 2021, doi: 10.1002/adma.202104688.
[138] S. D. Seddon *et al.*, 'Real-space observation of ferroelectrically induced magnetic spin crystal in $SrRuO_3$', *Nat. Commun.*, vol. 12, no. 1, p. 2007, Mar. 2021, doi: 10.1038/s41467-021-22165-5.
[139] D. Rusu *et al.*, 'Ferroelectric incommensurate spin crystals', *Nature*, vol. 602, no. 7896, pp. 240–244, Feb. 2022, doi: 10.1038/s41586-021-04260-1.
[140] F. Trier, P. Noël, J.-V. Kim, J.-P. Attané, L. Vila, and M. Bibes, 'Oxide spin-orbitronics: spin–charge interconversion and topological spin textures', *Nat. Rev. Mater.*, vol. 7, no. 4, pp. 258–274, Apr. 2022, doi: 10.1038/s41578-021-00395-9.
[141] J. Seidel, R. K. Vasudevan, and N. Valanoor, 'Topological Structures in Multiferroics – Domain Walls, Skyrmions and Vortices', *Adv. Electron. Mater.*, vol. 2, no. 1, p. 1500292, Jan. 2016, doi: 10.1002/aelm.201500292.
[142] S. Bhowal and N. A. Spaldin, 'Magnetoelectric Classification of Skyrmions', *Phys Rev Lett*, vol. 128, no. 22, p. 227204, Jun. 2022, doi: 10.1103/PhysRevLett.128.227204.
[143] C. Back *et al.*, 'The 2020 skyrmionics roadmap', *J. Phys. Appl. Phys.*, vol. 53, no. 36, p. 363001, Jun. 2020, doi: 10.1088/1361-6463/ab8418.
[144] T. Kikuchi, 'Stability of layered bismuth compounds in relation to the structural mismatch', *Mater. Res. Bull.*, vol. 14, no. 12, pp. 1561–1569, 1979, doi: https://doi.org/10.1016/0025-5408(72)90226-7.
[145] N. A. Lomanova, M. I. Morozov, V. L. Ugolkov, and V. V. Gusarov, 'Properties of aurivillius phases in the $Bi_4Ti_3O_{12}$-$BiFeO_3$ system', *Inorg. Mater.*, vol. 42, no. 2, pp. 189–195, Feb. 2006, doi: 10.1134/S0020168506020142.
[146] M. A. Zurbuchen *et al.*, 'Synthesis, structure, and electrical behavior of $Sr_4Bi_4Ti_7O_{24}$', *J. Appl. Phys.*, vol. 107, no. 2, p. 024106, 2010, doi: 10.1063/1.3273388.

[147] Y. Shimakawa, Y. Kubo, Y. Nakagawa, T. Kamiyama, H. Asano, and F. Izumi, 'Crystal structures and ferroelectric properties of $SrBi_2Ta_2O_9$and $Sr_{0.8}Bi_{2.2}Ta_2O_9$', *Appl. Phys. Lett.*, vol. 74, no. 13, pp. 1904–1906, Mar. 1999, doi: 10.1063/1.123708.
[148] J. Halpin and L. Keeney, 'Naturally Layered Aurivillius Phases: Flexible Scaffolds for the Design of Multiferroic Materials', *OAJ Mater. Devices*, vol. 5, no. 1, Dec. 2021, [Online]. Available: http://www.caip.co-ac.com/index.php/materialsanddevices/article/view/131
[149] R. A. Armstrong and R. E. Newnham, 'Bismuth titanate solid solutions', *Mater. Res. Bull.*, vol. 7, no. 10, pp. 1025–1034, 1972, doi: https://doi.org/10.1016/0025-5408(72)90154-7.
[150] C. H. Hervoches, A. Snedden, R. Riggs, S. H. Kilcoyne, P. Manuel, and P. Lightfoot, 'Structural Behavior of the Four-Layer Aurivillius-Phase Ferroelectrics $SrBi_4Ti_4O_{15}$ and $Bi_5Ti_3FeO_{15}$', *J. Solid State Chem.*, vol. 164, no. 2, pp. 280–291, 2002, doi: https://doi.org/10.1006/jssc.2001.9473.
[151] L. Zhang, H. Wang, Z. Chen, P. K. Wong, and J. Liu, 'Bi2WO6 micro/nano-structures: Synthesis, modifications and visible-light-driven photocatalytic applications', *Appl. Catal. B Environ.*, vol. 106, no. 1, pp. 1–13, Jul. 2011, doi: 10.1016/j.apcatb.2011.05.008.
[152] H. Irie, M. Miyayama, and T. Kudo, 'Structure dependence of ferroelectric properties of bismuth layer-structured ferroelectric single crystals', *J. Appl. Phys.*, vol. 90, no. 8, pp. 4089–4094, Oct. 2001, doi: 10.1063/1.1389476.
[153] S. Supriya, 'Tailoring layered structure of bismuth-based aurivillius perovskites: Recent advances and future aspects', *Coord. Chem. Rev.*, vol. 479, p. 215010, 2023, doi: https://doi.org/10.1016/j.ccr.2022.215010.
[154] R. E. Newnham, R. W. Wolfe, and J. F. Dorrian, 'Structural basis of ferroelectricity in the bismuth titanate family', *Mater. Res. Bull.*, vol. 6, no. 10, pp. 1029–1039, 1971, doi: https://doi.org/10.1016/0025-5408(71)90082-1.
[155] Y.-Y. Guo, A. S. Gibbs, J. M. Perez-Mato, and P. Lightfoot, 'Unexpected phase transition sequence in the ferroelectric $Bi_4Ti_3O_{12}$', *IUCrJ*, vol. 6, no. 3, pp. 438–446, May 2019, doi: 10.1107/S2052252519003804.
[156] Ismunandar *et al.*, 'Structural studies of five layer Aurivillius oxides: $A_2Bi_4Ti_5O_{18}$ (A=Ca, Sr, Ba and Pb)', *J. Solid State Chem.*, vol. 177, no. 11, pp. 4188–4196, 2004, doi: https://doi.org/10.1016/j.jssc.2004.07.032.
[157] D. Y. Suárez, I. M. Reaney, and W. E. Lee, 'Relation between tolerance factor and $T_c$ in Aurivillius compounds', *J. Mater. Res.*, vol. 16, no. 11, pp. 3139–3149, 2001, doi: 10.1557/JMR.2001.0433.
[158] M. Campanini, M. Trassin, C. Ederer, R. Erni, and M. D. Rossell, 'Buried In-Plane Ferroelectric Domains in Fe-Doped Single-Crystalline Aurivillius Thin Films', *ACS Appl. Electron. Mater.*, vol. 1, no. 6, pp. 1019–1028, 2019, doi: 10.1021/acsaelm.9b00180.
[159] A. Y. Birenbaum and C. Ederer, 'Potentially multiferroic Aurivillius phase$Bi_5FeTi_3O_{15}$: Cation site preference, electric polarization, and magnetic coupling from first principles', *Phys Rev B*, vol. 90, no. 21, p. 214109, Dec. 2014, doi: 10.1103/PhysRevB.90.214109.
[160] A. T. Giddings, M. C. Stennett, D. P. Reid, E. E. McCabe, C. Greaves, and N. C. Hyatt, 'Synthesis, structure and characterisation of the n=4 Aurivillius phase $Bi_5Ti_3CrO_{15}$', *J. Solid State Chem.*, vol. 184, no. 2, pp. 252–263, 2011, doi: https://doi.org/10.1016/j.jssc.2010.09.031.
[161] N. A. Benedek, J. M. Rondinelli, H. Djani, P. Ghosez, and P. Lightfoot, 'Understanding ferroelectricity in layered perovskites: new ideas and insights from theory and experiments', *Dalton Trans*, vol. 44, no. 23, pp. 10543–10558, 2015, doi: 10.1039/C5DT00010F.
[162] L. Keeney *et al.*, 'Magnetic Field-Induced Ferroelectric Switching in Multiferroic Aurivillius Phase Thin Films at Room Temperature', *J. Am. Ceram. Soc.*, vol. 96, no. 8, pp. 2339–2357, 2013, doi: https://doi.org/10.1111/jace.12467.
[163] A. Faraz *et al.*, 'Direct visualization of magnetic-field-induced magnetoelectric switching in multiferroic aurivillius phase thin films', *J. Am. Ceram. Soc.*, vol. 100, no. 3, pp. 975–987, 2017, doi: https://doi.org/10.1111/jace.14597.

[164] L. Keeney, C. Downing, M. Schmidt, M. E. Pemble, V. Nicolosi, and R. W. Whatmore, 'Direct atomic scale determination of magnetic ion partition in a room temperature multiferroic material', *Sci. Rep.*, vol. 7, no. 1, p. 1737, May 2017, doi: 10.1038/s41598-017-01902-1.
[165] N. Deepak, P. Carolan, L. Keeney, M. Pemble, and R. W. Whatmore, 'Tunable nanoscale structural disorder in Aurivillius phase, n = 3 $Bi_4Ti_3O_{12}$ thin films and their role in the transformation to n = 4, $Bi_5Ti_3FeO_{15}$ phase', *J Mater Chem C*, vol. 3, May 2015, doi: 10.1039/C5TC01064K.
[166] M. A. Zurbuchen *et al.*, 'Morphology, structure, and nucleation of out-of-phase boundaries (OPBs) in epitaxial films of layered oxides', *J. Mater. Res.*, vol. 22, no. 6, pp. 1439–1471, 2007, doi: 10.1557/JMR.2007.0198.
[167] 'Dislocations in Crystals', in *Crystallography and Crystal Defects*, John Wiley & Sons, Ltd, 2012, pp. 269–304. doi: https://doi.org/10.1002/9781119961468.ch9.
[168] W. Wang, J. Zhu, X.-Y. Mao, and X.-B. Chen, 'Properties of tungsten-doped $Bi_4Ti_3O_{12}$-$SrBi_4Ti_4O_{15}$ intergrowth ferroelectrics', *Mater. Res. Bull.*, vol. 42, no. 2, pp. 274–280, 2007, doi: https://doi.org/10.1016/j.materresbull.2006.06.003.
[169] V. Veenachary *et al.*, 'Magnetic and Magnetoelectric Properties of AurivilliusThree- and Four-Layered Intergrowth Ceramics', *Crystals*, vol. 13, no. 3, 2023, doi: 10.3390/cryst13030426.
[170] Y. Noguchi, M. Miyayama, and T. Kudo, 'Ferroelectric properties of intergrowth $Bi_3Ti_3O_{12}$–$SrBi_4$ $Ti_4O_{15}$ ceramics', *Appl. Phys. Lett.*, vol. 77, no. 22, pp. 3639–3641, 2000.
[171] L. Keeney, Z. Saghi, M. O'Sullivan, J. Alaria, M. Schmidt, and L. Colfer, 'Persistence of Ferroelectricity Close to Unit-Cell Thickness in Structurally Disordered Aurivillius Phases', *Chem. Mater.*, vol. 32, no. 24, pp. 10511–10523, 2020, doi: 10.1021/acs.chemmater.0c03454.
[172] I. MacLaren *et al.*, 'Local stabilisation of polar order at charged antiphase boundaries in antiferroelectric $(Bi_{0.85}Nd_{0.15})$ $(Ti_{0.1}Fe_{0.9})O_3$', *APL Mater.*, vol. 1, no. 2, Aug. 2013, doi: 10.1063/1.4818002.
[173] I. MacLaren *et al.*, 'The atomic structure and chemistry of Fe-rich steps on antiphase boundaries in Ti-doped $Bi_{0.9}Nd_{0.15}FeO_3$', *APL Mater.*, vol. 2, no. 6, p. 066106, 2014, doi: 10.1063/1.4884684.
[174] Y. Liu *et al.*, 'Controlled Growth and Atomic-Scale Mapping of Charged Heterointerfaces in $PbTiO_3$/$BiFeO_3$ Bilayers', *ACS Appl. Mater. Interfaces*, vol. 9, no. 30, pp. 25578–25586, 2017, doi: 10.1021/acsami.7b04681.
[175] D. Batuk *et al.*, '$Bi_{3n+1}Ti_7Fe_{3n-3}O_{9n+11}$Homologous Series: Slicing Perovskite Structure with Planar Interfaces Containing Anatase-like Chains', *Inorg. Chem.*, vol. 55, no. 3, pp. 1245–1257, 2016, doi: 10.1021/acs.inorgchem.5b02465.
[176] D. Batuk *et al.*, 'Crystal Structure, Defects, Magnetic and Dielectric Properties of the Layered $Bi_{3n+1}Ti_7Fe_{3n-3}O_{9n+11}$ Perovskite-Anatase Intergrowths', *Inorg. Chem.*, vol. 56, no. 2, pp. 931–942, 2017, doi: 10.1021/acs.inorgchem.6b02559.
[177] B. Aurivillius, 'Intergrowth of compounds between members of the bismuth titanate family and structures of the $LiBi_3O_4Cl_2$type-an architectural approach', *Chem. Scr.*, vol. 23, no. 3, pp. 143–156, 1984.
[178] J. F. Ackerman, 'The structures of $Bi_3PbWO_8Cl$ and $Bi_4NbO_8Cl$ and the evolution of the bipox structure series', *J. Solid State Chem.*, vol. 62, no. 1, pp. 92–104, 1986, doi: https://doi.org/10.1016/0022-4596(86)90220-3.
[179] A. M. Kusainova, P. Lightfoot, W. Zhou, S. Yu. Stefanovich, A. V. Mosunov, and V. A. Dolgikh, 'Ferroelectric Properties and Crystal Structure of the Layered Intergrowth Phase $Bi_3Pb_2Nb_2O_{11}Cl$', *Chem. Mater.*, vol. 13, no. 12, pp. 4731–4737, 2001, doi: 10.1021/cm011145n.
[180] S. Liu, W. Miiller, Y. Liu, M. Avdeev, and C. D. Ling, 'Sillen–Aurivillius Intergrowth Phases as Templates for Naturally Layered Multiferroics', *Chem. Mater.*, vol. 24, no. 20, pp. 3932–3942, 2012, doi: 10.1021/cm302342v.

[181] C. Zhong *et al.*, 'Lone-Pair-Induced Intra- and Interlayer Polarizations in Sillén-Aurivillius Layered Perovskite $Bi_4NbO_8Br$', *Inorg. Chem.*, vol. 61, no. 25, pp. 9816–9822, 2022, doi: 10.1021/acs.inorgchem.2c01358.
[182] A. Nakada *et al.*, 'Band Engineering of Double-Layered Sillén–Aurivillius Perovskite Oxychlorides for Visible-Light-Driven Water Splitting', *Chem. Mater.*, vol. 31, no. 9, pp. 3419–3429, 2019, doi: 10.1021/acs.chemmater.9b00567.
[183] H. Fujito *et al.*, 'Layered Perovskite Oxychloride $Bi_4NbO_8Cl$: A Stable Visible Light Responsive Photocatalyst for Water Splitting', *J. Am. Chem. Soc.*, vol. 138, no. 7, pp. 2082–2085, 2016, doi: 10.1021/jacs.5b11191.
[184] Y. Zhang, M.-G. Han, D. Sando, L. Wu, N. Valanoor, and Y. Zhu, 'Antiphase-Boundary-Engineered Domain Switching in a (110)-Oriented $BiFeO_3$ Film', *ACS Appl. Electron. Mater.*, vol. 3, no. 7, pp. 3226–3233, 2021, doi: 10.1021/acsaelm.1c00392.
[185] X.-K. Wei, A. K. Tagantsev, A. Kvasov, K. Roleder, C.-L. Jia, and N. Setter, 'Ferroelectric translational antiphase boundaries in nonpolar materials', *Nat. Commun.*, vol. 5, no. 1, p. 3031, Jan. 2014, doi: 10.1038/ncomms4031.
[186] J. Kim *et al.*, 'Superconducting $Sr_2RuO_4$ Thin Films without Out-of-Phase Boundaries by Higher-Order Ruddlesden–Popper Intergrowth', *Nano Lett.*, vol. 21, no. 10, pp. 4185–4192, 2021, doi: 10.1021/acs.nanolett.0c04963.
[187] H. Nakajima *et al.*, 'Charged domain boundaries stabilized by translational symmetry breaking in the hybrid improper ferroelectric $Ca_{3-x}Sr_xTi_2O_7$', *Commun. Mater.*, vol. 2, no. 1, p. 109, Nov. 2021, doi: 10.1038/s43246-021-00215-1.
[188] A. Kumar *et al.*, 'Effect of in situ electric-field-assisted growth on antiphase boundaries in epitaxial $Fe_3O_4$ thin films on MgO', *Phys Rev Mater*, vol. 2, no. 5, p. 054407, May 2018, doi: 10.1103/PhysRevMaterials.2.054407.
[189] S. Ruiz-Gómez *et al.*, 'Geometrically defined spin structures in ultrathin $Fe_3O_4$ with bulk like magnetic properties', *Nanoscale*, vol. 10, no. 12, pp. 5566–5573, 2018, doi: 10.1039/C7NR07143D.
[190] E. Gradauskaite, K. A. Hunnestad, Q. N. Meier, D. Meier, and M. Trassin, 'Ferroelectric Domain Engineering Using Structural Defect Ordering', *Chem. Mater.*, vol. 34, no. 14, pp. 6468–6475, 2022, doi: 10.1021/acs.chemmater.2c01178.
[191] L. Keeney, L. Colfer, and M. Schmidt, 'Probing Ferroelectric Behavior in Sub-10 nm Bismuth-Rich Aurivillius Films by Piezoresponse Force Microscopy', *Microsc. Microanal.*, vol. 28, no. 4, pp. 1396–1406, 2022, doi: 10.1017/S1431927621013726.
[192] K. Moore *et al.*, 'Charged Domain Wall and Polar Vortex Topologies in a Room-Temperature Magnetoelectric Multiferroic Thin Film', *ACS Appl. Mater. Interfaces*, vol. 14, no. 4, pp. 5525–5536, 2022, doi: 10.1021/acsami.1c17383.
[193] E. Gradauskaite *et al.*, 'Robust In-Plane Ferroelectricity in Ultrathin Epitaxial Aurivillius Films', *Adv. Mater. Interfaces*, vol. 7, no. 14, p. 2000202, Jul. 2020, doi: 10.1002/admi.202000202.
[194] K. Du *et al.*, 'Manipulating topological transformations of polar structures through real-time observation of the dynamic polarization evolution', *Nat. Commun.*, vol. 10, no. 1, p. 4864, Oct. 2019, doi: 10.1038/s41467-019-12864-5.
[195] N. Balke *et al.*, 'Enhanced electric conductivity at ferroelectric vortex cores in $BiFeO_3$', *Nat. Phys.*, vol. 8, no. 1, pp. 81–88, Jan. 2012, doi: 10.1038/nphys2132.
[196] T. Watanabe and H. Funakubo, 'Controlled crystal growth of layered-perovskite thin films as an approach to study their basic properties', *J. Appl. Phys.*, vol. 100, no. 5, p. 051602, 2006, doi: 10.1063/1.2337357.
[197] C. Glynn and C. O'Dwyer, 'Solution Processable Metal Oxide Thin Film Deposition and Material Growth for Electronic and Photonic Devices', *Adv. Mater. Interfaces*, vol. 4, no. 2, p. 1600610, Jan. 2017, doi: 10.1002/admi.201600610.
[198] L. Keeney, C. Groh, S. Kulkarni, S. Roy, M. E. Pemble, and R. W. Whatmore, 'Room temperature electromechanical and magnetic investigations of ferroelectric Aurivillius phase

$Bi_5 Ti_3 (Fe_x Mn_{1-x})O_{15}$ (x = 1 and 0.7) chemical solution deposited thin films', *J. Appl. Phys.*, vol. 112, no. 2, p. 024101, Jul. 2012, doi: 10.1063/1.4734983.
[199] E. Gradauskaite, N. Gray, M. Campanini, M. D. Rossell, and M. Trassin, 'Nanoscale Design of High-Quality Epitaxial Aurivillius Thin Films', *Chem. Mater.*, vol. 33, no. 23, pp. 9439–9446, Dec. 2021, doi: 10.1021/acs.chemmater.1c03466.
[200] X. Cao *et al.*, 'Epitaxial $Bi_9Ti_3Fe_5O_{27}$ thin films: a new type of layer-structure room-temperature multiferroic', *J Mater Chem C*, vol. 5, no. 31, pp. 7720–7725, 2017, doi: 10.1039/C7TC02666H.
[201] F. Wöhler and L. Uslar, 'Über metallisches wolfram und molybdän', *Just Lieb Ann Chem*, vol. 94, pp. 255–259, 1855.
[202] L. Mond, C. Langer, and F. Quincke, 'L.—Action of carbon monoxide on nickel', *J. Chem. Soc. Trans.*, vol. 57, pp. 749–753, 1890.
[203] A. C. Jones and M. L. Hitchman, Eds., *Chemical Vapour Deposition: Precursors, Processes and Applications*. The Royal Society of Chemistry, 2008. doi: 10.1039/9781847558794.
[204] 'CVD Equitment Corperation'. Accessed: Jul. 25, 2023. [Online]. Available: https://www.cvdequipment.com/systems/production-equipment/lpcvd-systems/
[205] 'AIXTRON'. Accessed: Jul. 25, 2023. [Online]. Available: https://www.aixtron.com/en/products/AIX%202800G4-TM_p89
[206] 'AIXTRON'. Accessed: Aug. 16, 2023. [Online]. Available: https://www.aixtron.com/en/products/G10-SiC_p2072
[207] L. Keeney and I. M. Povey, 'Vapor Phase Growth of Metal-Oxide Thin Films and Nanostructures', in *Tailored Functional Oxide Nanomaterials*, John Wiley & Sons, Ltd, 2022, pp. 1–42. doi: https://doi.org/10.1002/9783527826940.ch1.
[208] J. Schwarzkopf and R. Fornari, 'Epitaxial growth of ferroelectric oxide films', *Prog. Cryst. Growth Charact. Mater.*, vol. 52, no. 3, pp. 159–212, Sep. 2006, doi: 10.1016/j.pcrysgrow.2006.06.001.
[209] J.-O. Carlsson and P. M. Martin, 'Chapter 7 - Chemical Vapor Deposition', in *Handbook of Deposition Technologies for Films and Coatings (Third Edition)*, P. M. Martin, Ed., Boston: William Andrew Publishing, 2010, pp. 314–363. doi: 10.1016/B978-0-8155-2031-3.00007-7.
[210] Vincent Astié, Cyril Millon, Jean-Manuel Decams, and Ausrine Bartasyte, 'Direct Liquid Injection Chemical Vapor Deposition', in *Chemical Vapor Deposition for Nanotechnology*, Pietro Mandracci, Ed., Rijeka: IntechOpen, 2018, p. Ch. 2. doi: 10.5772/intechopen.80244.
[211] D. Kobayashi *et al.*, 'High-resolution synchrotron-radiation photoemission characterization for atomically-controlled $SrTiO_3$(001) substrate surfaces subjected to various surface treatments', *J. Appl. Phys.*, vol. 96, no. 12, pp. 7183–7188, Dec. 2004, doi: 10.1063/1.1814175.
[212] M. Kawasaki *et al.*, 'Atomic Control of the $SrTiO_3$ Crystal Surface', *Science*, vol. 266, no. 5190, pp. 1540–1542, Dec. 1994, doi: 10.1126/science.266.5190.1540.
[213] J. Zhang *et al.*, 'Depth-resolved subsurface defects in chemically etched $SrTiO_3$', *Appl. Phys. Lett.*, vol. 94, no. 9, p. 092904, Mar. 2009, doi: 10.1063/1.3093671.
[214] B. Prakash and S. Chakraverty, 'Realization of atomically flat steps and terraces like surface of $SrTiO_3$ (001) single crystal by hot water etching and high temperature annealing', *Solid State Commun.*, vol. 213–214, pp. 28–30, Jul. 2015, doi: 10.1016/j.ssc.2015.04.009.
[215] J. G. Connell, B. J. Isaac, G. B. Ekanayake, D. R. Strachan, and S. S. A. Seo, 'Preparation of atomically flat $SrTiO_3$surfaces using a deionized-water leaching and thermal annealing procedure', *Appl. Phys. Lett.*, vol. 101, no. 25, p. 251607, Dec. 2012, doi: 10.1063/1.4773052.
[216] C. Theis, J. Yeh, D. Schlom, M. Hawley, and G. Brown, 'The influence of vicinal $SrTiO_3$ surfaces on the growth and ferroelectric properties of epitaxial $Bi_4Ti_3O_{12}$ thin films', *Mater. Sci. Eng. B-Adv. Funct. Solid-State Mater.*, vol. 56, pp. 228–233, Nov. 1998, doi: 10.1016/S0921-5107(98)00244-X.
[217] P. Chekhonin *et al.*, 'Effect of substrate miscut on the microstructure in epitaxial $Pb(Mg_{1/3}Nb_{2/3})O_3$-$PbTiO_3$ thin films', *Mater. Charact.*, vol. 129, pp. 234–241, 2017, doi: https://doi.org/10.1016/j.matchar.2017.05.003.

[218] W. Röntgen, 'Über eine neue Art von Strahlen: vorläufige Mitteilung', *Sitzungsber Phys Med Gesell*, 1895.
[219] W. Friedrich, P. Knipping, and M. von Laue, 'interferenz-Erscheinungen bei Röntgenstrahlen. Sitzungsberichte der Mathematischen-Physikalischen Klasse der Königlich Bayerischen Akademie der Wissenschaften zu München', 1912.
[220] W. Bragg, 'Crystalline structures as reveal x-rays', *Nature*, vol. 93, no. 2318, pp. 124–126, 1914.
[221] S. E. Dann, *Reactions and characterization of solids*, vol. 2. Royal Society of Chemistry, 2000.
[222] W. L. Bragg, 'The structure of some crystals as indicated by their diffraction of X-rays', *Proc. R. Soc. Lond. Ser. Contain. Pap. Math. Phys. Character*, vol. 89, no. 610, pp. 248–277, 1913.
[223] W. H. Bragg and W. L. Bragg, 'The structure of the diamond', *Proc. R. Soc. Lond. Ser. Contain. Pap. Math. Phys. Character*, vol. 89, no. 610, pp. 277–291, 1913.
[224] A. Ben-Shem, L. Jenner, G. Yusupova, and M. Yusupov, 'Crystal Structure of the Eukaryotic Ribosome', *Science*, vol. 330, no. 6008, pp. 1203–1209, Nov. 2010, doi: 10.1126/science.1194294.
[225] G. Binnig, C. F. Quate, and Ch. Gerber, 'Atomic Force Microscope', *Phys. Rev. Lett.*, vol. 56, no. 9, pp. 930–933, Mar. 1986, doi: 10.1103/PhysRevLett.56.930.
[226] G. Binnig and H. Rohrer, 'Scanning tunneling microscopy', *Surf. Sci.*, vol. 126, no. 1, pp. 236–244, Mar. 1983, doi: 10.1016/0039-6028(83)90716-1.
[227] B. Voigtländer, *Atomic Force Microscopy*, 2nd ed. in NanoScience and Technology. Springer Cham. [Online]. Available: https://doi.org/10.1007/978-3-030-13654-3
[228] T. R. Albrecht, P. Grütter, D. Horne, and D. Rugar, 'Frequency modulation detection using high-Q cantilevers for enhanced force microscope sensitivity', *J. Appl. Phys.*, vol. 69, no. 2, pp. 668–673, Jan. 1991, doi: 10.1063/1.347347.
[229] Y. Martin, C. C. Williams, and H. K. Wickramasinghe, 'Atomic force microscope–force mapping and profiling on a sub 100-Å scale', *J. Appl. Phys.*, vol. 61, no. 10, pp. 4723–4729, May 1987, doi: 10.1063/1.338807.
[230] M. Nonnenmacher, M. o'Boyle, and H. K. Wickramasinghe, 'Kelvin probe force microscopy', *Appl. Phys. Lett.*, vol. 58, no. 25, pp. 2921–2923, 1991.
[231] Y. Martin and H. K. Wickramasinghe, 'Magnetic imaging by "'force microscopy'" with 1000 Å resolution', *Appl. Phys. Lett.*, vol. 50, no. 20, pp. 1455–1457, May 1987, doi: 10.1063/1.97800.
[232] P. Güthner and K. Dransfeld, 'Local poling of ferroelectric polymers by scanning force microscopy', *Appl. Phys. Lett.*, vol. 61, no. 9, pp. 1137–1139, Aug. 1992, doi: 10.1063/1.107693.
[233] N. S. Malvankar, S. E. Yalcin, M. T. Tuominen, and D. R. Lovley, 'Visualization of charge propagation along individual pili proteins using ambient electrostatic force microscopy', *Nat. Nanotechnol.*, vol. 9, no. 12, pp. 1012–1017, Dec. 2014, doi: 10.1038/nnano.2014.236.
[234] B. J. Rodriguez, C. Callahan, S. V. Kalinin, and R. Proksch, 'Dual-frequency resonance-tracking atomic force microscopy', *Nanotechnology*, vol. 18, no. 47, p. 475504, Oct. 2007, doi: 10.1088/0957-4484/18/47/475504.
[235] M. Knoll and E. Ruska, 'Das Elektronenmikroskop', *Z. Für Phys.*, vol. 79, no. 9, pp. 699–699, Sep. 1932, doi: 10.1007/BF01330526.
[236] M. Knoll, 'Aufladepotentiel und sekundäremission elektronenbestrahlter körper', *Z Techn Phys*, vol. 16, p. 467, 1935.
[237] M. Von Ardenne, 'Das elektronen-rastermikroskop. Praktische ausführung', *Z. Für Tech. Phys.*, vol. 19, no. 11, pp. 407–416, 1938.
[238] M. Von Ardenne, 'Das Elektronen-Rastermikroskop: Theoretische Grundlagen', *Z. Für Phys.*, vol. 109, no. 9–10, pp. 553–572, 1938.
[239] Rayleigh, 'XXXI. Investigations in optics, with special reference to the spectroscope', *Lond. Edinb. Dublin Philos. Mag. J. Sci.*, vol. 8, no. 49, pp. 261–274, Oct. 1879, doi: 10.1080/14786447908639684.

[240] Z. Chen *et al.*, 'Electron ptychography achieves atomic-resolution limits set by lattice vibrations', *Science*, vol. 372, no. 6544, pp. 826–831, May 2021, doi: 10.1126/science.abg2533.
[241] 'Themis Z TEM'. Accessed: Jul. 26, 2023. [Online]. Available: https://assets.thermofisher.com/TFS-Assets/MSD/Datasheets/Themis-Z-Datasheet.pdf
[242] L. A. Giannuzzi and F. A. Stevie, 'A review of focused ion beam milling techniques for TEM specimen preparation', *Micron*, vol. 30, no. 3, pp. 197–204, Jun. 1999, doi: 10.1016/S0968-4328(99)00005-0.
[243] L. Giannuzzi, R. Geurts, and J. Ringnalda, '2 keV Ga+ FIB Milling for Reducing Amorphous Damage in Silicon', *Microsc. Microanal. Off. J. Microsc. Soc. Am. Microbeam Anal. Soc. Microsc. Soc. Can.*, vol. 11, pp. 828–829, Aug. 2005, doi: 10.1017/S1431927605507797.
[244] E. Yücelen, I. Lazić, and E. G. T. Bosch, 'Phase contrast scanning transmission electron microscopy imaging of light and heavy atoms at the limit of contrast and resolution', *Sci. Rep.*, vol. 8, no. 1, p. 2676, Feb. 2018, doi: 10.1038/s41598-018-20377-2.
[245] I. Lazić and E. G. T. Bosch, 'Chapter Three - Analytical Review of Direct Stem Imaging Techniques for Thin Samples', vol. 199, P. W. Hawkes, Ed., in Advances in Imaging and Electron Physics, vol. 199. , Elsevier, 2017, pp. 75–184. doi: https://doi.org/10.1016/bs.aiep.2017.01.006.
[246] R. F. Egerton, 'An Introduction to EELS', in *Electron Energy-Loss Spectroscopy in the Electron Microscope*, R. F. Egerton, Ed., Boston, MA: Springer US, 2011, pp. 1–28. doi: 10.1007/978-1-4419-9583-4_1.
[247] F. Hofer, F. P. Schmidt, W. Grogger, and G. Kothleitner, 'Fundamentals of electron energy-loss spectroscopy', *IOP Conf. Ser. Mater. Sci. Eng.*, vol. 109, no. 1, p. 012007, Jan. 2016, doi: 10.1088/1757-899X/109/1/012007.
[248] B. D. Josephson, 'Possible new effects in superconductive tunnelling', *Phys. Lett.*, vol. 1, no. 7, pp. 251–253, Jul. 1962, doi: 10.1016/0031-9163(62)91369-0.
[249] A. M. Kraft, C. Rupprecht, and Y. C. Yam, 'Superconducting Quantum Interference Device (SQUID)', 2017.
[250] AlbinaY. Borisevich *et al.*, 'Mapping Octahedral Tilts and Polarization Across a Domain Wall in BiFeO3 from Z-Contrast Scanning Transmission Electron Microscopy Image Atomic Column Shape Analysis', *ACS Nano*, vol. 4, no. 10, pp. 6071–6079, Oct. 2010, doi: 10.1021/nn1011539.
[251] M. Campanini *et al.*, 'Imaging and quantification of charged domain walls in $BiFeO_3$', *Nanoscale*, vol. 12, no. 16, pp. 9186–9193, 2020, doi: 10.1039/D0NR01258K.
[252] M. Nord, P. E. Vullum, I. MacLaren, T. Tybell, and R. Holmestad, 'Atomap: a new software tool for the automated analysis of atomic resolution images using two-dimensional Gaussian fitting', *Adv. Struct. Chem. Imaging*, vol. 3, no. 1, p. 9, Feb. 2017, doi: 10.1186/s40679-017-0042-5.
[253] E. N. O'Connell *et al.*, 'TopoTEM: A Python Package for Quantifying and Visualizing Scanning Transmission Electron Microscopy Data of Polar Topologies', *Microsc. Microanal.*, vol. 28, no. 4, pp. 1444–1452, Aug. 2022, doi: 10.1017/S1431927622000435.
[254] E. O'Connell, M. Hennessy, and E. Moynihan, *PinkShnack/TEMUL:Zenodo*. [Online]. Available: 10.5281/zenodo.3832142
[255] F. de la Peña *et al.*, *hyperspy/hyperspy: Release v1.7.3 (v1.7.3). Zenodo*. 2022. [Online]. Available: https://doi.org/10.5281/zenodo.7263263
[256] M. M. J. Treacy, J. M. Newsam, and M. W. Deem, 'A general recursion method for calculating diffracted intensities from crystals containing planar faults', *Proc. R. Soc. Lond. Ser. Math. Phys. Sci.*, vol. 433, no. 1889, pp. 499–520, 1991, doi: 10.1098/rspa.1991.0062.
[257] M. M. J. Treacy, M. W. Deem, and J. M. Newsam, 'DIFFaX Manual'. Jul. 03, 2005. Accessed: Jul. 25, 2023. [Online]. Available: https://www.public.asu.edu/~mtreacy/DIFFaX_manual.pdf

[258] M. García-Guaderrama, L. Fuentes-Montero, A. Rodriguez, and L. Fuentes, 'Structural characterization of $Bi_6Ti_3Fe_2O_{18}$ obtained by molten salt synthesis', *Integr. Ferroelectr.*, vol. 83, no. 1, pp. 41–47, 2006, doi: 10.1080/10584580600949063.
[259] M. Krzhizhanovskaya *et al.*, 'Aurivillius Phases in the $Bi_4Ti_3O_{12}$/$BiFeO_3$ System: Thermal Behaviour and Crystal Structure', *Z. Für Anorg. Allg. Chem.*, vol. 631, no. 9, pp. 1603–1608, 2005, doi: https://doi.org/10.1002/zaac.200500130.
[260] P. Geerlings, F. De Proft, and W. Langenaeker, 'Conceptual Density Functional Theory', *Chem. Rev.*, vol. 103, no. 5, pp. 1793–1874, May 2003, doi: 10.1021/cr990029p.
[261] J. Hafner, 'Ab-initio simulations of materials using VASP: Density-functional theory and beyond', *J. Comput. Chem.*, vol. 29, no. 13, pp. 2044–2078, 2008, doi: https://doi.org/10.1002/jcc.21057.
[262] Y. Yin and Q. Li, 'A review on all-perovskite multiferroic tunnel junctions', *J. Materiomics*, vol. 3, no. 4, pp. 245–254, 2017, doi: https://doi.org/10.1016/j.jmat.2017.09.001.
[263] R. Ramesh and S. Manipatruni, 'Electric field control of magnetism', *Proc. R. Soc. Math. Phys. Eng. Sci.*, vol. 477, no. 2251, p. 20200942, 2021, doi: 10.1098/rspa.2020.0942.
[264] E. Gradauskaite, P. Meisenheimer, M. Müller, J. Heron, and M. Trassin, 'Multiferroic heterostructures for spintronics', *Phys. Sci. Rev.*, vol. 6, no. 2, p. 20190072, 2021, doi: doi:10.1515/psr-2019-0072.
[265] L. Baudry, I. Lukyanchuk, and V. M. Vinokur, 'Ferroelectric symmetry-protected multibit memory cell', *Sci. Rep.*, vol. 7, no. 1, p. 42196, Feb. 2017, doi: 10.1038/srep42196.
[266] S. N. V., K. B. Vinayakumar, and K. K. Nagaraja, 'Magnetoelectric Coupling in Bismuth Ferrite—Challenges and Perspectives', *Coatings*, vol. 10, no. 12, 2020, doi: 10.3390/coatings10121221.
[267] J. F. Scott, 'Room-temperature multiferroic magnetoelectrics', *NPG Asia Mater.*, vol. 5, no. 11, pp. e72–e72, Nov. 2013, doi: 10.1038/am.2013.58.
[268] R. Ramesh, 'Emerging routes to multiferroics', *Nature*, vol. 461, no. 7268, pp. 1218–1219, Oct. 2009, doi: 10.1038/4611218a.
[269] M. Lilienblum, T. Lottermoser, S. Manz, S. M. Selbach, A. Cano, and M. Fiebig, 'Ferroelectricity in the multiferroic hexagonal manganites', *Nat. Phys.*, vol. 11, no. 12, pp. 1070–1073, Dec. 2015, doi: 10.1038/nphys3468.
[270] G. A. Smolenskii and V. A. Bokov, 'Coexistence of Magnetic and Electric Ordering in Crystals', *J. Appl. Phys.*, vol. 35, no. 3, pp. 915–918, Jul. 2004, doi: 10.1063/1.1713535.
[271] Z. J. Huang, Y. Cao, Y. Y. Sun, Y. Y. Xue, and C. W. Chu, 'Coupling between the ferroelectric and antiferromagnetic orders in $YMnO_3$', *Phys Rev B*, vol. 56, no. 5, pp. 2623–2626, Aug. 1997, doi: 10.1103/PhysRevB.56.2623.
[272] M. J. Pitcher *et al.*, 'Tilt engineering of spontaneous polarization and magnetization above 300 K in a bulk layered perovskite', *Science*, vol. 347, no. 6220, pp. 420–424, 2015, doi: 10.1126/science.1262118.
[273] M. Schmidt *et al.*, 'Absence of Evidence ≠ Evidence of Absence: Statistical Analysis of Inclusions in Multiferroic Thin Films', *Sci. Rep.*, vol. 4, no. 1, p. 5712, Jul. 2014, doi: 10.1038/srep05712.
[274] W. S. Choi, M. F. Chisholm, D. J. Singh, T. Choi, G. E. Jellison, and H. N. Lee, 'Wide bandgap tunability in complex transition metal oxides by site-specific substitution', *Nat. Commun.*, vol. 3, no. 1, p. 689, Feb. 2012, doi: 10.1038/ncomms1690.
[275] A. Faraz *et al.*, 'Exploring ferroelectric and magnetic properties of Tb-substituted m = 5 layered Aurivillius phase thin films', *J. Appl. Phys.*, vol. 123, no. 12, Mar. 2018, doi: 10.1063/1.5009986.
[276] N. Lomanova, V. Semenov, V. Panchuk, and V. Gusarov, 'Structural Changes in the Homologous Series of the Aurivillius Phases $Bi_{n+1}Fe_{n-3}Ti_3O_{3n+3}$', *J. Alloys Compd.*, vol. 528, pp. 103–108, Jul. 2012, doi: 10.1016/j.jallcom.2012.03.040.

[277] R. D. Shannon, 'Revised effective ionic radii and systematic studies of interatomic distances in halides and chalcogenides', *Acta Crystallogr. Sect. A*, vol. 32, no. 5, pp. 751–767, Sep. 1976, doi: 10.1107/S0567739476001551.
[278] S. Susarla *et al.*, 'Atomic scale crystal field mapping of polar vortices in oxide superlattices', *Nat. Commun.*, vol. 12, no. 1, p. 6273, Nov. 2021, doi: 10.1038/s41467-021-26476-5.
[279] J. Ding, L. Wen, Y. Liu, and Y. Zhang, 'Origin of ferrimagnetism and the effect of octahedral tilting in double-perovskite compound $Sr_2CoRuO_6$', *J. Magn. Magn. Mater.*, vol. 535, p. 168035, 2021, doi: https://doi.org/10.1016/j.jmmm.2021.168035.
[280] S. G. Jeong *et al.*, 'Propagation Control of Octahedral Tilt in $SrRuO_3$ via Artificial Heterostructuring', *Adv. Sci.*, vol. 7, no. 16, p. 2001643, 2020, doi: https://doi.org/10.1002/advs.202001643.
[281] J. A. Schiemer, R. L. Withers, Y. Liu, and M. A. Carpenter, 'Ca-Doping of $BiFeO_3$: The Role of Strain in Determining Coupling between Ferroelectric Displacements, Magnetic Moments, Octahedral Tilting, and Oxygen-Vacancy Ordering', *Chem. Mater.*, vol. 25, no. 21, pp. 4436–4446, 2013, doi: 10.1021/cm402962q.
[282] A. M. Abakumov *et al.*, 'Frustrated Octahedral Tilting Distortion in the Incommensurately Modulated $Li_{3x}Nd_{2/3-x}TiO_3$ Perovskites', *Chem. Mater.*, vol. 25, no. 13, pp. 2670–2683, 2013, doi: 10.1021/cm4012052.
[283] P. Garcia-Fernandez, J. A. Aramburu, M. T. Barriuso, and M. Moreno, 'Key Role of Covalent Bonding in Octahedral Tilting in Perovskites', *J. Phys. Chem. Lett.*, vol. 1, no. 3, pp. 647–651, 2010, doi: 10.1021/jz900399m.
[284] P. F. Zhang, N. Deepak, L. Keeney, M. E. Pemble, and R. W. Whatmore, 'The structural and piezoresponse properties of c-axis-oriented Aurivillius phase $Bi_5Ti_3FeO_{15}$ thin films deposited by atomic vapor deposition', *Appl. Phys. Lett.*, vol. 101, no. 11, p. 112903, 2012, doi: 10.1063/1.4752007.
[285] M. Schumacher, P. K. Baumann, and T. Seidel, 'AVD and ALD as Two Complementary Technology Solutions for Next Generation Dielectric and Conductive Thin-Film Processing', *Chem. Vap. Depos.*, vol. 12, no. 2–3, pp. 99–108, 2006, doi: https://doi.org/10.1002/cvde.200500027.
[286] A. Faraz *et al.*, 'Direct visualization of magnetic-field-induced magnetoelectric switching in multiferroic aurivillius phase thin films', *J. Am. Ceram. Soc.*, vol. 100, no. 3, pp. 975–987, 2017, doi: https://doi.org/10.1111/jace.14597.
[287] A. Faraz, N. Deepak, M. Schmidt, M. E. Pemble, and L. Keeney, 'A study of the temperature dependence of the local ferroelectric properties of c-axis oriented $Bi_6Ti_3Fe_2O_{18}$ Aurivillius phase thin films: Illustrating the potential of a novel lead-free perovskite material for high density memory applications', *AIP Adv.*, vol. 5, no. 8, p. 087123, 2015, doi: 10.1063/1.4928495.
[288] M. Alexe, J. F. Scott, C. Curran, N. D. Zakharov, D. Hesse, and A. Pignolet, 'Self-patterning nano-electrodes on ferroelectric thin films for gigabit memory applications', *Appl. Phys. Lett.*, vol. 73, no. 11, pp. 1592–1594, 1998, doi: 10.1063/1.122214.
[289] G. Kresse and D. Joubert, 'From ultrasoft pseudopotentials to the projector augmented-wave method', *Phys Rev B*, vol. 59, no. 3, pp. 1758–1775, Jan. 1999, doi: 10.1103/PhysRevB.59.1758.
[290] J. P. Perdew and W. Yue, 'Accurate and simple density functional for the electronic exchange energy: Generalized gradient approximation', *Phys Rev B*, vol. 33, no. 12, pp. 8800–8802, Jun. 1986, doi: 10.1103/PhysRevB.33.8800.
[291] J. P. Perdew, K. Burke, and M. Ernzerhof, 'Generalized Gradient Approximation Made Simple', *Phys Rev Lett*, vol. 77, no. 18, pp. 3865–3868, Oct. 1996, doi: 10.1103/PhysRevLett.77.3865.
[292] S. L. Dudarev, G. A. Botton, S. Y. Savrasov, C. J. Humphreys, and A. P. Sutton, 'Electron-energy-loss spectra and the structural stability of nickel oxide: An LSDA+U study', *Phys Rev B*, vol. 57, no. 3, pp. 1505–1509, Jan. 1998, doi: 10.1103/PhysRevB.57.1505.

[293] Z.-G. Mei, S. Shang, Y. Wang, and Z.-K. Liu, 'Thermodynamics of multiferroic $BiFeO_3$: Applications for the deposition of $BiFeO_3$ thin films', *Appl. Phys. Lett.*, vol. 98, no. 13, p. 131904, Mar. 2011, doi: 10.1063/1.3573809.
[294] L. Craco, S. S. Carara, and S. Leoni, 'Electronic structure of $BiFeO_3$ in the presence of strong electronic correlations', *Phys. Rev. B*, vol. 99, no. 4, p. 045112, Jan. 2019, doi: 10.1103/PhysRevB.99.045112.
[295] H. J. Monkhorst and J. D. Pack, 'Special points for Brillouin-zone integrations', *Phys Rev B*, vol. 13, no. 12, pp. 5188–5192, Jun. 1976, doi: 10.1103/PhysRevB.13.5188.
[296] K. Momma and F. Izumi, '*VESTA 3* for three-dimensional visualization of crystal, volumetric and morphology data', *J. Appl. Crystallogr.*, vol. 44, no. 6, pp. 1272–1276, Dec. 2011, doi: 10.1107/S0021889811038970.
[297] F. M. F. de Groot, M. Grioni, J. C. Fuggle, J. Ghijsen, G. A. Sawatzky, and H. Petersen, 'Oxygen 1s x-ray-absorption edges of transition-metal oxides', *Phys Rev B*, vol. 40, no. 8, pp. 5715–5723, Sep. 1989, doi: 10.1103/PhysRevB.40.5715.
[298] L. F. Kourkoutis *et al.*, 'Atomic-resolution spectroscopic imaging of oxide interfaces', *Philos. Mag.*, vol. 90, pp. 4731–4749, 2010.
[299] J. M. Perez-Mato *et al.*, 'Multiple instabilities in $Bi_4Ti_3O_{12}$ : A ferroelectric beyond the soft-mode paradigm', *Phys. Rev. B*, vol. 77, p. 184104, 2008.
[300] L. Nistor, G. van Tendeloo, and S. Amelinckx, 'The paraelectric-ferroelectric phase transition of $Bi_4Ti_3O_{12}$ studied by electron microscopy', *Phase Transit.*, vol. 59, no. 1–3, pp. 135–153, 1996, doi: 10.1080/01411599608220041.
[301] T. Hirata and T. Yokokawa, 'Variable-temperature X-ray diffraction of the ferroelectric transition in $Bi_4Ti_3O_{12}$', *Solid State Commun.*, vol. 104, no. 11, pp. 673–677, 1997, doi: https://doi.org/10.1016/S0038-1098(97)00401-8.
[302] C. H. Hervoches and P. Lightfoot, 'A Variable-Temperature Powder Neutron Diffraction Study of Ferroelectric $Bi_4Ti_3O_{12}$', *Chem. Mater.*, vol. 11, no. 11, pp. 3359–3364, 1999, doi: 10.1021/cm991090d.
[303] F. Kubel and H. Schmid, 'X-ray room temperature structure from single crystal data, powder diffraction measurements and optical studies of the aurivillius phase $Bi_5(Ti_3Fe)O_{15}$', *Ferroelectrics*, vol. 129, no. 1, pp. 101–112, 1992, doi: 10.1080/00150199208016980.
[304] J. R. Whyte and J. M. Gregg, 'A diode for ferroelectric domain-wall motion', *Nat. Commun.*, vol. 6, no. 1, p. 7361, Jun. 2015, doi: 10.1038/ncomms8361.
[305] P. Sharma *et al.*, 'Nonvolatile ferroelectric domain wall memory', *Sci. Adv.*, vol. 3, no. 6, p. e1700512, 2017, doi: 10.1126/sciadv.1700512.
[306] P. Sharma *et al.*, 'Conformational Domain Wall Switch', *Adv. Funct. Mater.*, vol. 29, no. 18, p. 1807523, 2019, doi: https://doi.org/10.1002/adfm.201807523.
[307] H. Müller-Buschbaum, 'The Crystal Chemistry of High-Temperature Oxide Superconductors and Materials with Related Structures', *Angew. Chem. Int. Ed. Engl.*, vol. 28, no. 11, pp. 1472–1493, 1989, doi: https://doi.org/10.1002/anie.198914721.
[308] N. Deepak, P. F. Zhang, L. Keeney, M. E. Pemble, and R. W. Whatmore, 'Atomic vapor deposition of bismuth titanate thin films', *J. Appl. Phys.*, vol. 113, no. 18, p. 187207, 2013, doi: 10.1063/1.4801985.
[309] A. M. Miller, M. Lemon, M. A. Choffel, S. R. Rich, F. Harvel, and D. C. Johnson, 'Extracting information from X-ray diffraction patterns containing Laue oscillations', *Z. Für Naturforschung B*, vol. 77, no. 4–5, pp. 313–322, 2022, doi: doi:10.1515/znb-2022-0020.
[310] V. S. Kopp *et al.*, 'X-ray diffraction from nonperiodic layered structures with correlations: analytical calculation and experiment on mixed Aurivillius films', *Acta Crystallogr. Sect. A*, vol. 68, no. 1, pp. 148–155, Jan. 2012, doi: 10.1107/S0108767311044874.
[311] E. Thune, A. Fakih, C. Matringe, D. Babonneau, and R. Guinebretière, 'Understanding of one dimensional ordering mechanisms at the (001) sapphire vicinal surface', *J. Appl. Phys.*, vol. 121, no. 1, p. 015301, 2017, doi: 10.1063/1.4973341.

[312] N. Deepak, P. Carolan, L. Keeney, P. F. Zhang, M. E. Pemble, and R. W. Whatmore, 'Bismuth Self-Limiting Growth of Ultrathin $BiFeO_3$ Films', *Chem. Mater.*, vol. 27, no. 19, pp. 6508–6515, 2015, doi: 10.1021/acs.chemmater.5b03034.
[313] M. Mietschke *et al.*, 'Influence of the polarization anisotropy on the electrocaloric effect in epitaxial PMN-PT thin films', *J. Appl. Phys.*, vol. 120, no. 11, p. 114102, 2016, doi: 10.1063/1.4962858.
[314] D. Nečas and P. Klapetek, 'Gwyddion: an open-source software for SPM data analysis', *Open Phys.*, vol. 10, no. 1, pp. 181–188, 2012, doi: doi:10.2478/s11534-011-0096-2.
[315] G. Gottstein, *Physical foundations of materials science*, vol. 3. Springer, 2004.
[316] D. J. Smith and J. L. Hutchison, 'Intergrowths and defect structures in $Bi_9Ti_3Fe_5O_{27}$ revealed by high-resolution electron microscopy', *J. Microsc.*, vol. 129, no. 3, pp. 285–293, 1983, doi: https://doi.org/10.1111/j.1365-2818.1983.tb04185.x.
[317] I. MacLaren *et al.*, 'Novel Nanorod Precipitate Formation in Neodymium and Titanium Codoped Bismuth Ferrite', *Adv. Funct. Mater.*, vol. 23, no. 6, pp. 683–689, 2013, doi: https://doi.org/10.1002/adfm.201201835.
[318] L. Q. Wang, B. Schaffer, I. MacLaren, S. Miao, A. J. Craven, and I. M. Reaney, 'Atomic scale structure and chemistry of anti-phase boundaries in $(Bi_{0.85}Nd_{0.15})(Fe_{0.9}Ti_{0.1})O_3$ceramics', *J. Phys. Conf. Ser.*, vol. 371, no. 1, p. 012036, Jul. 2012, doi: 10.1088/1742-6596/371/1/012036.
[319] M. A. Zurbuchen, G. Asayama, D. G. Schlom, and S. K. Streiffer, 'Ferroelectric Domain Structure of $SrBi_2Nb_2O_9$ Epitaxial Thin Films', *Phys Rev Lett*, vol. 88, no. 10, p. 107601, Feb. 2002, doi: 10.1103/PhysRevLett.88.107601.
[320] R. K. Vasudevan *et al.*, 'Deterministic arbitrary switching of polarization in a ferroelectric thin film', *Nat. Commun.*, vol. 5, no. 1, p. 4971, Sep. 2014, doi: 10.1038/ncomms5971.
[321] N. Balke *et al.*, 'Deterministic control of ferroelastic switching in multiferroic materials', *Nat. Nanotechnol.*, vol. 4, no. 12, pp. 868–875, Dec. 2009, doi: 10.1038/nnano.2009.293.
[322] U. Aschauer, R. Pfenninger, S. M. Selbach, T. Grande, and N. A. Spaldin, 'Strain-controlled oxygen vacancy formation and ordering in $CaMnO_3$', *Phys Rev B*, vol. 88, no. 5, p. 054111, Aug. 2013, doi: 10.1103/PhysRevB.88.054111.
[323] S. Farokhipoor and B. Noheda, 'Local conductivity and the role of vacancies around twin walls of (001)−$BiFeO_3$ thin films', *J. Appl. Phys.*, vol. 112, no. 5, p. 052003, 2012, doi: 10.1063/1.4746073.
[324] A. Snedden, S. M. Blake, and P. Lightfoot, 'Oxide ion conductivity in Ga-doped Aurivillius phases—a reappraisal', *Solid State Ion.*, vol. 156, no. 3, pp. 439–445, 2003, doi: https://doi.org/10.1016/S0167-2738(02)00690-2.
[325] E. E. McCabe and C. Greaves, 'Structural and magnetic characterisation of $Bi_2Sr_{1.4}La_{0.6}Nb_2MnO_{12}$ and its relationship to "$Bi_2Sr_2Nb_2MnO_{12}$"', *J Mater Chem*, vol. 15, no. 1, pp. 177–182, 2005, doi: 10.1039/B413732A.
[326] M. A. Zurbuchen *et al.*, 'Synthesis and characterization of an n=6 Aurivillius phase incorporating magnetically active manganese, $Bi_7(Mn,Ti)_6O_{21}$', *Appl. Phys. Lett.*, vol. 91, no. 3, p. 033113, 2007, doi: 10.1063/1.2756163.
[327] R. Whatmore, 'Ferroelectric Materials', in *Springer Handbook of Electronic and Photonic Materials*, S. Kasap and P. Capper, Eds., Cham: Springer International Publishing, 2017, pp. 1–1. doi: 10.1007/978-3-319-48933-9_26.
[328] L. Keeney *et al.*, 'Ferroelectric Behavior in Exfoliated 2D Aurivillius Oxide Flakes of Sub-Unit Cell Thickness', *Adv. Electron. Mater.*, vol. 6, no. 3, p. 1901264, Mar. 2020, doi: 10.1002/aelm.201901264.
[329] J. S. Speck, A. Seifert, W. Pompe, and R. Ramesh, 'Domain configurations due to multiple misfit relaxation mechanisms in epitaxial ferroelectric thin films. II. Experimental verification and implications', *J. Appl. Phys.*, vol. 76, no. 1, pp. 477–483, Jul. 1994, doi: 10.1063/1.357098.

[330] D. Ichinose, T. Shimizu, O. Sakata, T. Yamada, and H. Funakubo, 'Domain structure transition from two to three dimensions in tensile strained (100)/(001)-oriented epitaxial tetragonal PZT film', *Appl. Phys. Lett.*, vol. 113, no. 13, p. 132905, Sep. 2018, doi: 10.1063/1.5042470.
[331] D. Ichinose, T. Shimizu, O. Sakata, T. Yamada, Y. Ehara, and H. Funakubo, 'Domain structure transition in compressively strained (100)/(001) epitaxial tetragonal PZT film', *J. Appl. Phys.*, vol. 129, no. 2, p. 024101, Jan. 2021, doi: 10.1063/5.0031803.
[332] K. Coleman, J. Walker, T. Beechem, and S. Trolier-McKinstry, 'Effect of stresses on the dielectric and piezoelectric properties of $Pb(Zr_{0.52}Ti_{0.48})O_3$ thin films', *J. Appl. Phys.*, vol. 126, no. 3, p. 034101, Jul. 2019, doi: 10.1063/1.5095765.
[333] G. L. Brennecka, W. Huebner, B. A. Tuttle, and P. G. Clem, 'Use of Stress To Produce Highly Oriented Tetragonal Lead Zirconate Titanate (PZT 40/60) Thin Films and Resulting Electrical Properties', *J. Am. Ceram. Soc.*, vol. 87, no. 8, pp. 1459–1465, Aug. 2004, doi: 10.1111/j.1551-2916.2004.01459.x.
[334] T. Jiang *et al.*, 'Spatial distribution of crystalline quality in N-type GaN grown on patterned sapphire substrate', *Opt. Mater. Express*, vol. 6, no. 6, pp. 1817–1826, Jun. 2016, doi: 10.1364/OME.6.001817.
[335] M. F. Schubert *et al.*, 'Effect of dislocation density on efficiency droop in GaInN⁄GaN light-emitting diodes', *Appl. Phys. Lett.*, vol. 91, no. 23, p. 231114, Dec. 2007, doi: 10.1063/1.2822442.
[336] H. Wang *et al.*, 'Dome-shaped patterned sapphire substrate with optimized curvature to enhance the efficacy of light emitting diodes', *RSC Adv.*, vol. 4, no. 79, pp. 41942–41946, 2014, doi: 10.1039/C4RA04053H.
[337] L. Keeney and I. M. Povey, 'Vapor Phase Growth of Metal-Oxide Thin Films and Nanostructures', in *Tailored Functional Oxide Nanomaterials*, John Wiley & Sons, Ltd, 2022, pp. 1–42. doi: https://doi.org/10.1002/9783527826940.ch1.
[338] T. Maity, S. Goswami, D. Bhattacharya, and S. Roy, 'Superspin Glass Mediated Giant Spontaneous Exchange Bias in a Nanocomposite of \mathrmBiFeO_3\mathrm\text\ensuremath-\mathrmBi_2\mathrmFe_4\mathbfO_9', *Phys Rev Lett*, vol. 110, no. 10, p. 107201, Mar. 2013, doi: 10.1103/PhysRevLett.110.107201.
[339] L. Keeney, P. F. Zhang, C. Groh, M. E. Pemble, and R. W. Whatmore, 'Piezoresponse force microscopy investigations of Aurivillius phase thin films', *J. Appl. Phys.*, vol. 108, no. 4, p. 042004, Aug. 2010, doi: 10.1063/1.3474959.
[340] S. Sun and X. Yin, 'Progress and Perspectives on Aurivillius-Type Layered Ferroelectric Oxides in Binary $Bi_4Ti_3O_{12}$-$BiFeO_3$ System for Multifunctional Applications', *Crystals*, vol. 11, no. 1, 2021, doi: 10.3390/cryst11010023.
[341] F. K. Lotgering, 'Topotactical reactions with ferrimagnetic oxides having hexagonal crystal structures—I', *J. Inorg. Nucl. Chem.*, vol. 9, no. 2, pp. 113–123, Feb. 1959, doi: 10.1016/0022-1902(59)80070-1.
[342] I. Ismailzade, V. Nesterenko, F. Mirishli, and P. Rustamov, 'X-ray Diffraction Study of the $Bi_4Ti_3O_{12}$–$BiFeO_3$ System', *Kristallografiya*, vol. 12, no. 3, pp. 468–473, 1967.
[343] S. Sun *et al.*, 'Structural and Physical Properties of Mixed-Layer Aurivillius-Type Multiferroics', *J. Am. Ceram. Soc.*, vol. 99, no. 9, pp. 3033–3038, Sep. 2016, doi: 10.1111/jace.14312.
[344] S. Sun *et al.*, 'The nanoscale control of disorder-to-order layer-stacking boosts multiferroic responses in an Aurivillius-type layered oxide', *J. Mater. Chem. C*, vol. 9, no. 14, pp. 4825–4837, 2021, doi: 10.1039/D1TC00309G.
[345] N. A. Lomanova, 'Aurivillius Phases $Bi_{m+1}Fe_{m-3}Ti_3O_{3m+3}$: Synthesis, Structure, and Properties (a Review)', *Russ. J. Inorg. Chem.*, vol. 67, no. 6, pp. 741–753, Jun. 2022, doi: 10.1134/S0036023622060146.
[346] M. García-Guaderrama, L. Fuentes, A. Márquez-Lucero, and O. Blanco, 'Structural stability and cation disorder in Aurivillius phases', *Mater. Res. Bull.*, vol. 47, no. 11, pp. 3850–3854, Nov. 2012, doi: 10.1016/j.materresbull.2012.08.038.

[347] S. Palchoudhury, M. Baalousha, and J. R. Lead, 'Chapter 5 - Methods for Measuring Concentration (Mass, Surface Area and Number) of Nanomaterials', in *Frontiers of Nanoscience*, vol. 8, M. Baalousha and J. R. Lead, Eds., Elsevier, 2015, pp. 153–181. doi: 10.1016/B978-0-08-099948-7.00005-1.
[348] A. Y. Birenbaum and C. Ederer, 'Controlling the cation distribution and electric polarization with epitaxial strain in Aurivillius-phase $Bi_5FeTi_3O_{15}$', *Appl. Phys. Lett.*, vol. 108, no. 8, p. 082903, Feb. 2016, doi: 10.1063/1.4942668.
[349] Ł. Kurzawski and K. Malarz, 'Simple Cubic Random-Site Percolation Thresholds for Complex Neighbourhoods', *Rep. Math. Phys.*, vol. 70, no. 2, pp. 163–169, Oct. 2012, doi: 10.1016/S0034-4877(12)60036-6.
[350] A. Y. Birenbaum, A. Scaramucci, and C. Ederer, 'Magnetic order in four-layered Aurivillus phases', *Phys. Rev. B*, vol. 95, no. 10, p. 104419, Mar. 2017, doi: 10.1103/PhysRevB.95.104419.
[351] P. Mandal *et al.*, 'Designing switchable polarization and magnetization at room temperature in an oxide', *Nature*, vol. 525, no. 7569, pp. 363–366, Sep. 2015, doi: 10.1038/nature14881.
[352] J. Halpin, 'Synthesis and Characterisation of Aurivillius Phase Materials', University College Cork, 2021.
[353] X. Liang *et al.*, 'Roadmap on Magnetoelectric Materials and Devices', *IEEE Trans. Magn.*, vol. 57, no. 8, pp. 1–57, Aug. 2021, doi: 10.1109/TMAG.2021.3086635.
[354] O. Yu. Gorbenko, S. V. Samoilenkov, I. E. Graboy, and A. R. Kaul, 'Epitaxial Stabilization of Oxides in Thin Films', *Chem. Mater.*, vol. 14, no. 10, pp. 4026–4043, Oct. 2002, doi: 10.1021/cm021111v.
[355] N. Sinha *et al.*, 'Piezoelectric aluminum nitride nanoelectromechanical actuators', *Appl. Phys. Lett.*, vol. 95, no. 5, p. 053106, Aug. 2009, doi: 10.1063/1.3194148.
[356] M. Ueda *et al.*, 'Development of an X-Band Filter Using Air-Gap-Type Film Bulk Acoustic Resonators', *Jpn. J. Appl. Phys.*, vol. 47, no. 5S, p. 4007, May 2008, doi: 10.1143/JJAP.47.4007.
[357] Z. Quan, M. Wang, X. Zhang, H. Liu, W. Zhang, and X. Xu, 'Excellent ferroelectricity of 50 nm-thick doped HfO2 thin films induced by annealing with a rapid-heating-temperature process', *AIP Adv.*, vol. 10, no. 8, p. 085024, Aug. 2020, doi: 10.1063/5.0013511.
[358] S. D. Mahapatra *et al.*, 'Piezoelectric Materials for Energy Harvesting and Sensing Applications: Roadmap for Future Smart Materials', *Adv. Sci.*, vol. 8, no. 17, p. 2100864, Sep. 2021, doi: 10.1002/advs.202100864.
[359] P. Scherrer, 'Nachr Ges wiss goettingen', *Math Phys*, vol. 2, pp. 98–100, 1918.
[360] G. D. Palkar, D. N. Sitharamarao, and A. K. Dasgupta, 'Self-diffusion of bismuth in bismuth oxide', *Trans Faraday Soc*, vol. 59, no. 0, pp. 2634–2638, 1963, doi: 10.1039/TF9635902634.
[361] S. Shimada, K. Kodaira, and T. Matsushita, 'Crystal growth of bismuth titanates and titanium oxide from melts in the system $Bi_2O_3$-$V_2O_5$-$TiO_2$', *J. Cryst. Growth*, vol. 41, no. 2, pp. 317–320, 1977.
[362] I. N. Stranski and L. Krastanow, 'Zur Theorie der orientierten Ausscheidung von Ionenkristallen aufeinander', *Monatshefte Für Chem. Verwandte Teile Anderer Wiss.*, vol. 71, no. 1, pp. 351–364, Dec. 1937, doi: 10.1007/BF01798103.
[363] F. C. Frank, J. H. van der Merwe, and N. F. Mott, 'One-dimensional dislocations. I. Static theory', *Proc. R. Soc. Lond. Ser. Math. Phys. Sci.*, vol. 198, no. 1053, pp. 205–216, 1949, doi: 10.1098/rspa.1949.0095.
[364] J. Nordlander, M. D. Rossell, M. Campanini, M. Fiebig, and M. Trassin, 'Epitaxial integration of improper ferroelectric hexagonal $YMnO_3$ thin films in heterostructures', *Phys. Rev. Mater.*, vol. 4, no. 12, p. 124403, Dec. 2020, doi: 10.1103/PhysRevMaterials.4.124403.
[365] G. W. Brown, M. E. Hawley, C. D. Theis, J. Yeh, and D. G. Schlom, 'Atomic force microscopy examination of the evolution of the surface morphology of $Bi_4Ti_3O_{12}$ grown by molecular beam epitaxy', *Thin Solid Films*, vol. 357, no. 1, pp. 13–17, Dec. 1999, doi: 10.1016/S0040-6090(99)00466-6.

[366] A. D. Rae, J. G. Thompson, R. L. Withers, and A. C. Willis, 'Structure refinement of commensurately modulated bismuth titanate, $Bi_4Ti_3O_{12}$', *Acta Crystallogr. Sect. B*, vol. 46, no. 4, pp. 474–487, Aug. 1990, doi: 10.1107/S0108768190003251.
[367] L. Keeney, L. Colfer, D. Dutta, M. Schmidt, and G. Wei, 'What lies beneath? Investigations of atomic force microscopy-based nano-machining to reveal sub-surface ferroelectric domain configurations in ultrathin films', *Microstruct. Accept.*, vol. 3, Sep. 2023, doi: 10.20517/microstructures.2023.41.
[368] M. Fleischer and W. E. Richmond, 'The manganese oxide minerals, a preliminary report', *Econ. Geol.*, vol. 38, no. 4, pp. 269–286, Jun. 1943, doi: 10.2113/gsecongeo.38.4.269.
[369] P D Battle, C R A Catlow, J Drennan, and A D Murray, 'The structural properties of the oxygen conducting δ phase of $Bi_2O_3$', *J. Phys. C Solid State Phys.*, vol. 16, no. 17, p. L561, Jun. 1983, doi: 10.1088/0022-3719/16/17/003.
[370] D. Hesse, N. D. Zakharov, A. Pignolet, A. R. James, and S. Senz, 'TEM Cross-Section Investigations of Epitaxial $Ba_2Bi_4Ti_5O_{18}$ Thin Films on $LaNiO_3$ Bottom Electrodes on $CeO_2$/YSZ-Buffered Si(100)', *Cryst. Res. Technol.*, vol. 35, no. 6–7, pp. 641–651, Jul. 2000, doi: 10.1002/1521-4079(200007)35:6/7<641::AID-CRAT641>3.0.CO;2-Z.
[371] P. T. Mathew, B. J. Rodriguez, and F. Fang, 'Atomic and Close-to-Atomic Scale Manufacturing: A Review on Atomic Layer Removal Methods Using Atomic Force Microscopy', *Nanomanufacturing Metrol.*, vol. 3, no. 3, pp. 167–186, Sep. 2020, doi: 10.1007/s41871-020-00067-2.
[372] F. Zhang *et al.*, 'Investigation of AFM-based machining of ferroelectric thin films at the nanoscale', *J. Appl. Phys.*, vol. 127, no. 3, p. 034103, Jan. 2020, doi: 10.1063/1.5133018.
[373] T.-J. Park, S. Sambasivan, D. A. Fischer, W.-S. Yoon, J. A. Misewich, and S. S. Wong, 'Electronic Structure and Chemistry of Iron-Based Metal Oxide Nanostructured Materials: A NEXAFS Investigation of $BiFeO_3$, $Bi_2Fe_4O_9$, α-$Fe_2O_3$, γ-$Fe_2O_3$, and Fe/$Fe_3O_4$', *J. Phys. Chem. C*, vol. 112, no. 28, pp. 10359–10369, 2008, doi: 10.1021/jp801449p.
[374] R. Sæterli, S. M. Selbach, P. Ravindran, T. Grande, and R. Holmestad, 'Electronic structure of multiferroic $BiFeO_3$ and related compounds: Electron energy loss spectroscopy and density functional study', *Phys Rev B*, vol. 82, no. 6, p. 064102, Aug. 2010, doi: 10.1103/PhysRevB.82.064102.
[375] J. B. Goodenough, *Magnetism and the chemical bond*, vol. 1. Interscience publishers, 1963.
[376] J. B. Goodenough, 'Jahn-Teller Phenomena in Solids', *Annu. Rev. Mater. Sci.*, vol. 28, no. 1, pp. 1–27, 1998, doi: 10.1146/annurev.matsci.28.1.1.
[377] B. Gilbert *et al.*, 'Multiple Scattering Calculations of Bonding and X-ray Absorption Spectroscopy of Manganese Oxides', *J. Phys. Chem. A*, vol. 107, no. 16, pp. 2839–2847, 2003, doi: 10.1021/jp021493s.
[378] L. A. J. Garvie and A. J. Craven, 'High-resolution parallel electron energy-loss spectroscopy of Mn $L_{2,3}$-edges in inorganic manganese compounds', *Phys. Chem. Miner.*, vol. 21, no. 4, pp. 191–206, Aug. 1994, doi: 10.1007/BF00202132.
[379] H. Tan, J. Verbeeck, A. Abakumov, and G. V. Tendeloo, 'Oxidation state and chemical shift investigation in transition metal oxides by EELS', *Ultramicroscopy*, vol. 116, pp. 24–33, 2012, doi: https://doi.org/10.1016/j.ultramic.2012.03.002.
[380] L. A. J. Garvie and P. R. Buseck, 'Ratios of ferrous to ferric iron from nanometre-sized areas in minerals', *Nature*, vol. 396, no. 6712, pp. 667–670, Dec. 1998, doi: 10.1038/25334.
[381] C. Colliex, T. Manoubi, and C. Ortiz, 'Electron-energy-loss-spectroscopy near-edge fine structures in the iron-oxygen system', *Phys Rev B*, vol. 44, no. 20, pp. 11402–11411, Nov. 1991, doi: 10.1103/PhysRevB.44.11402.
[382] G. van der Laan and I. W. Kirkman, 'The 2p absorption spectra of 3d transition metal compounds in tetrahedral and octahedral symmetry', *J. Phys. Condens. Matter*, vol. 4, no. 16, p. 4189, Apr. 1992, doi: 10.1088/0953-8984/4/16/019.

[383] L. Li *et al.*, 'Defect-Induced Hedgehog Polarization States in Multiferroics', *Phys Rev Lett*, vol. 120, no. 13, p. 137602, Mar. 2018, doi: 10.1103/PhysRevLett.120.137602.